

Copyright

By

Jorge Andrés Ramos Grez

2003

This Dissertation Committee for Jorge Andrés Ramos Grez  
Certifies that this is the approved version of the following dissertation:

**SURFACE MODIFICATION OF CERAMIC AND METALLIC ALLOY  
SUBSTRATES BY LASER RASTER-SCANNING**

**Committee:**

---

David L. Bourell, Supervisor

---

Joseph J. Beaman

---

John R. Howell

---

Desiderio Kovar

---

Arumugan Manthiram

**SURFACE MODIFICATION OF CERAMIC AND METALLIC ALLOY  
SUBSTRATES BY LASER RASTER-SCANNING**

**by**

**Jorge Andrés Ramos Grez, B.S.MechEng.; M.S.Eng.; M.S.**

**Dissertation**

Presented to the Faculty of the Graduate School of

the University of Texas at Austin

in Partial Fulfillment

of the Requirements

for the Degree of

**Doctor of Philosophy**

**The University of Texas at Austin**

**December 2003**

## **Dedication**

*To my adorable and beloved Sole, Catita and Benjamín  
for the countless moments I was absent from home  
while pursuing my doctoral degree.*

## **Acknowledgements**

First of all I would like to acknowledge specially my supervising professor, Dr. David L. Bourell, for his dedicated guidance throughout these last four years. I also want to express my gratitude to Dr. Joseph J. Beaman, Chairman of the Mechanical Engineering Department, for being part of my doctoral committee and allowing me to be a member of the Laboratory of Freeform Fabrication (LFF).

My most sincere gratitude goes to the remaining members of the doctoral committee: Dr. Desiderio Kovar, Dr. Aramugan Manthiram and Dr. John Howell for the willingness to help me answer many questions that I encountered during my research as well as for revising this manuscript.

I would also like to acknowledge Dr. Kris Wood, Director of the LFF, for providing continuous funding through several research projects during most of my graduate years as well as to Cindy Pflughoft for solving all kind of administrative issues I encountered during my research.

My most sincere thanks to Dr. Suman Das for rigorously explaining me the use of the high temperature work stations available at the LFF. To Dr. Madhav Rao Govindaraju and Mr. Sonny West, from Karta Technologies, Inc., San Antonio, Texas, and to Dr. Ozden Ochoa, Professor at Texas A&M Mechanical Engineering Department, for their endless technical and emotional support on the “Carbon-Carbon Composites Laser Fusion Coatings” project that was funded by Karta Technologies,

Inc. To Mr. Timothy Fuesting from Rolls-Royce North America, Indianapolis, Indiana for providing useful suggestions as well as funding for the "Direct Laser Single layer Deposits" project.

To the Office of Naval Research for funding the project "Surface Engineering for SFF Processes", Grant N°: N00014-00-1-0334. I would also like to thanks 3D Systems, Inc. (former DTM Corporation) for providing LaserForm ST-100™ samples for testing.

To Mr. Jeremy Murphy for his direct and acute collaboration in producing the Mar-M 247 single layer deposits, as well as for the early surface roughness measurements he performed on the laser polished indirect-SLS surfaces.

To Dr. Hideki Kyogoku, Kinki University, HigashiHiroshima, Japan for letting me participate of his TiNi shape memory alloy research as well as to Dr. Virendra Bansal, Kanpur Institute of Technology, Kanpur, India for the useful discussion on solidification theory of laser fused TiC coatings.

I would like to acknowledge my wife Soledad Cahis for the meticulous schematic drawings and graphs she helped me prepare and that I proudly included in this dissertation manuscript.

Last but not least my sincere wishes of gratitude and success to all my fellow graduate colleagues, faculty members and professors that I met during my 4 years at the Materials Science and Engineering Program at The University of Texas Austin for their enriching suggestions and unforgettable philosophical discussions.

**SURFACE MODIFICATION OF CERAMIC AND METALLIC ALLOY  
SUBSTRATES BY LASER RASTER-SCANNING**

Publication No. \_\_\_\_\_

Jorge Andrés Ramos Grez, Ph.D.

The University of Texas at Austin, 2003

Supervisor : David L. Bourell

This work describes the feasibility of continuous wave laser-raster scanning processing under controlled atmospheric conditions as employed in three distinct surface modification processes: (a) surface roughness reduction of indirect-Selective Laser Sintered 420 martensitic stainless steel-40 wt. % bronze infiltrated surfaces (b) Si-Cr-Hf-C coating consolidation over 3D carbon-carbon composites cylinders (c) dendritic solidification structures of Mar-M 247 confined powder precursor grown from polycrystalline Alloy 718 substrates. A heat transfer model was developed to illustrate that the aspect ratio of the laser scanned pattern and the density of scanning lines play a significant role in determining peak surface temperature, heating and cooling rates and melt resident times. Comprehensive characterization of the surface of the processed specimens was performed using scanning electron microscopy

(SEM), energy dispersive spectroscopy (EDS), optical metallography, X-ray diffraction (XRD), and, in certain cases, tactile profilometry. In Process (a), it was observed that a 24 % to 37 % roughness  $R_a$  reduction could be accomplished from the as-received value of  $2.50 \pm 0.10$  microns for laser energy densities ranging from 350 to  $500 \text{ J/cm}^2$ . In Process (b), complete reactive wetting of carbon-carbon composite cylinders surface was achieved by laser melting a Si-Cr-Hf-C slurry. Coatings showed good thermal stability at  $1000^\circ\text{C}$  in argon, and, when tested in air, a percent weight reduction rate of  $-6.5 \text{ wt.\%/hr}$  was achieved. A soda-glass overcoat applied over the coated specimens by conventional means revealed a percent weight reduction rate between  $-1.4$  to  $-2.2 \text{ wt.\%/hr}$ . Finally, in Process (c), microstructure of the Mar-M 247 single layer deposits, 1 mm in height, grown on Alloy 718 polycrystalline sheets, resulted in a sound metallurgical bond, low porosity, and uniform thickness. Polycrystalline dendrites grew preferentially along the [001] direction from the substrate up to 400 microns. Above that height, dendrites appear to shift towards the [100] growth direction driven by the thermal gradient and solidification front velocity. This research demonstrated that surface modification by high-speed raster-scanning a high power laser beam under controlled atmospheric conditions is a feasible and versatile technique that can accomplish diverse purposes involving metallic as well as ceramic surfaces.



## Table of Contents

List of Tables	xvii
List of Figures	xviii
Chapter I. Introduction	1
1.1 Background and motivation	1
1.2 Research approach and dissertation structure	3
1.3 Surface modifications by laser melting	5
1.3.1 Addition of coating elements to substrates that undergo melting	6
1.3.1.1 Illustrative case study: Cr-Ni coating onto a 347H stainless steel substrate by raster scanning a laser beam	9
1.3.2 Addition of coating elements to substrates that do not undergo melting	12
1.3.2.1 Illustrative case study: SiC-Cr coating on C/C composite tubes by conventional laser cladding	14
1.3.3 Laser induced surface rippling during melting	17
1.4 Laser surface polishing of indirect-SLS metallic parts	19
1.4.1 Surface shallow melting regime	23
1.4.2 Surface over melting regime	27
1.5 Laser fused ceramic coatings on Carbon-Carbon composites	29
1.6 Direct laser solidified MAR-M 247 superalloy	32
1.7 References	35

Chapter II. Theoretical Background	39
2.1 Mechanics of a raster-scanned laser beam: interaction with a flat surface	39
2.1.1 Energy density relationship between a line and raster scan sources	40
2.1.2 Surface temperature evolution during laser scanning	45
2.1.2.1 Illustration of numerical results	52
2.1.3 Advantages of a raster-scan beam delivery system	55
2.1.4 Surface features observed after laser melting by raster scanning	59
2.2 Laser surface polishing mechanisms: modeling the melting regimes	63
2.2.1 Analytical modeling of Surface Shallow Melting	63
2.2.1.1 Energetics of the model	65
2.2.1.2 Kinetics of the model	69
2.2.1.3 Arithmetic average surface roughness estimation	73
2.2.2 Analytical modeling of Surface Over Melting	74
2.2.3 Envelopment solidification of LaserForm ST-100 <sup>TM</sup> indirect-SLS material	81
2.2.4 Surface smoothing by oxides formation during the melt residence time	85
2.2.5 Summary of surface modification mechanisms	88
2.3 Laser fusion coatings of C/C composites	91
2.3.1 Laser processing of ceramics	92
2.3.2 Wetting and bonding during laser coating of C/C composites	93
2.3.2.1 Rate of spreading at the initiation of wetting under a laser beam	95

2.3.2.2 Interfacial bond strength	101
2.3.2.3 Reactive wetting	103
2.3.3 Thermal stress and thermal shock effect on coatings	105
2.3.3.1 The coefficient of thermal expansion	106
2.3.3.2 Thermal stresses and shock resistance of coatings	107
2.3.3.3 Conditions for crack growth	109
2.3.4 Thermal stress distribution in cylindrical coatings	112
2.3.4.1 Stress distribution in a two-layer cylinder during cooling	113
2.3.4.2 Thermal distribution in a two-layer cylinder during cooling	118
2.3.5 Criteria to determine formation of certain cracking patterns on coatings	121
2.3.6 Changes in crack growth orientation in coatings	124
2.3.7 Measurement of the critical fracture toughness in thin brittle coatings	126
2.3.7.1 Stress intensity factor for a center-loaded half-penny shape crack	127
2.3.7.2 Direct-crack measurement indentation technique	129
2.3.8 Multi-layer coatings for C/C composites	132
2.3.8.1 Binary phase diagram analysis	137
2.3.8.2 Initial chromium layer	141
2.3.8.3 Intermediate refractory layer	141
2.3.8.4 Use of metal chloride salts	143
2.3.8.5 External glassy layer: a crack sealant approach	145

2.3.9 Performance of coated C/C composite cylinders	146
2.3.9.1 Weight loss test	147
2.3.9.2 Thermomechanical analysis	148
2.3.9.3 Differential temperature analysis	148
2.4 Directionally grown superalloy deposits by laser melting	149
2.4.1 Solidification during raster scan laser melting	149
2.4.1.1 Solidification growth stability	153
2.4.1.2 Columnar growth reorientation	154
2.4.1.3 Columnar to equiaxed transition	155
2.4.2. Estimation of the thermal gradient in the melt	157
2.5 References	158
Chapter III. Experimental	164
3.1 Description of the laser processing hardware	164
3.1.1 CO2 laser based processing apparatus	165
3.1.2 Nd: YAG laser based processing apparatus	170
3.2 Laser polishing of indirect-SLS metal surfaces	172
3.2.1 Surface roughness measurements	174
3.2.2 Laser polishing methodology	176
3.2.3 Surface profilometry at the laser polished tracks	177
3.2.4 SEM and EDAX analysis of polished specimens	178
3.2.5 X-ray diffraction analysis	179

3.3 Coating cylindrical C/C composites by “Laser Induced Cementation”	179
3.3.1 Laser coating methodology	180
3.3.2 Glass sealant coating methodology	186
3.3.3 Weight loss testing to determine oxidation resistance	187
3.3.4 Light optical microscopy, SEM and EDAX analysis of coated specimens	188
3.3.5 X-ray diffraction analysis	189
3.3.6 Indentation crack measurement for fracture toughness determination	190
3.3.7 Thermo mechanical and differential thermal analysis	192
3.4 “Powder Masking” technique for laser directional solidification	193
3.4.1 Sample preparation and process description	196
3.4.2 Characterization techniques	197
3.5 Additional laser surface engineering projects	198
3.5.1 Coating of 347H stainless steel slab specimens	199
3.5.2 Coating of planar C/C composites	201
3.5.3 Casting of a shape memory alloy by laser melting	203
3.5.4 Laser cladding of C/C composite tubes	204
3.5.5 Linear motion device for coating slab specimens	207
3.6 References	209
Chapter IV. Results and Discussion	211
4.1 Laser polished Fe - Cu indirect-SLS parts	211

4.1.1 LaserForm ST-100™ surface morphology	211
4.1.2 Processing parameters	213
4.1.3 Surface roughness measurements	215
4.1.4 SEM and EDAX cross sectional analysis	221
4.1.5 SEM and EDAX surface analysis	229
4.1.5.1 Low laser power range	229
4.1.5.2 High laser power range	238
4.1.6 X-ray diffraction analysis	252
4.1.7 Modeling results	253
4.1.7.1 Surface temperature evolution	254
4.1.7.2 Surface shallow melting	259
4.1.7.3 Surface over melting	265
4.2 Laser Induced Cementation of cylindrical C/C composites	270
4.2.1 Preliminary results: planar C/C composite surfaces	271
4.2.2 Refractory coatings achieved on C/C composites cylinders	283
4.2.2.1 Overall shape and appearance refractory coatings	283
4.2.2.2 Light optical microscopy of bulk microstructure of refractory coatings	292
4.2.2.3 Scanning electron microcopy of surface and bulk microstructure of refractory coatings	297

4.2.2.4 EDAX spectra and mapping of coating phases	328
4.2.2.5 X-ray diffraction analysis	338
4.2.2.6 Determination of the coefficient of linear thermal expansion	345
4.2.2.7 Differential thermal analysis	349
4.2.2.8 Determination of the fracture toughness of a laser processed coating	351
4.2.2.9 Coating fracture analysis	352
4.2.2.10 Weight loss oxidation testing	365
4.3 Single layer superalloy deposits by powder masking technique	371
4.3.1 Optical macrographs and micrographs of deposits	371
4.3.2 Optical micrographs of dendritic structure	375
4.3.3 Plot of maximum growth rate (G) versus maximum rate of solidification (R )	379
4.4 References	381
Chapter V. Conclusions and Suggestions	383
5.1 Laser polished Fe - Cu indirect-SLS parts	383
5.1.1 Surface roughness modeling	385
5.1.1.1 Surface shallow melting	385
5.1.1.2 Surface over melting	385
5.1.2 Suggestions for future work	386
5.2 Oxidation protection barrier coatings for C/C composites	387
5.2.1 Suggestions for future work	391

5.3 Directionally grown superalloy deposits	392
5.3.1 Suggestions for future work	393
5.4 Mechanics of the laser raster-scanning surface interaction	394
5.5 References	395
Appendix A-I. Modeling code for laser raster-scan temperature history	396
Appendix A-II. Modeling code for surface shallow melting	400
Appendix A-III. Modeling code for surface over melting	408
Appendix A-IV. Modeling code for fracture criteria	415
Appendix B-I. Processing parameters used in surface polishing of flat surfaces and surface roughness measurement results	431
Appendix B-II. Processing parameters used in laser fusion coatings of C/C flat specimens and laser induced cementation of C/C composite cylinders	435
Appendix B-III. Process parameters of single layer laser powder masked deposits	441
References	442
Vita	450



## List of Tables

Table 4.1. Operational window used in CO <sub>2</sub> laser polishing trials of indirect-SLS parts. The material system considered is 60 wt.% 420 stainless steel-40 wt.% bronze.	214
Table 4.2. Semi-quantitative chemical analysis (atomic %) of the surface of as-received and laser polished surface parts.	252
Table 4.3. Definition of variables used in modeling the SSM mechanism.	261
Table 4.4. Definition of variables used in modeling the SOM mechanism.	266
Table 4.5. Crack propagation criterion based on coating thickness and time of cooling.	360

## List of Figures

Figure 1.1.	Schematic drawing of the selective laser surface processing experimental set up.	10
Figure 1.2.	Optical micrograph of Specimen #16 longitudinal section of Cr-Ni coating-substrate interface, as-coated, x200.	11
Figure 1.3.	Optical micrograph of Specimen #5 showing Cr-Ni coating-substrate interface cross-section, no heat treatment, x200.	11
Figure 1.4.	Close up image of a typical laser cladding head and a C/C composite tube mounted on rotary shaft.	15
Figure 1.5.	SEM image of the cross section of tube #1 at 100x, showing cracks, pores and an uneven coating surface.	16
Figure 1.6.	SEM image of the cross section of tube #1 at 500x, showing a damaged substrate as well as porosity in the coating.	16
Figure 1.7.	SEM image of laser Cr-Ni coating surface morphology, as-coated, 2500x.	18
Figure 1.8.	Laser rippling formation on a 347H stainless steel laser raster scan remelted surface, 80x.	19
Figure 1.9.	Schematic diagram of the laser polishing process.	23
Figure 1.10.	SEM image of as-received 420 stainless steel-40 wt.% bronze indirect-SLS sample surface, 1000x.	24
Figure 1.11.	(a) SEM image of 240 W Nd:YAG laser polished 420 stainless steel-40 wt.% bronze indirect-SLS slab, 60x; (b) SEM image of interface zone of same sample, 200x.	26
Figure 1.12.	Schematics of the liquid transport with ascending time, $t_d > t_c > t_b > t_a$ .	27
Figure 1.13.	Schematic of a surface periodic structure formation during SOM mechanism.	28
Figure 1.14.	Schematic distribution of reinforced C/C (RCC) panels and reusable surface insulation (RSI) tiles in a space orbiter [adapted from 33].	30
Figure 2.1.	Schematic of the typical laser raster-scan fusion coating process.	41
Figure 2.2.	Schematic illustration of the overlapping of raster scans tracks.	43

Figure 2.3.	Typical heating cycle followed by the corresponding cooling cycle after the source is turned off or displaced from the location.	48
Figure 2.4.	Typical sequence of heating and cooling cycle when a complete back and forth raster scan is performed.	52
Figure 2.5.	Surface temperatures at a fixed position versus interaction time for raster-scan processing and line-source processing for 3 different processes.	54
Figure 2.6.	Infrared thermal image of raster scanned laser beam over carbon-carbon composite substrate. The average temperature in the hot zone is 1160 °C.	58
Figure 2.7.	Longitudinal and traverse temperature profiles along the thickness and width of the rectangular zone respectively as shown in Figure 2.6.	58
Figure 2.8.	Selective laser surface melting of (a) Specimen #9 using single-line with 57 % of overlap and (b) Specimen #7 using a raster-scanned with 30 % overlap.	59
Figure 2.9.	Macrograph of the surface of Cr-Ni coated Specimen #16, showing several of the resulting selective laser raster-scanned tracks, 10x.	60
Figure 2.10.	SEM image of longitudinal section of a TiC coating on 347H stainless steel laser raster-scanned, 4000x.	61
Figure 2.11.	SEM image of a longitudinal section of a TiC-50at.% Ni on 347H stainless steel, 50x.	62
Figure 2.12.	Schematic of laser polishing mechanism. (a) Schematic of hemispherical cap surface prior to laser impingement on the surface; (b) Schematic of the surface after the laser has melted the caps.	65
Figure 2.13.	Schematics of the model. (a) Domain for the lumped energy balance. (b) Neighboring close packed spherical segments embedded inside a triangular slab.	67
Figure 2.14.	Schematic of the relationship between radial melt depth, $R - r_m$ , and filled trough height, $z_f$ .	69
Figure 2.15.	Free body diagram of pressure forces acting at the surface of the melt.	70
Figure 2.16.	Schematic representation of the solidifying front during solidification of a melted particle.	72

Figure 2.17.	Schematic drawings for the determination of the surface roughness $R_a$ value. Idealized cross section after laser polishing.	74
Figure 2.18.	Schematic of the rippling phenomenon encountered in the SOM mechanism (based on Anthony and Cline [11]).	75
Figure 2.19.	Phase dia gram of Fe-Cu system (from Hansen [18]).	83
Figure 2.20.	Fe-Cu-Cr vertical section at 10 wt.% Cr (from Raghavan [19]).	85
Figure 2.21.	Ellingham diagram, showing the variation of free energy with temperature for certain oxides (adapted from Gaskell [20] & Khanna [21]).	87
Figure 2.22.	Schematic drawing of the sequence of surface modification mechanisms.	89
Figure 2.23.	Schematic of the lateral force exerted on liquid surface by the laser beam.	97
Figure 2.24.	Schematic of the laser assisted wetting process at a rough interface	101
Figure 2.25.	Illustration of the stress-state developed at the interface of a thin cylindrical coating.	113
Figure 2.26.	Schematic illustration of the superposition of a full cylinder and a hollow cylinder (after Green [51]).	116
Figure 2.27.	Schematic drawing of the heat transfer on cooling of a two-layer cylinder.	119
Figure 2.28.	Schematic of a halfpenny center-loaded crack (adapted from Lawn [50]).	129
Figure 2.29.	Schematic illustration of the final morphology due to the 4-layer coating strategy followed after the LIC process.	134
Figure 2.30.	Si-Cr binary phase diagram (after Hansen [18]).	139
Figure 2.31.	(a) Si-Hf binary phase diagram; (b) Hf-Cr binary phase diagram (after Moffatt [65]).	139
Figure 2.32.	Schematics of the cross section of the solidification mechanisms in raster scan laser melting of Mar-M 247 superalloy powder.	157
Figure 3.1.	Overall view of the 1.4 kW c.w. CO <sub>2</sub> laser processing equipment.	165
Figure 3.2.	Close up view of the processing chamber.	166
Figure 3.3.	Calibration curve for CO <sub>2</sub> laser power versus input voltage.	167

Figure 3.4.	Calibration scan speed versus value of sp parameter at ss = 760.	169
Figure 3.5.	Calibration curve for rough vacuum versus time.	170
Figure 3.6.	Overall view of the 250W Nd:YAG laser processing apparatus.	172
Figure 3.7.	Schematic of the laser polishing process.	173
Figure 3.8.	Schematic of segment analysis of a surface profiled track.	176
Figure 3.9.	Distribution of profile measurements across polished tracks.	177
Figure 3.10.	Spray painting of cylindrical sample using a Badger™ air-spraying gun.	182
Figure 3.11.	Sample #37 after the Si-40Cr slurry was air-spray coated.	182
Figure 3.12.	Schematic drawing of the “Laser Induced Cementation” process.	184
Figure 3.13.	Sequence of images of Sample #47 being laser induced cemented.	186
Figure 3.14.	Horizontal furnace operating at 1000 °C under direct air with a coated cylindrical sample being weighted loss tested.	188
Figure 3.15.	Schematic of a indenter`s impression and radial cracks formed.	191
Figure 3.16.	Schematic of how to register the powder masks to substrate.	194
Figure 3.17.	Overall schematics of the mask-powder-substrate arrangement during selective laser melting.	195
Figure 3.18.	Cross-section schematic of the mask-powder-substrate arrangement indicating principal heat flow paths.	196
Figure 3.19.	Schematic diagram of laser coating of TiC/TiC-Ni on 347H steel.	200
Figure 3.20.	Schematic diagram of laser melting of a shape memory alloy powder.	204
Figure 3.21.	Typical rotary shaft sample holder and laser cladding head.	206
Figure 3.22.	Linear translation stage mounted inside of CO <sub>2</sub> laser processing chamber.	208
Figure 3.23.	Calibration curve for the speed of linear motion stage versus voltage.	209
Figure 4.1.	SEM image of the surface of indirect-SLS part having an R <sub>a</sub> = 7-9 μm, 120x.	213

Figure 4.2.	SEM image of the surface of indirect-SLS part having an $R_a = 2\text{-}5 \mu\text{m}$ , 250x.	213
Figure 4.3.	Operational window for several laser processes. Adapted from Steen [1]. The dark box near “Welding” and “Melting” indicates the utilized $\text{CO}_2$ laser polishing operational window.	214
Figure 4.4.	Percentage normalized $R_a$ roughness variation of indirect-SLS stainless steel grade 420–40 wt.% bronze infiltrated versus (a) increasing traveling speed (b) increasing energy density.	216
Figure 4.5.	Percentage normalized $R_a$ roughness variation of indirect-SLS stainless steel grade 420–40 wt.% bronze infiltrated versus (a) increasing traveling speed (b) increasing energy density.	219
Figure 4.6.	Percent normalized $R_a$ roughness variation of indirect-SLS stainless steel grade 420–40 wt.% bronze infiltrated versus (a) increasing traveling speed (b) increasing energy density.	220
Figure 4.7.	As-received layered cross section of Specimen #1, 35x.	222
Figure 4.8.	s-received bulk region of Specimen #1, 2000x.	222
Figure 4.9.	As-received surface region of Specimen #1, 1500x.	223
Figure 4.10.	Elemental mapping of (a) Fe composition, (b) Cu composition and (c) Cr composition of the as-received surface region in between laser polished tracks of Specimen #2.	224
Figure 4.11.	Laser polished surface region in Specimen #1, track 4 done at 225 W and 1.68 mm/s speed, 1000x.	226
Figure 4.12.	Elemental mapping of laser polished track surface shown in Figure 4.11. (a) Fe distribution, (b) Cu distribution, (c) Cr distribution, (d) Sn distribution.	227
Figure 4.13.	Laser polished surface region in Specimen #4, track 1 done at 565 W and 5.66 mm/s speed, 1500x.	228
Figure 4.14.	Laser polished surface region in Specimen #2, done at 334 W and 4.62 mm/s, 150x.	228
Figure 4.15.	Laser polished track #4, 50x. Processing parameters, resulting % roughness $R_a$ variation and track width: 334 W, $v_t = 2.22 \text{ mm/s}$ , $v_s = 333 \text{ mm/s}$ , % $R_aV = +9\%$ , $w = 1.42 \text{ mm}$ .	230

- Figure 4.16. Laser polished track #6, 50x. Processing parameters, resulting % roughness  $R_a$  variation and track width: 334 W,  $v_t = 1.64$  mm/s,  $v_s = 246$  mm/s, %RaV = -18%,  $w = 1.61$  mm. 231
- Figure 4.17. Laser polished track #12, 35x. Processing parameters, resulting % roughness  $R_a$  variation and track width: 334 W,  $v_t = 0.86$  mm/s,  $v_s = 129$  mm/s, %RaV = -22%  $w = 1.93$  mm. 232
- Figure 4.18. High magnification image showing two consecutive periodic peaks in track #12, 180x. 233
- Figure 4.19. Magnified inner zone of different laser scanned track processed at 334 W (a) track #1:  $v_s = 693$  mm/s and  $v_t = 4.6$  mm/s at 500x, (b) track #4:  $v_s = 333$  mm/s and  $v_t = 2.2$  mm/s at 500x, (c) track #6:  $v_s = 246$  mm/s and  $v_t = 1.6$  mm/s at 500x, (d) track #12:  $v_s = 129$  mm/s and  $v_t = 0.86$  mm/s at 800x. 235
- Figure 4.20. Magnified inner zone of different laser scanned track processed at 334 W, 2500x (a) track #1:  $v_s = 693$  mm/s and  $v_t = 4.6$  mm/s (b) track #6:  $v_s = 246$  mm/s and  $v_t = 1.6$  mm/s (c) track #12:  $v_s = 129$  mm/s and  $v_t = 0.86$  mm/s. 237
- Figure 4.21. Laser polished track #3 in Specimen #3, 150x. Processing parameters, resulting roughness variation: 420 W,  $v_t = 2.65$  mm/s,  $v_s = 396$  mm/s, %RaV = +56%. 240
- Figure 4.22. Laser polished track #3 in Specimen #4, 150x. Processing parameters, resulting roughness variation: 565 W,  $v_t = 2.71$  mm/s,  $v_s = 406$  mm/s, %RaV = -29%. 240
- Figure 4.23. Magnified inner zone of Specimen #3 laser scanned track #3, 500x. Processing parameters : 420 W,  $v_t = 2.65$  mm/s,  $v_s = 396$  mm/s. 241
- Figure 4.24. Magnified inner zone of Specimen #4 laser scanned track #3, 500x. Processing parameters: 565 W,  $v_t = 2.71$  mm/s,  $v_s = 406$  mm/s. 241
- Figure 4.25. Magnified inner zone of Specimen #3 laser scanned track #3, 2000x. Processing parameters: 420 W,  $v_t = 2.65$  mm/s,  $v_s = 396$  mm/s. Al-rich oxide particles embedded on a Cu-rich phase matrix. 242
- Figure 4.26. Magnified inner zone of Specimen #4 laser scanned track #3, 2000x. Processing parameters: 565 W,  $v_t = 2.71$  mm/s,  $v_s = 406$  mm/s. Showing a layer of Fe-rich phase on top of Cu-rich phase. 243

Figure 4.27.	Border region of Specimen #3 between as-received and laser polished track #3, 350x. Processing parameters: 420 W, $v_t = 2.65$ mm/s, $v_s = 396$ mm/s.	244
Figure 4.28.	Energy dispersive chemical spectrum of as-received zone near border of laser polished track #3 in Specimen #3.	244
Figure 4.29.	Magnified inner zone of Specimen #3 laser scanned track #3, 2000x. Showing a cluster of spherical particles embedded in a dark-colored phase.	246
Figure 4.30.	Energy dispersive chemical spectrum of spherical particle in laser polished track #3 in Specimen #3.	246
Figure 4.31.	Magnified inner zone of Specimen #3 laser scanned track #3, 1500x. Showing a light-colored phase.	247
Figure 4.32.	Magnified inner zone of Specimen #4 laser scanned track #3, 2000x. Processing parameters: 565 W, $v_t = 2.71$ mm/s, $v_s = 406$ mm/s. Showing a dark-colored phase and light-colored phase.	248
Figure 4.33.	Energy dispersive chemical spectrum of spherical particle in laser polished track #3 in Specimen #4.	249
Figure 4.34.	Magnified inner zone of Specimen #4 laser scanned track #3, 2000x. Showing a Fe-rich phase.	250
Figure 4.35.	Energy dispersive chemical spectrum of Fe-rich phase in laser polished track #3 in Specimen #4.	251
Figure 4.36.	Energy dispersive chemical spectrum of Cu-rich phase in laser polished track #3 in Specimen #4.	251
Figure 4.37.	X-ray diffraction pattern of generic as-received indirect-SLS surface.	253
Figure 4.38.	Surface temperature profile of raster-scan-spot energy source and line-energy source at 565 W laser power and 3.71 mm/s traveling speed (85 % heat losses accounted for in the model).	255
Figure 4.39.	Infrared thermal image of interaction zone for a 565 W raster-scan laser beam traveling at 3.71 mm/s and scan speed 557 mm/s. Emissivity parameter was set to 0.9.	256
Figure 4.40.	Surface temperature profile of two raster-scan energy sources of laser power 420 W and 565 W and 397 mm/s and 406 mm/s scan speed, respectively (80 % total energy losses accounted for).	258



Figure 4.41.	Surface temperature profile of raster-scan-spot energy source at constant energy density for different laser power of 420 W and 565 W and 115 mm/s and 151 mm/s scan speed, respectively (80 % total energy losses accounted for).	259
Figure 4.42.	Plot of modeled percent roughness $R_a$ variation versus high traveling speeds for average particle radius size of 10 $\mu\text{m}$ .	263
Figure 4.43.	Plot of the modeled solidification and spreading average times versus scan speed for $R_p = 10 \mu\text{m}$ at 565 W.	264
Figure 4.44.	Plot of experimental and modeled percent surface roughness $R_a$ variation data versus traveling speed for Specimen #2.	267
Figure 4.45.	Plot of the measured average surface wavelength $\lambda$ versus scan speed in Specimen #2.	269
Figure 4.46.	As-machined C/C composite sample.	272
Figure 4.47.	SEM image of 3D weaved C/C composite rough surface, 1000x.	272
Figure 4.48.	Surface of specimen #6, Si coating indicating signs of incomplete wetting of the surface, 50x. Surface has been coarse polished.	274
Figure 4.49.	Surface of Specimen #16, 1500x of Si-10wt.%HfC coating indicating a eutectic like morphology.	275
Figure 4.50.	Surface of the coated surface of Specimen #16, showing a network of cracks, 200x.	276
Figure 4.51.	Specimen #71, first coating layer consisting of Si-20SiC-5Ti-5Al.	277
Figure 4.52.	Specimen 67. Tapered specimen showing first coating layer consisting of Si-15HfC-10Ir-5Ti.	277
Figure 4.53.	Surface of Specimen #71 illustrating surface of final layer of Si-15HfC-10Ir-5Ti (wt.%) laser fused coating, 200x.	278
Figure 4.54.	Specimen #261 prepared for weight loss testing, coating consisted of Si-10SiC-10CrCl <sub>3</sub> -30HfC and SILBOND™ overcoat layer.	279
Figure 4.55.	Specimen #270, after being laser fusion coated at both sides.	280
Figure 4.56.	Percent weight reduction versus heating time at 1000 °C in flowing air 2 cfh for different planar specimens.	281
Figure 4.57.	Surface of Specimen #270 after weight loss testing for 2 hours, 100x.	282

Figure 4.58.	(a) Rendered CAD image of C/C composite cylinder. (provided by West [15]) (b) Bare as-machined 3D C/C composite cylinder.	283
Figure 4.59.	Theoretical temperature profile obtained at the surface of a coated C/C composite cylinder during the LIC process.	285
Figure 4.60.	Specimen # C2 as coated and prepared for weight loss testing.	287
Figure 4.61.	Specimen #17 after the LIC coating process. Surface is covered completely and appears smooth, homogenous and silver in color.	287
Figure 4.62.	Specimen #18 after the LIC coating process. Surface is covered completely and appears smooth and uniform.	288
Figure 4.63.	Specimen # 24 as LIC processed, surface is covered completely but lumps are spread over the coating. Stem has been removed.	289
Figure 4.64.	Specimen # 29 as LIC processed before final coating, surface is fully Covered and uniform. Metal stem holder is shown at the right hand side.	289
Figure 4.65.	Specimen # 32 as LIC processed, surface is covered totally and appears smooth.	290
Figure 4.66.	Specimen # 40 after first $\text{CrCl}_3$ -50Cr layer has been LIC applied. Almost a 100% coating coverage has been obtained.	291
Figure 4.67.	Specimen # 40 after the second Si-25Cr-5 $\text{CrCl}_3$ -5C layer has been LIC laser fused. A smooth coating has been obtained all over the surface.	292
Figure 4.68.	Cross-section of Specimen #2, 500x. A reaction layer has formed at the interface.	293
Figure 4.69.	Cross-section of Specimen #2, 200x. Indicating that good wetting is achieved over the surface of the C/C composite aided by capillarity.	294
Figure 4.70.	Cross-section of Specimen #3, 500x. Showing a Cr/Cr-carbide thin layer.	295
Figure 4.71.	Interface of Specimen #5, 1000x. A reaction product layer at the interface is clearly seen along the surface of the C/C composite.	296
Figure 4.72.	Interface of Specimen #5, 1000x. Illustrating the light phase embedded in the Si-rich matrix.	297
Figure 4.73.	Surface of Specimen #2, 1000x. Showing $\text{SiO}_2$ phase and SiC embedded particles in the Si-rich matrix phase.	298

Figure 4.74.	Cross-section of Specimen #3, 2500x. Showing the Cr/Cr <sub>x</sub> C <sub>y</sub> product layer over the composite surface.	299
Figure 4.75.	Cross-section of Specimen #5, 50x. Showing thickness uniformity and good coating spreading over C/C substrate.	300
Figure 4.76.	Cross-section of Specimen #5, 1000x. Indicating the α-Si matrix and the Si-Hf “white” phase.	301
Figure 4.77.	Cross-section of Specimen #8, 450x. Showing a uniform coating 200 μm thick. A micron size reaction layer at the interface can be observed.	302
Figure 4.78.	Coefficient of thermal expansion of the Si-35HfC powder mixture before and after heat treatment at 750°C, measured at different temperatures in air up to 850 °C. A first order transition occurs when the HfC becomes oxidized at 590°C.	303
Figure 4.79.	Magnified microstructure of Specimen #8, 10000x. Si-rich phase (gray), Si-Hf phase (white) and Si-Cr (light-gray) phase are seen.	304
Figure 4.80.	Cross-section of Specimen #18, no heat treatment, 100x. A coating thickness of approximately 350 μm is shown.	305
Figure 4.81.	Cross-section of Specimen #18, no heat treatment, 500x. Indicating that reacting wetting is achieved over the surface.	306
Figure 4.82.	Cross-section of Specimen #18, no heat treatment, 2000x. A Si carbide layer 4-8 μm thick is observed at the interface.	307
Figure 4.83.	Cross-section of Specimen #18, no heat treatment, 5000x. The α-Si matrix contains three distinct embedded phases.	308
Figure 4.84.	Cross-section of Specimen #18, after 2 hours and 30 minutes of heat treatment, 250x. Coating thickness is approximately 300 μm.	308
Figure 4.85.	Cross-section of Specimen #18, after 2 hours and 30 minutes of heat treatment, 2500x. Detachment along phase boundaries is observed.	309
Figure 4.86.	Cross-section of Specimen #18, after 2 hours 30 minutes of heat treatment, 2500x. The SiC product layer at the interface remained compositionally unchanged after the treatment.	310
Figure 4.87.	Cross-section of Specimen #18 after 2 hours and 30 minutes at 1150 °C in argon, 60x.	311

Figure 4.88.	Surface of Specimen # 31, after coated with SILBOND™. Multiple cracks are present due to the shrinkage of the ethyl-silicate solution on curing.	312
Figure 4.89.	Surface of Specimen # 31, after coated with SILBOND™ and cured at 300°C for 10 minutes. Previously shown cracks have not healed, instead the crack openings are wider.	312
Figure 4.90.	Surface of Specimen #41, showing the glass-modified overcoat obtained from the sodium silicate using the LIC process, 50x.	313
Figure 4.91.	Surface of Specimen #42, showing the glass-modified overcoat obtained from silica and sodium silicate using the LIC process, 50x.	314
Figure 4.92.	Cross-section of Specimen #45, 300x. Showing the glass modified overcoat, the refractory coating and the C/C substrate.	315
Figure 4.93.	Cross-section of Specimen #45, upper interface at 1000x. Indicating that Good wetting of the refractory coating by the glass-modified overcoat has been achieved.	316
Figure 4.94.	Cross-section of Specimen #45, refractory coating at 1000x. Three distinct phases can be observed: gray, light gray and white.	319
Figure 4.95.	Cross section of Specimen #45, interface with substrate at 1000x. Two distinct phases can be observed: gray and light gray.	320
Figure 4.96.	Cross section of Specimen #45, interface at 4000x. Reactive wetting of CrSi <sub>2</sub> phase over C/C fiber.	320
Figure 4.97.	Cross section of Specimen # 41, after weight loss tests at 1000 °C for 3 Hours in air, 150x.	321
Figure 4.98.	Cross-section of Specimen #42, after weight loss test, 2000x. A close up of the C/C fibers and carbonaceous matrix near the interface is shown.	322
Figure 4.99.	Cross-section of Specimen #43, after weight loss test for 20 hours at 1000 °C in air, 100x.	323
Figure 4.100.	Cross-section of Specimen # 43, after weight loss test, 500x. A sound microstructure integrity near the interface with the C/C substrate is shown.	324

Figure 4.101. Cross-section of Specimen # 43, after weight loss test, 500x. A sound microstructure integrity near the interface with the glass modified overcoat is shown.	325
Figure 4.102. Surface of Specimen #46, after weight loss test for 5 hours at 1000 °C in air, 40x. Porosity has developed on the surface of the sodium glass-modified overcoat.	326
Figure 4.103. Surface of Specimen #46, after weight loss test, 350x. Channeling cracks are present at the surface.	327
Figure 4.104. EDAX spectrum of reaction product layer at the interface of Specimen #3 showing intense Cr and C peaks.	328
Figure 4.105. EDAX spectrum of Specimen #18, after weight loss test for 2 hr 30 minutes. (a) gray phase showing a strong Si peak (b) light gray phase showing strong Si (b) peak and less intense Cr, Hf and C peaks. (c) white phase showing strong (c) Hf and Si peaks.	330
Figure 4.106. (a) Surface of glass-modified overcoat in Specimen #46 (b) EDAX spectrum of surface spot.	331
Figure 4.107. (a) Surface of glass-modified overcoat on Specimen #47 selected for elemental mapping (b) Si distribution (c) oxygen distribution (d) Na distribution.	332
Figure 4.108. (a <sub>1</sub> ) Specimen #45 (not weight loss tested) (b <sub>1</sub> ) Cr distribution (c <sub>1</sub> ) Hf distribution (d <sub>1</sub> ) Si distribution (a <sub>2</sub> ) Specimen #43 after weight loss test (b <sub>2</sub> ) Cr distribution (c <sub>2</sub> ) Hf distribution (d <sub>2</sub> ) Si distribution.	333
Figure 4.109. Comparison of EDAX spectra of the Hf-Si “white” phase (a) before and (b) after heat treatment due to weight loss testing.	334
Figure 4.110. (a) Specimen #45, upper interface with glass-modified overcoat (b) Si distribution (c) Cr distribution (d) Hf distribution (e) Na distribution (f) oxygen distribution.	335
Figure 4.111. (a) Specimen #45, lower interface with C/C composite (b) Si distribution (c) Cr distribution (d) C distribution.	336
Figure 4.112. EDAX spectra of the (a) upper interface region in Specimen #45 and (b) lower interface region in Specimen #45.	337
Figure 4.113. XRD pattern of chromium coated surface of Specimen #3.	338

Figure 4.114. X-ray diffraction pattern of the Si-35HfC (wt.%) powder mixture used in Specimen #8 (a) before and (b) after a heat treatment at 750°C for 1 hour in air. It can be observed that the HfC has been almost completely oxidized to HfO <sub>2</sub> while no presence of SiO <sub>2</sub> is indicated.	340
Figure 4.115. XRD pattern of the surface of silicon coated Specimen #C15.	341
Figure 4.116. XRD pattern for Si-25Cr-5C (wt.%) mixture heated up to 875°C in air.	342
Figure 4.117. XRD pattern of Si-15HfCl <sub>4</sub> -15Cr (wt.5) mixture heated up to 875°C in air.	343
Figure 4.118. XRD pattern of Specimen #48 coated with a CrCl <sub>3</sub> -30Cr, Si-25Cr-5C and Si-15HfCl <sub>4</sub> -15Cr layers (all in wt.%) by the LIC process.	344
Figure 4.119. TMA plot of laser processed coating material consisting of Si-20Cr-7HfCl <sub>4</sub> -3C in wt.%.	346
Figure 4.120. TMA plot of precursor powder mixture consisting of Si-20Cr-7.5HfCl <sub>4</sub> -2.5C in wt.%.	347
Figure 4.121. CTE plot during heating stage of laser processed coating material consisting of Si-20Cr-7HfCl <sub>4</sub> -3C in wt%.	348
Figure 4.122. CTE plot during heating stage of precursor powder mixture consisting of Si-20Cr-7.5HfCl <sub>4</sub> -2.5C wt%.	348
Figure 4.123. DTA plot of laser processed coating consisting of Si-20Cr-7HfCl <sub>4</sub> -3C wt%.	349
Figure 4.124. DTA plot of powder mixture consisting of Si-20Cr-7.5HfCl <sub>4</sub> -2.5C wt%.	350
Figure 4.125. Plot of the indentation half diagonal, semi-crack length, Vickers hardness and fracture toughness as a function of applied load.	352
Figure 4.126. Simulated radial temperature distribution during cooling of a coated cylinder from an initial temperature of 1563 K (a) after 1 ms (b) after 0.5 s.	354
Figure 4.127. Simulated thermal gradient distribution during cooling of a coated cylinder (a) after 1 ms (b) after 0.5 s.	355
Figure 4.128. Plot of the plane stress state, $\sigma_r$ and $\sigma_\theta$ , along the radial direction from the center of the substrate to the coating surface.	356
Figure 4.129. Plot of the plane stress and plane strain hoop stress, $\sigma_\theta$ , as well as the axial stress in plane strain, $\sigma_z$ , along the radial direction from the interface to the coating surface.	358

Figure 4.130. Plot of the plane stress and plane strain radial stress, $\sigma_r$ , along the radial direction from the interface to the coating surface.	359
Figure 4.131. Surface of Specimen #2, 500x. Crack channeling has occurred.	361
Figure 4.132. Cross-section of overall coating layer in Specimen #5, 500x. A radial crack has extended completely towards the C/C substrate.	362
Figure 4.133. Cross-section of Specimen #8, 1000x. A radial crack through the coating and a spalling crack along the substrate can be observed.	363
Figure 4.134. Cross-section of Specimen # 42, after weight loss test, 200x. Delamination of the overcoat from the refractory coating as occurred.	364
Figure 4.135. Cross-section of Specimen #43, after weight loss test for 20 hours at 1000 °C in air, 150x. A penny shape crack is seen in the refractory coating.	365
Figure 4.136. Specimen # C2 after weight loss test at 1000 °C in flowing air.	366
Figure 4.137. Percent weight reduction versus heating time of several specimens tested within a 1000-1150 °C temperature range in still and flowing air and argon.	367
Figure 4.138. Percent weight reduction versus heating time at 1000 °C in air. Test performed at Wright-Patterson AFB Materials Laboratory, using a dedicated TGA unit.	369
Figure 4.139. Stereo macrograph of the cross-section of a Mar-M 247 deposit over Alloy 718 substrate corresponding to Specimen 21, 25x.	372
Figure 4.140. Macrographs of the etched cross-section of a Mar-M 247 deposit over Alloy 718 substrate corresponding to Specimen #22, 50x (Courtesy of Rolls-Royce America).	373
Figure 4.141. Micrograph of the cross-section of Specimen #21, 100x. Showing the deposit-substrate interface.	374
Figure 4.142. Micrograph of the cross-section of a Mar-M deposit over CMSX-4 alloy substrate, 50x. The upper region of the deposit.	375
Figure 4.143. Micrograph of the cross-section of a Mar-M deposit over directionally grown CSMX-4 alloy substrate, 100x. The upper middle region of the deposit.	375

Figure 4.144.	Micrograph of the columnar dendritic region above the cellular region in Specimen 51, 200x.	376
Figure 4.145.	Micrograph of the cross-section of a Mar-M deposit over 718 alloy substrate corresponding to Specimen #52, 200x, showing the dendritic structure.	377
Figure 4.146.	Micrograph of middle region of specimen 53, 100x. Transition from [001] (below) to [100] (above) polycrystalline dendritic orientation.	377
Figure 4.147.	Micrograph of the cross-section of Specimen 55, 100x. Showing polycrystalline dendrites above the cellular region.	378
Figure 4.148.	Micrograph of the longitudinal section of Specimen 55, 200x. Showing reorientation of dendrites.	379
Figure 4.149.	Solidification processing map for the SLLD of Ni-base superalloy powder (Ref. 23 and Appendix B-III).	380



# CHAPTER I. INTRODUCTION

## 1.1 BACKGROUND AND MOTIVATION

Since the invention of the CO<sub>2</sub> laser by Kumar Patel in 1964 at Bell Laboratories [1], continuous-wave high-power coherent (in space and time) energy sources in the infrared region (i.e., 10.6 microns) became available to investigators in the field of materials processing and manufacture. Also that same year and at the same research site the development of the solid state Nd:YAG laser by Geusic, *et al.*[1] took place, pushing this research towards maturity due to reduction in physical size of the laser that increased portability as well as lowered wavelength (1.06 microns). This allowed fiber optics to be used as wave guides and facilitated the spatial deposition of energy on materials. Moreover, its capacity to deliver infrared coherent energy in pulsed mode opened up new venues in materials processing research. Since then, research on laser-materials interaction has taken place at numerous sites around the world such as industrial research centers, national laboratories and universities. During late 1970s and the 1980s the quantity of publications centered in laser materials processing using these two types of lasers has increased immensely [2,3] with multiple topics ranging from laser cutting and welding to laser surface

modification such as laser melting, alloying and cladding of different types of materials (e.g. alloys of metals, ceramics and polymers).

By the early 1980s shorter wavelengths in the red, green and ultraviolet became available through the commercialization of the semiconductor laser, nonlinear optics to achieve frequency doubling, tripling and quadrupling of Nd:YAG laser light and the Eximer laser.

It was also in the mid 1980s that the need to deposit low-power infrared laser energy selectively in space over the surface of materials became a necessity for the development of certain rapid prototyping technologies that were evolving at that time. One particular case was the development of the Selective Laser Sintering (SLS) process created at The University of Texas at Austin [4]. Energy deposition in 2D space was achieved by modulating laser energy using galvanometer driven mirrors. The main advantage of the “galvo-mirrors” was the fact that the laser beam could be raster-scanned at much higher speeds along any planar trajectory than any conventional positioning mechanism available such as CNC x-y tables.

By raster-scanning a focused laser beam along a zig-zag pattern, galvanometer driven mirrors allowed the creation of a “psuedo-energy-line” source capable of sustaining an homogenous melting front of certain width. The average traveling speed (slow-direction) of this front is a function of the average

scan speed (fast direction) and the density of scanning lines. The latter in turn determined the degree of scanning-line overlap for a given beam spot diameter size. However, it was not until early 1990s that high-laser-power handling galvo-mirror delivery systems were developed. By 1998 Das *et al.* [5] at The University of Texas at Austin constructed two such SLS stations capable of harnessing up to 1.4 kW from a CO<sub>2</sub> laser and 500 W from a Nd:YAG for research purposes. These unique materials processing units became the focal point for this research work.

This work involved a series of materials surface modification related topics, all of which took advantage of modulating the delivery of infrared laser energy spatially over specimens of distinct nature and geometry under controlled atmospheric conditions.

## **1.2 RESEARCH APPROACH AND DISSERTATION STRUCTURE**

This dissertation focuses on three distinct and specific surface modification processes:

- (a) Surface roughness reduction of indirect-Selective Laser Sintered 420 martensitic stainless steel–40 wt. % bronze infiltrated metallic flat surfaces
- (b) Si-Cr-Hf-C coating consolidation on 3D carbon–carbon composite cylinders

(c) Dendritic solidification structures of Mar-M 247 confined powder precursor grown from polycrystalline Alloy 718 substrates

In all these applications, a high-power continuous wave laser beam actuated by two high-speed raster-scanning mirrors was utilized under controlled atmospheric conditions. A theoretical heat transfer model developed by the author served to understand better how the dimensions of the laser scanned pattern (width and length), percentage overlap of scan lines, the laser beam power and scan speed determined average and peak surface temperature, heating and cooling rates and melt residence time for each of the aforementioned processes. This analysis also provided an equivalence relationship to match the Andrew's number associated with a raster-scan process with that of a single-line-source process of known number value.

The theoretical background encompassed in each of the mentioned processes is thoroughly presented in Chapter II. Development of several analytical models to help understand and predict some the observed behaviors of processes (a) and (c) are included in this chapter, too.

In Chapter III the experimental set up and processing parameters used in each of the applications are described in detail as well as all the characterization techniques employed to assess certain properties of the resulting modified surfaces.

Chapter IV illustrates the most significant characterization and modeling results obtained for each of the investigated processes and it provides in depth discussion based on the theoretical background of Chapter II.

Finally in Chapter V, main conclusions are drawn based on the obtained results are presented in conjunction with several recommendations for future investigation lines of similar characteristics.

### **1.3 SURFACE MODIFICATIONS BY LASER MELTING**

Surface melting of materials that undergo fusion prior to sublimation can be readily achieved by a continuous traveling heat source (e.g., a high-power focused laser beam), the bulk acting as a heat sink during the solidification stage. The resulting solidified material has the same chemical composition of the parent material. Nonetheless, if a high solidification rate is attained, it may produce a different microstructure with potentially enhanced mechanical properties.

When the laser treated substrate does not melt but instead sublimes at a certain temperature, the atoms detach among themselves from the substrate forming a vapor film over the substrate. The vapor film may absorb all or a fraction of the incoming laser radiation, increasing its temperature and expanding vigorously. During the sudden gas expansion a recoil pressure is exerted on the surface of the substrate aiding the expulsion of the gaseous species as these are

being formed. This causes an erosion front to propagate into the substrate leaving a groove in the material. When highly energetic short-lived pulses of laser light impinge over surfaces of such types of materials, then the process is referred as “Laser Ablation”.

### **1.3.1 Addition of coating elements to substrates that undergo melting**

A common practice is to pre-place or inject an alloy powder at the surface of the material prior to or during the surface melting process to alter the chemical composition of the melt pool. Another variation is to melt a different material placed on the surface so that mixing with the substrate material is limited to the minimum required to produce effective bonding. When a laser beam is employed as the heat source, the latter two laser melting techniques are referred respectively as laser alloying and laser cladding [2,3,6].

Under certain combinations of elements and processing parameters, the substrate and coating materials may both exist in the liquid phase at the same time and thus a metallurgical bond is formed. At the coating-substrate interface an alloy forms from the elements in the coating and substrate as diffusion in the liquid phase occurs rapidly. Typically the alloy composition at the interface will be at least that of the maximum solid solubility limit of one of the elements. Metallurgical bonds can be extremely strong, narrow in thickness and free of impurities.

As reported by Belforte in Reference 2, by 1977 laser surface treatment processes such as laser cladding and laser alloying were patented by Avco Everett Research Laboratory Inc. Laser cladding was then described as a process in which the focused laser beam melts a pre-positioned material causing it to flow over the surface of a metal, freeze and form a protective or wear resistant layer. On the other hand, in laser alloying the depth of melt is thin and alloying elements are added simultaneously. Surfaces with superior properties were thus achieved by both techniques. However, the main difference between them is that in cladding low dilution of elements is desired while in alloying the contrary is the goal. The precursor cladding or alloying material is commonly delivered in powder form as it is less costly than other forms (foils, rods, etc.). Besides, less material is used. In both processes, the surface can be tailored to produce the characteristics of an expensive metal on a less costly base metal. Belforte further indicated that the depth of the alloyed layer, which coincides with the diffusion depth of the alloying elements, is controlled by the laser power and dwell time. The alloyed zone exhibited a fine, homogenous microstructure.

According to Steen [3], the ideal power distribution to be used in laser techniques such as surface melting, alloying and cladding is one that gives a uniform temperature over the area to be treated. This requires a dimpled power distribution. Commonly used methods for spreading a laser beam are:

defocusing, two axis scanning beams, kaleidoscopes, and segmented mirrors among others.

Numerical modeling by Powel [6] showed that a low dilution liquid-solid bond was obtained in laser cladding of pre-placed powder for a wide operational window. The higher thermal conductivity of the substrate compared to that of the powder increases the thermal load thus causing a solidification front to be established as soon as the liquid encounters the substrate. Conde *et al.* indicate in [7], that lower porosity, lower oxide inclusions content and high integrity of fusion bonding between the surface layer and the substrate are advantages when compared with traditional coating techniques such as plasma spraying.

Recently in [8], Ready explains in laser alloying the mass of the material melted on the workpiece is larger than the mass of the added material whereas in laser cladding the mass of the molten bath on the workpiece is less than the mass of the added material.

Feng *et al.* state in [9] that laser applications in the surface treatment of metals, particularly in the formation of surface alloys, have grown rapidly in recent years. Laser surface melting is one such process leading to a fine microstructure and to the dissolution or redistribution of precipitates or inclusions.



**1.3.1.1 *Illustrative case study: Cr-Ni coating onto a 347H stainless steel substrate by raster scanning a laser beam [10]***

Surface modification by high-speed raster-scanning of a focused high power gaussian laser beam is a versatile technique that can be used for many potential industrial applications where oxidation resistance is required. One such application is the exterior coating of heat exchanger stainless steel tubes used in boilers.

Figure 1.1 shows a schematic drawing of the laser surface modification technique used. A CO<sub>2</sub> laser beam (TEM<sub>00</sub>) actuated by two high-speed galvanometer mirrors was selectively raster-scanned over the surface of pre-deposited coatings consisting of 50Cr-50Ni. The dimensions of the specimens were 6 mm in height x 12.5 mm in width x 50 mm in length. The laser power on the surface ranged from 770-790 W, with a spot diameter of approximately 0.35 +/-0.05 mm. The traverse speed used varied from 3 to 5 mm/s, the scan speed ranged from 380 to 675 mm/s, and the galvanometer mirrors were programmed to generate 40 scan-lines/mm. The processing was done inside of a sealed chamber that was vacuumed to 200 mTorr and back filled with argon or nitrogen.

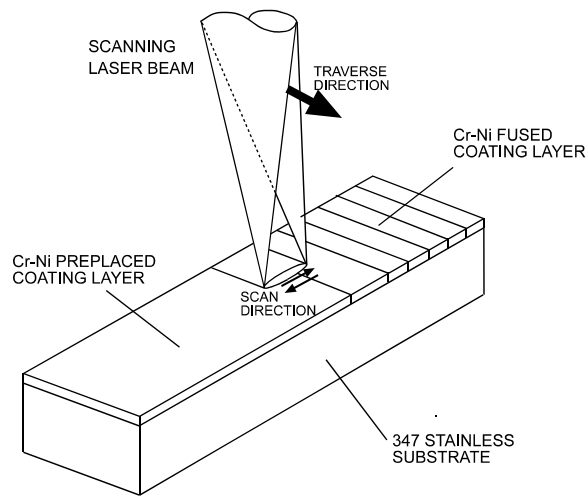


**Figure 1.1. Schematic drawing of the selective laser surface processing experimental set up.**

Figure 1.2 shows that a coating of approximately  $150\ \mu\text{m}$  was achieved in Specimen #16 with a sharp and homogenous interface. This specimen was processed under nitrogen using a laser beam power of 770 W and a scan speed of 675 mm/s, the calculated energy density corresponds to  $285\ \text{J}/\text{cm}^2$  for a beam diameter of 0.4 mm. The coating mass applied was 620 mg being equivalent to a coating thickness of  $124\ \mu\text{m}$ , indicating that the substrate must have melted down approximately  $25\ \mu\text{m}$ . The austenite and ferrite phases are indistinguishable from one another, however a fine dispersion of speckles can be seen all over the coating and substrate; these probably correspond to second-phase precipitates (i.e.,  $\sigma$  intermetallic or  $\text{M}_x\text{C}_y$  carbide).

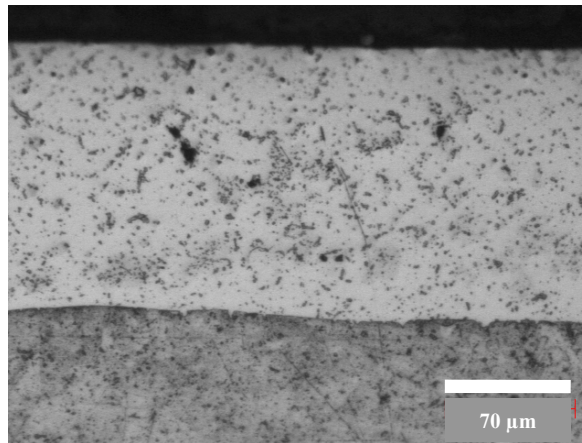


Figure 1.2. Optical micrograph of Specimen #16 longitudinal section of Cr-Ni coating-substrate interface, as-coated, x200.

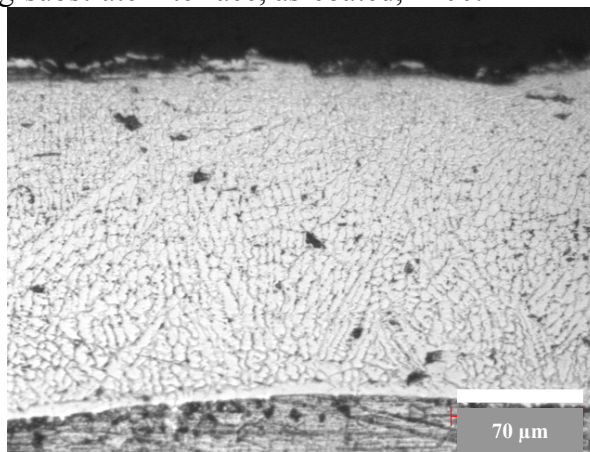


Figure 1.3. Optical micrograph of Specimen #5 showing Cr-Ni coating-substrate interface cross-section, no heat treatment, x200.

Figure 1.3 shows a cross section of Specimen #5 in which, a coating thickness of approximately 200 μm was achieved. This sample was processed in argon with 770 W and a scan speed of 383 mm/s, the calculated energy density corresponded to 502 J/cm<sup>2</sup> for a beam diameter of 0.4 mm. A cellular front grows

15  $\mu\text{m}$  from the substrate interface, followed by dendritic growth. The dendrites are not growing perpendicular to the substrate but with an angle with respect to the substrate normal, which is in agreement with the solidification morphology achieved with moving heat sources. Dendrites have an average cross-section width of approximately 3-4  $\mu\text{m}$ . Some porosity and blow-holes are observed in both samples 5 and 16.

The surface protective coatings produced by this fast selective laser fusion technique demonstrated strong metallurgical bonding, homogeneous dilution of elements present in the coating and substrate, low porosity, and constant thickness of up to 200  $\mu\text{m}$ .

### **1.3.2 Addition of coating elements to substrates that do not undergo melting**

When a substrate undergoes a direct solid to vapor phase transition without first melting (e.g., graphite, diamond, SiC, HfC, etc.) conventional laser alloying and cladding become cumbersome techniques for achieving good quality coatings. If the coating materials melt at a temperature higher than the sublimation point of the substrate, the latter will vaporize vigorously impeding a direct contact between the melt and the substrate as the evolving gases push the coating material away from the substrate. Moreover, trapped gases in the resulting coating will result in pores, voids and cracks. On the contrary, if the coating

material melts at a lower temperature than the sublimation temperature of the substrate, the bonding mechanism available between coating and the substrate is wetting. If complete substrate wetting takes place by coating over a rough or porous substrate, mechanical interlocking is the major bonding mechanism. Simultaneously, if the coating and substrate elements are chemically compatible, compound formation can be achieved at the wetted interface if the temperature is high enough; however this reactive layer will be almost mono-atomic in size. For the reacted layer to thicken, diffusion of chemical species from the substrate into the un-reacted coating must occur. Because diffusion driven processes are time and temperature dependent, conventional laser melting techniques become less effective as these provide short-lived temperature bursts, making diffusion limited.

As an illustrative example let us consider a 3D C/C composite substrate laser coated with pure silicon. It is estimated that for carbon atoms to diffuse 1 micron into silicon at its melting point, at least 10 seconds of diffusion time are at least necessary [11]. The interaction time employed in conventional laser melting technique typically corresponds to 0.1 to 0.01 seconds. Thus, under this condition a reacted SiC layer, not more than 10 nm thick, would be expected to form. If the traveling speed of the laser beam were lowered to increase the interaction time, then the melted material would experience a higher residence time. However, it would be exposed in one hand to the effect of a surface tension gradient caused by

thermal gradients in the melt and on the other hand to contaminants such as oxygen resulting in surface rippling and lumps, respectively. These features destroy the overall surface coating quality. Simultaneously, substrate integrity damage may occur at slow traveling speed due to excess heat input from the focused laser beam onto the substrate.

One alternative to overcome the diffusion driven bonding process as shown by Snell *et al.* [12] is to use the laser energy to chemically decompose a compound containing the elements needed for the coating. On decomposition, the remaining elements of the compounds are volatilized. During that process highly reactive radicals are formed that react rapidly with the substrate forming a thin, yet strongly bonded coating layer. This layer in certain cases can be sufficient for altering the substrate properties to the required specifications.

#### ***1.3.2.1 Illustrative case study: SiC-Cr coating on C/C composite tubes by conventional laser cladding***

Currently, laser coating technology such as laser cladding has evolved into a mature tool that has been transferred to the metal work industry. The author had the opportunity to perform research studies at “Laser Cladding Services” (LCS), an industrial laser facility located in Houston, Texas. The available equipment were considered conventional in the sense that no raster-scanning mirrors were used to deliver the energy onto the work piece and that the atmospheric protection

consisted only of a gas shroud applied directly over the interaction zone. The equipment included a 6 kW TEA (Transversely Excited at Atmospheric pressure) CO<sub>2</sub> laser whose laser beam was delivered to the workpiece by a CNC gantry system.

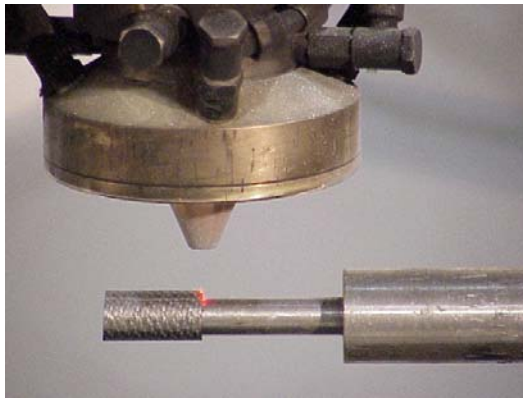


Figure 1.4. Close up image of a typical laser cladding head and a C/C composite tube mounted on rotary shaft.

Figure 1.4 shows the industrial laser cladding set up utilized at LCS to apply a SiC-Cr coating on C/C composites tubes by means of conventional laser cladding technique. The powder was fed to the interaction zone coaxially with the laser beam along the nozzle. The shaft rotated at a constant angular speed to match the traversing speed of the laser head for a given step size.

Figure 1.5 and 1.6 correspond to a C/C tube that was laser clad with a blend of SiC and Cr fine powders at LCS. Figure 1.6 is the cross-section of a SiC-30Cr laser cladding at 100x showing full wetting but cracks and considerable porosity. The specimen was laser clad at 900 J/cm<sup>2</sup> using 1.5 kW of power, a 5

mm size beam diameter and a traveling speed of 33.3 mm/s. The coating mass flow was 7 g/min. From Figure 1.6 the darker phase corresponds to SiC while the lighter phase corresponds to Cr.

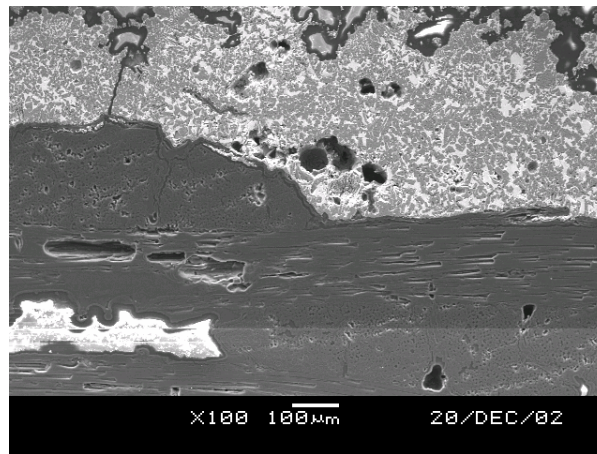


Figure 1.5. SEM image of the cross section of tube #1 at 100x, showing cracks, pores and an uneven coating surface.

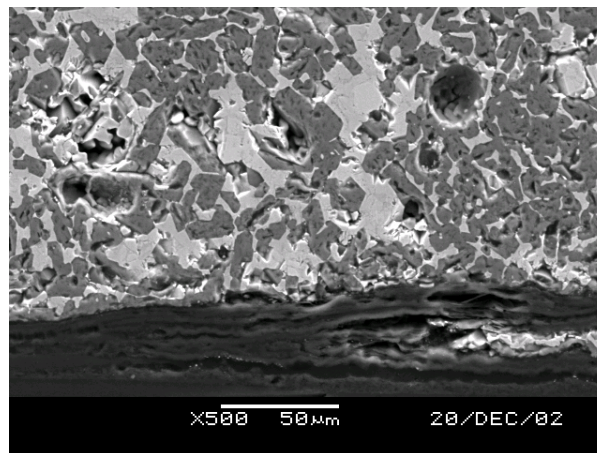


Figure 1.6. SEM image of the cross section of tube #1 at 500x, showing a damaged substrate as well as porosity in the coating.



### **1.3.3 Laser induced surface rippling during melting**

Since high power lasers have been used in materials processing research, observation of regularly spaced striations on metal surfaces after laser induced melting has already been reported [13-15]. The physical properties of the material as well as the laser process condition (i.e., power and speed) appear to determine the formation of such surface periodical structures. In some instances, these surface waves are attributed to an electrodynamic effect caused by the interaction of the laser radiation with surface electromagnetic waves causing modulation of the energy absorbed into the metal [13]. These resonant periodic structures have periods determined by the wavelength polarization and incident angle of the laser radiation [13]. However, experimental data reported in [14] showed that the typical length of these structures for carbon steels is of the order of 400 to 500 microns. Under these circumstances it has been concluded that it is most likely that these “large” wavelength features are not a consequence of the electrodynamic effect only, but are also impacted by the generation and relaxation of thermo-capillary oscillations on the molten surface layer by surface tension gradients induced during the motion of the laser beam. The periodic structures formed this way become frozen before relaxing completely as the cessation of the heat input from the energy source causes fast quenching of the melt [13-15].

The laser fusion Cr-Ni coated surface of a 347 stainless steel specimen is shown at higher magnifications in Figure 1.7, a rippling pattern typical of laser surface melting is observed, perhaps due to rapidly frozen capillary waves.

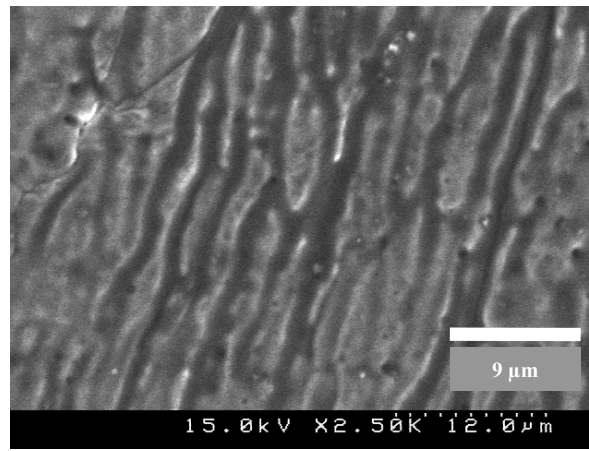


Figure 1.7. SEM image of laser Cr-Ni coating surface morphology, as-coated, 2500x.

Figure 1.8 shows a rippling pattern obtained over the surface of a laser remelted 347H stainless steel using a raster scanning laser beam. The rippling pattern forms a 45° angle with respect to the raster-scan pattern.

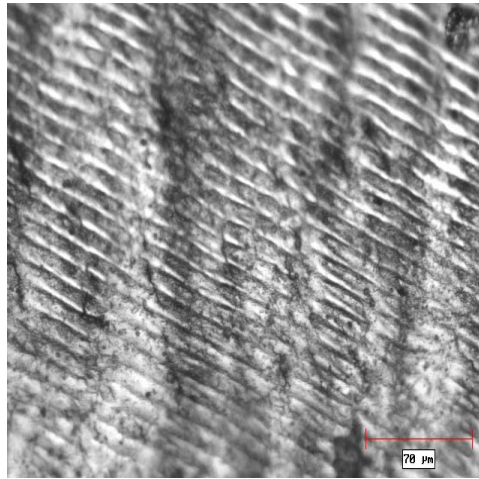


Figure 1.8. Laser rippling formation on a 347H stainless steel laser raster scan remelted surface, 80x. (Photograph taken by V. Bansal).

#### **1.4 LASER SURFACE POLISHING OF INDIRECT-SLS METALLIC PARTS**

Rapid Prototyping has proven to be a successful technique in shortening the manufacturing cycle for parts with complex geometry [16,17]. Selective Laser Sintering (SLS) is one such RP technology that benefits from the advantage of building up a solid object from polymer, ceramic and metal-alloyed materials in powder form [16-18]. To build objects out of metal alloys, two variations of the SLS are currently available, namely, indirect and direct SLS. The former requires post-infiltration of a SLS formed green part (high melting point metal) by metal of low fusion point. The latter technique, as its name indicates, involves consolidation of metal powder by direct laser induced local fusion. However, the surface roughness achieved during the manufacture of rapid prototyping articles

by these SLS techniques is still in the range of several microns [18]. At the same time, a sub-micron surface roughness  $R_a$  value is determinant when functional mechanical parts are to be built [18,19]. This is an issue yet to be solved along the path of rapid manufacturing evolution.

Transition from Rapid Prototyping towards Rapid Manufacturing of functional parts requires adequate reduction of surface roughness [16,20]. Surface finishing is a major barrier to achieving functional parts by means of rapid prototyping as recently elucidated by Connolly [19]. Direct or indirect Selective Laser Sintered (SLS) metal parts, regardless of the material system used, inherently present a grainy surface finish due to powder particle size, layer-wise building sequence and to some degree the spreading of the powder by the roller mechanisms [16,21].

Current finishing techniques used to reduce roughness of SFF parts are hand polishing and abrasive flow grinding. These techniques are tedious and time consuming although effective in reducing surface roughness. Less commonly used techniques are electro-polishing, shot-peening, ultrasonic and vibratory bowl abrasion [22]. A more sophisticated approach currently used is robotic arm polishing; however, the trajectory of the polishing tool must be determined a priori by 3D profilometry or some other means thus increasing the complexity and cost of this post process [23].

Laser surface processing is emerging as a suitable technique for reducing surface roughness in metals, ceramics and polymer materials as it offers several modification regimes depending on the laser processing parameters (i.e., power density and interaction time), namely: melting and ablation. [2,3,7-9].

In 2000 Alexander Bestenlehrer founder of Laser Finishing Center (LCF) AG was granted a U.S. patent for a method and device that process arbitrary 3D shaped surfaces by means of a high energy pulsed lasers, in particular for polishing and texturing of steel work pieces [24]. The process is based on laser surface ablation achieved by means of a high energy density pulsed laser of up to  $200 \text{ J/cm}^2$  in the green to ultraviolet wavelength range, typically from copper vapor or KrF excimer lasers. Recently in Reference 25, it is reported that by a combination of pulsed and c.w. laser radiation LCF has been able to smooth the surfaces of milled and eroded tools steels. A 100 W diode pumped Q-switched Nd:YAG laser operating at 40 ns pulses and a power density of  $10^6 \text{ W/cm}^2$  at the spot location achieved a surface roughness  $R_a$  of 0.25 microns on selected steels at a polishing rates of 2.5 to 4 min/cm<sup>2</sup>. Penetration melt depths are reported to be in the order of 50 microns.

Previous work by Wang *et al.* [26] indicated that fused silica surfaces could be polished from 2.0  $\mu\text{m}$  to 0.05  $\mu\text{m}$  (i.e. peak-to-valley distance) by means of a 25 W CO<sub>2</sub> focused continuous wave laser. The polishing mechanism in this

case is melting of a micron size layer of material flowing under the action of surface tension. A wide laser polishing operational window from 500 to 1100 J/cm<sup>2</sup> existed for this material system. This is consistent with earlier work by Temple [27] who polished quartz surfaces with an energy density of 796 J/cm<sup>2</sup>.

An intermediate step in solving this problem is to employ the hardware available to the SLS process, specifically a high power laser unit and galvanometer scanner mirrors, to provide for laser polishing of the rapid prototyped object.

Pursuing this objective, early experimental results obtained by the author and co-workers showed decrements in  $R_a$  values up to 3 times the as-received values on indirect-SLS parts made from LaserForm ST-100<sup>TM</sup>, an alloy system commercialized by 3D Systems, Inc. This alloy consists of a 420 stainless steel matrix, 40 wt.% infiltrated with bronze (5 wt.% tin). Two surface modification regimes are believed to exist: shallow surface melting (SMM) and surface over-melt (SOM). The onset of each regime is dictated by the energy density (i.e., ratio of laser power to scan speed and beam diameter) as well as the initial roughness  $R_a$  value prior to laser surface polishing.

The schematic drawing of the laser polishing process utilized to reduce the surface roughness of LaserForm ST-100<sup>TM</sup> indirect SLS parts is illustrated in

Figure 1.9. A focused laser beam of sufficient power to melt the surface of the object was raster-scanned at high speed along a rectangular track.

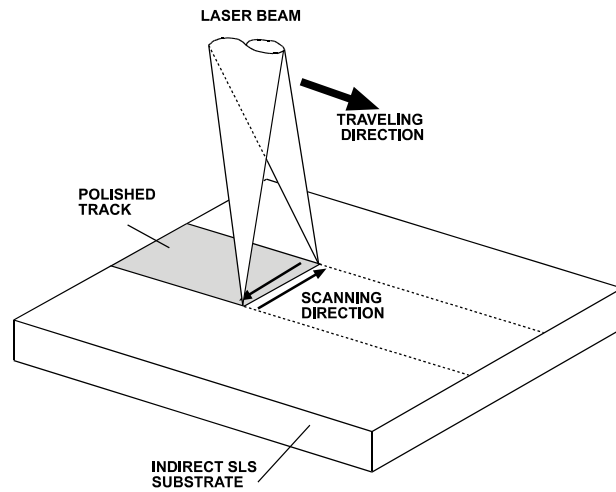


Figure 1.9. Schematic diagram of the laser polishing process.

#### 1.4.1 Surface shallow melting regime

The surface of the indirect-SLS made part may be assumed to consist of peak and valley regions as observed by scanning electron microscopy (SEM), Figure 1.10. When a laser beam of sufficient energy density (e.g.,  $500 \text{ J/cm}^2$ ) impinges on such a surface morphological apexes reach the melting temperature. If the scan speed of the laser beam is fast enough, only a short depth of melt develops on the surface. A fraction of a molten peak mass then flows into a valley driven by the liquid surface curvature, surface tension gradient, gravity and laser

beam pressure [3,28]. This “surface-shallow-melting” (SSM) mechanism lowers the peak-to-valley height, thus reducing the surface roughness

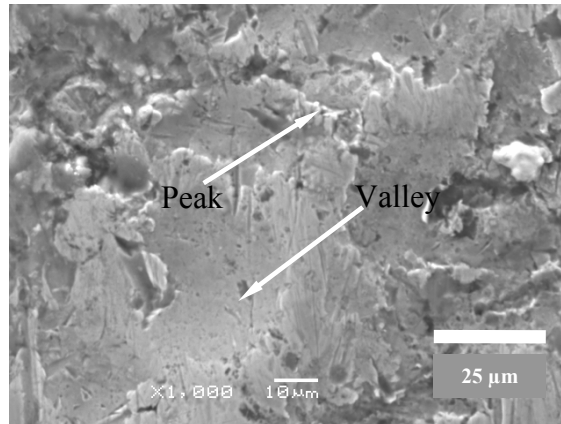


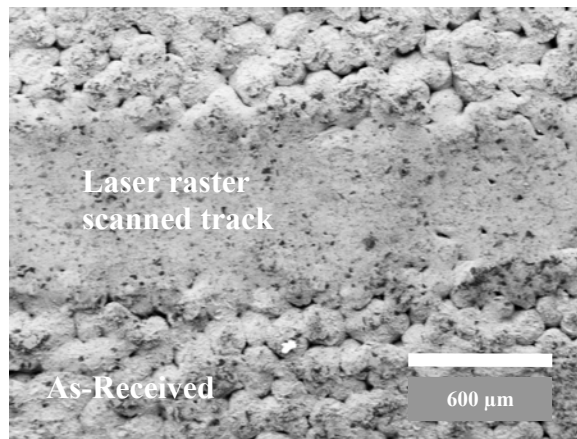
Figure 1.10. SEM image of as-received 420 stainless steel–40 wt.% bronze indirect-SLS sample surface, 1000x.

A rough SLS metallic surface can be simplistically envisioned as consisting of close packed spheres with diameter equal to the average diameter of the precursor powder utilized. A peak corresponds to the apex of a sphere, and a valley corresponds to the trough formed in between three neighbor tangent spheres. When a laser beam impinges on such a surface, the surface of the spheres enclosed in the beam diameter will reach the melting temperature after a certain interaction time. Metallic surfaces inherently possess high reflectivity to infrared wavelength [3,7-9]. However, the coupling of the laser energy should be mostly uniform over each sphere surface, i.e. from peak to valley, considering that multiple reflections at the trough aid infrared absorption.

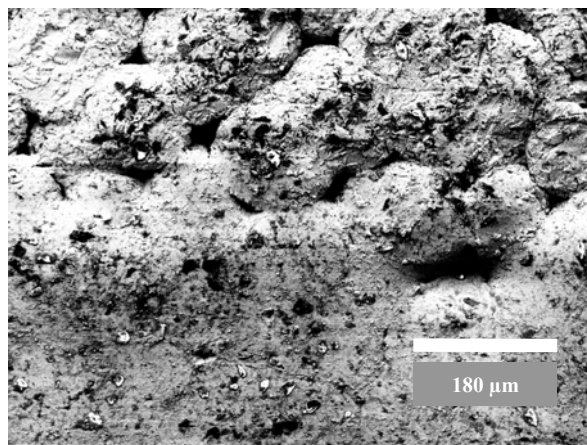


At the onset of melting, the local curvature of the established liquid surface at the trough becomes large enough to effectively drive spreading of the molten mass from the powder apex towards the trough to minimize the local curvature of the liquid. Liquid flows into the trough by capillary pressure aided by its reduction in viscosity. The action of Marangoni forces and possibly laser pressure should also be considered [3,14]. If the average time of liquid flow is shorter than the average solidification time of the melt then this “shallow-surface-melting” (SMM) mechanism can effectively reduce the peak-to-valley height, thus lowering the  $R_a$  surface roughness.

Figure 1.11a shows a scanning electron microscope image of the Nd:YAG laser polished indirect-SLS sample ( $9\ \mu\text{m}$  as-received  $R_a$  value), from which it can be seen that the as-received surface consists of sintered close packed spherical caps, corresponding to liquid bronze sintered 420 stainless steel powder particles of average radii size  $75\ \mu\text{m}$ . Where the laser beam has raster scanned across the surface, the sphere caps have been smoothed reducing roughness to  $3.0\ \mu\text{m}$   $R_a$ . Figure 1.11b illustrates the latter phenomenon at a higher magnification, it can be seen that at the interface between the as-received and polished zone some sphere caps became semi-melted.



(a)



(b)

Figure 1.11. (a) SEM image of 240 W Nd:YAG laser polished 420 stainless steel–40 wt.% bronze indirect-SLS slab, 60x; (b) SEM image of interface zone of same sample, 200x.

A schematic illustration of the liquid metal transport into the troughs with increasing time is shown in Figure 1.12.

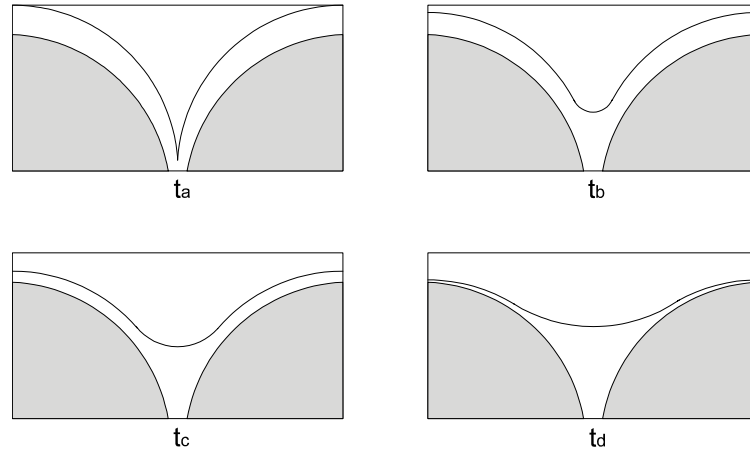


Figure 1.12. Schematics of the liquid transport with ascending time,  $t_d > t_c > t_b > t_a$ .

#### 1.4.2 Surface over melting regime

If the scan speed of the laser beam is relatively slow, “surface-over-melting” (SOM) of the peaks and valleys takes place. In this mechanism, the surface then becomes completely molten. Low-frequency high-amplitude surface periodic structures develop and relax during the laser beam motion, thus potentially increasing the roughness  $R_a$  value [15]. These morphologies were also identified by means of optical and scanning electron microscopy (SEM). For a fixed laser power, SSM shows a reduction in roughness  $R_a$  below the initial value with decreasing scanning speed up to a limiting value. Further decrease in scan speed causes onset of the SOM mechanism with increase in roughness  $R_a$  with

speed reduction. As shown in Figure 1.13 beam motion causes the molten material underneath it to be pulled away towards the solidifying front, thus forming a ripple.

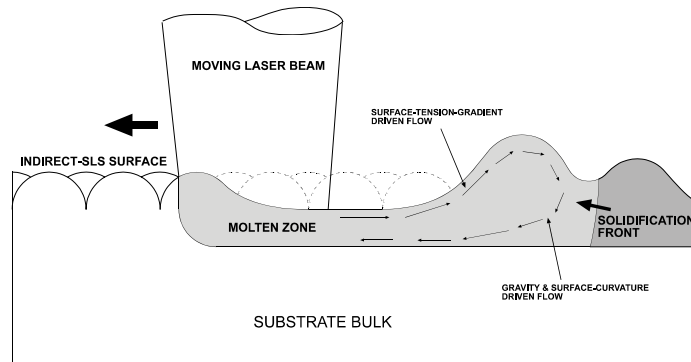


Figure 1.13. Schematic of a surface periodic structure formation during SOM mechanism.

This mass flow phenomenon is driven by the surface temperature difference between the laser beam and the solidifying zone caused by the motion of the laser beam [14]. This temperature difference creates a surface tension gradient of different sign that exerts a shear force on the liquid surface towards the solidifying front. Gravity and surface curvature effects counter this external shear force.

Once the thermal gradient vanishes, these forces will restore the surface height to the free level. However, viscous forces will delay this relaxation process. The periodic structure thus formed will only relax until the solidification

front freezes it [15], assuming that the time for solidification is small relative to the time required for complete relaxation.

### **1.5 LASER FUSED CERAMIC COATINGS ON CARBON-CARBON COMPOSITES**

The surface of carbon-carbon (C/C) composite functional parts used in space vehicles (e.g. rocket nozzles, nose cones and wing leading edges) requires environmental protection especially during atmosphere reentry maneuvers. Oxidation at high temperatures is deleterious to the performance of the C/C composites, which start oxidizing at 400 °C in air. For example, during reentry of the Shuttle into the earth's atmosphere, its surface reaches 1260 °C where ceramic tiles are used up to 1460 °C at the nose tip and airfoil leading edges, where graphite composites must be employed [29]. Tiles primarily consist of fine SiO<sub>2</sub> glassy fiber whereas panels consist of 3D C/C composites. Figure 1.14 shows the approximate layout of the tiles and panels on the orbiter surface. RCC stands for reinforced C/C panels, designed to withstand up to 1460 °C. HRSI is the high temperature reusable surface insulation tile designed for 1260 °C temperature regime. LRSI is the low temperature reusable surface insulating tiles designed for temperature in the range of 400 °C to 650 °C. Total number of RCC panels at the nose cap is 44 while the remaining number of RSI titles is 30,812. Difference between HRSI and LRSI is only the surface coating applied to the tile .For the

reentry, whereas for the latter it consists of a silica/alumina coating designed to reflect the sun's radiation during the orbiting phase of the mission [29].

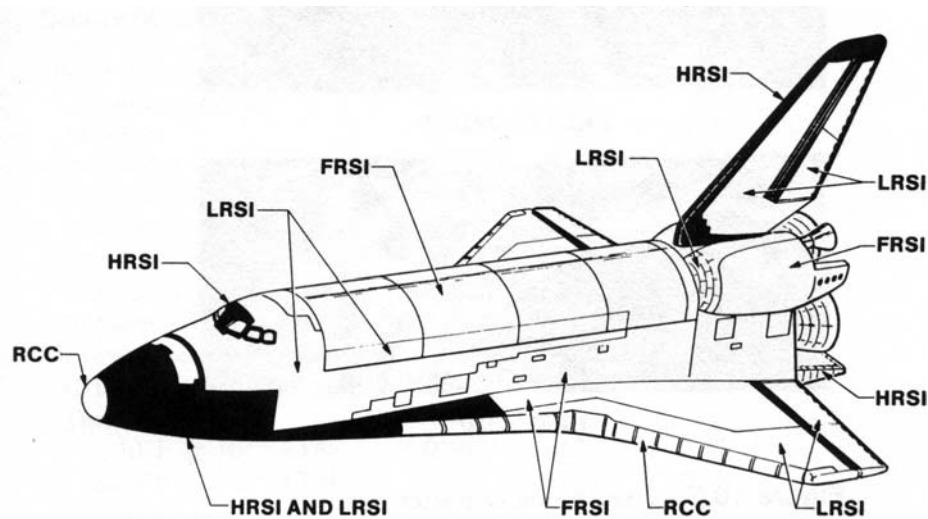


Figure 1.14. Schematic distribution of reinforced C/C (RCC) panels and reusable surface insulation (RSI) tiles in a space orbiter [adapted from Ref.29].

For more than 30 years, single and multi-layer coating techniques have been investigated to enhance the performance of C/C composite materials at high temperatures. Chemical vapor deposition (CVD) is widely used to deposit SiC layers over C/C composites; however, this is a slow and cumbersome process and requires operation under high vacuum conditions. Diffusion-based processes such as pack cementation or fused slurry techniques are also being used to form oxidation resistant coatings. However, these processes require that all of the part surface must be coated and they too need several hours for processing [30, 31].

The purpose of the research was to develop a laser fusion methodology to deposit protective coatings to improve oxidation resistance of C/C composites.

As discussed in earlier sections, when the substrate is a ceramic material that decomposes rather than melts (e.g. carbon-carbon composite), coatings with good bonding characteristics and with overall wetting of the substrate are less likely to be obtained during laser fusion. Poor interfacial characteristics in laser fused samples can be attributed to lack of proper fusion temperature and inadequate dwell time as well as the presence of contaminants such as oxygen and moisture that alter the surface tension balance. Moreover, coating thickness, differences in coefficient of thermal expansion (CTE) between the coating and substrate have a major impact on the delamination or spallation behavior of the coatings [32]. Surface wetting by the chemical slurry depends on the solubility, bonding compatibility, chemical reactivity of the substrate, and the coating constituents [33]. The degree of superheat of the molten slurry will also determine the viscosity of the coating as well as the reaction kinetics. The surface roughness of the samples may increase the interface area contributing to an increase in interfacial strength. However, a rough surface may have poor integrity because of poor wetting and sharp grooves [34]. Finally, the residence time of the molten slurry over the substrate will in turn control the thickness and evenness of the interface.

## **1.6 DIRECT LASER SOLIDIFIED MAR-M 247 SUPERALLOY**

In 1998 Das *et al.* [35] developed a technique for the production of abrasive turbine blade tips based on selective laser melting a pre-placed layer of material along the contour of the tip. Direct laser fabrication of components was achieved from a bed of loose cermet powder consisting of Mar-M 247 nickel superalloy matrix (73 wt.%) mixed with Ti coated cubic boron nitride (9 wt.%) and Ti coated alumina (18 wt.%). The powders were mechanically blended, poured into molds and leveled to ensure constant layer thickness. Tip shape processing was done by two alternative methods. The first method consisted in selectively laser raster scanning the shape of the blade tip out of a powder bed container. The second method was to laser process a rail-shaped tip from powder contained in a mold. In both cases, the powder was processed successfully under high vacuum ( $< 10^{-5}$  Torr) within an energy density window of 2400-3878 J/cm<sup>2</sup>. It was observed that the mold material affected the thermal profile generated and thus the solidification microstructure of the component. Ceramic containers insulated the bottom surface of the powder bed and set up a uniform thermal gradient resulting in partially directional solidification or equiaxed growth. Steel and superalloy containers produced fine dendrite spacing in the solidification microstructure.



Gäumann *et al.* [36] in 1999 developed a laser cladding technique called Epitaxial Laser Metal Forming (E-LMF) that combines the advantages of near net shape manufacturing with close control of the solidification microstructure. When laser power and solidification rates are precisely controlled, columnar dendritic growth can be stabilized, thereby avoiding nucleation and growth of equiaxed grains in the laser clad. In this manner it is feasible to deposit a single crystal clad by epitaxial growth onto a single crystal substrate. A fine dendritic morphology with low residual porosity is achieved due to the high solidification rates and temperature gradients reached during the process. This methodology was demonstrated using CMSX-4 superalloy powder over single crystal substrates of the same material. The volume fraction of equiaxed grains  $\phi$  ahead of the solid-liquid interface was calculated numerically as a function of solidification conditions: thermal gradient in the liquid  $G_L$ , local solidification rate  $R_L$ , density of nucleation sites  $N_0$  and nucleation undercooling  $\Delta T_n$ . The  $\phi$  parameter determined the columnar to equiaxed transition (CET) and it must be less than 0.66% to assure columnar growth according to Hunt [37]. It was determined for this alloy that the critical value of  $N_0$  and  $\Delta T_n$  corresponded to  $2 \times 10^{15} \text{ m}^{-3}$  and 2.5 °C, respectively, for high values of  $G_L$ . Micrographs showed that initially, the primary growth direction of the dendrites was perpendicular to the substrate and there was a systematic change in growth morphology close to the surface of the

cladding, due to a change in dendrite growth direction. The columnar growth of the dendrites was suddenly altered at about half the cladding height. An electron back scattered diffraction (EBSD) map showed no signs of other grains at this location. This new growth morphology was due to a tilting of the primary growth direction by 90° due to a change in the shape of the isotherms, where dendrite arms of the columnar dendrites changed into dendrite trunks. Nonetheless, some grains appearing at the surface of the clad were due partly to the changing solidification conditions at the edge of the clad. That is, the thermal gradient was reduced and the solidification rate increased. Impingement of powder particles that might not be completely molten at the surface can also affect the number of nucleation sites favoring the CET. The primary arm spacing in the deposits corresponded to 11  $\mu\text{m}$ .

The objective of this research is to build up the knowledge and capability for restoration of Ni-base superalloy single crystal components (e.g. aircraft combustion engine turbine blades) to near original properties and dimensions at a small fraction of the cost of replacing the blades. Selective laser melting (SLM) is the chosen technology to perform this restoration due to the hardware availability and previous research experience [35]. As mentioned earlier, it is crucial to develop the ability to tailor the microstructure of the deposited material as it is being laid. Complete epitaxial growth from the substrate material into the

solidifying deposited layer is the main requirement. In the present research single-track, single-layers of Mar-M 247 material were successfully deposited over polycrystalline Ni-base Alloy 718 flat sheets by means of mask confinement of the alloy powder followed by SLM. Feasibility of epitaxial solidification growth within the deposits was demonstrated.

### 1.7 REFERENCES

1. J. Hecht, Laser Pioneers 2<sup>nd</sup> edition (Press Academic, 1992).
2. J.F. Ready, ed., Lasers in Modern Industry (Society of Manufacturing Engineers, 1979).
3. W.M. Steen, Laser Material Processing, 2<sup>nd</sup> edition, (Springer Verlag, 1993).
4. C.R. Deckard, “Method and apparatus for producing part by selective sintering”, US Patent 4863538 (September 1989).
5. S. Das, Ph.D. Dissertation, University of Texas at Austin, December, 1998.
6. J.Powell, P.S. Henry and W.M. Steen, “Laser cladding with preplaced powder: analysis of thermal cycling and dilution effects”, *Surface Engineering*, 4, 141-149, (1988).
7. A. Conde, R. Colaco, R. Vilar, J. de Damborenea, “Corrosion behavior of steels after laser surface melting”, *Materials & Design*, 21, 441-445 (2000).
8. J.F. Ready, D.F. Farson, and T. Feeley, eds., LIA Handbook of Laser Materials Processing (Laser Institute of America, Magnolia Publishing Inc., 2001).
9. J.Feng, M.G.S. Ferreira, R. Vilar, “Laser cladding of Ni-Cr/Al<sub>2</sub>O<sub>3</sub> composite coatings on AISI 304 stainless steel”, *Surface and Coatings Technology*, 88 212-218 (1996).

9. J.Feng, M.G.S. Ferreira, R. Vilar, "Laser cladding of Ni-Cr/Al<sub>2</sub>O<sub>3</sub> composite coatings on AISI 304 stainless steel", *Surface and Coatings Technology*, 88 212-218 (1996).
10. Ramos *et al.*, "Surface modification of 347 stainless steel by rapid mirror scanning of a high power CO<sub>2</sub> laser", Proceedings of International Conference of Applied Lasers and Electro Optics, October 2002.
11. P. Shewmon, Diffusion in Solids, 2<sup>nd</sup> edition, (TMS, 1989).
12. L. Snell, A. Nelson and P. Molian, "A novel laser technique for oxidation-resistance coating of carbon-carbon composite", *Carbon*, 39, 991-999 (2001).
13. A.M. Prokhorov, V.I.Konov, I. Ursu and I.N.Mihăilescu, Laser Heating of Metals, (Adam Hilger, 1990) pp.115-124.
14. T.R. Anthony and H.E. Cline, *J. Applied Physics*, Vol. 48, No 9, 3888-3894 (1977).
15. V.S. Avanesov and M.A. Zuev, "Investigation of surface topography after melting by laser beam", SPIE, Vol. 2713, 340-343.
16. J.J.Beaman, J.W.Barlow, D.L.Bourell, and R.H.Crawford, Solid Freeform Fabrication: A New Direction in Manufacturing, (Kluwer Academic, 1997).
17. J.A. McDonald, C.J. Ryall and D.I. Wimpenny, Rapid Prototyping Casebook, (Professional Engineering Publishing, 2001).
18. L. Lü, J. Fuh and Y.S. Wong, Laser Induced Materials and Processes for Rapid Prototyping, (Kluwer Academic, 2001).
19. J. Connolly, Direct Rapid Manufacturing – Is it Possible?, *Time Compression Technologies*, May (2001), pp. 46-47.
20. M. Burns, Automated Fabrication: Improving Productivity in Manufacturing (Prentice-Hall, 1993).
21. I.Y.Tumer *et al.*, "Characterization of surface fault patterns with application to a layered manufacturing process", *Journal of Manufacturing Systems*, 17 (1) (1998).

22. J.D. Spencer, R.C. Cobb, and P.M. Dickens, "Vibratory finishing of stereolithography Parts", *SFF Symposium Proc.*, 4, 27-39 (1993).
23. D.Shi and I.Gibson, "Surface finishing of selective laser sintering parts with robot", *SFF Symposium Proc.*, 9, 27-35 (1998).
24. A. Bestenlehrer, "Polierwerkstatt fuer Stahlformen," US Patent 6043452, (March 2000).
25. U.K. Jarosch *et al*, "From welding to polishing", *Industrial Laser Solutions*, April (2003), pp.10-12.
26. H.-Y.Wang, D.L.Bourell, and J.J.Beamon, "Laser polishing of silica slotted rods", *Materials Science and Technology*, v. 19, (2003).
27. P.A. Temple, D. Milam, and W.H. Lowdermilk, *Applied Optics*, 21, 3249 (1982).
28. N. Eustathopoulos, M.G. Nicholas, and B. Drevet Wettability at High Temperatures. Pergamon Materials Series Volume 3, Editor R.W. Cahn, (Pergamon, 1999).
- 29 S. Musikant, What Every Engineer Should Know About Ceramics , (Marcel Dekker, 1991).
- 30 T. Morimoto, Y. Ogura, M. Kondo, and T. Ueda, "Multilayer coating for carbon-carbon composites"; *Carbon*, v.33, No 4, 351-357 (1995).
- 31 C. Isola, P.Appendino, F. Bosco, M. Ferraris, and M.Salvo, "Protective glass coating for carbon-carbon composites." *Carbon*, v. 36, No 7-8, 1213-1218 (1998).
32. J.W. Hutchinson and Z. Suo, "Mixed mode cracking in layered materials"; in v. 29, Advances in Applied Mechanics. Edited by . J.W. Hutchinson and T.Y. Wu. (Academic Press, Inc., 1992).
33. J.V. Naidich, "The wettability of solids by liquid metals" *Prog. Surf. Memb. Sci.*, 14, 353-484 (1981).

34. X.B. Zhou and J. Th.M. De Hosson, "Influence of surface roughness on the wetting angle", *J. Mater. Res.*, v.10, N° 8, 1984-1992 (1995).
35. S. Das *et al.*, "Direct laser fabrication of a gas turbine engine component – microstructure and properties – part I", *SFF Symposium Proc*, 10, 1-9 (1998).
36. M. Gäumann *et al.*, "Epitaxial laser metal forming: analysis of microstructure formation", *Mat. Sci. Eng. A*, 271, 232-241 (1999).
- 37 J.D. Hunt, "Steady state columnar and equiaxed growth of dendrites and eutectic", *Mat. Sci. Eng.*, 65, 75-83 (1984).

## **CHAPTER II. THEORETICAL BACKGROUND**

In this Chapter the theoretical aspects of many of the phenomena observed during the three different investigated processes are described and developed analytically to facilitate the discussion of the empirical results presented in Chapter IV. Results from the analytical models presented here are also incorporated in Chapter IV.

### **2.1 MECHANICS OF A RASTER-SCANNED LASER BEAM: INTERACTION WITH A FLAT SURFACE**

Laser processing of materials involves laser-surface interactions. Commonly, focused or defocused laser beams have been used to treat surfaces by moving the latter relative to the beam or vice versa. This “single-beam” approach allows a certain percentage of beam overlap to occur and is typically achieved by conventional mechanical actuators (e.g., CNC x-y table). In recent years, the use of high-power laser beams actuated by high-speed scanning mirrors has opened up novel surface raster-scan processing venues as extremely rapid motion of the beam ( $> 0.5$  m/s) and high percentage overlap ( $> 99.9\%$ ) can be attained. This in turn, permits precise distribution of laser energy along specific geometric patterns such as rectangles, circles, triangles or almost any complex closed region.

Because of this processing scheme, each point at the surface of the material experiences multiple high-frequency heating-cooling (HC) cycles during the overall laser scanning time. HC cycle period is a function of position along the scanning direction and overall geometry of the scanning pattern.

### **2.1.1 Energy density relationship between a line and raster scan sources**

The Andrew's number is a measure of the energy deposited per unit area over the surface of a material by a moving energy source. It can also be expressed as the power deposited over an area that is being continuously displaced per unit time, thus for a given laser power,  $P$ , focused at a spot of diameter,  $D$ , which moves with a traveling speed,  $V_t$ , the Andrew's number becomes,

$$A_s = \frac{P}{D \cdot V_t} \quad (2.1)$$

If the energy source were no longer circular but of rectangular shape, with dimensions  $D$  and  $W$ , where  $W$  corresponds to the width of the source and  $D$  the thickness; in the case of  $W \gg D$ , the source can be considered a line source having its speed  $V_L$  perpendicular to  $W$ . The Andrew's number then becomes

$$A_L = \frac{P}{W \cdot V_L} \quad (2.2)$$



If such linear source moved a length  $L$ , then the overall rastered area would be  $L \cdot W$ , and the time taken to cover that area is,  $\Delta t = \frac{L}{V_L}$ , and the total energy density deposited is,  $\frac{P \cdot \Delta t}{L \cdot W}$ , which corresponds to Eq. 2.1, when  $\Delta t$  is substituted in.

Now let us consider what happens when the area,  $L \cdot W$ , is rastered not by a line source of width  $W$ , but by a spot source of diameter  $D$ , that scans parallel to the width  $W$  of the area. Figure 2.1 shows a schematic illustration of the typical laser raster scan process.

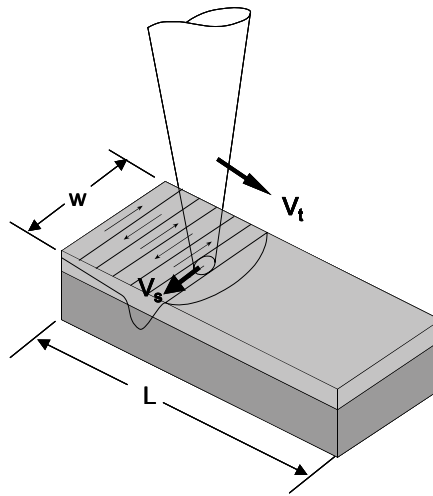


Figure 2.1. Schematic of the typical laser raster-scan fusion coating process.

It can also be assumed that there is no overlap of the spot source as it travels back and forth over the width  $W$  at a speed  $V_s$  (generally faster than the

traveling speed  $V_t$ ), so that at each edge, its perpendicular position is offset a distance  $D$ . The number of scan-lines required to cover the area  $L \cdot W$  is,

$$N = \frac{L}{D} \quad (2.3)$$

In this situation the time taken to cover the area  $L \cdot W$  becomes,

$$\Delta t_{r-s} = \frac{N \cdot W}{V_s} = \frac{L \cdot W}{D \cdot V_s} \quad (2.4)$$

and the total energy deposited over area,  $L \cdot W$ , by the raster-scanned source now becomes,

$$\frac{P \cdot \Delta t}{L \cdot W} = A_{r-s} = \frac{P}{D \cdot V_s} \quad (2.5)$$

We can then conclude that to achieve the same Andrew's number associated to area,  $L \cdot W$ , and a fixed laser power,  $P$ , from Eq. 2.1 and 2.5 the following equivalence relation must hold,

$$\frac{V_L}{V_s} = \frac{D}{W} \quad (2.6)$$

The equivalence between the traveling speed of a line source of width  $W$  relates to the raster-scan speed of a spot source of diameter  $D$  by the quotient,  $D/W$ , which is generally less than 1.

We may allow a certain amount of overlapping between successive scanned lines and define the percentage of overlap as,

$$\phi = 1 - \frac{\Delta x}{D} \quad (2.7)$$

where  $\Delta x$  is the distance between the corresponding edges of two successive scanned lines as illustrated in Figure 2.2 .

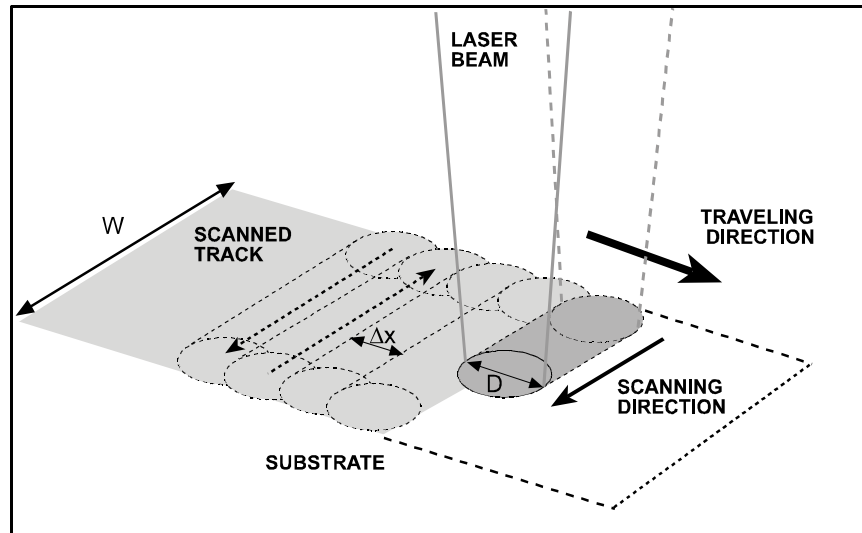


Figure 2.2. Schematic illustration of the overlapping of raster scans tracks.

Then, the number of scan lines,  $N_{ov}$ , needed to cover area,  $L \cdot W$ , is,

$$N_{ov} = \frac{L}{(1-\phi) \cdot D} \quad (2.8)$$

The time taken to cover such area now becomes,

$$\Delta t_{ov} = \frac{L \cdot W}{(1-\phi) \cdot D \cdot V_s} \quad (2.9)$$

and the total energy deposited over  $L \cdot W$  by the raster-scanned and overlapped source is,

$$\frac{P \cdot \Delta t}{L \cdot W} = A_{\text{rsoV}} = \frac{P}{(1-\phi) \cdot D \cdot V_s} \quad (2.10)$$

The equivalence relationship then becomes,

$$\frac{V_L}{V_s} = \frac{D}{W} \cdot (1-\phi) \quad (2.11)$$

Verifying Eq. 2.5 when  $\phi = 0$ , i.e., when no overlap exists. When  $\phi$  is non-zero, the average traveling speed,  $V_t$ , of the raster scanned source becomes,

$$V_t = \frac{L}{\Delta t_{\text{rsoV}}} = (1-\phi) \cdot \frac{D}{W} \cdot V_s \quad (2.12)$$

Corresponding to Eq. 2.11. This means that the traveling speed of the line source is the same as the average traveling speed of the raster scanned source.

Equation 2.10 is a useful relationship that allows one to compare surfaces that have been laser processed and thus modified by line or raster scanned sources, keeping constant in both cases the Andrew's number by varying  $\phi$  and  $V_s$ , when  $W$ ,  $D$  and  $V_L$  (or equally  $V_t$ ) are kept constant.

Understanding the influence of scan geometry and overlapping on raster-scan surface processing provides a method to tailor the surface peak temperature as well as the heating and cooling rates and so to affect the solidification or sintering conditions and therefore the mechanical properties of the parts obtained.

### 2.1.2 Surface temperature evolution during laser scanning

At a given point a distance  $z$  from the surface, the temperature rise due to the heating portion of the HC cycle can be modeled through the analytical solution to the 1-D, semi-infinite, flux boundary conditioned heat conduction problem. The core of the heat conduction problem is the well-known parabolic differential equation in one-dimensional space:

$$\frac{\partial^2 T}{\partial z^2} = \frac{1}{\alpha} \cdot \frac{\partial T}{\partial t} \quad (2.13)$$

The initial temperature is  $T_0$  over all the domain, and at the surface of the specimen ( $z = 0$ ), the flux boundary condition is,

$$K \cdot \left. \frac{dT}{dz} \right|_{z=0} = I \quad (2.14)$$

where  $I$  is the power density of the laser beam,

$$I = \frac{(1-\mathfrak{R}) \cdot P}{A} \quad (2.15)$$

$\mathfrak{R}$  incorporates the effect of the surface reflectivity, which is a strong function of the laser wavelength, as well as radiative and convective surface heat losses. The area illuminated by the beam,  $A$ , can be circular as in the case of a raster-scanned-source (i.e.,  $\pi D^2/4$ ) or rectangular for a line-source (i.e.,  $W \cdot D$ ). The second boundary condition need to solve the problem corresponds to that of symmetry at a value of  $z$  equals to minus infinity (i.e.,  $dT/dz = 0$  at  $z = -\infty$ ).

The analytical solution to this problem provides a uniaxial temperature distribution in closed form as a function of position and time in the semi-infinite solid [1]:

$$T(z,t) = \frac{2 \cdot I}{K} \cdot \left( e^{-\frac{z^2}{4 \cdot \alpha \cdot t}} \left( \frac{\alpha \cdot t}{\pi} \right)^{0.5} - \frac{z}{2} \cdot \operatorname{erfc} \left( \frac{z}{(4 \cdot \alpha \cdot t)^{0.5}} \right) \right) \quad (2.16)$$

Here,  $\alpha$  and  $K$  correspond to the thermal diffusivity and heat conductivity of the solid, respectively, and  $\operatorname{erfc}(\ )$  is the complementary error function. When evaluated at  $z=0$ , Eq. 2.16 then simplifies to

$$T(z,t)|_{z=0} = T(t) = \frac{I}{K} \cdot \left( \frac{4 \cdot \alpha \cdot t}{\pi} \right)^{0.5} \quad (2.17)$$

Linear superposition theory can then be applied to obtain both the heating and the cooling portion of the HC cycle [1-3]. The latter initiates after the heat source has interacted for a given time interval,  $D/V_s$ , which is equivalent to being turned off. This corresponds to the following surface boundary condition,

$$K \cdot \left. \frac{dT}{dz} \right|_{z=0} = \begin{cases} I & \text{for } 0 < t \leq \frac{D}{V_s} \\ 0 & \text{for } t > \frac{D}{V_s} \end{cases} \quad (2.18)$$

The resulting expression has the form,

$$T_{HC}(t, \tau_0) = T(t) \cdot H(t) - T(t - \tau_0) \cdot H(t - \tau_0) \quad (2.19)$$

and  $H(t)$ , corresponds to the Heaviside step function and  $\tau_0$  is half the laser interaction time interval or heating time,  $D/2V_s$ . This is the time one half the laser spot size spends traveling over a specific surface coordinate. This time interval causes increase in local surface temperature and corresponds to the first term on the right hand side of Eq. 2.19. The heating cycle is immediately followed by a cooling cycle that corresponds to the second term on the right hand side of Eq. 2.19. The complete HC cycle is illustrated in Figure 2.3.

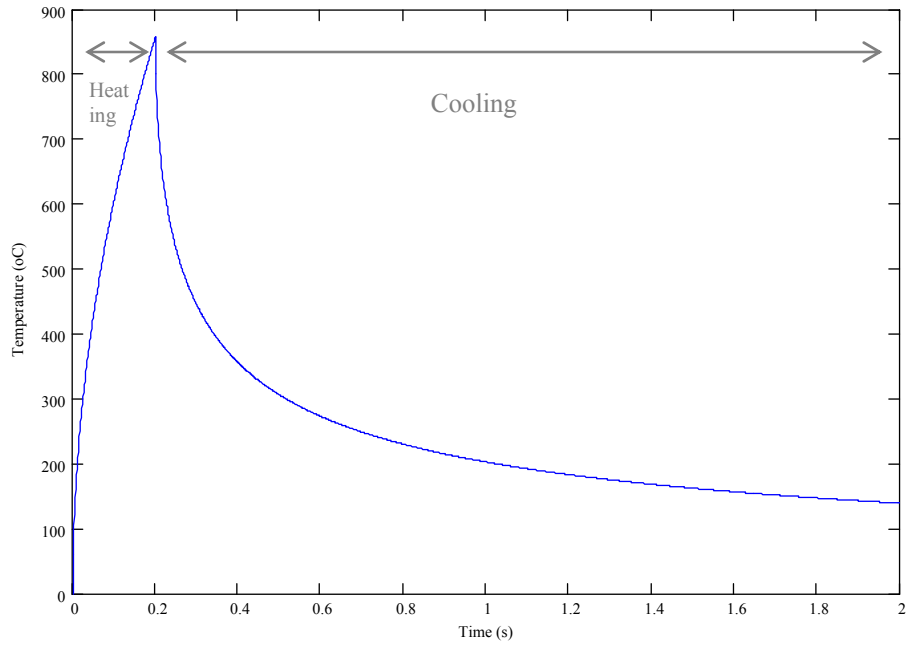


Figure 2.3. Typical heating cycle followed by the corresponding cooling cycle after the source is turned off or displaced from the location.

Linear superposition theory can be further applied to determine the superposition of thermal histories due to multiple overlaps. An arbitrary  $x$  position, along the scan-width  $W$  is considered, measured from the left edge (Figure 2.2). The temperature evolution during the initial heating at each complete raster scan cycle, is determined by

$$f_{\text{Initial}}(t, \tau_1, \tau_2) = \sum_{i=0}^{\frac{1}{1-\phi}} (1-(1-\phi) \cdot i) \cdot [T(t - \tau_1) \cdot H(t - \tau_1) - T(t - \tau_2) \cdot H(t - \tau_2)] \quad (2.20)$$



The summation limit,  $1/(1-\phi)$ , refers to the number of times the laser has to scan over its spot area to raster it completely. After every scan, the beam is offset a percentage,  $1-\phi$ , of the total spot width, so the intensity of the heat flux experienced by the space coordinate,  $x$ , is assumed to decay as  $1-(1-\phi)^i$ , where,  $i$ , is the summation index corresponding to the raster scan number count.  $\tau_1$  corresponds to one full raster scan time interval in which the source travels from  $x$  and back to it,

$$\tau_1 = \frac{2 \cdot W \cdot i}{V_s}$$

and,  $\tau_2$ , corresponds to the same interval plus half a heating cycle  $D$ , this is,

$$\tau_2 = \frac{2 \cdot W \cdot i + \frac{D}{2}}{V_s}$$

Additionally, the temperature evolution during the time it takes the source to travel from  $x$  to the right edge of the width and then back to the former is,

$$f_{\text{Right}}(t, \tau_3, \tau_4) = \sum_{i=0}^{\frac{1}{1-\phi}} (1-(1-\phi)^i) \cdot [T(t-\tau_3) \cdot H(t-\tau_3) - T(t-\tau_4) \cdot H(t-\tau_4)] \quad (2.21)$$

Function  $\tau_3$ , corresponds to the cooling interval as the beam moves away from  $x$  to  $W$  and from  $W$  to back  $x$ , by,

$$\tau(x)_3 = \frac{2 \cdot W \cdot i + 2 \cdot (W - x)}{V_s}$$

and function  $\tau_4$ , corresponds to the same cooling interval plus one heating cycle  $D$  when  $0 < x < W$ ,  $D/2$  when  $x = 0$ , and zero heating interval when  $x = W$ .

Function  $\tau_4$  is expressed as,

$$\tau(x)_4 = \frac{2 \cdot W \cdot i + 2 \cdot (W - x) + D \cdot \left( 1 - \frac{1}{2} (\delta(x - 0) + 2 \cdot \delta(x - W)) \right)}{V_s}$$

In the previous cases,  $\delta(\ )$ , corresponds to the Dirac-delta function, and is included to discriminate the position of interest,  $x$ , from being at a left or right edge instead of an inner position. Similarly, the temperature evolution during the time it takes the source to travel from  $x$  to the left edge of the width, and then back to the former is given by a similar expression,

$$f_{\text{Left}}(t, \tau_5, \tau_6) = \sum_{i=0}^{\frac{1-\phi}{1-\phi}} (1-(1-\phi) \cdot i) \cdot [T(t-\tau_5) \cdot H(t-\tau_5) - T(t-\tau_6) \cdot H(t-\tau_6)] \quad (2.22)$$

which only differs in the form in which the cooling intervals,  $\tau_5$  and  $\tau_6$ , are expressed, that is:

$$\tau_5 = \frac{2 \cdot W \cdot (i + 1)}{V_s}$$

$$\tau(x)_6 = \frac{2 \cdot W \cdot (i + 1) + \frac{D}{2} \cdot (1 - \delta(x-0))}{V_s}$$

The difference between  $\tau_5$  and  $\tau_6$  intervals is one half the heating interval when  $x > 0$ . Thus, the temperature profile at a given position,  $x$ , for a raster scan processing, as a function of time is,

$$T(t, x)_{\text{Raster-Scan}} = f(t, \tau_1, \tau_2)_{\text{Initial}} + f(t, \tau_3, \tau_4)_{\text{Right}} + f(t, \tau_5, \tau_6)_{\text{Left}} \quad (2.23)$$

To illustrate the use of Eq. 2.23, a plot of a typical sequence of heating and cooling cycle when two complete back and forth raster scans are performed is presented in Figure 2.4. The continuous lines correspond to the temperature measured at the center of the width while the dotted line corresponds to the temperature as measured at either one of the edges. The first peak is narrower as it

corresponds to half the total heating interval,  $D/2V_s$ , whereas the other peaks correspond to a full heating interval.

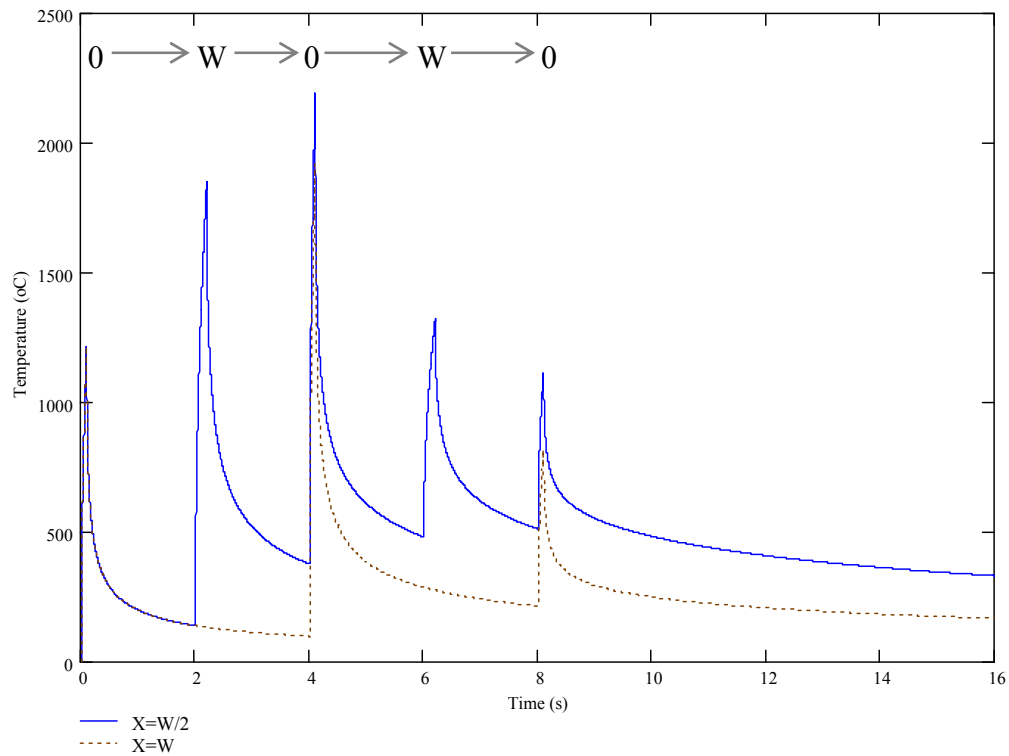


Figure 2.4. Typical sequence of heating and cooling cycle when two complete back and forth raster scans are performed.

### 2.1.2.1 Illustration of numerical results

Numerical implementation of Eq. 2.23 was done and the temperature profiles results are plotted in Figure 2.5. The implementation of this model is presented in Appendix A-I. These temperature profiles were evaluated at half the

width of the scan pattern. These results were used to compare the thermal histories of 3 different laser surface processes, namely: (a) laser surface polishing of flat 420 stainless steel-40wt.% bronze surfaces, (b) laser induced cementation of C/C composite cylinders and (c) Mar-M 247 direct laser single layer masked deposition. However, to compare the different temperature profiles, the material properties and the laser power and spot diameter on all three processes were equally assigned. Temperature independent materials properties for 420 stainless steel-40wt.% bronze alloy were considered, the laser power was made equal to 250 W, the spot size was 0.4 mm. Variables among all these processes were: width  $W$  and length  $L$  of the scanned rectangular region, number of scanning lines,  $N$ , percentage overlap,  $\phi$ , and scan speed,  $V_s$ , along width. These variables were assigned different values for each of the three processes. In process (a)  $W/L = 0.04$ ,  $N=2000$  lines/inch,  $\phi=96.88$ ,  $V_s=500$  mm/s, in process (b) in process the ratio  $W/L = 0.08$ ,  $N= 4000$  lines/inch,  $\phi= 99.68\%$  ,  $V_s=417$  mm/s (c)  $W/L = 0.04$ ,  $N=7000$  lines/inch,  $\phi= 99.11\%$ ,  $V_s=700$  mm/s. From Eq. 2.10 the equivalent Andrew's numbers are,  $40 \text{ J/mm}^2$ ,  $468 \text{ J/mm}^2$  and  $100 \text{ J/mm}^2$ , respectively.

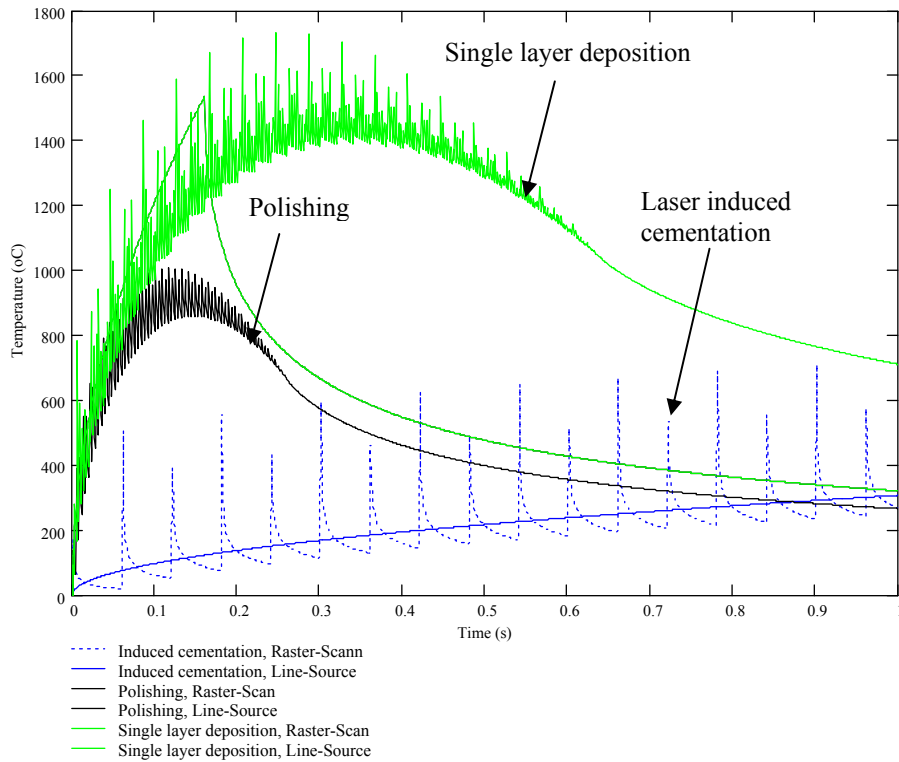


Figure 2.5. Surface temperatures at a fixed position versus interaction time for raster-scan processing and line-source processing for 3 different processes.

From Figure 2.5 it can be observed that for a diffusion-driven process like the laser induced cementation, long-width short-length scanned regions ( $W/L=5$ ) with high number of scan lines ( $N=4000$ ), provides a low average temperature with spaced out sharp temperature peaks, whereas for narrow-width long-length scanned regions ( $W/L=0.04$ ) with lower number of scan lines ( $N=2000$ ) as in laser polishing the average temperature is higher but short lived whereas the temperature peaks are shorter and much closer together. When increasing the

number of scan lines ( $N=7000$ ) keeping the same width-to-length ratio as in single layer masked deposition, the average temperature is higher and also lasts longer, and the peak temperatures are less spaced out.

The temperature history obtained for a line source of equal power and traveling speed, along the length direction, is also plotted in Figure 2.5 for comparison purposes. In the case of processes (a) and (c), the temperature profile is the same in both cases the associated Andrew's number is the same and equal to  $100 \text{ J/mm}^2$ . In this case a much higher temperature is obtained with the line-source as well as steeper heating and cooling rates. In the case of process (b), the associated Andrew's number is  $480 \text{ J/mm}^2$ , and the temperature is not much higher than obtained for a raster-scan source. The peak temperatures from the latter source are higher in this particular case. It is worth noticing that in process (c) the Andrew's numbers of the line and raster-scan sources are the same and that for process (b) these are very close.

### **2.1.3 Advantages of a raster-scan beam delivery system**

Among the advantages of using a laser beam for coating surfaces it is found that this type of energy source can be controlled by optical means and very high power densities, i.e. power over illuminated spot area, can be achieved exceeding  $10^8 \text{ W/cm}^2$ . As light carries negligible momentum, the beam exerts

almost no inertia to the workpiece; moreover thermal/mechanical deformation of the latter is negligible. A focused laser beam produces localized melting of surface material, making it possible for small areas to be modified without altering the integrity of the substrate bulk. Melted regions can experience rapid cooling rates of the order of  $10^5$  -  $10^8$  °C/s [3-5].

Further advantages of a high-speed raster-scan laser beam delivery system over the conventional x-y motion of a focused or defocused laser beam, are:

- (i) Creation of moving line-energy source allowing for uniform and more homogenous temperature distribution over space as measured by the author a using real time infrared thermal imaging system.
- (ii) Fast and precise selective surface energy deposition.
- (iii) Enhanced mixing of coating material and substrate inside the melting zone due to rapid motion of the laser beam.
- (iv) Longer melt resident time due to induced Marangoni's flow.
- (v) Space modulation of energy input by changing the percentage of scan-line overlapping, thus controlling the heat input and consequently the depth of melt, melt resident time and temperature gradients in the liquid.

The principal disadvantage of a raster-scan system is the difficulty to vary the focal position of the beam, especially if it must be done in real time. If the



focusing lens is located before the scanning mirrors, then its focal length must be considerably long, making it difficult to achieve a small width of focus unless very wide optics are used. If the focusing optic is located after the scanning mirrors then a lack of focusing accuracy appears due to aspherical aberration. Additionally, handling kilowatts of power also required the laser beam to be expanded considerably so that the power density impinging on the scanning mirrors falls below a surface damage threshold limit.

Figure 2.6 shows a thermal image of the area scanned by the laser beam obtained by using a real time infrared camera (Mikron). In this experimental set up a high power CO<sub>2</sub> laser beam focused down to 0.35±0.05 mm was scanned at a speed ( $V_s$ ) up to 10 m/min using a scan density of 1000 raster lines/inch. The traveling speed ( $V_t$ ) used was of the order of 55-80 mm/min. The longer axis of the rectangle corresponds to the width of the specimen (i.e., 12 mm) and the minor axis measures between 2-3 mm. The temperature inside the rectangular zone is almost constant during the entire process as indicated by a longitudinal and transverse profile analysis shown in Figure 2.7.

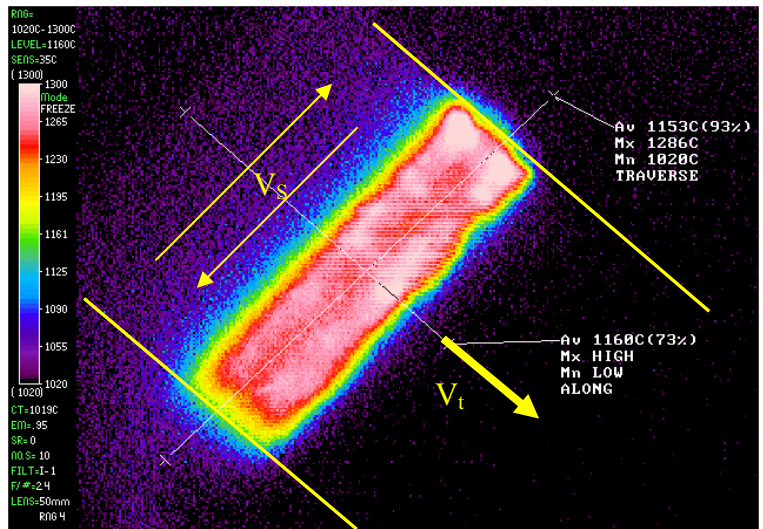


Figure 2.6. Infrared thermal image of raster scanned laser beam over carbon-carbon composite substrate. The average temperature in the hot zone is 1160 °C.

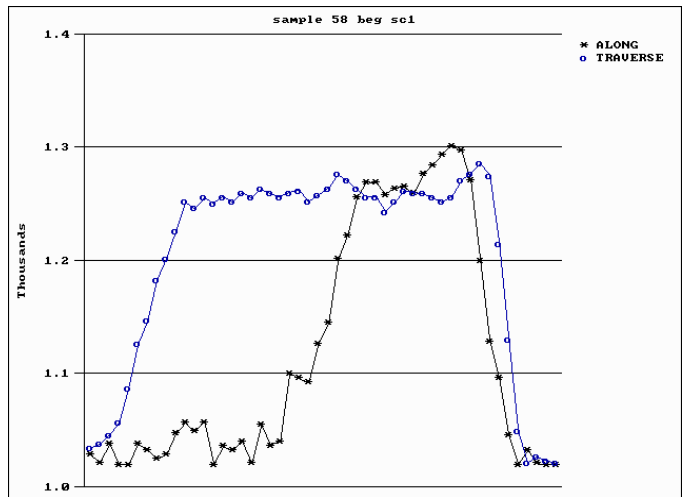


Figure 2.7. Longitudinal and transverse temperature profiles along the thickness and width of the rectangular zone respectively as shown in Figure 2.6.

The maximum temperature reached is approximately 1300°C, while the average temperature in the heated region lies between 1153-1160°C. At the front and rear

edges and at the lateral sides of the rectangular zone, the temperature gradient is of the order of  $-560^{\circ}\text{C}/\text{mm}$ .

#### **2.1.4 Surface features observed after laser melting by raster scanning**

Figures 2.8a and 2.8b show laser surface remelting results on 347H stainless steel slabs achieved using multiple single-line passes (Figure 2.8a) and multiple raster-scanned tracks (Figure 2.8b). Figure 2.9 shows a macrograph of the surface of a Cr-Ni coated 347 stainless steel by means of the selective laser raster-scan technique. The resolidified tracks have almost similar width (i.e., 1.5 mm) and texture appearance; a 37 % overlap (i.e.  $\phi = 0.37$ ) exists between them.

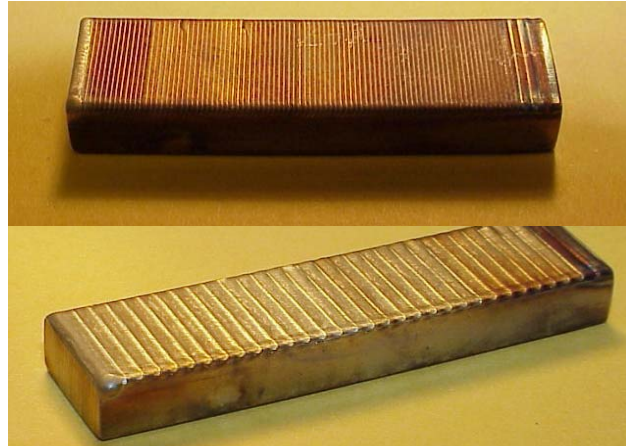


Figure 2.8. Selective laser surface melting of (a) Specimen #9 using single-line with 57 % overlap and (b) Specimen #7 using a raster-scanned with 30 % overlap.

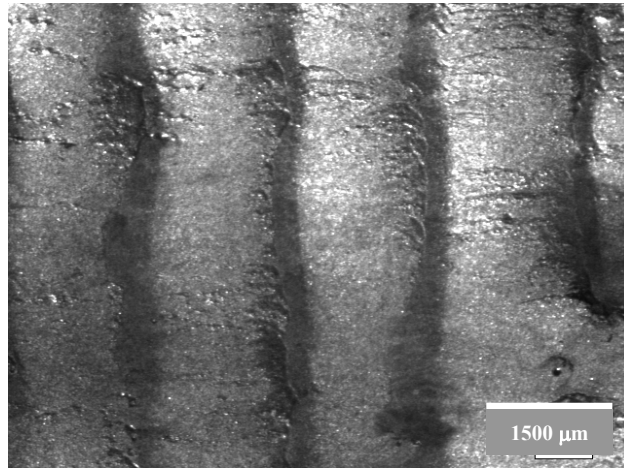


Figure 2.9. Macrograph of the surface of Cr-Ni coated Specimen #16, showing several of the resulting selective laser raster-scanned tracks, 10x.

The effect on microstructure of high percentage of overlap  $\phi$  which corresponds to a large number of scan lines per unit length, can be illustrated in Figure 2.10. This image shows a longitudinal section of a 347 stainless steel specimen coated with a layer TiC product of a laser fusion using the raster-scan scheme. At the 347 stainless steel substrate, a fine layer of material has melted and resolidified epitaxially and on top of it, a TiC structure has solidified in a particular manner resembling a lamellae structure. The observed multi-layered solidification structure growing perpendicular to the substrate may be caused by the repeated melting and solidifying of the TiC induced by the raster-scanned laser beam. In this image the laser beam goes in and out of the image plane and simultaneously advances parallel to the interface line.

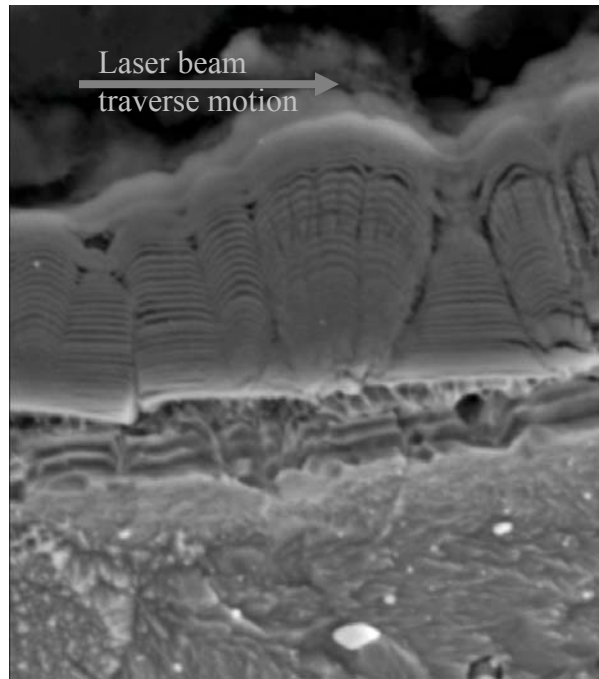


Figure 2.10. SEM image of longitudinal section of a TiC coating on 347H stainless steel laser raster-scanned, 4000x. (Photograph taken by J.Ramos and V.Bansal).

Another interesting phenomenon observed on a laser-coated specimen using a raster scanned beam is that of a dragging-front of coating material. Figure 2.11 shows the longitudinal section of a 347 steel specimen coated with a TiC-50 at.% Ni that was laser raster-scanned. At one position along the middle of the coating line, a “hump” of material has solidified above the substrate without wetting it. This feature may indicate that the pseudo-line source created by the raster-scanned beam provided a uniform surface tension gradient ahead that dragged caked coating material into the melting front, depleting the immediate

substrate of coating material. This dragging of material also caused mass to accumulate at the melting front to the point at which this liquid “hump” collapsed by gravity and viscous forces. However, solidification occurred faster than the spreading of the liquid over the surface, with the resulting frozen overhung shape. Curiously, semi-quantitative EDAX analysis of the coating indicated that a concentration of Ni higher than 50 at.% was present at the frozen hump whereas at the bonded coating (left of the image) the coating was richer in TiC. This may additionally indicate that the molten Ni segregated in front of the molten TiC, instead of forming a single liquid, as it was the last phase to solidify.

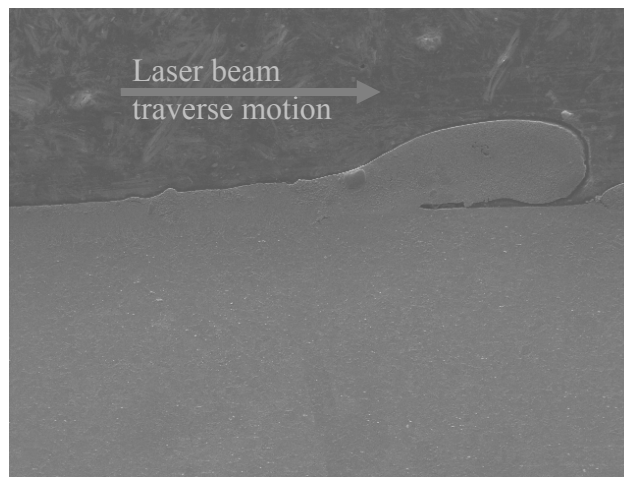


Figure 2.11. SEM image of a longitudinal section of a TiC-50at.% Ni on 347H stainless steel, 50x.

More information regarding the experimental arrangement and processing parameters of these trials can be found in Chapter III.

## **2.2 LASER SURFACE POLISHING MECHANISMS: MODELING THE MELTING REGIMES**

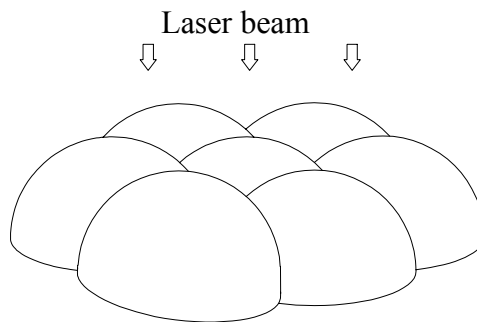
Mechanisms that contribute to smoothing of a 420 grade stainless steel – bronze (LaserForm ST-100™) surface during a raster scan laser surface melting are those of shallow melting, onset of over melt and oxide layer formation. These mechanisms are fully described and/or modeled to understand which physical, geometrical and processing properties are relevant in achieving reduction in surface roughness.

### **2.2.1 Analytical modeling of Surface Shallow Melting**

As confirmed by Figures 1.12a and 1.12b, the surface of the indirect-SLS metal samples may in certain cases consist of precursor powder particles coated with an infiltration alloy. The surface roughness then relates to the average height difference between the particle peaks and valleys. This observation enables development of a model for the estimation of the  $R_a$  surface roughness, asserting that the surface is made of an array of close packed hemispheres as shown schematically in Figure 2.12a. The impinging coupled laser energy, spread over many such hemispheres, elevates the surface temperature of each hemispherical cap to the melting point. The established melting front is assumed to penetrate into the sphere to a certain radial depth. Subsequently, the liquid mass spreads

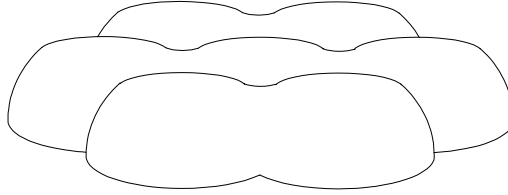
towards the trough to reduce the curvature of the liquid surface there. Figure 2.12b illustrates the resulting polished surface morphology.

The present model is divided into two independent stages, namely: energetic and kinetic. The energetic stage includes a lumped energy balance to determine the amount of mass that is being melted as a function of laser power and interaction time. This is necessary to determine the new height of the cusps. A mass balance is then applied to determine the maximum trough filled height. One necessary condition to be fulfilled is that the sphere height must be greater than or at least equal to the trough filled height. On the other hand, the kinetic stage involves estimation of the solidification and spreading times independently by means of heat transfer and pressure equilibrium relationships, respectively. A second necessary condition for reduction of the peak-to-valley height difference is the spreading time being shorter than the solidification time. The implementation of this model is presented in Appendix A-II.



(a)





(b)

Figure 2.12. Schematic of laser polishing mechanism. (a) Schematic of hemispherical cap surface prior to laser impingement on the surface; (b) Schematic of the surface after the laser has melted the caps.

### 2.2.1.1 Energetics of the model

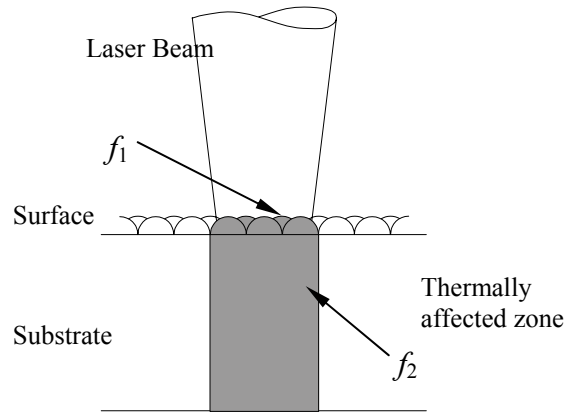
The first step is to establish a lumped conservation of energy relationship, Eq. 2.22, that accounts for radial melting and superheating of the close-packed spherical surface (radius  $R_p$ ) due to a flux of energy, i.e. a stationary laser beam of power  $P$  impinging during a given time interval  $\Delta t$ .  $\mathfrak{R}$  is the overall surface energy loss due to the reflection of the laser beam, as well as by convection and radiation heat transfer.  $C_{p_s}$  and  $C_{p_l}$  are the average specific heat capacities of the solid and liquid, respectively, while  $T_M$  and  $T_0$  are the melting and initial temperature of the substrate. The parameter,  $f_1$ , is introduced to account for the number of spherical caps that are being melted and superheated to  $T_{MAX}$  underneath the laser spot beam of diameter  $D_L$ . This parameter is defined in Eq.

2.25. A second parameter,  $f_2$ , accounts for the substrate volume underneath the laser beam that is thermally affected. It corresponds to a cylindrical volume having a diameter equal to that of the laser beam and a length,  $\delta - R_p$ , equal to the thickness of the substrate below the first layer of particles, (see Figure 2.13a). The lumped energy balance is expressed in terms of the variable  $r$ , the particle sphere radius associated with the particle liquid-solid interface.

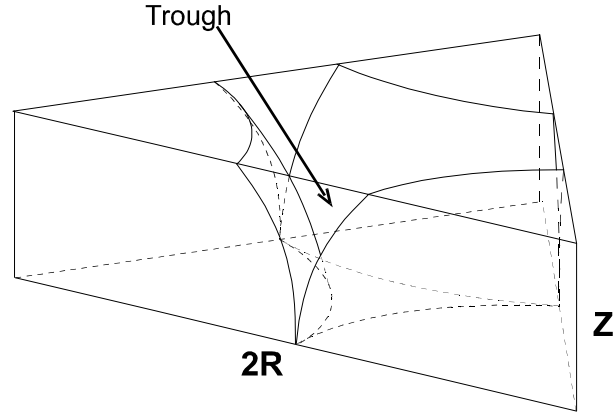
$$P(1 - \mathfrak{R})\Delta t = \frac{2}{3} \pi f_1 \rho \left( (R_p^3 - r^3) [Cp_s (T_m - T_0) + L + Cp_l (T_{MAX} - T_m)] + r^3 Cp_s (T_m - T_0) \right) + f_2 \rho Cp_s (T_{AVG} - T_0) \quad (2.24)$$

$$f_1 = \frac{D_L^2}{4 \cdot R_p^2} \quad (2.25)$$

$$f_2 = \frac{\pi}{4} \cdot D_L^2 \cdot (\delta - R_p) \quad (2.26)$$



(a)



(b)

Figure 2.13. Schematics of the model. (a) Domain for the lumped energy balance. (b) Neighboring close packed spherical segments embedded inside a triangular slab.

$T_{AVG}$  corresponds to the volume averaged transient temperature distribution established in the solid by the laser beam. The latter is approximated by Eq. 2.27, which arises from transient conduction heat transfer already described in Section 2.1.1.

$$T(z,t) = \frac{2}{K} \cdot \frac{P}{\pi \frac{D_L^2}{4}} \cdot \left( e^{-\frac{x^2}{4\alpha t}} \left( \frac{\alpha t}{\pi} \right)^{0.5} - \frac{z}{2} \operatorname{erfc} \left( \frac{z}{(4\alpha t)^{0.5}} \right) \right) \quad (2.27)$$

Eq. 2.27 is a reasonable and economical approximation for the temperature field in this model as the laser beam covers a large surface area during the process (i.e. 1D heat flow), the volume fraction of molten material is a minimum and the thickness of the part is relatively large compared to the particle size.

As previously stated in Section 2.1.1 the time interval of exposure of a moving laser beam over a spherical cap is determined by the spot beam diameter and scan speed,  $v_s$ ; it is given by Eq. 2.28. This expression is a good approximation for the time an effective stationary laser beam heats up the surface [3-5].

$$\Delta t_{\text{INTERACTION}} = \frac{D_L}{v_s} \quad (2.28)$$

Once the cubic polynomial given by Eq. 2.24 has been solved for  $r$  inside of the domain  $[0-R_p]$ , the new hemisphere radius,  $r = r_m$ , is determined and the volume of melt enclosed by one hemispherical cap of outer radius  $R_p$ , and inner radius  $r_m$  is calculated from,

$$V_{\text{MOLTEN}} = \frac{2}{3} \pi (R_p^3 - r_m^3) \quad (2.29)$$

The mass contained in the molten volume  $V_{\text{MOLTEN}}$  is then assumed to redistribute evenly in the six neighboring troughs that surround the hemispherical cap. The volume of a single filled trough is determined by the close packed configuration and corresponds to the volume of an equilateral triangular slab of side  $2R_p$  and height  $z$  minus the volume of half a spherical segment of height  $z$  and radius  $r_m$ , Eq. 2.30, as shown in Figure 2.13b. The liquid is assumed to stabilize into a uniform flat surface. This simplification means that the trough-filled height is a maximum although, in fact, surface tension would tend to lower

this height to minimize its surface area. To find the filled-valley height,  $z_f$ , Eq. 2.30 is set equal to Eq. 2.29; this is illustrated in Figure 2.14.

$$V_{\text{FILLED}}(z) = \sqrt{3}R_p^2 \cdot z - \frac{1}{12}\pi \cdot z \cdot (6r_m^2 - 2z^2) \quad (2.30)$$

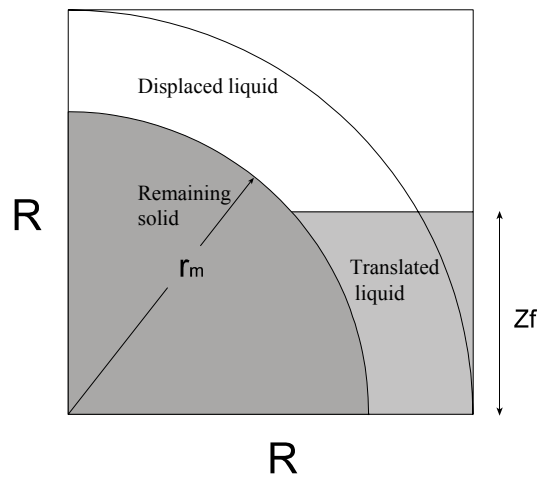


Figure 2.14. Schematic of the relationship between radial melt depth,  $R - r_m$ , and filled trough height,  $z_f$ .

### 2.2.1.2 Kinetics of the model

Immediately after surface melting of the spherical caps has occurred, filling of the trough voids by the available liquid metal takes place relying on capillary pressure driven by the pronounced curvature of the liquid surface at the center of the trough. This pressure draws the liquid fronts towards the center of the trough, coalescing and raising the surface while lowering its curvature. Because the liquid and solid are assumed to have the same composition, the

wetting contact angle is close to zero [6,7], thus providing extended wetting over the hemispheres. Moreover, the liquid metal has low viscosity thus the viscous drag pressure opposing the capillary pressure is minimum as well as the hydrostatic pressure [6]. The pressure balance at a liquid surface element, after it has raised a height  $z$ , is illustrated in Figure 2.15,

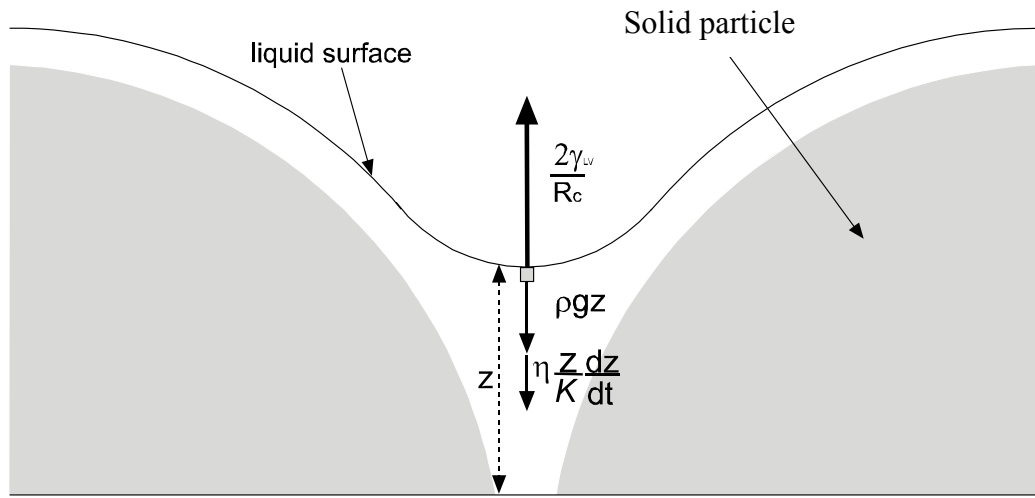


Figure 2.15. Free body diagram of pressure forces acting at the surface of the melt.

The balance of pressures on the element can be written as,

$$-\gamma_{LV} \left( \frac{1}{R_{c_1}(z)} + \frac{1}{R_{c_2}(z)} \right) + \eta \frac{z}{K} \frac{dz}{dt} + \rho g z = \rho z \frac{d^2 z}{dt^2} \approx 0 \quad (2.31)$$

The first term corresponds to Laplace equation for the pressure excess across a curved liquid surface and depends on two radii of curvature ( $R_{c_1}$  and

$Rc_2$ ) and the surface energy  $\gamma_{LV}$  [7]. For a fluid,  $\gamma_{LV}$  is uniform in all directions and is single valued decreasing with increasing temperature. If the radius of curvature is located outside of the liquid the exerted pressure is negative [6]. The second term in Eq. 2.31 corresponds to the viscous drag pressure and can be obtained by means of Darcy's law where  $\eta$  is the viscosity of the liquid metal and  $K$  a permeability constant [8]. Finally, the hydrostatic pressure is added as the last term on the left-hand side of Eq. 2.31. However, under the length scale of the model it has minimal effect. The inertia term on the right hand of Eq. 2.31 is set equal to zero; thus, an equilibrium of pressure terms is imposed on the fluid element [8]. This expression can be integrated after separation of variables to obtain an expression for the time of spreading  $\Delta t_{\text{spreading}}$  as a function of the filled height,  $z_f$ .

$$\Delta t_{\text{SPREADING}} = \int_0^{z_f} \left[ \frac{2 \cdot \gamma_{LV}}{R_c(z)} - \rho g z \right] \frac{\eta \cdot z}{K} dz \quad (2.32)$$

The liquid displacement should occur rapidly at temperatures above the melting temperature [6]. The spreading process continues up to a point where the equilibrium contact angle is reached over the surface of the melted caps.

Finally, spreading of the liquid approaches equilibrium if the solidification time of the liquid is longer than the spreading time. The solidification time,  $\Delta t_{\text{SOLIDIFICATION}}$ , can be estimated from a simplified heat transfer balance in which the radial solidification front velocity is considered constant as illustrated in Figure 2.16.

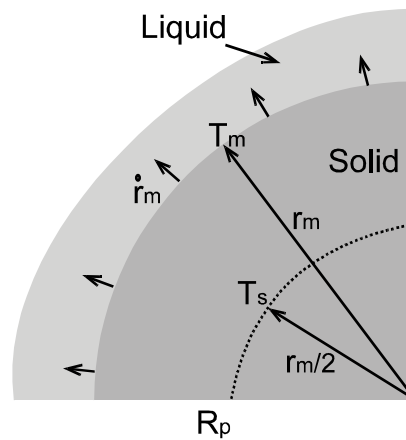


Figure 2.16. Schematic representation of the solidifying front during solidification of a melted particle.

This velocity is driven by the extraction of latent heat by a steady state heat flux transfer from the liquid into the adjacent solidified material [9]. The expression for the solidification time corresponds to,

$$\Delta t_{\text{SOLIDIFICATION}} = \frac{L \cdot \rho}{2K} \cdot \frac{(R_p^2 - r_m^2)}{T \left( \frac{R_p + r_m}{2} \right) - T_m} \quad (2.33)$$



Here,  $L$  corresponds to the latent heat of solidification, and  $K$  is the thermal conductivity of the solid.

### 2.2.1.3 Arithmetic average surface roughness estimation

The arithmetic average surface roughness  $R_a$  is given by the following expression [10],

$$R_a = \frac{\int_0^R |z(r) - \bar{z}| dr}{R} \quad (2.34)$$

where,

$$z(r) = \sqrt{r_m^2 - r^2}$$

Eq. 2.34 describes an arithmetic average between continuous surface heights and depressions as measured from previously computed mean height,  $\bar{z}$  (see Figure 2.17), computed as,

$$\bar{z} = \frac{\pi \cdot r_m^2}{4R} - \left[ \frac{r_m^2}{2R} \arcsin\left(\frac{z_f}{r_m}\right) + \frac{z_f \cdot R_f}{2R} \right] + z_f$$

where,

$$R_f = \sqrt{r_m^2 - z_f^2}$$

By performing integration of Eq. 2.34 one can obtain a closed-form expression for the arithmetic average roughness,

$$R_a = \frac{\bar{R}}{R_f} \sqrt{r_m^2 - \bar{R}^2} - \frac{r_m^2 \cdot i}{R_f} \ln \left[ \bar{R} \cdot i + \sqrt{r_m^2 - \bar{R}^2} \right] + \frac{r_m^2 \cdot i}{2R_f} \ln [r_m] \quad (2.35)$$

$$- \frac{1}{2} \sqrt{r_m^2 - R_f^2} + \frac{r_m^2 \cdot i}{2R_f} \ln \left[ R_f \cdot i + \sqrt{r_m^2 - R_f^2} \right] + \left( 1 - \frac{\bar{R}}{R_f} \right) 2\bar{z} - z_f$$

where,

$$\bar{R} = \sqrt{r_m^2 - \bar{z}^2}$$

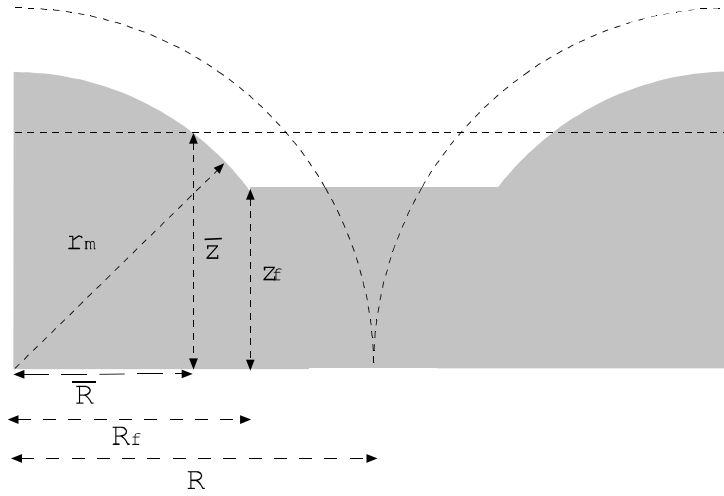


Figure 2.17. Schematic drawings for the determination of the surface roughness  $R_a$  value. Idealized cross section after laser polishing.

### 2.2.2 Analytical modeling of Surface Over Melting

The thermo-physical model presented here describes the amplitude behavior of the observed surface micro-relief and estimates the resulting surface roughness  $R_a$ . It is assumed that the surface relief formed acquires the shape of a sinusoid of fixed propagation vector,  $\mathbf{k}$  and spatial phase  $\varphi$ .  $R_a$  values were measured from laser polished tracks that showed an increment in roughness with

reducing scan speed above the as-received value, as well as the characteristic surface wavelength of each track  $\lambda$ . These measurements provided data to validate the model. The implementation of this model is presented in Appendix A-III.

Figure 2.18 illustrates a schematic diagram of the different variables that are involved in the formation of a surface relief  $\Delta h$  whenever a laser beam traverses the surface of the material causing a depth of melt  $h$ .

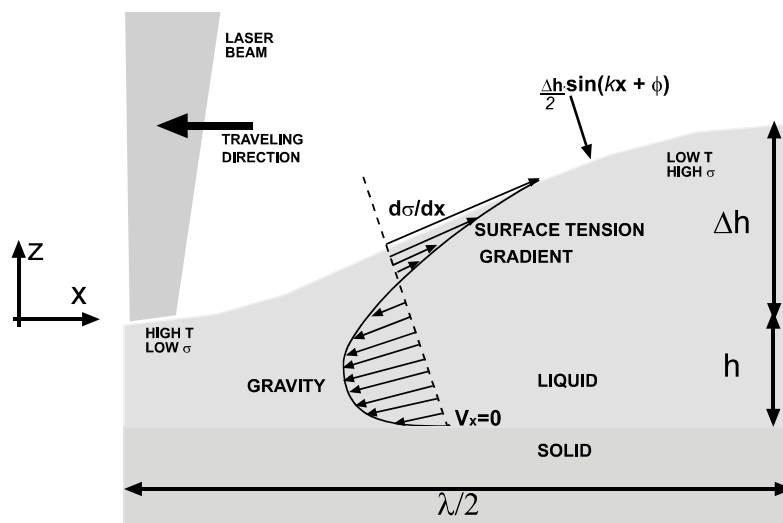


Figure 2.18. Schematic of the rippling phenomenon encountered in the SOM mechanism (based on Anthony and Cline [11]).

Anthony and Cline [11] modeled analytically this surface-rippling phenomenon observed during laser surface melting of metals. The steady-state form of the Navier-Stokes equation (i.e., Newton's Second law) for an incompressible fluid in two dimensions ( $x, z$ ) over a horizontal surface was solved

analytically together with the continuity equation, Eq. 2.36 and 2.37. Fluctuations in the fluid velocity  $v_x$  were considered only in the  $z$  direction and momentum terms were neglected.

$$-\frac{\partial p}{\partial x} + \frac{\partial}{\partial z} \left( \mu \frac{\partial v_x}{\partial z} \right) = 0 \quad (2.36)$$

$$\int_{-h}^{\Delta h} v_x dz = 0 \quad (2.37)$$

$p$  is the pressure tensor and  $\mu$  is the dynamic viscosity of the fluid. The main assumption is that the only restoring force acting on the fluid comes from the hydrostatic pressure head difference along the  $x$  direction. In other words, the effect of gravity  $g$  was accounted for as a pressure gradient due to the increase in surface height. This yields,

$$\frac{\partial p}{\partial x} = \rho g \frac{\partial z}{\partial x} \Big|_{z=\Delta h} \quad (2.38)$$

Boundary conditions include the existence of a surface tension gradient at the surface of the fluid caused by the surface temperature difference at the laser beam center and where the solidification front is located. A zero velocity in the  $x$  direction is also assumed at the solid-liquid interface.

$$\text{at } z = \Delta h \quad \frac{\partial \sigma}{\partial x} = \mu \frac{\partial v_x}{\partial z} = \frac{\partial \sigma}{\partial T} \frac{dT}{dx} \quad (2.39)$$

$$\text{at } z = -h \quad v_x = 0 \quad (2.40)$$

$T$ ,  $\sigma$  and  $\rho$  are the surface temperature, surface tension and density, respectively. For most metals, the surface tension of the liquid phase decreases with increasing temperature. This exerts a shear force that pulls the liquid away from the laser beam center (maximum temperature) towards the solidified zone (minimum temperature) thus forming a surface wave of maximum height,  $\Delta h$ . The expression for this maximum height as presented in [11] as shown as Figure 2.18 is,

$$\Delta h_{\text{MAX}} = \frac{3}{2} \cdot \frac{\Delta T}{\rho g h} \cdot \frac{d\sigma}{dT} \quad (2.41)$$

This expression determines the maximum surface height achieved. This height varies directly with the surface temperature change  $\Delta T$  between the laser beam and solidification front (i.e.,  $T_L - T_m$ ) and surface tension temperature coefficient. It also varies inversely with the depth of melt  $h$  and the gravity term,  $\rho g$ . There is no term that incorporates the effects of the surface curvature on the formation of the maximum height. The author proposes the following modification to Eq. 2.38 and 2.41, considering that the surface attains a sinusoidal shape having a characteristic wavelength  $\lambda$ . This is,

$$\frac{\partial p}{\partial x} = \left( \rho g \frac{\partial z}{\partial x} + \sigma \frac{\partial^3 z}{\partial x^3} \right)_{z=\Delta h} \quad (2.42)$$

$$\Delta h_{\text{MAX}} = \frac{3}{2} \cdot \frac{\Delta T}{\left( \rho g + \sigma \left( \frac{2\pi}{\lambda} \right)^2 \right) h} \cdot \frac{d\sigma}{dT} \quad (2.43)$$

In this situation gravity and surface curvature provide restoring forces that act against the effect of the surface tension gradient during the laser interaction. Once the laser beam has moved a considerable distance away (greater than  $\lambda/2$ ), the surface thermal gradient vanishes and the established periodic surface wave commences to relax driven by these restoring forces (i.e., gravity and curvature). Opposing these forces is the component of the pressure tensor of the fluid, namely the viscous force which is proportional to the dynamic viscosity  $\mu$  of the fluid and the velocity gradient. No momentum terms were added to Eq. 2.38; however, this could be important in fast scans. An expression for the relaxation of the surface height as a function of time  $t$ , for times less than the local solidification time of the melt is given by,

$$\Delta h(t) = \Delta h_{\text{MAX}} \cdot \exp\left(-\frac{\mu}{\rho} \cdot \left(\frac{2\pi}{\lambda}\right)^2 \cdot t\right) \quad (2.44)$$

It can be readily shown that the decaying exponential term is typical of an overdamped harmonic oscillatory system, and it has been also reported before in [12]. To determine the surface temperature change due to a moving laser beam we resort to the known Rosenthal's steady-state analytical solution to the semi-

infinite temperature field for a concentrated energy source moving with constant velocity [13]:

$$T(x,y,z) = \frac{P \cdot (1 - \mathfrak{R})}{2\pi \cdot K_{\text{MOD}}} \cdot \frac{1}{\sqrt{x^2 + y^2 + z^2}} \exp\left(-\frac{v_s}{2\alpha} \cdot \left(x + \sqrt{x^2 + y^2 + z^2}\right)\right) + T_0 \quad (2.45)$$

where  $P$ ,  $R$ ,  $v_s$ , and  $\alpha$  have already been defined.  $K_{\text{MOD}}$  is the modified heat conductivity that incorporates the enthalpy of melting. This expression becomes infinite when evaluated at  $x = y = z = 0$ , i.e. immediately below the laser beam. However, at distances greater than  $0.01D$  from the center of the laser beam give a compromise for evaluating the surface temperature beneath the laser,  $T_L$ .

At the same time, Eq. 2.45 serves the purpose of estimating a value of the depth of melt,  $h$ . Although this expression does not consider the phase change from solid to liquid when the temperature field reaches the melting point, this effect can be approximated by modifying the heat conductivity  $K$  into  $K_{\text{MOD}}$  such that it includes the latent heat of fusion of the material [14].

Obtaining the maximum depth of melt means finding the coordinates  $(x_{\text{max}}, z_{\text{max}})$  for  $y = 0$  from Eq. 2.45. The maximum depth of melt,  $z_{\text{max}} = -h$ , occurs at half the length value of the major axis of the surface isothermal ellipse (i.e., at  $T=T_m$ ). By making  $y = 0$  and  $z = 0$ , and solving Eq. 2.45 for  $x$ , two values are found, and  $x_{\text{max}}$  is the average of the latter two roots. Then,  $z_{\text{max}}$  is found by

solving Eq. 2.45 again this time evaluating it at  $y = 0$  and  $x = x_{\max}$ , and the negative root corresponds to  $h$ . Equation 2.45 also can provide a way to determine the solidification time, since the heat flow at the maximum depth of melt can be determined from it. This is obtained by taking the first derivative with respect to  $z$ , and evaluating it at  $(x_{\max}, 0, z_{\max})$ . The average solidification front velocity at the maximum depth of melt can be then obtained by using the Stefan condition [15], taking into account the specific latent heat of solidification of the alloy  $L$ .

$$\bar{v}_{\text{SOLIDIFICATION}} = \frac{-K \left. \frac{\partial T}{\partial z} \right|_{z=h}}{\rho L} \quad (2.46)$$

This velocity can then be used to estimate the average solidification time,

$$t_{\text{SOLIDIFICATION}} = \frac{2h}{\bar{v}_{\text{SOLIDIFICATION}}} \quad (2.47)$$

Finally, the estimation of the average arithmetic surface roughness  $R_a$  can be assessed simply by evaluating half of the maximum height after a relaxation time equal to  $t_{\text{SOLIDIFICATION}}$ , since of the resulting surface has been assumed sinusoidal in shape. Thus,

$$R_a = \frac{\Delta h(t_{\text{SOLIDIFICATION}})}{2} \quad (2.48)$$



### **2.2.3 Envelopment solidification of LaserForm ST-100<sup>TM</sup> indirect-SLS material**

From the description of the LaserForm ST-100<sup>TM</sup> material system given in Chapter 1 and the fact that a stainless steel grade 420 contains approximately 12-14 wt.% Cr and 0.15 wt.% C [16], an equivalent weight percentage of Fe of a 57.8 wt% would exist if only Fe and Cu are considered. From the Fe-Cu phase diagram shown in Figure 2.19, it can be observed that on rapidly cooling from the melt, a typical feature of laser surface melting, the liquidus line is crossed at 1440 °C for that composition, and the first solid to form is  $\gamma$ -Fe which would increasingly dissolve up to 8.5 wt% Cu until the liquid had reached a temperature of 1094 °C. This temperature corresponds to the invariant peritectic temperature for that system. Slightly above that temperature the lever rule indicates that 62 wt.% would solidify as  $\gamma$ -Fe(91.5 wt% Fe) and the remaining wt.% would be copper enriched liquid having a 96 wt.% Cu. Up to that temperature, it is expected to obtain a solidified layer of  $\gamma$ -Fe having a slight compositional gradient of Cu. On top of this layer, the Cu-enriched liquid would then continue solidifying. However, the peritectic transformation is a sluggish phenomenon [17] as the maintenance of equilibrium requires sufficient time for composition adjustments by diffusion. In the peritectic transformation diffusion must take place between the reactant phases (i.e.,  $\gamma$  and L) through the formed solid product layer (i.e., (Cu)). Therefore on further rapid-cooling, the  $\gamma$ -Fe already solidified will be

“enveloped” or “surrounded” by a thin (Cu) layer having a composition of 4 wt.% Fe. This prevents further contact between  $\gamma$ -Fe and the liquid and the peritectic reaction is suppressed. The liquid above that layer of composition 2.8 wt.% Fe will then continue solidifying down to a temperature of 1083 °C, however only as a (Cu) phase due to the hindering of the peritectic reaction. The solidified (Cu) phase will show a further decrease of its Fe content with decreasing temperature. Finally, on cooling down to room temperature, the  $\gamma$ -Fe would then undergo an eutectoid decomposition at 835 °C and a resulting  $\alpha$ -Fe matrix with Cu precipitates. The (Cu) layer would decrease its Fe solubility limit to almost zero and  $\alpha$ -Fe would then precipitate out of the Cu matrix.

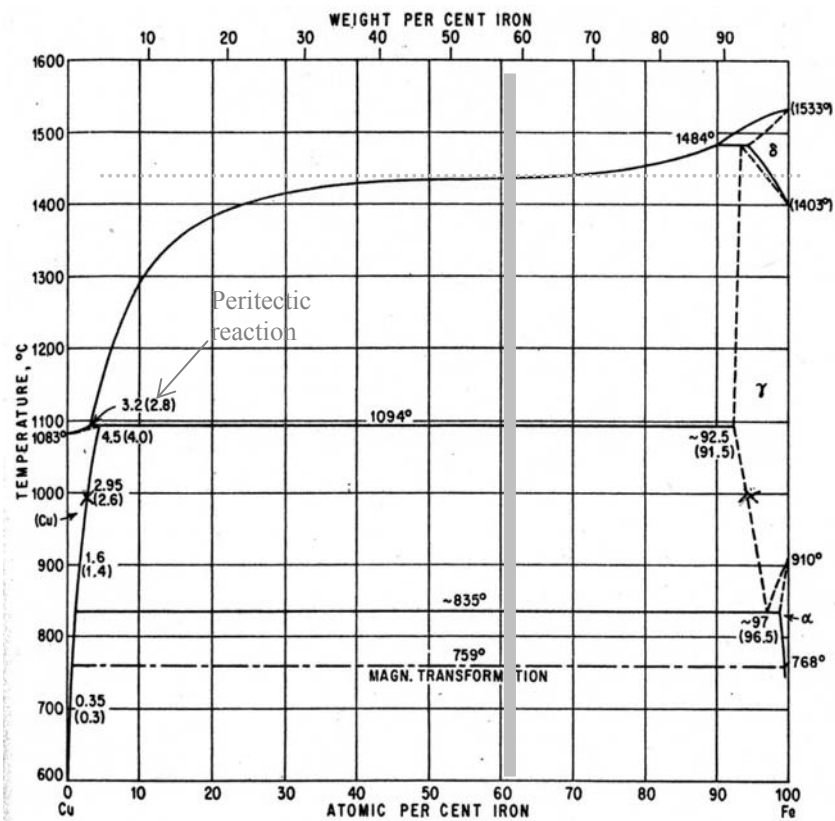


Figure 2.19 Phase diagram of Fe-Cu system (from Hansen [18]).

The presence of Cr in the real material system must not be underestimated. A pseudo-binary Fe-Cu phase-diagram for a 17 wt.% Cr would certainly aid the understanding of the hindered peritectic solidification. Nonetheless, Fe-Cu-Cr phase diagram vertical section for a 10 wt. % Cr and 0.1 wt.% C is provided by Raghavan [19] and is illustrated in Figure 2.20. It can be observed that Cr alters the Fe rich zone of the diagram mostly by extending the  $\delta$ -Fe + liquid region and slightly broadening the peritectic and eutectoid isothermal lines. The  $\alpha$  and  $\delta$

phases are also stabilized within regions coexisting with the  $\gamma$  and (Cu) phases. Raghavan indicates that with increasing Cr content the solubility of Cu in the  $\gamma$  phase decreases at first but then increases, and that the eutectoid temperature rises gradually at first and then more rapidly.

By studying the Cu-Cr phase diagram [18] at 1320 °C, Cr would start solidifying from a Cu-rich liquid (i.e., 22 wt.% Cr) up to a eutectic temperature of 1080 °C, followed by eutectic decomposition. The pseudo-binary Fe-Cu phase diagram [19] also shows that at 1450 °C, Fe would start solidifying from the Fe-rich liquid (i.e., 56.7 wt.% Fe) as a  $\gamma$  phase initially. During the solidification of the Fe-Cu-Cr system, solid Cr would form simultaneously with Fe from the liquid at a 1500-1440 °C temperature range, thus potentially stabilizing a  $\gamma$ -(Fe,Cr) phase instead of the previously considered  $\gamma$ -Fe phase. Because the peritectic reaction of the Fe-Cu system and the eutectic reaction of the Cu-Cr system occurs at similar temperatures (1094 °C and 1080 °C, respectively), the likelihood that the eutectic reaction will prevail is higher as it involves faster diffusion through the Cu-rich liquid. The remaining liquid above this layer will solidify not as (Cu) phase alone but as a eutectic of (Cu) and  $\gamma$ -(Fe,Cr), at least until the Cr in the liquid is depleted. At 870°C  $\gamma$ -(Fe,Cr) starts decomposing into  $\alpha$ -(Fe,Cr) until the 800°C isotherm line is crossed.

On the other hand the presence of Sn in the real material should not introduce any change in the solidification phases already mentioned. This conclusion is based on the fact that the equilibrium phase diagram for Cu-Sn shows that the (Cu) (5 wt.% Sn) phase extends from a liquidus temperature of approximately 1070 °C to a solvus temperature of 300 °C continuously without any phase changes.

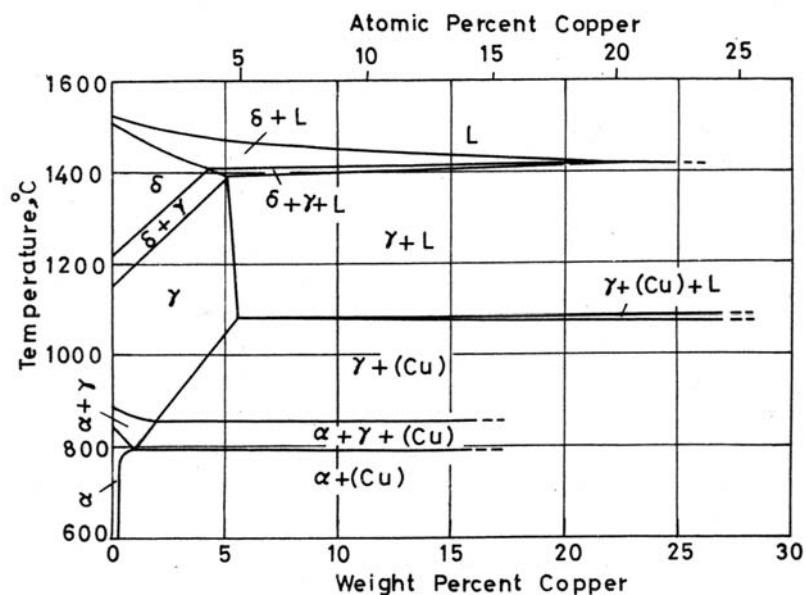


Figure 2.20. Fe-Cu-Cr vertical section at 10 wt.% Cr (from Raghavan [19]).

#### 2.2.4 Surface smoothing by oxide formation during the melt residence time

If laser polishing by melting is performed under a finite partial pressure of oxygen, then species inside the molten pool may have sufficient time to mix and

react with the atmospheric and surface-adsorbed oxygen to form stable oxides. During solidification these oxides are likely to be segregated at the solidifying front and at the surface due to the high wetting angle the liquid forms on them and their lower density that favors flotation. The large surface tension gradients induced by the laser raster scan produce strong convective currents in the melt pool during the resident time which can last up to 100-200 ms. This, added to fact that diffusion in the liquid occurs rapidly, allows formation of certain oxides depending on the liquid temperature and the partial pressure of oxygen.

From the Ellingham diagram illustrated in Figure 2.21 it can be concluded that for a temperature range of 1440 to 1080 °C (i.e., liquidus temperature range for the Fe-Cu system) and a partial pressure of oxygen of  $10^{-5}$  atm, iron, chromium and silicon can readily form oxides whereas for copper it may be less likely. Silica will be the most stable oxide, followed by chromia (i.e.,  $\text{Cr}_2\text{O}_3$ ) and then by the oxides of iron, especially the spinel  $\text{Fe}_3\text{O}_4$ .  $\text{Cu}_2\text{O}$  may form still but in low relative amounts.

When these oxides reach the surface of the melt, they will have time to stabilize, grow and expand before the solidification front reaches them. The results will be large pallets of oxides embedded in the solidified (Cu) matrix. Oxides tend to grow faceted due to their entropy of formation, so the pallets will

be smoother than the (Cu) matrix especially if the latter has undergone rippling formation. In this way the oxides will tend to reduce the roughness of the surface.

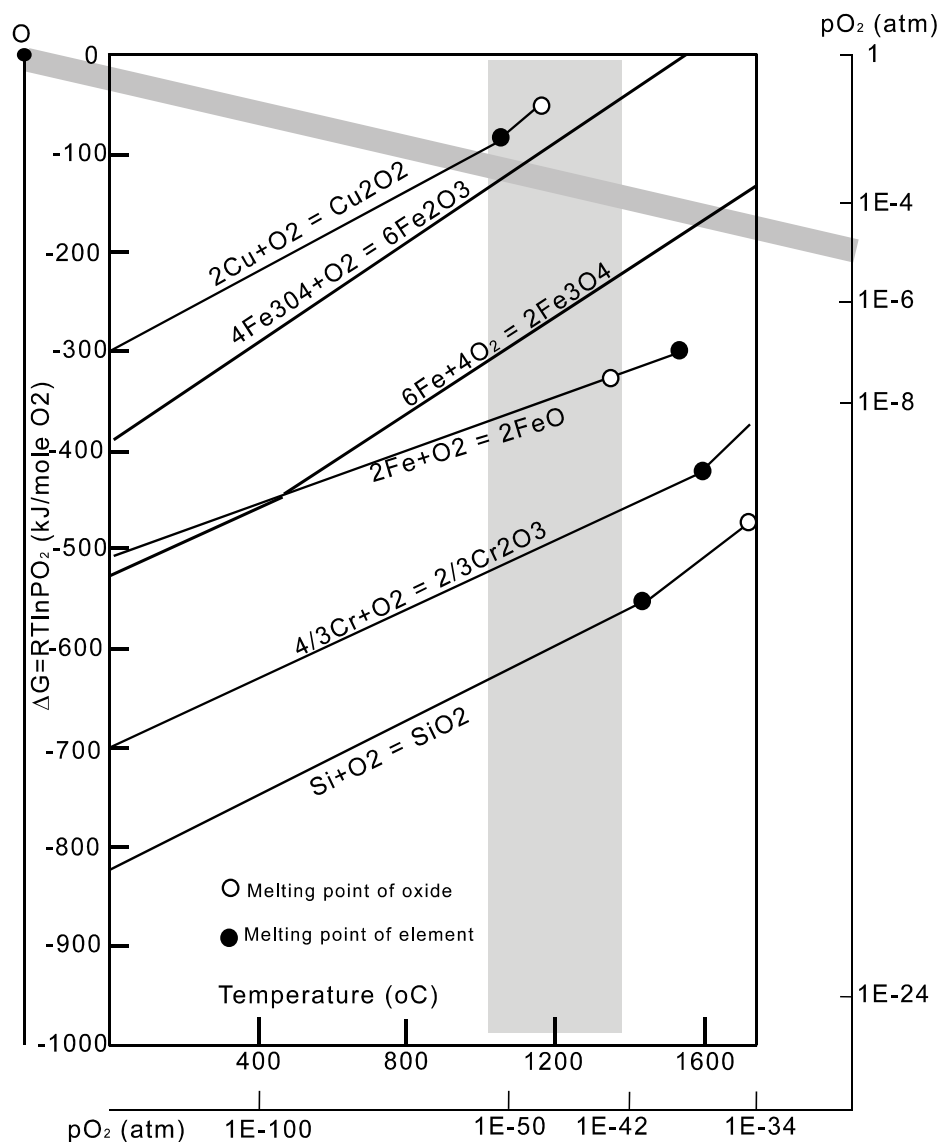


Figure 2.21 Ellingham diagram, showing the variation of free energy with temperature for certain oxides (adapted from Gaskell [20] & Khanna [21]).

### 2.2.5 Summary of surface modification mechanisms

From the previous description of the SSM and SOM models and the consideration of the solidification and oxidation behavior of the LaserForm ST-100 material system, it is possible to describe a sequence of surface modification mechanisms that will depend mostly on the depth of melt,  $h$  and the overheating of the liquid  $\Delta T$ , that the surface of the material is experiencing. The former scales approximately with the square root of the laser power to scan speed ratio [22], whereas the superheating scales linearly with the laser power and inversely with the square root of the scan speed [3], see Eq. 2.17. An interesting feature of this material system is the uppermost surface rich in copper that extends down to 10-30 microns, after which the liquid-sintered stainless steel particles appear. This particular feature separates the surface mechanisms onto five mechanisms as illustrated in Figure 2.20. These depend on depth of melt  $h$  and melt superheating  $\Delta T$ . Each mechanism is briefly explained below:

*Surface shallow melting:* Smoothing occurs for power levels high enough to start surface melting and rapid scan speeds so that the depth of melt  $h$  does not go beyond the valley-level, which in this material system corresponds to peak-to-valley distance of 10-20 microns. The superheating  $\Delta T$  of the melt in this case is not considerable either.



*Surface over melt I:* Once the depth of melt has increased below the valley-level then the first mode of SOM occurs. According to Anthony and Cline the possibility of total rippling reduction exists for a given combination of high  $h$  and relatively lower  $\Delta T$  so that  $\Delta h_{\max}$  is minimized and the relaxation of the surface completes the smoothing of the surface.

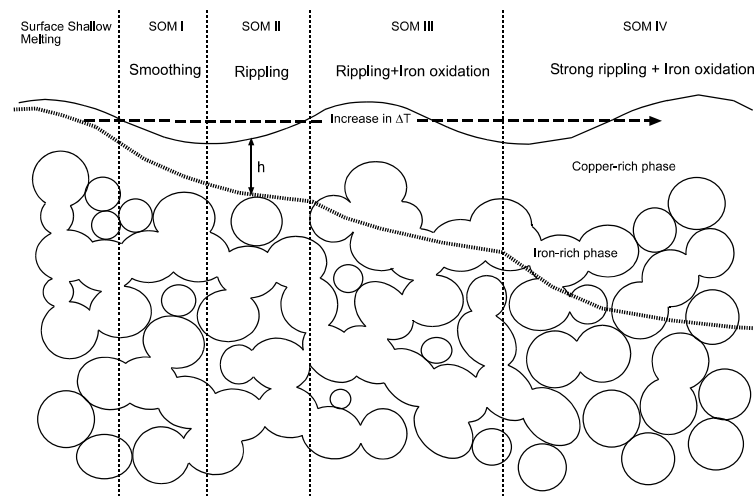


Figure 2.22. Schematic drawing of the sequence of surface modification mechanisms.

*Surface over melt II:* the depth of melt and superheating have both increased but the latter is now relatively higher than in SOM-I (due to its linear dependence on power), so that  $\Delta h_{\max}$  is large and the relaxation of the surface is not enough to smooth the surface; therefore, it solidifies with ripples. An increase

in surface roughness is then expected with further increase in  $\Delta T$ . Up to this point only the bronze phase has melted.

*Surface over melt III:* the depth of melt is deeper than 30 microns, and the stainless steel phase is now melted and mixed with the bronze phase. Because of the fierce stirring in the laser zone and the high surface temperature, iron in the liquid phase will be oxidized even at low oxygen partial pressure ( $< 10^{-6}$  atm) more readily than copper, which is known to be a weak oxide former. On solidification, iron oxide plates are then formed at the surface. These are inherently faceted and show flat surface characteristics thus reducing the roughness increase caused by the rippling effect. A drop in the surface roughness is then expected to occur.

*Surface over melt IV:* Finally, if the depth of melt and superheating of the liquid are further increased, the composition of the liquid reaches its nominal level and the oxidation of the iron on the surface attains its maximum level. However, rippling keeps increasing, so an increase on the surface roughness is expected.

### 2.3 LASER FUSION COATINGS OF C/C COMPOSITES

For more than 50 years investigators worldwide have attempted to coat carbon and more recently C/C composites with metallo-ceramic compounds to enhance their oxidation resistance at high temperatures [23,24]. In an inert atmosphere or in vacuum, carbon fibers retain their strength, modulus and other mechanical properties to temperatures in excess of 2000 °C. However, when composites containing carbon fibers are exposed to an oxidizing environment above 400 °C, the carbon fibers react with oxygen and are rapidly burnt away [25].

Several techniques, other than laser based, such as vacuum fusion, pack cementation, chemical vapor deposition, organic impregnation and sol-gel have been used to consolidate coating on C/C composites [26-29]. Because of the low coefficient of thermal expansion ( $10^{-6} \text{ K}^{-1}$ ) and high thermal conductivity (200 W/mK) of C/C composites [30] most coating techniques and materials systems used have failed in producing crack-free coatings [31,32]. This has promoted other investigators to develop post processing techniques to heal cracks in these types of coatings [33]. New venues for achieving metallo-ceramic coatings on C/C composites with good integrity (i.e., free of cracks and homogenous thickness) must then be explored, one being the laser fusion of coatings under an inert atmosphere.

### 2.3.1 Laser processing of ceramics

Laser processing of ceramic coatings is still in its infancy, as this process requires good wetting between liquid coating and solid substrate within a short period of time [34]. Rapid wetting of the coating over the substrate of the order of 100 ms is required. If the wetting process were sluggish, the interface would not adhere completely before solidification is completed. According to Fellowes *et al.* [35], who performed laser cladding of silica powder on inclined metallic substrates, laser coating with ceramic materials poses many process difficulties.

However, a laser fusion coating methodology for ceramic substrates that sublime, as in the case of C/C composites, that is primarily based on the laser-induced chemical reduction of a carefully selected mixture of metals/elements to form complex phase coatings has shown promising results [36,37]. Metal salts can be reduced to their native states by the application of laser irradiation. For example, a metal salt such as nickel formate can be reduced to form nickel by laser exposure. The elements then get fused in the surface layers of the C/C substrate.

When a continuous ceramic coating results after rapid solidification of the precursor material (e.g., a laser melted track), large differences in coefficient of thermal expansion (CTE) with the substrate will tend to form microcracks in the coating. Localized and inhomogenous heating of the coating material establishes a

steep thermal gradient followed then by rapid cooling thus creating high tensile residual stresses, provided the CTE of the coating is larger than that of the substrate. At temperatures above half their melting point, most ceramics become capable of accommodating these tensile strains by various transport mechanisms, yet at lower temperatures, mismatch strains result in surface cracks, channeling of cracks, spallation and delamination of the ceramic coating [38]. Fracture may take place either through the coating or along the interface depending on the interfacial bond strength, magnitude of the CTE difference and the thermal gradient across the coating and substrate.

### 2.3.2 Wetting and bonding during laser coating of C/C composites

To obtain bonding of a preplaced precursor coating with a C/C substrate by laser beam melting, the molten coating must first wet the substrate. Under equilibrium conditions, wetting is described by the wetting angle  $\theta$  through Young's equation [39],

$$\cos \theta_Y = \frac{\sigma_{SV} - \sigma_{LS}}{\sigma_{LV}} \quad (2.49)$$

where the wetting angle  $\theta_Y$  corresponds to the angle between the liquid-vapor surface tension,  $\sigma_{LV}$ , and the liquid-solid surface tension,  $\sigma_{LS}$ , at the triple line

point. The degree of interfacial bonding between the liquid and the solid surface is determined by the work of adhesion  $W_a$  between the coating and substrate and is described by Dupré's equation [7],

$$W_a = \sigma_{LV}(1 + \cos \theta_Y) \quad (2.50)$$

When  $\cos \theta_Y$  becomes unity, equilibrium is reached at the triple line between the solid-vapor surface tension and the sum of the liquid-vapor and liquid-solid surface tension. Only then, spontaneous wetting or spreading of a liquid over a solid may occur. The work of adhesion,  $W_a^0$  then acquires a maximum value equal to  $2\sigma_{LV}$ . It is this term that reflects the interaction energy between the solid and the liquid phases [7]. Furthermore, the work of spreading  $W_s$  is defined as the difference between the work of adhesion under spontaneous wetting conditions and the work of adhesion for an equilibrium contact angle greater than zero,

$$W_s = W_a^0 - W_a \quad (2.51)$$

Real solid surfaces never satisfy completely the condition for the Young equation to be valid, namely chemical homogeneity and perfect smoothness

[7,40]. If the substrate is inherently rough then the equilibrium contact angle must be modified according to Wenzel's relationship,

$$\cos \theta_w = s_r \cdot \cos \theta_Y \quad (2.52)$$

where,  $s_r$ , corresponds to the ratio of the actual surface area and the corresponding planar area; this makes  $s_r > 1$ . The increase in surface area contributes to an increase in interface strength provided complete wetting occurs. It has been observed that grooves perpendicular to the triple line present almost no energy barriers to the movement of the triple line and the macroscopic angle is equal to  $\theta_w$ . For wetting liquids, roughness always promotes wetting, and it is possible to obtain perfect wetting,  $\theta_w = 0^\circ$ , if  $s_r$  is greater than  $(\cos \theta_Y)^{-1}$ . Grooves in this case can act as open capillaries, reinforcing wetting. However, sharp grooves can pin-point the triple line, hindering wetting [7,40].

### ***2.3.2.1 Rate of spreading at the initiation of wetting under a laser beam***

The molten material region in contact with the rough substrate under the laser beam should establish initially a large wetting angle,  $\theta_w^0$ , which would decay exponentially to a final equilibrium wetting angle  $\theta_w^F$ , provided enough time is available, as reported on reactive wetting experiments of sessile drops by

Landry and Eustathopoulos [41]. Observations for sessile drops have also been reported on the exponential decrease of the cosine of the wetting angle with time [42]. Moreover, at high initial wetting angles the rate of growth of the sessile-drop base is the highest and of the order of 0.15 mm/s as observed in the wetting of Cu-Cr on C by Voitovitch *et al.* [43]. However, during laser processing, temperature changes occur very rapidly making the melt resident time short-lived, and therefore spreading should not have sufficient time to develop unless an external force is exerted upon the liquid by the laser beam.

It is the opinion of the author that when laser coating a surface with pre-placed precursor material is performed, external work must be done on the liquid zone above the substrate to overcome the work of spreading. This work arises from the hydrodynamic forces imparted on the liquid driven by the thermal gradient induced in the liquid by the moving beam. Among the physical forces acting on the liquid, i.e., gravity, surface tension and viscous drag, momentum change and surface tension gradient due to temperature changes at the surface of the liquid, also known as the Marangoni force, can be of considerable magnitude [3,11]. This surface tension gradient should exert a surface lateral force  $F_s$  perpendicular to the motion of the laser beam during the time interval the laser acts on the liquid zone, i.e.,  $D_L/v_s$ . This force should displace the triple line



laterally outwards by an amount  $\Delta l$ . Thus, the external work on the liquid can be estimated from the total work of the lateral force when displaced by  $\Delta l$ , as

$$W_{\text{external}} = F_s \cdot \Delta l \quad (2.53)$$

The surface lateral force can be expressed as a function of the surface tension variation with temperature times the thermal gradient at the liquid surface both projected on the horizontal plane. The liquid surface is assumed to have a semicircular cross section according to Figure 2.22. So, Eq. 2.53 becomes,

$$W_{\text{external}} = D_L \int_0^{\frac{\pi}{2}} \frac{d\sigma_{LV}}{dT} \cdot \frac{dT}{ds} \cos\varphi ds \cdot \Delta l \quad (2.54)$$

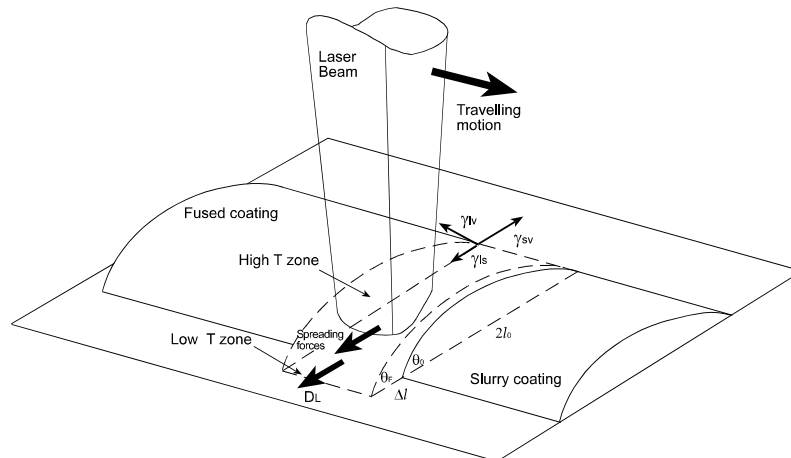


Figure 2.23. Schematic of the lateral force exerted on liquid surface by the laser beam.

Where  $\cos \varphi$  is the cosine director along the horizontal direction. Moreover, assuming a constant surface tension variation with temperature and that the maximum temperature change between the cusp of the liquid and the triple line point is constant and equal to  $\Delta T$ , then Eq. 2.54 simplifies to,

$$W_{\text{external}} = -D_L \frac{d\sigma_{LV}}{dT} \cdot \frac{dT}{ds} \int_0^{\pi/2} \cos \varphi ds \cdot \Delta l \quad (2.55)$$

where the minus sign accounts for the decrease in surface tension with temperature. The cosine integral equates to 1. If now the external work is made equal to the work of spreading given by Eq. 2.51 times the spread area (i.e.,  $D_L \Delta l$ ) then Eq. 2.55 can be rearranged, in the following manner,

$$\sigma_{LV} (\cos \theta_w^f - \cos \theta_w^0) \cdot D_L \cdot \Delta l = -D_L \cdot \frac{d\sigma_{LV}}{dT} \cdot \frac{\Delta T}{\pi/2} \cdot \Delta l \quad (2.56)$$

Simplifying Eq. 2.56, an expression for the cosine of the equilibrium final contact angle can be obtained after the surface of the liquid has experienced a  $\Delta T$  change.

This is after the laser beam has traversed its own diameter:

$$\cos \theta_w^f = \cos \theta_w^0 - \frac{2}{\sigma_{LV}} \cdot \frac{d\sigma_{LV}}{dT} \cdot \frac{\Delta T}{\pi} \quad (2.57)$$

By approximating the surface temperature of the liquid by Eq. 2.17, the final equilibrium contact angle becomes a function of the laser interaction time,

$$\cos \theta_w^f = \cos \theta_w^0 - \frac{2}{\sigma_{LV}} \cdot \frac{d\sigma_{LV}}{dT} \cdot \frac{\frac{I}{K} \cdot \sqrt{\frac{4 \cdot \alpha \cdot D_L}{\pi \cdot v_s}} - T_m}{\pi} \quad (2.58)$$

No experimental data is available to verify this relationship; nonetheless, the data available from Cu-Cr sessile drop experiments on vitreous carbon [43] substrates can be used to estimate the value of the final contact angle. Let us first consider that a 900 W laser beam is focused down to 0.4 mm and moves with a scanning speed of 40 mm/s, and that the temperature of the triple line corresponds to that of the melting point. For Cr,  $d\sigma_{LV}/dT = -0.33 \text{ mJ/mm}^2/\text{K}$  and  $\sigma_{LV}$  at the melting point is  $1628 \text{ mJ/mm}^2$ , and  $\theta_w^0 = 145^\circ$ .  $\theta_w^f$  then becomes  $132^\circ$ . This result is independent of the original liquid width,  $2l_0$ . The kinetics of spreading is assumed to occur instantaneously. This implies that the length  $\Delta l$  would be infinite and thus it cannot be obtained from Eq. 2.58.

Considering the initial rate of spreading reported by Voitovich *et al.* [43] for the wetting of Cu-Cr system over vitreous carbon (i.e., 0.15 mm/s), a similar or higher rate of spreading should occur under forced spreading conditions. The spreading rate at the triple line should also take place onto the surface defects of the substrate, such as porosity and grooves, as in the case of C/C composites. These are typically micron-sized features, so the spreading time required to completely wet these surface areas is expected to be considerably small, of the order of the laser interaction times (i.e., 100 ms). Therefore, it is the opinion of the author that complete wetting of the carbon rough surface by a liquid should be expected to occur under the short melting times induced by the laser beam, thus creating strong mechanical interlocking. Figure 2.24 illustrates the wetting process that occurs when a predeposited slurry coating is fused by a raster-scanned laser beam. A product layer has formed at the rough interface and above it, the coating has solidified. At the laser-material interaction zone, a chemical reaction takes place at the interface where the molten coating is in direct contact with the substrate rough features; some surface areas ahead of the laser beam have not yet been wetted by the molten coating.

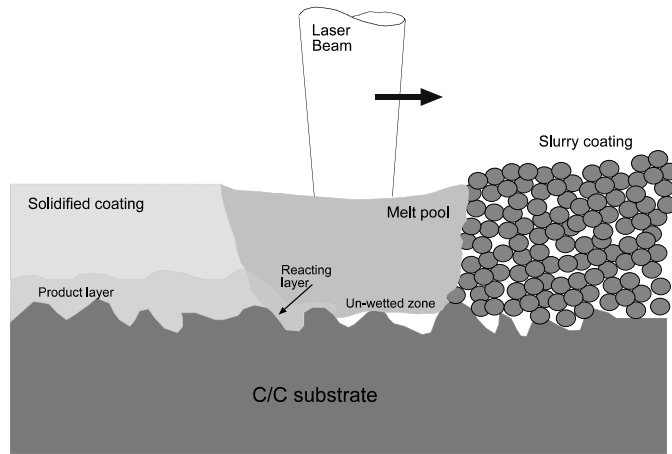


Figure 2.24. Schematic of the laser assisted wetting process at a rough interface.

### 2.3.2.2 Interfacial bond strength

Once the coating material is in direct contact with the substrate surface, physical and chemical interactions between the atoms across the common interface contribute to the work of adhesion between coating and substrate. This interfacial free energy of adhesion corresponds to the energy required to separate the substrate from the coating, from their equilibrium distance to infinity. It can simplistically be expressed as [7],

$$W_a^0 = -\frac{Z \cdot m_1}{\omega} \cdot \epsilon_{AB} \quad (2.59)$$

In this equation,  $Z$  is the number of near neighbors in the bulk of the crystal,  $m_1$  is the fraction of broken bonds at the surface of A or B per atom,  $\epsilon_{AB}$  is

the bond pair energy defined negative, and  $\omega$  is the surface area per atom. This model considers that A and B are monotonic solids that are chemically inert towards each other. Both A and B have the same crystal lattice, volume and are perfectly matched at the interface. Adhesion and cohesion results from atomic interaction between nearest neighbors.

A more elaborate expression for the work of adhesion was developed by Zhou [44]. It incorporates the physical interactions as described by the London interaction potential (i.e., the attraction between fluctuating dipoles) and a chemical interaction related to the free energy of bonding between the coating and the substrate  $\Delta G_{sc}$ . The algebraic expression for the work of adhesion becomes

$$W_a^0 = \pi \cdot n_s \cdot n_c \frac{\alpha_s \cdot \alpha_c}{8R^4} \left[ \frac{I_s \cdot I_c}{I_s + I_c} \right] \frac{n_{\text{bond}}}{N_{\text{bond}}} \cdot \frac{\Delta G_{sc}}{2} \quad (2.60)$$

where the subscript, s and c, are for substrate and coating, respectively. I, is the first ionization potential and  $\alpha$  is the polarizing ability, n is the number of atoms per unit surface area of the interface,  $n_{\text{bond}}$  is the density of ionically bonded atoms,  $N_{\text{bond}}$  is the number of bonds and R is the equilibrium distance.

According to De Hosson *et al.* [34], smaller lattice misfit between the coating and the substrate may also lead to a smaller interface separation contributing to a larger stabilization energy based on electrostatics.

### 2.3.2.3 Reactive wetting

Coating elements that chemically react with the substrate can improve wetting and interfacial bonding. It has been concluded that the higher the reactivity in the system, the better the wettability [7]. However, it is the final interfacial chemistry at the triple line rather than the intensity of the interfacial reaction that governs the system. The free energy of the chemical reaction between the reactive element and the substrate reduces the interface energy by increasing the work of adhesion [34]. This way the formation of a reaction product at the liquid substrate interface is facilitated. The initial equilibrium contact angle  $\theta_0$  is said to decrease with time during the chemical reaction according to the following expression,

$$\cos\theta = \cos\theta_0 - \frac{\Delta\sigma(t)}{\sigma_{LV}^0} - \frac{\Delta G(t)}{\sigma_{LV}^0} \quad (2.61)$$

where,  $\Delta\sigma(t)$ , is the change in the solid-liquid surface free energy during the reaction and  $\Delta G(t)$  is the free energy of the reaction, respectively [7].

Let us consider the laser coating of a pure metal,  $M_1$  (e.g., Cr), over a C/C composite substrate. A chemical reaction between metal and carbon atoms takes place leading to the formation of a metal-carbide layer provided the carbide of the metal exists and is thermodynamically favorable, and sufficient time is permitted for formation. One additional step, to further reduce the interface energy and to increase the kinetics of the carbide formation is by decomposition of a salt of the metal (e.g., hydrous  $CrCl_3$ ) instead of laser melting  $M_1$  directly over the carbon-based substrate. The large amount of heat liberated from the exothermic reaction when decomposing a metal-salt also helps to diminish the laser energy density applied over the precursor. The reaction product will form a thin layer over the substrate; further thickening of this layer requires diffusion of C species from the substrate across the product layer into  $M_1$ . Lack of time and temperature will impede the process.

The metal-carbide product layer formed may facilitate the wetting and bonding of a second coating layer based on an element  $M_2$  chemically compatible with the previously deposited metal and carbon. This element or compound need not necessarily be metal based; it can consist for example of an element like silicon. However,  $M_2$  must form a stable compound with  $M_1$  so that the negative free energy of formation will drive the decomposition of the already formed  $M_1C$  carbide favoring the formation of  $M_2C$ . In this manner, if  $M_2C$  is less stable than



$M_1C$  it should facilitate wetting of the un-reacted  $M_2$  and  $M_1M_2$  compound over it. From Eq. 2.60 it can be seen that the non-equilibrium work of adhesion scales linearly with the free energy of bonding, so it should be larger for more stable compound products.

If during laser coating the wetted material chemically reacts with the substrate, the reaction product layer would form if it occurs at a fast enough kinetic rate before the temperature falls below the critical temperature to activate the reaction. If this chemical reaction is exothermic, high temperatures may be sustained for longer times, and the reaction may be self-sustained as long as reactants continue being supplied.

### **2.3.3 Thermal stress and thermal shock effect on coatings**

Whenever the thermal expansion or contraction of a body is impeded, thermal stresses appear. If large enough, they may cause yielding, fracture or buckling of the component. It is common to distinguish between thermal stress caused by external constraint and those that appear without external constraint due to temperature gradients in the body [2,45,46]. For the case of fracture initiation, failure occurs when the thermal stress exceeds the material's fracture strength  $\sigma_f$ .

### 2.3.3.1 *The coefficient of thermal expansion*

As the temperature in a solid is raised, the anharmonicity of the atomic bond pushes the atoms apart, increasing their mean spacing. The coefficient of thermal linear expansion is a measure of the increase in mean spacing between atoms as temperature is raised in the solid. It is defined as,

$$\alpha = \frac{1}{\ell} \frac{d\ell}{dT} \quad (2.62)$$

Diamond, silicon and silica have covalent bonds and low anharmonicity (i.e., are almost linear elastic even at large strains), giving them a low coefficient of thermal expansion (CTE). Composites can also have low values of the CTE because the reinforcing fibers (e.g., carbon) expand very little [45]. The coefficient of thermal expansion is inversely proportional to Young's modulus; diamond for example has the highest elastic modulus and the lowest CTE. Additionally, the elastic modulus of most materials scales approximately with their melting point  $T_m$ , giving the following relationship for the coefficient of thermal expansion,

$$\alpha = \frac{\gamma_G}{100 \cdot T_m} \quad (2.63)$$

For solids, the thermal strain just before they melt depends only on  $\gamma_G$ , the Gruneisen parameter which is roughly a constant. Some materials with low

coordination number such as Silica can absorb energy preferentially in transverse modes leading to very small values of  $\gamma_G$  and a low thermal expansion coefficient.

### ***2.3.3.2 Thermal stresses and shock resistance of coatings***

A temperature change  $\Delta T$  applied to a constrained body or a sudden change  $\Delta T$  in the surface temperature of an unconstrained body, induces a misfit stress defined as,

$$\sigma = \frac{E \cdot \alpha \cdot \Delta T}{C} \quad (2.64)$$

where C corresponds to  $1 - \nu$  for biaxial constraint or normal quenching. This stress can be as large as 1 MPa/K, so for a temperature drop of 1000 K the misfit stress can be of the order of 1 GPa. If the latter then exceeds the local strength of the material, yielding or cracking may result.

The thermal shock resistance is the maximum temperature difference through which a material can be quenched suddenly, without damage. When heat transfer at the surface is poor and the thermal conductivity of the solid is high (thereby reducing thermal gradients) the thermal stress is less than given by equation 2.64 by a factor A, approximately determined by

$$A = \frac{\frac{t \cdot h}{K}}{1 + \frac{t \cdot h}{K}} \quad (2.65)$$

where  $t$  is the thickness of material, and  $h$  the convective-radiative heat coefficient. The term  $\frac{t \cdot h}{K}$  is the Biot number. The equation defining thermal shock resistance then becomes,

$$\Delta T_{\text{MAX}} = \frac{C}{A} \cdot \frac{\sigma_f}{\alpha \cdot E} \quad (2.66)$$

According to Rossi [47], thermal shock resistance is expected to increase with increasing microcrack density. Significantly, less thermal shock damage is found in oxide-matrix composite coating having SiC dispersed particles. A network of microcracks can relieve the mismatch thermal stresses generated upon cooling from the fabrication temperature.

In the case of a thin coating applied to an underlying substrate, the biaxial misfit stress produced by a sudden change in temperature  $\Delta T$  on the coating corresponds to [48],

$$\sigma = \frac{E \cdot \Delta\alpha \cdot \Delta T}{C} \quad (2.67)$$

where,  $\Delta\alpha = |\alpha_s - \alpha_c|$ . Whichever phase region has the larger value of  $\alpha$  will be the region in tension on cooling. If the body undergoes a thermal gradient, there will exist a stress gradient from the surface of the coating to the core of the substrate [49]. Therefore, the coating initiation-controlled thermal shock resistance is defined by the temperature change that can be tolerated without fracture of the coating; this is

$$\Delta T_{\text{Max}} = \frac{C}{A} \cdot \frac{\sigma_f}{\Delta\alpha \cdot E} \quad (2.68)$$

where C and A have been previously defined.

### **2.3.3.3 Conditions for crack growth**

The necessary condition for a crack to grow in a material is that sufficient external work must be done, or elastic energy released, to supply the surface energy of the two new surfaces that are created. This is

$$G > 2\gamma \quad (2.69)$$

where  $G$  is the elastic energy release rate and  $\gamma$  the surface energy, both in joules per surface area. The elastic energy release is obtained by equating the elastic energy release on crack growth to the energy required for a crack to grow [45]. The elastic energy that is released as the crack advances represents a driving force for crack propagation and the surface free energy represents a retarding force. Cracks will propagate when the driving force is larger than the retarding force. As the driving force scales with the square of the crack size and the retarding force scales linearly with the crack size, cracks below a certain size will not propagate spontaneously whereas larger cracks will [34].

The crack propagation criteria can also be expressed by means of the stress-intensity factor at the Griffith equilibrium:

$$K = \sqrt{E \cdot G} = K_{IC} \quad (2.70)$$

where,  $K_{IC}$ , is the critical stress-intensity factor for a tensile opening mode. From Eq. 2.70, the critical opening mode toughness is then expressed as,

$$G_{IC} = \frac{K_{IC}^2}{E} \quad (2.71)$$

The latter expression is a measure of the apparent fracture surface energy. When a ceramic fractures, the energy absorbed is only slightly more than the surface energy. On the other hand, when metals and composites fracture the energy absorbed is vastly greater, usually because of plasticity associated with crack propagation [45,50]. The stress concentration at the tip of a crack generates a process zone: a plastic zone in ductile solids, a zone of microcracking in ceramics, a zone of delamination, debonding and fiber pull-out in composites. Within the process zone, work is done against plastic and frictional forces. It is this work which accounts for the difference between the measured fracture energy  $G_{IC}$  and the true surface energy  $2\gamma$ . The amount of energy dissipated must scale roughly with the strength of the material and with the process zone size  $d_y$ . This size is found by equating the stress field of the opening mode crack,

$$\sigma = \frac{K_I}{\sqrt{2\pi \cdot r}} \quad (2.72)$$

at  $r = d_y/2$ , to the strength of the material  $\sigma_f$  giving,

$$d_y = \frac{K_{IC}}{\pi \cdot \sigma_f^2} \quad (2.73)$$

$d_y$  varies enormously, from atomic dimensions for very brittle ceramics and glasses to almost 1 meter for the most ductile of metals [45].

#### **2.3.4 Thermal stress distribution in cylindrical coatings**

The present research is principally focused on thin coatings applied over cylindrical C/C composites. These cylinders are coated by a “laser induced cementation” process during which the temperature of the substrate and coating reach a homogenous high temperature above that of the melting point of the coating system. When the laser is turned off, misfit thermal stresses are created due to the fast cooling rate experienced by the cylinder. Cooling in this case occurs by convection and radiation. It starts at the surface of the coating and propagates by conduction into the bulk of the composite. After the temperature of the coating has dropped below half its melting point (in absolute units), the change in temperature is still higher at the coating surface than at the substrate. Additionally, the CTE of the coating is at least one order of magnitude greater than that of the C/C substrate. These two effects make the coating contract more than the substrate; at this temperature the strains can no longer be accommodated in the ceramic material, so a tensile “hoop” stress distribution develops in the coating, with a maximum at the interface. Because the coating thickness can be of the order of a 20<sup>th</sup> of the substrate radius, a radial stress should also develop in the



coating. The latter should be much smaller but of compressive character, with a maximum at the interface and zero at the coating surface, as indicated in Figure 2.25.

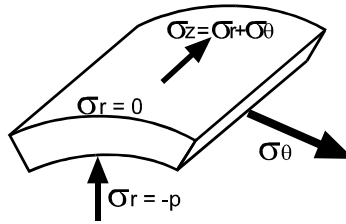


Figure 2.25. Illustration of the stress-state developed at the interface of a thin cylindrical coating.

#### 2.3.4.1 Stress distribution in a two-layer cylinder during cooling

The stress state found in a coated cylinder that experiences a decrease in radial temperature  $\Delta\theta(r)$  can be calculated as a one-dimensional problem considering only radial displacements, i.e.,  $u = u(r)$ . Two assumptions can be made: plane-stress and plane-strain. Under plain-stress, a cylindrical disc is considered so that the radial and tangential stresses are non-zero while the longitudinal stress is made zero. Under plain-strain, a tri-axial stress state exists but the longitudinal strain is constant, equal to  $\epsilon_0$ . From the generalized Hooke's law for plane problems in a cylindrical coordinate system, the radial and tangential stress can be expresses as [2,46],

$$\sigma_{rr} = \frac{E^*}{1-\nu^{*2}} \left[ \varepsilon_{rr} + \nu^* \varepsilon_{\theta\theta} - (1 + \nu^*) \cdot \alpha^* \cdot \Delta\theta(r) + (1 + \nu^*) \cdot c^* \right] \quad (2.74)$$

$$\sigma_{\theta\theta} = \frac{E^*}{1-\nu^{*2}} \left[ \nu^* \cdot \varepsilon_{rr} + \varepsilon_{\theta\theta} - (1 + \nu^*) \cdot \alpha^* \cdot \Delta\theta(r) + (1 + \nu^*) \cdot c^* \right]$$

where,

$$\varepsilon_{rr} = \frac{du(r)}{dr} \quad \varepsilon_{\theta\theta} = \frac{u(r)}{r} \quad \varepsilon_{r\theta} = 0 \quad (2.75)$$

Moreover, the elastic constants will take the following form depending on whether plane-strain or plane-stress is adopted,

$$E^* = \begin{cases} \frac{E}{1-\nu} & \text{plane-strain} \\ E & \text{plane-stress} \end{cases} \quad \nu^* = \begin{cases} \frac{\nu}{1-\nu} & \text{plane-strain} \\ \nu & \text{plane-stress} \end{cases}$$

$$\alpha^* = \begin{cases} (1+\nu)\alpha & \text{plane-strain} \\ \alpha & \text{plane-stress} \end{cases} \quad c^* = \begin{cases} \nu\varepsilon_0 & \text{plane-strain} \\ 0 & \text{plane-stress} \end{cases}$$

At the same time, the one-dimensional equilibrium equation in the radial direction is,

$$\frac{d\sigma_{rr}}{dr} + \frac{\sigma_{rr} - \sigma_{\theta\theta}}{r} = 0 \quad (2.76)$$

Replacing Eqs. 2.74 and 2.75 into Eq. 2.76, yields the following one-dimensional differential equation,

$$\frac{d}{dr} \left[ \frac{1}{r} \cdot \frac{d(u \cdot r)}{dr} \right] = (1 + \nu^*) \cdot \alpha^* \cdot \frac{d\Delta\theta}{dr} \quad (2.77)$$

Its general solution has the form

$$u(r) = (1 + \nu^*) \cdot \alpha^* \cdot \frac{1}{r} \int_a^b \Delta\theta(r) \cdot r dr + C_1 r + \frac{C_2}{r} \quad (2.78)$$

Substituting this expression back into Eq. 2.75 and the resulting strains back into Eq. 2.74, an expression for the radial and tangential stress is obtained.

The original problem to solve consists of a two-layer cylinder. The solution for the radial distribution of the stresses [51] can be obtained by a superposition of a substrate cylinder of radius  $h_s$  having a negative external pressure,  $-p$ , acting on its exterior surface, and a hollow cylinder (coating) of thickness,  $h_c$ , having a positive internal pressure,  $p$ , acting on the inner wall as shown in Figure 2.26.

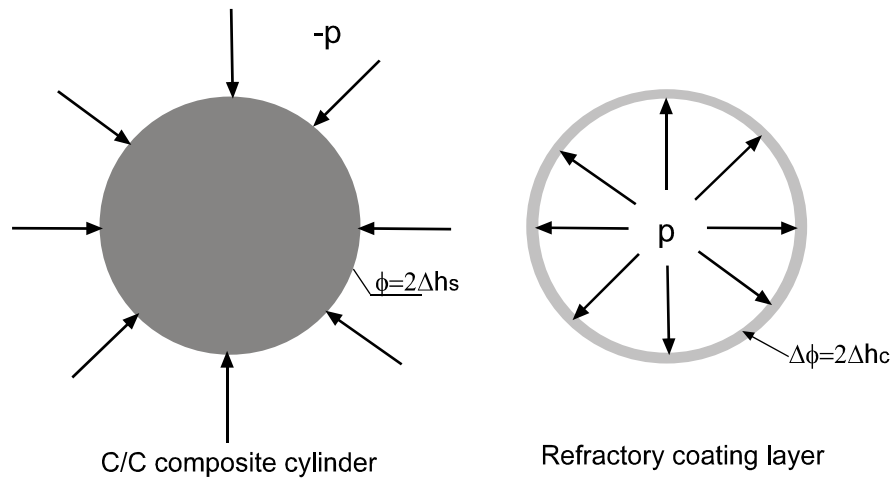


Figure 2.26. Schematic illustration of the superposition of a full cylinder and a hollow cylinder (after Green [51]).

The boundary conditions of the problem are,

$$\begin{aligned}
 \sigma_{rr}|_{h_s} &= p & \sigma_{rr}|_{h_s} &= -p \\
 \sigma_{rr}|_{h_s+h_c} &= 0 & \sigma_{rr}|_0 &= 0
 \end{aligned}
 \tag{2.79}$$

Substitution of this boundary condition into Eq. 2.74, allows solution for the magnitude of the pressure  $p$ ,

$$p = -\frac{\alpha_s^* \cdot E_s^*}{h_s^2} \int_0^{h_s} \Delta\theta_s(r) \cdot r dr + E_s^* \alpha_s^* \cdot \Delta\theta_s(0) + \frac{E_s^*}{1-\nu_s^*} \cdot \nu_s \epsilon_0 \tag{2.80}$$

The radial and tangential stress distributions in the coating have the form,

$$\sigma_{c_{rr}}(r) = -\frac{\alpha_c^* \cdot E_c^*}{r^2} \int_{h_c}^{h_s+h_c} \Delta\theta_c(r) \cdot r dr + \frac{E_c^*}{1-\nu_c^*} \cdot C1_c - \frac{E_c^*}{1+\nu_c^*} \cdot \frac{C2_c}{r^2} + \frac{E_c^*}{1-\nu_c^*} \cdot \nu_c \varepsilon_0 \quad (2.81)$$

$$\sigma_{c_{\theta\theta}}(r) = \frac{\alpha_c^* \cdot E_c^*}{r^2} \int_{h_c}^{h_s+h_c} \Delta\theta_c(r) \cdot r dr - \alpha_c^* \cdot E_c^* \cdot \Delta\theta(r) + \frac{E_c^*}{1-\nu_c^*} \cdot C1_c + \frac{E_c^*}{1+\nu_c^*} \cdot \frac{C2_c}{r^2} + \frac{E_c^*}{1-\nu_c^*} \cdot \nu_c \varepsilon_0$$

where  $C1_c$  and  $C2_c$  are equal to,

$$C1_c = p \cdot \frac{1-\nu_c^*}{E_c^*} + \frac{C2_c}{h_c^2} \cdot \frac{1-\nu_c^*}{1+\nu_c^*} + \nu_c \cdot \varepsilon_0 \quad (2.82)$$

$$C2_c = \frac{1-\nu_c^*}{E_c^*} \left[ \frac{1}{h_s^2} - \frac{1}{h_s^2+h_c^2} \right]^{-1} \cdot \left[ \frac{\alpha_c^* \cdot E_c^*}{h_s^2+h_c^2} \int_{h_s}^{h_s+h_c} \Delta\theta_c(r) \cdot r dr + p \right]$$

The radial and tangential stress distributions in the substrate have the form,

$$\sigma_{s_{rr}}(r) = -\frac{\alpha_s^* \cdot E_s^*}{r^2} \int_0^{h_s} \Delta\theta_s(r) \cdot r dr + \frac{E_s^*}{1-\nu_s^*} \cdot C1_s - \frac{E_s^*}{1+\nu_s^*} \cdot \frac{C2_s}{r^2} + \frac{E_s^*}{1-\nu_s^*} \cdot \nu_s \varepsilon_0 \quad (2.83)$$

$$\sigma_{s_{\theta\theta}}(r) = \frac{\alpha_s^* \cdot E_s^*}{r^2} \int_0^{h_s} \Delta\theta_s(r) \cdot r dr - \alpha_s^* \cdot E_s^* \cdot \Delta\theta_s(r) + \frac{E_s^*}{1-\nu_s^*} \cdot C1_s + \frac{E_s^*}{1+\nu_s^*} \cdot \frac{C2_s}{r^2} + \frac{E_s^*}{1-\nu_s^*} \cdot \nu_s \varepsilon_0$$

where  $C1_s$  and  $C2_s$  are equal to,

$$C1_s = (1 - \nu_s^*) \cdot \alpha_s^* \cdot \Delta\theta_s(0) \quad (2.84)$$

$$C2_s = 0$$

The longitudinal stress distribution  $\sigma_{zz}$  becomes

$$\sigma_{zz} = \begin{cases} \sigma_{\theta\theta} + \sigma_{rr} \text{ plane-strain, free ends} \\ 0 \quad \text{plane-stress} \end{cases} \quad (2.85)$$

#### ***2.3.4.2 Thermal distribution in a two-layer cylinder during cooling***

During the laser process employed to fabricate refractory coatings over cylindrical C/C composites, the coating material and the substrate both achieved a homogenous temperature, corresponding to the melting point of the coating system. This stationary temperature was achieved by rotating the cylinder while the laser beam was raster-scanned along the longitudinal axis of the cylinder. More details can be found in Chapter III. A heat transfer balance between the input energy from the laser beam and the loss of energy by radiation and convection from the outer surface allowed reaching a constant temperature. On removing the laser source from the surface of the cylinder, convection and radiation cause cooling of the specimen so that heat flows from the substrate through the coating into the surroundings.

Özsisik [52] developed the exact analytical set of solutions for a two-layer cylinder that undergoes heating or cooling by means of convection having an initial temperature distribution along the radial direction (see Figure 2.27). The solution is based on the orthogonal expansion technique.

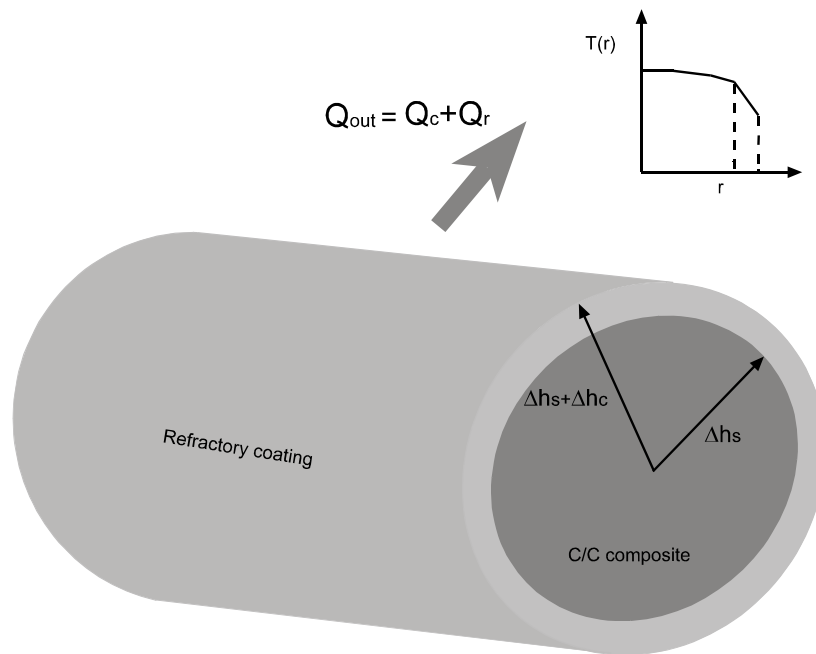


Figure 2.27. Schematic drawing of the heat transfer on cooling of a two-layer cylinder.

Two solutions are thus developed, one for the substrate,  $\theta_s$ , and one for the coating,  $\theta_c$ .

$$\theta_s(r,t) = \sum_{n=1}^{\infty} \frac{\exp(-\beta_n^2 t)}{N_n} J_0\left(\frac{\beta_n}{\sqrt{\alpha_s}} r\right) \left[ \begin{aligned} & \frac{K_s}{\alpha_s} \int_0^{h_s} J_0\left(\frac{\beta_n}{\sqrt{\alpha_s}} r\right) F_s(\rho) d\rho + \\ & \frac{K_c}{\alpha_c} \int_{h_s}^{h_c} \left( A_n J_0\left(\frac{\beta_n}{\sqrt{\alpha_c}} \rho\right) + B_n Y_0\left(\frac{\beta_n}{\sqrt{\alpha_c}} \rho\right) \right) F_c(\rho) d\rho \end{aligned} \right] \quad (2.86)$$

$$\theta_c(r,t) = \sum_{n=1}^{\infty} \frac{\exp(-\beta_n^2 t)}{N_n} \left( A_n J_0\left(\frac{\beta_n}{\sqrt{\alpha_c}} r\right) + B_n Y_0\left(\frac{\beta_n}{\sqrt{\alpha_c}} r\right) \right) \left[ \begin{aligned} & \frac{K_s}{\alpha_s} \int_0^{h_s} J_0\left(\frac{\beta_n}{\sqrt{\alpha_s}} r\right) F_s(\rho) d\rho + \\ & \frac{K_c}{\alpha_c} \int_{h_s}^{h_c} \left( A_n J_0\left(\frac{\beta_n}{\sqrt{\alpha_c}} \rho\right) + B_n Y_0\left(\frac{\beta_n}{\sqrt{\alpha_c}} \rho\right) \right) F_c(\rho) d\rho \end{aligned} \right] \quad (2.87)$$

where,  $J_0$  and  $Y_0$ , are Bessel functions of first and second kind both of order zero, respectively.  $F_c$  and  $F_s$  are the initial temperature distribution along the radial direction for the coating and substrate.  $\beta_n$  are the eigenvalues obtained by solving the following transcendental equation,

$$\begin{vmatrix} J_0(\gamma) & -J_0\left(\frac{a}{b}\eta\right) & -Y_0\left(\frac{a}{b}\eta\right) \\ KJ_1(\gamma) & -J_1\left(\frac{a}{b}\eta\right) & -Y_1\left(\frac{a}{b}\eta\right) \\ 0 & \frac{H}{\eta} J_0(\eta) - J_1(\eta) & \frac{H}{\eta} Y_0(\eta) - Y_1(\eta) \end{vmatrix} = 0$$



where,  $a$  and  $b$ , correspond to the inner and outer radii of the cylinder, respectively. The coefficients  $A_n$  and  $B_n$  are obtained by solving the following system of equations,

$$\begin{bmatrix} J_0\left(\frac{a}{b}\eta\right) & Y_0\left(\frac{a}{b}\eta\right) \\ J_1\left(\frac{a}{b}\eta\right) & Y_1\left(\frac{a}{b}\eta\right) \end{bmatrix} \begin{bmatrix} A_n \\ B_n \end{bmatrix} = \begin{bmatrix} J_0(\gamma) \\ KJ_1(\gamma) \end{bmatrix}$$

Finally,  $\gamma$ ,  $\eta$ ,  $K$  and  $H$  are normalized variables which are functions of the eigenvalues, the geometry and the physical properties involved in the problem. The implementation of this model is presented in Appendix A-IV.

### **2.3.5 Criteria to determine formation of certain cracking patterns on coatings**

The process of delamination versus perpendicular cracks and channeling is determined by the relative strength of the ceramic and the interface and by the thickness of the coating. If the interface is extremely strong, then delamination may occur by fracture through the ceramic parallel to the interface or the substrate (i.e., spallation) and both processes are determined by the fracture strength of the material.

According to Hutchinson and Suo [38], a unifying dimensionless number  $Z$  is defined such that the energy release rate of a crack in an infinitely extended thin coating is,

$$G = Z \cdot \frac{\sigma^2 \cdot h}{E} \cdot (1 - \nu) \quad (2.88)$$

where  $\sigma$  is a biaxial stress assumed tensile and homogenous across the coating depth.  $E$ ,  $\nu$  and  $h$  are Young's modulus, Poisson's ratio and the coating thickness, respectively. The  $Z$  number was first introduced by Evans, *et al.* [53] and is a dimensionless driving force depending on the cracking pattern and elastic mismatch. The part multiplied by  $Z$  corresponds to the elastic strain energy stored in a unit area of coating. Given the mechanical properties and a homogenous misfit stress, a specific cracking pattern is inhibited if the coating is thinner than a critical thickness,

$$h_{\text{critical}} = \frac{G \cdot E}{Z \cdot (1 - \nu) \cdot \sigma^2} \quad (2.89)$$

The first cracking pattern of interest is that of a *surface crack* which nucleates from a flaw and is arrested by the interface. In this case, the stress is not

high enough for the crack to channel through the coating. The driving force available for surface cracks is high as indicated by a  $Z$  number equal to 3.951. A second cracking pattern is that of *channeling*, which is an unstable process. Once activated it arrests only until it encounters another channel or an edge. The associated  $Z$  number is lower than that for surface cracks and equal to 1.976.

When a crack in the coating can propagate further to cause *substrate damage*, the  $Z$  value is the largest and equal to 3.951. Such crack may be stabilized at a certain depth, since the misfit stress operates in the coating. If the crack diverts and runs parallel to the interface at a certain depth, then *substrate spalling* occurs. This mode required  $K_{II}$  to be zero and has a very low  $Z$  value equal to 0.343. Finally, *delamination* may start from edge defects or channel bottoms. The latter is stable and is exploited to introduce precracks for certain types of fracture specimens such as the 4-point flexure specimen. The  $Z$  number that relates to delamination is 1.028 for initiation and 0.5 for steady state.

According to De Hosson *et al.* [34, 54], when a planar coating does not delaminate, edge moments have to be applied to prevent bending. These edge moments are produced by the stress component in the  $z$ -direction over the interface. If  $\sigma_{zz}$  is large enough, delamination may take place and  $\sigma_{zz}$  is then removed by bending of the coating. At this point, no further cracking through the thickness of the coating will occur. On the other hand, if  $\sigma_{zz}$  is not large enough to

cause delamination then it is reduced by crack opening but is unchanged in the rest of the coating.

### **2.3.6 Changes in crack growth orientation in coatings**

Thin coatings of ceramics can be subjected to appreciable residual stress of the order of a gigapascal. [38]. Once cracks have nucleated from flaws, and the elastic energy store provides sufficient driving force for them to grow. Cracks then grow at any angle with respect to the interfacial plane. A crack will grow as the driving force  $G$  reaches the fracture resistances,  $G_c$ ,  $G_s$ , or  $G_i$ , depending on whether the crack is propagating in the coating, substrate or along the interface. The opening mode fracture resistance is adequate for thin coatings and substrates, but mixed mode resistance must be used for interfaces. In this particular case, the stress intensity factor,  $K$ , becomes complex, this is,

$$K = K_I + iK_{II} \quad (2.90)$$

with,  $K_I$  and  $K_{II}$  are respectively the opening or tensile mode and the sliding or in-plane shear mode stress intensity factors.

For a crack that propagates at an interface, the complex stress-intensity factor relates to the critical energy release rate (plane strain) as [55],

$$G_{\text{critical}} = \frac{\left[ \frac{1-\nu_c}{\mu_c} + \frac{1-\nu_s}{\mu_s} \right]}{4\cosh^2(\pi\varepsilon)} K \cdot K^* \quad (2.91)$$

where  $\varepsilon$  is the bimaterial constant [56,57] that relates to the elastic properties of the materials on both sides of the interface.

The orientation of the crack path is determined by the components of the complex stress intensity factor,  $K_I$  and  $K_{II}$ . If the thermal gradient is perpendicular to the interfacial plane then cracks will tend to develop vertically. If a crack extends all through the coating depth to the interface it may be blunted if the substrate is strong. Additionally, the formation of a channeling of cracks with regular spacing in the coating may prevent steady-state crack growth along the interface. However, when the interface is weak, the crack will propagate along the interface under pure opening mode (i.e.,  $K_{II} = 0$ ) and delamination of the coating may occur by cleavage fracture along the interface [Hutchinson]. However, as the stress intensity factors will normally be higher for mode II than for mode I, due to the higher friction of mode II, a crack parallel to the interface may often consist of small mixed mode (at 45°) cracks growing together [34].

In (Fe,Cr)-spinel coatings formed on austenitic stainless steel by laser cladding of  $\text{Cr}_2\text{O}_3$  precursor powder, cracks in the ceramic coating were observed

outside the laser track in the heat affected zone [34]. These were oriented vertically in the coating and did not cause delamination of the coating. Cracks ran all the way through the coating and were blunted when they reach the metallic substrate. However, some cracks that started in the heat affected zone and were perpendicular to the surface of the coating bent towards the interface.

### **2.3.7 Measurement of the critical fracture toughness in thin brittle coatings**

Determination of the fracture toughness of a coating material is decisive in determining the critical thickness of the coating to avoid formation of certain crack patterns. If the coating material is fabricated from several chemical elements, a law of mixture using the fracture toughness of individual elements may not be adequate, as it does not include information regarding second phase formation, their geometry and distribution.

Indentation fracture yields valuable information on the fundamental processes of brittle fracture in covalent-ionic solids. Additionally, it provides “controlled flaws” for evaluating strength properties, and it serves as a simple microprobe for determining material fracture parameters such as toughness. Its origins date back to 1880 with the studies of Hertz on conical fracture at elastic contacts between curved glass surfaces. Aucherbach in 1890 showed empirically that the critical load to initiate a cone fracture in a flat specimen is proportional to

the radius of the indenting sphere. However, according to Hertz, fracture should occur only when the maximum tensile stress in the Hertzian field equals the bulk strength of the material, implying that the load is proportional to the radius of the indenter squared. Solution to this paradox required the development of modern fracture mechanics [50].

Today, the radial crack system is the most widely used of all brittle testing methodologies in the mechanical evaluation of brittle materials. Radial-median cracks produced in elastic-plastic fields by diamond pyramid indenters have become of central importance. It requires knowledge of the contact stress field within which the crack evolves. Such fields are determined principally by geometrical factors (indenter shape) and materials properties (i.e.,  $E$ , indentation hardness  $H$ , and stress-intensity  $K$ ). One feature of these stress fields is the presence of extreme gradients in the near contact region, specifically at the indenter corners and edges. It is the tensile component of these stress fields that governs the crack patterns.

#### ***2.3.7.1 Stress intensity factor for a center-loaded half-penny shape crack***

Consider a linear-elastic half-space subjected to a normal point load,  $P$ . This configuration corresponds to the axially symmetric Boussinesq field. The field is characterized by two scaling quantities, the contact dimension  $a$  and the

mean contact pressure  $p_0 = P/\pi a^2$ . The principal normal stresses of the Boussinesq field are so defined that  $\sigma_{11} > \sigma_{22} > \sigma_{33}$  almost everywhere:  $\sigma_{11}$  is tensile at all points with maxima at the surface and along the 45° diagonal;  $\sigma_{22}$  is tensile subsurface;  $\sigma_{33}$  is compressive everywhere. Brittle cracks have a tendency to propagate along paths normal to the greatest tensile stresses. Cracks will then lie on either quasi-conical  $\sigma_{11} - \sigma_{33}$  or median  $\sigma_{22} - \sigma_{33}$  trajectory surfaces; these are known as cone-cracks.

For cracks in distributed internal loading the use of Green's function allows obtaining of the stress intensity factor for an infinite body. What the Green's function does is to weight the integral in favor of the stresses closest to the crack tip. Considering a half-penny crack center-loaded at the inner walls (see Figure 2.28), the stress intensity factor then becomes,

$$K = \frac{2}{\sqrt{\pi c}} \cdot \int_0^c \frac{r \cdot \sigma(r)}{\sqrt{c^2 - r^2}} dr \quad (2.92)$$

For concentrated forces at the crack walls of a half-crack system,  $P = \pi r \sigma(r) dr$ ; then Eq. 2.92 reduces to,

$$K_c = \chi \cdot \frac{P}{c^{1.5}} \quad (2.93)$$

where,  $\chi$ , is a dimensionless constant.



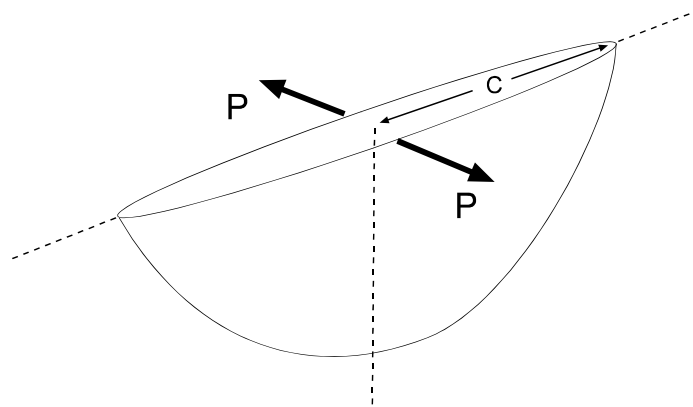


Figure 2.28. Schematic of a halfpenny center-loaded crack (adapted from Lawn [50]).

In 1956, Roesler was the first to find a far-field solution for the cone-crack problem by dimensional analysis. The stress-intensity factor associated with this problem has the similar form of Eq. 2.92, the only difference being the interpretation of  $\chi$ . In this case,  $\chi$  depends on the Poisson's ratio and therefore is a materials constant. Its value has to be determined by fitting empirical data, i.e.,  $P$  versus  $c^{1.5}$ , to a straight line.

### **2.3.7.2 Direct-crack measurement indentation technique**

Indentation provides a simple procedure for toughness evaluation. Sharp indenters have the advantage that the test can be performed on standard hardness testing equipment. According to Lawn [50], Vickers or Knoop diamond pyramids

used in hardness testing produced two basic types of crack pattern: radial-median (halfpenny shape) and lateral.

One such indentation procedure available is the “direct-rack measurement” technique. It consists in the measurement of the immediate post-indentation radial crack size  $c_l$  as a function of load without the applied stress in an inert environment. As described before, the critical toughness for a center-loaded half-penny shape crack is given by Eq. 2.93, however in this case,  $\chi = \xi_0 (\cot \Phi)^{\frac{2}{3}} \cdot \left(\frac{E}{H}\right)^{0.5}$ , and corresponds to the residual stress field intensity at complete unloading.  $E$  and  $H$  are the Young’s modulus of the material and the hardness value measured by the indentation, respectively. So Eq. 2.93 becomes,

$$K_c = \xi_0 (\cot \Phi)^{\frac{2}{3}} \cdot \left(\frac{E}{H}\right)^{0.5} \cdot \frac{P}{c_l^{1.5}} \quad (2.94)$$

where  $\Phi$  is the indenter half-angle, and the dimensionless constant  $\xi_0$  is fitting parameter depends on the nature of the deformation. The quantity  $H/E$  is an important parameter, as  $H$  quantifies the loading half-cycle and  $E$  the unloading half-cycle. Higher  $H/E$  (e.g. hard ceramics) corresponds to lower residual field intensity, indicating a pronounced radial extension during the unloading half-

cycle. The geometrical parameter  $\xi_0$  has been obtained by fitting  $P$  versus  $c_1^{1.5}$  to a straight line.

Advantages of this technique are its extreme simplicity and that many indentations per surface can be done. Among the disadvantages, it is difficult to measure crack size, even on polished surfaces, at small and ill-defined indents, especially in coarse-grained polycrystals. Moreover, it shows moderate dependency on  $H/E$  and large dependency on geometrical parameter  $\xi_0$  which is itself sensitive to deformation mode.

As a means of measuring absolute toughness, this indentation technique is simple, but limited. Departures from the calibrated curves in excess of a factor of two may occur for the worst behaved materials. Reliability of the measurements of a given material can be better than 20%.

When the indentation size is too large the assumption of a point loaded force does not hold precisely, and Eq. 2.94 deviates from reality. Another factor relative to the size of the indentation is the size of the grains that made up the structure of the material. If these are of a comparable size, then cracks may propagate in between grain boundaries and not along the indentation diagonals. [58].

### 2.3.8 Multi-layer coatings for C/C composites

To prevent fracture and delamination of the coating during its fabrication process as well as degradation during the thermal cycling during extended-life service operations, a four coating sequence was developed, namely: chromium carbide bond-layer, silicon based refractory diffusion-barrier-layer, silicon based refractory erosion-barrier-layer and a final silica modified glass sealant-layer. According to Westwood *et al.* [25], most promising coatings for oxidation protection of C/C composites are those composed of several ceramic layers designed to protect against the aforementioned failure modes in addition to possessing a self-healing capability by formation of glassy phases on exposure to oxygen.

Westwood *et al.* further suggests that at least one component of the coating system must have low oxygen permeability to form an effective barrier to the ingress of oxygen. According to Sheehan [26], oxygen permeabilities should not exceed  $10^{-9} \text{ gm}\cdot\text{cm}^{-1}\cdot\text{s}^{-1}$  to prevent more than a 2% weight loss in thin uncracked dense coatings. As cracks are almost unavoidable, Westwood *et al.* [25] emphasized that a glass or a glass-forming compound should be present so that it can flow into and seal any crack that may develop. Additionally, it is necessary to reduce the carbon diffusion outwards from the substrate as some layer of the coating may contain oxides and so be reduced by carbon.

The first US patent regarding coating of graphite articles was granted in 1934 to Johnson. The coating system then proposed consisted of a surface conversion to SiC and vitreous glaze overlay coatings based on alkali and alkaline earth addition to the traditional glass formers [59]. Sheehan [26] indicates that other patents on coating system for graphite have followed since this one until 1960. In the early 1970s development of coating systems for C/C composites directed to flight-related applications began. Surprisingly, the original shuttle orbiter thermal protection coating system is based on Johnson's patent.

More recently, in 1996 Joshi and Lee were granted a patent [60] on a two coating system composed primarily of a first layer of 60 wt.% Si - 30 wt.% Hf - 10 wt.% Cr and a second layer of 59 wt.% Si - 30 wt.% Hf - 10 wt.% Cr and 1 wt.% C. The processing method used to form and consolidate the coating over the C/C substrate is known as fused slurry or vacuum fusion treatment. In this process the composite is dipped first in a premixed viscous slurry and then fired at a temperature range of 1300°C to 1450°C for 20 to 120 minutes under a vacuum of  $10^{-5}$  torr. These conditions provided sufficient time for equilibrium transformation to occur and a coating layer formed over the substrate. Layer thickness was controlled by the viscosity of the slurry and the amount of slurry deposited on the specimen.

In the present research, the author and collaborators developed a 4-coating system, as seen in Figure 2.29, after several experimental attempts. It consists of a first bond-layer of 70 wt.%  $\text{CrCl}_3$  - 30 wt.% Cr, a second refractory layer of 70 wt.% Si - 25 wt.% Cr - 5 wt.% C, a third layer of 70 wt.% Si - 15 wt.% Cr - 15 wt.%  $\text{HfCl}_4$  and a glass modified 50 wt.%  $\text{SiO}_2$  - 50 wt.%  $\text{Na}_2\text{O}$  layer. The first three slurry coatings were consolidated by a “laser induced cementation” (LIC) process on 3D C/C composite cylinders. The fourth layer was applied by conventional furnace inert-gas firing processes. In LIC process, the laser beam was scanned over the surface axis of the rotating cylinder for 4 minutes. The overall temperature of the slurry became homogenous and of the order of  $1400^\circ\text{C}$ . Where the laser was impinging momentarily the temperature was considerably higher.

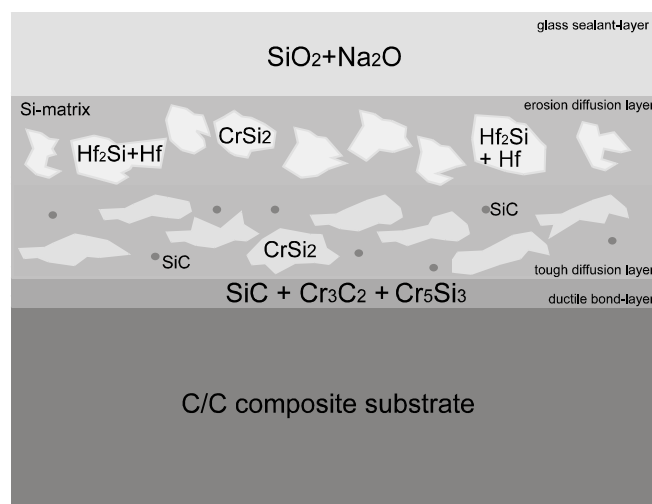


Figure 2.29. Schematic illustration of the final morphology due to the 4-layer coating strategy followed after the LIC process.

Chlorides of Cr and Hf were used as precursor materials to obtain Cr and Hf metals due to their low cost, chemical stability and organometallic compound formation with the liquid media used to form the slurry. These organometallic compounds have a strong binding property [61] and thus allow the slurry to attach firmly to the substrate of the cylinders on drying.

The quaternary coating chemistry used (i.e., Si, Cr, Hf and C) is very adequate. Silicon (diamond cubic structure) has a high enough melting point of 1412 °C, and it is chemically compatible with carbon, so that it forms SiC at the interface reducing C diffusion into the coating layer. SiC is the most common primary oxygen barrier together with Si<sub>3</sub>N<sub>4</sub> [25,26]. However, in the case of the latter, C and N can potentially form cyanide compounds at high temperatures, which are known to be extremely hazardous [58]. SiC also has a low CTE mismatch with the C/C composite substrate of 0.15% at 500 °C above the coating application temperature that is only surpassed by a 0.12 of Si<sub>3</sub>N<sub>4</sub> [26]. Moreover, silicon in the presence of air forms a silica scale, which is an excellent oxygen diffusion barrier as it has a low oxygen permeability of 10<sup>-10</sup> gm\*cm<sup>-1</sup>s<sup>-1</sup>, but it lacks good erosion protection at temperatures above 1770°C [26]. Additionally, silica can also be reduced to SiO by hydrogen, leading to accelerated degradation. Another disadvantage of silicon is that it is brittle and thus it possesses low fracture toughness (i.e., 7 MPam<sup>0.5</sup>). However, all these disadvantages can be solved by

the addition of Cr and Hf. These two elements are considered refractory metals because of their high melting points of 1860 °C and 2222 °C, respectively. These elements are mutually chemically compatible, forming HfCr binary Laves phases of Type C14, C15 [61]. They are also compatible with Si, forming silicides with higher melting point than that of Si. The CTE mismatch between Cr, Hf and Si is low, too.

Cr is a ductile and tough element ( $K_{IC} = 65 \text{ MPa}\cdot\text{m}^{0.5}$ ) with bcc structure and of Type A2 and O<sup>9</sup>h space group. It has a boiling of 2672 °C [61]. Cr can serve the purpose of accommodating strains caused by the CTE mismatch during thermal cycling. Cr is also a stronger carbide former than Si but a weaker oxide former relative to the latter as seen in the Ellingham diagrams [21]. In this respect, the purpose of the first layer CrCl<sub>3</sub>-Cr layer serves a two fold purpose: first to form a Cr<sub>3</sub>C<sub>2</sub> (orthorhombic) layer that will allow better wetting and bonding of the subsequent refractory layer, second to increase the amount of Cr content near the interface to increase the local toughness to blunt through coating cracks.

Hafnium metal has an  $\alpha$ -hcp structure at room temperature. It poses low volatility at high temperatures above its melting point, and its boiling point is 4600 °C. At 1750 °C, it undergoes a phase transformation from  $\alpha$ -hcp to  $\beta$ -hcp [61]. It forms hafnia (HfO<sub>2</sub>) when exposed to air at high temperatures. This oxide shows the highest temperature of 2475 °C at which the oxide vapor pressure is 10<sup>-</sup>



shows the highest temperature of 2475 °C at which the oxide vapor pressure is  $10^{-3}$  mm compared to other metal oxides, which is an appropriate vapor pressure for an oxide to be used for erosion protection [26]. However, hafnia's fluorite structure is open and permits fast oxygen diffusion. Hence, its oxygen permeability is high and equal to  $10^{-9}$  gm\*cm<sup>-1</sup>s<sup>-1</sup> . Moreover, hafnia must be stabilized like ZrO<sub>2</sub> against undesirable phase changes which occur during heating and cooling.

Finally, graphite has been added with the main objective to form a fine dispersion of SiC particles in the Si matrix. This can facilitate the formation of a fine grain structure during solidification from the melt that limits the crack length and aids in isolating the cracks in selected phases [62]. SiC particles may also serve two opposite purposes: to create a network of microcracks in the coating and so relieve the tensile misfit thermal stresses [47], and to act as crack arrestors reducing the development of through-coating cracks [62]. The author believes that the former mechanism is more likely to occur, reducing through-coating cracks.

#### **2.3.8.1 Binary phase diagram analysis**

Formation of a coating from its constituent elements can be explained using a phase diagram only when the time allowed for a given phase transformation to take place is enough to reach equilibrium. This is normally the

case for a product phase formed directly from a liquid phase, even at high cooling rates. This is because the diffusion between chemical species in the liquid state can be up to three orders of magnitude faster than in the solid state [17,22,63]

The ternary phase diagram for the Si-Hf-Cr systems has not been yet constructed. However, the following ternary phases have been observed [64]: CrHfSi (type  $\text{Co}_2\text{Si}$ , Pnma space group),  $\text{CrHfSi}_2$  (Pbam space group),  $\text{Cr}_3\text{Hf}_2\text{Si}$  ( $\text{P}_63/\text{mmc}$ ) and  $\text{Cr}_5\text{Hf}_6\text{Si}_7$  (Pnma space group).

The availability of the binary phase diagrams for the Si-Hf, Si-Cr and Hf-Cr allow for better understanding of the possible transformation and phase products in this ternary system. From Figures 2.30 and 2.31a, for composition of 15-25 weight % of Cr and 3.5 to 7.5 wt% Hf it can be seen that eutectic reactions occur in both cases at 25 wt% Cr and 9.7 wt% Hf, respectively. The eutectic temperature in both cases is very similar and equal to 1320-1330 °C. Therefore, for the Si-Cr system a hypereutectic reaction occurs and for the Si-Hf system a hypoeutectic reaction takes place. The morphologies of the products are then eutectics of Si and  $\text{CrSi}_2$  and of Si and  $\text{HfSi}_2$ . Calculation using Thermo-Calc [65] software confirmed the existence of these products even for the ternary mixture. Additionally, from Figures 2.30 and 2.31a it can be observed that these silicides are stable up to temperatures higher than that of the melting point of Si, specifically 1550°C and 1543 °C.

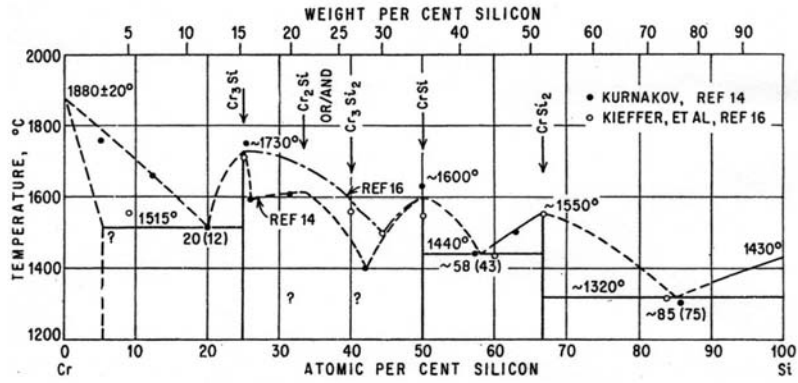


Figure 2.30 Si-Cr binary phase diagram (after Hansen [18]).

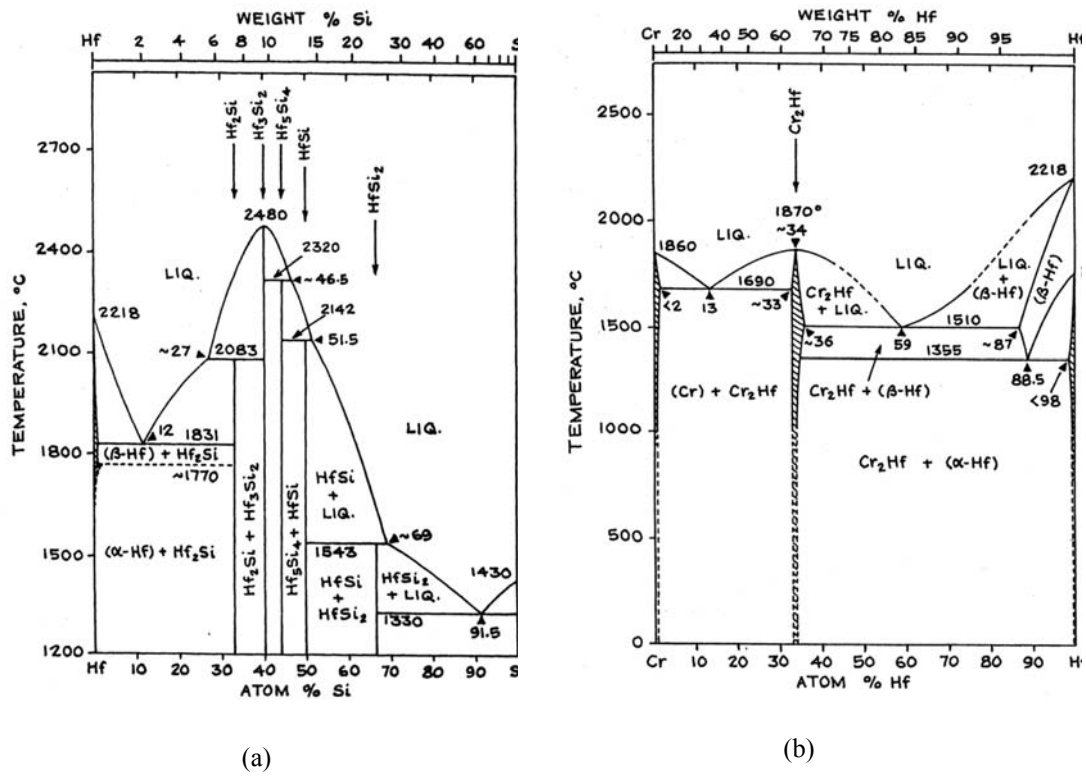


Figure 2.31. (a) Si-Hf binary phase diagram; (b) Hf-Cr binary phase diagram (after Moffatt [66]).

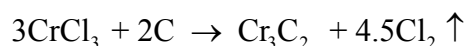
From Figure 2.31b it can be noticed that the first eutectic reaction of the Hf-Cr system occurs at approximately 30 wt% Hf and at a high temperature of 1690°C. Therefore, at relative composition of 15.7 wt% Hf in a pure Hf-Cr system, a hypoeutectic reaction would take place. The eutectic products (Cr) and a Cr<sub>2</sub>Hf intermetallic phase would then be formed provided the temperature of the melt falls in between 1690°C and 1860°C.

The Cr<sub>2</sub>Hf intermetallic has an even higher melting temperature of 1870°C. Because of the high liquidus temperatures in this system, it is not likely that this phase will form at the eutectic temperature of the Si-Cr and Si-Hf (i.e., 1330°C) systems as confirmed by Thermo-Calc.

It may be worth mentioning that in the LIC process the overall maximum isotherm in the coating may well lie above 1400°C and that it may last for up to 4 minutes. This allows for a long enough transformation time for the liquid state eutectic reactions that occur below this temperature to reach equilibrium. Where the laser beam is impinging, the local isotherm is higher and short-lived but it never goes below the overall isotherm level. This temperature peak may aid the formation of the Cr<sub>2</sub>Hf intermetallic if enough time is allowed.

### **2.3.8.2 Initial chromium layer**

Cr shows a higher negative free energy of formation of its carbide  $\text{Cr}_3\text{C}_2$  at equilibrium conditions than Si does when forming SiC. Moreover, the availability of Cr as a hydrous salt ( $\text{CrCl}_3$ ) allowed experimenting with its decomposition at low laser power levels over the C/C substrate. The heat from the laser beam provides the activation energy for the chlorine ion to dissociate from the  $\text{CrCl}_3$  molecule. It is known that  $\text{CrCl}_3$  decomposes into  $\text{CrCl}_2$  and  $\text{Cl}^-$  at  $1300^\circ\text{C}$  [61]. If higher temperatures are provided then the  $\text{CrCl}_2$  should dissociate completely into  $\text{Cr}^{2+}$  and  $\text{Cl}^-$ . The  $\text{Cl}^-$  ions should recombine into gaseous  $\text{Cl}_2$  and leave the  $\text{Cr}^{2+}$  cations free to react with the carbon surface. These free Cr cations should then form a strong bond with the carbon surface. The hypothetical reaction is of the form,

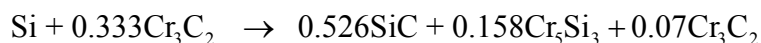


By adding pure Cr to the  $\text{CrCl}_3$ , the exothermic heat during the decomposition process should melt the Cr metal forming a ductile layer over the  $\text{Cr}_3\text{C}_2$  phase product and thus facilitate crack blunting.

### **2.3.8.3 Intermediate refractory layer**

Following the  $\text{Cr}_3\text{C}_2$  layer, a second coating consisting of Si-25Cr-5C (in wt.%) can be applied over the former to understand the effect that silicon,

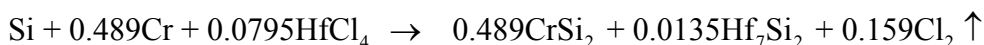
chromium and graphite particles have in enhancing the formation of a SiC interface. The hypothetical chemical reaction, expressed in molar weight, at the interface at 1300 °C (i.e., eutectic temperature for the Si-25wt.% Cr system), where it is assumed that silicon interacts with the already formed chromium carbide, is expressed in molar weight, according to Thermo-Calc [65],



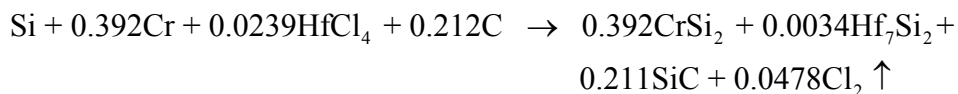
From an Ellingham diagram for carbides [21] the free energy of formation of some chromium carbides (i.e.,  $\text{Cr}_7\text{C}_3$  and  $\text{Cr}_{23}\text{C}_6$ ) is more negative than the one corresponding to silicon carbide. Results from ThermoCalc obtained at 1300 °C provide the Gibbs energy of formation for SiC to be equal to  $-1.52 \cdot 10^5$  kJ/mole while for  $\text{Cr}_3\text{C}_2$  it corresponds to  $-3.78 \cdot 10^5$  kJ/mole and for  $\text{Cr}_5\text{Si}_3$  is  $-8.82 \cdot 10^5$  kJ/mole. Therefore, at first one might think that the reaction should not take place. However, the free energy of formation of the chromium silicide ( $\text{Cr}_5\text{Si}_3$ ) is even more negative, driving the reaction towards the right (total Gibbs energy  $-7.09 \cdot 10^5$  kJ/mole from Thermo-Calc). So, a less stable carbide layer, SiC, would form at the interface having a small fraction of unreacted  $\text{Cr}_3\text{C}_2$ . This should in theory facilitate the wetting of the unreacted Si and  $\text{Cr}_3\text{Si}$  coating material that remains molten above the interface. To determine which of the two carbide

coatings, Cr or Si, provided higher bonding strength, the work of adhesion could be estimated from Eq. 2.48.

A third coating system based on Si-15Cr-15HfCl<sub>4</sub> can be deposited on top of the previous one to incorporate Hf and additional Cr metal into the coating. When reacting this mixture at 1210°C, the following products in molar weight are obtained,



In principle the last two coatings could be applied together with a total stoichiometry of Si-20Cr-7.5HfCl<sub>4</sub>-2.5C (in weight %). Thermo-Calc gives as products the following compounds expressed in molar weight:



This reaction was calculated at 1210 °C, at a temperature of 1240°C a single liquid phase forms together with SiC.

#### **2.3.8.4 Use of metal chloride salts**

Chlorides of Cr and Hf may facilitate slurry preparation as these salts show good intermixing with pure Si, Cr and C as well as solubility in the liquid media used, isopropyl alcohol. Cr forms innumerable organometallic compounds

like hexa-carbonyl  $\text{Cr}(\text{CO})_6$  when mixing  $\text{CrCl}_3$  with phenyl-magnesium in ether. This is an exceptional unreactive compound. Formation of such compounds is characteristic of all d-group transition metals. Moreover, these compounds are oxidized by oxygen at significant rates even at room temperature.

$\text{Cr}^{3+}$  has also a strong affinity to form coordination compounds. These are susceptible to hydrolysis and formation of polynuclear complexes by an olation polymerization consisting in chains of rings of  $\text{Cr}^{3+}$  cations connected via bridging OH- groups [61].

In the observed phenomenon it appears that the metal cation and Cl anion adheres to the isopropyl carbon backbone to form a long chained compound. This new compound serves for better adherence of the slurry to the C/C composite substrate reducing the chances of coating break up during the laser processing.

However, Cl ions are being produced during the interaction with the laser beam. Most of these ions will then recombine to form  $\text{Cl}_2$  molecules at temperature of 1300 °C and evolved as gas during the process. However, a high probability exists for Cl<sup>-</sup> ions or other Cl-based compounds of Si to remain dissolved in the coating. Chlorine is detrimental to preservation of the structure of the coating as it can assist in crack formation at high temperature as well as reach with the refractory layer and the glass sealant overcoat.



#### ***2.3.8.5 External glassy layer: a crack sealant approach***

A Silica modified glass type slurry was used as the external coating to provide a sealant for the cracks present in the refractory coating. It consisted of  $\text{SiO}_2$  and  $\text{Na}_2\text{CO}_3$  (sodium carbonate) fine powders mixed with a sodium silicate solution to form a sticky paste. It was then fired in a furnace under argon atmosphere after application on the LIC coated C/C cylinder. Silica is a glass former whereas soda is a glass modifier. The combination of both compounds allows formation of a glass with low glass transition temperature ( $400^\circ\text{C}$ ) and yet high melting point ( $1100^\circ\text{C}$ ) [67]. Moreover, a low viscosity glass is achieved at temperatures above the melting point. Due to the low  $T_g$  value of this glass, the temperature range available for thermal shock is also lower than when using a pure silica glass sealant, thus minimizing cracking of the glass coating.

At temperatures above  $T_g$  the glass softens and it can flow inside of the cracks that are present in the first Si based coating driven by capillarity. This crack sealant mechanism becomes more effective as the temperature is raised and the viscosity of the glass is lowered. This crack infiltration process provides oxidation protection to the substrate zones exposed through the crack channels.

One drawback of using alkali metals like Na as the glass modifier is the extreme chemical reactivity of this specie posing a stability problem with other phases and elements in the coating. It is also very volatile at temperatures above

its boiling point (883°C) so it facilitates erosion of the glass surface. Nonetheless, as a first attempt to prove the effectiveness of a crack sealant overcoat layer, Na modified silica is a convenient starting point.

### **2.3.9 Performance of coated C/C composite cylinders**

The coated C/C composite cylinders served the purpose to determine the effectiveness of the coating layers applied in preventing oxidation of the substrate when exposed to a temperature of 1000°C in air atmosphere. Factors that can alter the integrity of the applied coating, and so deteriorate its oxidation barrier properties, are primarily the presence of crack patterns from the coating process itself or by thermal stresses induced during service. Chemical reactivity among the different coating layers may cause severe damage to the coating, exposing the substrate to a direct contact with air. Finally, when the specimen is held at a high service temperature for a prolonged time, formation of second phases may induce internal volume changes and help nucleate cracks. Partial melting of certain coating regions may also take place weakening the coating interface bonding.

Information regarding these phenomena can be obtained a priori by several techniques, namely: thermo-gravimetric analysis, thermo-mechanical analysis and differential temperature analysis.

### **2.3.9.1 *Weight loss test***

Certain materials undergo loss or gain of mass on heating under certain atmospheric conditions (e.g., air stream). The variation in mass can be tracked by measuring the change in weight. This technique is also referred as thermogravimetric analysis (TGA). In the case of C/C composites it is well known that at temperatures above 450°C in the presence of air, carbon recombines with oxygen to form gaseous CO<sub>2</sub> molecules, resulting in loss of mass by decomposition. Other materials like silicon may gain weight in the presence of an atmosphere rich in oxygen by oxide scale (i.e., SiO<sub>2</sub>) formation that remains attached to the material substrate.

In TGA, the weight of the material has to be recorded in time by some means as the material is being held at a high temperature. This is not an easy task to carry out unless sophisticated equipment is available that can perform in-situ weight measurements at elevated temperatures. Alternatively, if the specimen is too large to fit inside a standard TGA instrument, it can be heated inside a conventional furnace, removed from the furnace, allowed to cool down and then weighed it on a standard micro-scale. The times of removal, weighing and reinsertion of the specimen need to be recorded. However, if the specimen tested this way is brittle, then the thermal cycling induced by moving the specimen in and out from the furnace may induce thermal stresses that deteriorate the coating.

In the particular case of coated C/C composites, any source of cracks at the coating may increase the rate of oxidation of the specimen tested and therefore alter the performance of the coating as an oxidation barrier. One way to minimize the effects of thermal cycling is by moving the specimen in and out at a very slow pace so that cooling and heating occur gradually. This, however, may alter the precision of the recorded time at which the weight is measured.

### ***2.3.9.2 Thermomechanical analysis***

A thermomechanical analyser (TMA) gives information regarding the deformation of a solid in a uniaxial direction as a function of temperature as the specimen is slowly heated and then allowed to cool. By normalizing the slope of the elongation versus temperature plot, the coefficient of thermal expansion of a solid can be obtained at each temperature. Determination of the CTE is critical for obtaining the misfit stress state distribution in the coating and substrate during cooling.

### ***2.3.9.3 Differential thermal analysis***

The differential thermal analyser (DTA) allows determination of phase changes in a solid that may occur at specific temperatures on heating and cooling, such as formation of new phases, onset of melting and solidification. The local

change in temperature measured relative to a standard specimen is recorded, so that an increase in temperature will indicate that a phase transition has occurred in the solid so that heat has evolved (exothermic reaction). On the other hand, a decrease in the relative temperature indicates that a phase transition has taken place in which heat has been absorbed (endothermic reaction). This technique is specifically useful to determine the temperature range of melting and solidification of compounds as well as temperatures at which second phases appear.

## **2.4 DIRECTIONALLY GROWN SUPERALLOY DEPOSITS BY LASER MELTING**

### **2.4.1 Solidification during raster scan laser melting**

When a laser beam raster scans over the surface of a material along a straight path with constant traveling speed and with enough power to cause melting, a dynamic thermal equilibrium between heat supply and heat extraction is established [3-5,22,68-71], determining the rate of advance of the solidification front [34]. Under this pseudo-steady-state condition, the shape of the molten pool remains constant for a given laser traveling speed  $v_t$  [3,4,22,68,69]. The shape of the melting pool is also a function of the laser power  $P$  and speed as well as the heat conductivity and thermal diffusivity of the material. High speed and power and low thermal diffusivity promote the formation of a “comet-shaped” melting

pool, whereas low speed and power and high thermal diffusivity provide the conditions for a semi-spherical shaped melt pool. If the substrate has a low thermal conduction coefficient the melt pool is elongated instead of semi-spherical [34]. Others factors that determine the shape of the fusion zone are convection due to buoyancy and surface tension gradient [69].

According to De Hosson *et al.*[34], the high rate of advance of the solidification front is due to high cooling rate experienced by the melt pool during any type of laser treatment. The maximum rate of advance of the solidification front occurs at the rear of the melt pool. Moreover, the continuous process of melting material at the front of the melt pool that solidifies at the rear of the melt pool causes the solidification front to follow the temperature field.

During solidification of the melt pool, growth of columnar grains proceeds closely to the direction of the maximum thermal gradient in the molten pool, i.e., normal to the rear fusion boundary [22,69,70]. The columnar grain morphology thus depends on the molten pool geometry. A spherically shaped melt pool will reveal curved and tapered columnar grains owing to a shift in the direction of the maximum thermal gradient in the liquid from the fusion boundary towards the liquid free surface. In contrast, a comet-shaped melt pool produces straight and broad columnar grains, as the direction of the maximum temperature gradient in the melt does not change significantly during the solidification process [69].

The growth rate  $R$  of the columnar grains is also geometrically related to the traveling speed of the heat source and the shape of the fusion zone. Since the shape of the melt pool remains constant during the pseudo-steady-state,  $R$  varies with position along the rear fusion boundary. At each position along this fusion boundary, the columnar grains grow parallel with respect to the thermal gradient in the melt pool. If the angle between the growth direction (i.e., thermal gradient direction) and the laser beam traveling speed  $v_t$  direction is taken as  $\theta$  then the steady state nominal growth rate  $R_N$  becomes [22,69-71],

$$R_N = v_t \cos \theta \quad (2.95)$$

Elongation of the rear part of the melt pool causes increase in area of solidification front and the nominal growth velocity  $R_N$  is reduced because in this situation  $\theta$  is larger over most of the solidification front.

In cubic metals and alloys, it is common to observe that the  $\langle 100 \rangle$  direction corresponds to the major dendrite growth direction [22,34,69,70]. Because of the existence of preferred growth directions in a material that minimize the free energy at the solid-liquid interface [15], the local growth rate of a crystal  $R_L$  will be higher than or equal to the nominal rate  $R_N$  provided the same driving force acts in both conditions. For example, if  $\varphi$  is the angle between the

fusion boundary normal and the  $\langle 100 \rangle$  direction, then the relationship between  $R_L$  and  $R_N$  is given by,

$$R_L = \frac{R_N}{\cos \varphi} \quad (2.96)$$

$R_L$  will increase with increasing misalignment of the crystal with respect to the direction of the maximum thermal gradient in the melt zone. However, the driving force for the growth of the misaligned grains (i.e., constitutional undercooling ahead of the solid/liquid interface) is small and they are soon outgrown by grains that have a crystal orientation closer to that of the maximum thermal gradient (i.e., maximum driving force) [15].

Moreover, in the case of laser deposition of single-layers, if the thermal conductivity of the substrate is several times larger than that of the deposited layer, the thermal gradient is approximately vertical in the deposited layer, so solidification occurs from the interface to the top of the surface layer. Dendrites then form a columnar structure perpendicular to the interface [34].

Even though these columnar grains may not be oriented along an easy growth direction of the material (e.g.,  $\langle 100 \rangle$ ), the growth mode of the atoms inside each columnar grain follows an easy growth direction. So, we can conclude that thermal gradient in the liquid determines the macroscopic orientation of the



solidified columnar structure, and that microscopic orientation within the columnar grain is a material property.

#### ***2.4.1.1 Solidification growth stability***

The stability of the solidification front is controlled by the extent of the constitutional undercooling ahead of the advancing interface. It is influenced by factors such as the alloying or impurity elements present, local growth rate  $R_L$ , and thermal gradient in the melt zone  $G_L$ . A high  $G_L/R_L$  ratio provides a planar solidification front. At lower  $G_L/R_L$  ratio, the morphology changes to cellular, cellular-dendritic or dendritic depending on the degree of constitutional undercooling ahead of the advancing front [69,70].

Normally in laser melting processes, the  $G_L/R_L$  ratio at the fusion boundary is large enough to facilitate planar solidification. The temperature gradient in the melt zone decreases with distance from the fusion boundary and a cellular-dendritic type of substructure is observed in the central areas of the melt pool. The substructure may change from dendritic to equiaxed close to the free surface if the degree of constitutional undercooling in front of the advancing interface is sufficiently large [22,69,70]. This is common whenever the surface of the liquid loses heat by radiation [34].

#### **2.4.1.2 Columnar growth reorientation**

A columnar grain can adjust its orientation during solidification to accommodate a shift in the direction of the maximum temperature gradient in the melt pool by means of two mechanisms: bowing or re-nucleation.

During bowing, a continuous change in the crystal orientation will result in curved columnar grains. The adjustment of the crystal orientation is promoted by multiple branching of dendrites present within the grains. Alternatively, the reorientation can be accommodated by the presence of defects at the solid/liquid interface, e.g. screw dislocations, twin boundaries and rotation boundaries. Under these circumstances, the growth rate of the dendrites will never exceed the laser beam traveling speed  $v_t$  [22,69-71].

Under the second mechanism, heterogeneous nucleation is the main driving force since the fused metal often contains a high number of second phase particles. Reorientation of the columnar grains will occur when the cell/dendrite alignment angle reaches a critical value that depends on the nucleation potency of the catalyst particles. Nucleation of new grains ahead of the advancing columnar interface can also occur from random solid dendrite fragments contained in the melt pool. Alternatively, since the partially melted base grains at the fusion boundary are loosely held together by the liquid between them, there is a possibility that some of these grains may detach themselves from the base metal

and be trapped in the solidification front. Like dendrite fragments, such partially melted grains can act as seed crystals [69].

In the particular case of Cr oxide deposited over stainless steel by laser cladding, dendrites all seemed to originate from a thin, homogenous layer at the interface of certain thickness [34,54]. Over almost the entire width of the laser track the dendrites are almost vertical, except for a tilt of about  $10^\circ$  in the direction of the laser beam movement. At the edges of the laser pool the dendrites are tilted over larger angles. Only the secondary arms of the dendrites are developed. The spacing between dendrites is of 10 to 20 microns. Dendrites broaden at the tip of the coating. At 30 to 80  $\mu\text{m}$  from the coating the dendrites are oriented differently. The orientation the dendrites is changed by the heat flow to surrounding atmosphere.

#### ***2.4.1.3 Columnar to equiaxed transition***

An equiaxed zone is often observed close to the free surface of the melt pool. The melt becomes undercooled by the extensive segregation of solute where the growing solidification front impinges. This makes the crystals hotter than the liquid and gives rise to radial heat flow away from the crystals in the same direction as that of growth [22,69]. For a given alloy system containing a fixed number of heterogeneous nucleation sites, it is reasonable to assume that the

columnar to equiaxed transition occurs when the  $G_L/R_L$  ratio drops below a certain critical value  $f$  [69]:

$$f_{\text{critical}} > G_L/R_L \quad (2.97)$$

Figure 2.32 illustrates a cross section of the raster scan laser melting of a layer of pre-placed powder over a substrate under pseudo-steady-state thermal conditions. The melt pool geometry is constant and the solidification front initially along the [001] orientation bows towards a direction given by the normal to the fusion boundary. Near the free surface of the melt pool a columnar to equiaxed transition occurs due to reduction in the thermal gradient in the liquid and increase in local growth rate.

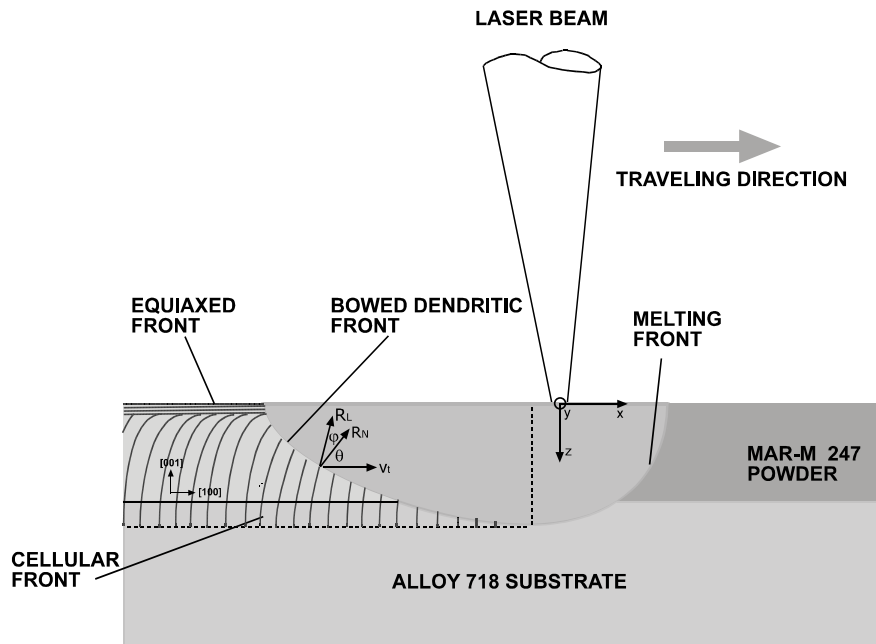


Figure 2.32. Schematic of the cross section of the solidification mechanisms in raster scan laser melting of Mar-M 247 superalloy powder.

#### 2.4.2. Estimation of the thermal gradient in the melt

For a thick plate (i.e. semi-infinite domain), the steady state solution to the three-dimensional heat transfer problem is predicted by the Rosenthal's solution [13,69] given by Eq. 2.20. From this solution, the thermal gradient at the fusion boundary  $G_L$  at the free surface of the melt pool (i.e.,  $y = 0, z = 0$ ) behind the laser beam can be obtained by differentiation with respect to  $x$  [22,69]. It corresponds to

$$G_L = \frac{2\pi K(T_m - T_0)^2}{P \cdot \eta} \quad (2.98)$$

where  $K$  is the thermal conductivity of the material,  $T_m$  is the melting temperature,  $T_o$  is the pre-heating temperature and  $\eta$  is the amount of laser power coupling into the material. At the free surface of the melt it can be assumed that  $R_L = v_t$  and according to Equation 2.97 at the critical condition, the following relationship is obtained,

$$P_{\text{critical}} = \frac{2 K(T_m - T_o)^2}{\eta \cdot f_{\text{critical}} \cdot v_t} \quad (2.99)$$

Therefore critical combinations of  $P$  and traveling speed  $v_t$  will cause transition from columnar to equiaxed at the free surface of the deposit. From Equation 2.99, a decrease in  $P$  must be compensated by a corresponding increase in  $v_t$  to maintain dendritic growth up to the surface [69].

## 2.5 REFERENCES

1. H.S. Carls and J.C. Jaeger, Conduction of Heat in Solids, (Oxford, 1996).
2. B. Boley, J. Weiner, Theory of Thermal Stresses, (Dover, 1988).
3. W.M. Steen, Laser Material Processing, 2<sup>nd</sup> ed., (Springer Verlag, 1993).
4. D. Schuocker, High Power Lasers in Production Engineering, (Imperial College Press, World Scientific, 1999).

5. J.F. Ready, D.F. Farson, and T. Feeley, eds., LIA Handbook of Laser Materials Processing (Laser Institute of America, Magnolia Publishing Inc. 2001).
6. R.M. German, Liquid Phase Sintering, (Plenum Press, New York 1985).
7. N. Eustathopoulos, M.G. Nicholas, and B.Drevet, Wettability at High Temperatures. Pergamon Materials Series, ed. R.W. Cahn, (Elsevier Science, 1999).
8. T.S. Piwonka, “The influence of the mold/metal interface on casting quality in sand castings”, Solidification Science and Processing, Eds. I. Ohnaka, and D.M.Stefanescu, (TMS publishing, 1995).
9. F. P. Incropera, Fundamentals of Heat and Mass Transfer, 4th ed. (New York, 1996).
10. M.C. Shaw, Metal Cutting Principles, (Oxford Science Publications, 1997).
11. T.R. Anthony and H.E. Cline, *J. Applied Physics*, v. 48, No 9, 3888-3894 (1977).
12. V.S. Avanesov and M.A. Zuev, “Investigation of surface topography after melting by laser beam”, SPIE, v.2713, 340-343.
13. D. Rosenthal, *Trans. ASME*, v. 68, 849-865 (1946).
14. Ø. Grong, N. Christensen, *J. Mater. Sci. and Tech.*, v. 2, 967-973 (1986).
15. W. Kurz, D.J. Fisher, Fundamentals of Solidification, 4<sup>th</sup> ed. (Trans Tech Publication , 1998).
16. R.W.K. Honeycombe and H.K.D.H Bahadeshia, Steels: Microstructure and Properties, 2<sup>nd</sup> ed., (Edward Arnold, 1995).
17. P. Gordon , Principles of Phase Diagrams in Materials Systems, (Krieger, 1983).
18. M. Hansen and K Anderko, Constitution of Binary Alloys, (McGraw Hill, 1958).

19. V. Raghavan, Phase Diagram of Ternary Iron Alloys, Part 6B, (Indian Institute of Metals, Calcutta, 1992).
20. David R. Gaskell, Introduction to the Thermodynamics of Materials, 3<sup>rd</sup> ed., (Taylor Francis, 1995).
21. A.S. Khanan, High Temperature Oxidation and Corrosion, (ASM International, 2002).
22. M. A. Ootoni, Elements of Rapid Solidification, Springer Series in Materials Science 29, (SpringerVerlag, 1998).
23. J.D. Buckley, "Carbon-Carbon: an overview", *Ceram. Bull.*, v. 67, 2, 364-368 (1988).
24. J. R. Strife and J.E. Sheenan, "Ceramic coatings for carbon-carbon composites", *Ceram. Bull.*, v. 67, 2, 369-374 (1988).
25. M. E. Westwood *et al.*, "Review: oxidation protection for carbon fibre composites", *Journal of Material Science*, 31, 1389-1397 (1996).
26. J.E. Sheehan, "Oxidation protection for carbon fiber composites", *Carbon*, v. 27, 5, 709-715 (1989).
27. A. Joshi, J.S. Lee, "Microstructure and properties of protective coatings and carbon processed by fused slurry method", 39<sup>th</sup> International SAMPE Symposium, April (1994).
28. D.W. McKee, C.L. Spiro, E.J. Lamby, "The inhibition of graphite oxidation by phosphorous additives", *Carbon*, v. 22, 3, 285-290 (1984).
29. J.N. Stuecker, D.A. Hirshfeld, D.S. Martin, "Oxidation protection of carbon-carbon composites by sol-gel ceramic coatings", *Journal of Materials Science*, 34, 5443-5447 (1999).
30. H. D. Batha, C.R. Rowe, "Structurally reinforced carbon-carbon composites", Engineered Materials Handbook, v.1, Composites, ASM International, Metals Park, OH, 922-924 (1987).



31. H.S. Hu, A. Joshi, J.S. Lee, "Microstructural evaluations of Si-Hf-Cr fused slurry coating on graphite for oxidation protection", *J. Vac. Sci. Technol.* A9, 3, 1535-1938 (1991).
32. J.L. Smialek, "Processing of fused silicide coatings for carbon-based materials", Proc. of 7<sup>th</sup> annual Conf. on Composites & Advanced Ceramics Materials, 757-783 (1983).
33. F.F. Lange, "Healing of surface cracks in ceramics", Proc. Symposium Science of Ceramics Machining and Surface Finishing, 233-236 (1970).
34. J. Th. M. De Hosson, "Laser synthesis and properties of ceramics", in Intermetallic and Ceramic Coatings, Eds. N.B. Dahotre and T.S. Sudarshan, (Marcel Dekker, 1999).
35. F.C.J. Fellowes, W.M. Steen, K.S. Coley, *Eng. Matter.*, 46-47 (1990).
36. R. Govindarajuand and J.A. Ramos, "Development of laser fusion coatings for improving oxidation resistance of carbon-carbon composites", 46<sup>th</sup> International SAMPE Symposium, April 2001.
37. L. Snell, A. Nelson, P. Molian, "A novel laser technique for oxidation-resistant coating of carbon-carbon composite", *Carbon*, v. 39, n 7, 991-999 (2001).
38. J.W. Hutchinson, Z. Suo, "Mixed mode cracking in layered materials", in Advances in Applied Mechanics, (Academic Press, 1992).
39. T. Young, *Philosophical Transactions of The Royal Society of London*, 95, 65 (1805).
40. X.B. Zhou and J.Th.M. De Hosson, "Influence of surface roughness on the wetting angle", *J. Matter. Res.*, v.10, 8, 1984-1992 (1995).
41. K. Landry and N. Eustathopoulos, *Acta. Matter.* v.44, No 10, 3923-3932.
42. J.C. Ambrose, M.G. Nicholas and A.M. Stoneham, *Acta. Metall. Mater.* 40, 2483 (1992).

43. R. Voitovitch, A. Mortesen, F. Hodaj and N. Eutathoupoulos, *Acta Mater.* v.47 1117-1128 (1999).
44. X.B. Zhou, "Reaction coatings on metals by laser processing – a study on interface structures and wetting phenomena", Ph.D. Dissertation Thesis, University of Groningen, The Netherlands, October 1995.
45. M.F. Ashby, Materials Selection in Mechanical Design, (Butterworth Heinemann, 1992).
46. N. Noda, R.B. Hetnarski and Y. Tanigawa, Thermal Stresses, (Lastran, 2000).
47. R.C. Rossi, *Ceram. Bull.* 48(7), 736, (1969).
48. D. Burgreen, Elements of Thermal Stress Analysis, (C.P. Press, 1971).
49. R.W. Hertzberg, Deformation and Fracture Mechanics of Engineering Materials, 4<sup>th</sup> ed., (Wiley, 1996).
50. B. Lawn, Fracture of Brittle Solids, 2<sup>o</sup> ed., (Cambridge, 1998).
51. D. Green, An introduction to Mechanical Properties of Ceramics, (Cambridge 1998).
52. N. Özisik, Heat Conduction, 2<sup>nd</sup> ed., (John Willey, 1993).
53. A.G. Evans, M.D. Drory, M.S. Hu, "The cracking and decohesion of thin films, *J. Matter. Res.* 3, 1043-1049 (1988).
54. X.B. Zhou and J.Th.M.De Hosson, *Acta Metall.*, 39, 226, (1991).
55. M.F. Kanninen, Advanced Fracture Mechanics, (Oxford University Press, 1985).
56. J. Dundurs, *Journal of Applied Mechanics*, 36, 650 (1968).
57. J. R. Rice, *Journal of Applied Mechanics*, 55, 98 (1988).
58. D. Kovar, private communication.
59. H.V. Johnson, US Pat. 1,948,382 (February 20,1934).
60. A. Joshi L.S. Lee, US Pat. 5,554,390 (September 10, 1996).

61. J.C. Bailar, H.J. Emeleus, R. Nyholm and A.F. Trotman-Dickenson, Eds., Comprehensive Inorganic Chemistry, v.3, (Elmsford, N. Y., 1973).
62. A. Joshi, L.S. Lee, “ Coatings with particulate dispersions for high temperature oxidation protection of carbon and C/C composites”, *Composites - Part A: Applied Science and Manufacturing*, v. 28, No 2, 181-189 (1997).
63. P. G. Shewmon, Diffusion in Solids, (TMS, 1990).
64. P. Villars, A. Prince, H. Okamoto, Hand book of Ternary Alloy Phase Diagrams, v.7, (ASM, 1995).
65. ThermoCalc™ Software AB.
66. J.H. Westbrook, Ed., Moffatt's Handbook of Binary Phase Diagrams, (Genium Publishing Corp., 1997).
67. M.W. Barsoum, Fundamental of Ceramics, (McGraw Hill, 1997).
68. N.B. Dahotre, Lasers in Surface Engineering: Surface Engineering Series, v. 1, (ASM International, 1999).
69. Ø. Grong, Metallurgical Modelling of Welding, Materials Modelling Series, (The Institute of Materials, 1994).
70. D.A. Porter and K.E. Easterling, Phase Transformations in Metals and Alloys, 2<sup>nd</sup> ed., (Chapman & Hall, 1992).
71. M. McLean, Directionally Solidified Materials for High Temperature Service, (The Metals Society, London 1983).

## **CHAPTER III. EXPERIMENTAL**

The experimental hardware and procedures used in the different laser based surface processes described in previous chapters are detailed here. The characterization techniques employed to analyze the resulting modified surfaces, coatings and deposits are also explained in this Chapter.

### **3.1 DESCRIPTION OF THE LASER PROCESSING HARDWARE**

The laser processing hardware available for the different research projects consisted of two laser-based high temperature workstations that were previously designed and built by the Laser Freeform Fabrication team [1]. One workstation included a high power CO<sub>2</sub> laser while the second one had a Nd:YAG laser source incorporated. These machines were built with the capabilities for direct multi-layer and single-layer selective laser sintering of high melting point metallic powders, respectively. Nonetheless, this present research demonstrated the flexibility of these systems to process different materials with different surface geometries with minor modifications to the systems.

### 3.1.1 CO<sub>2</sub> laser based processing apparatus

Experiments involving laser polishing of metals and coatings of C/C composites were carried out using an axial-flow high power CO<sub>2</sub> laser (Convergent Energy) located at the Pickle Research Campus of The University of Texas at Austin. Figure 3.1 shows an image of the laser processing apparatus.

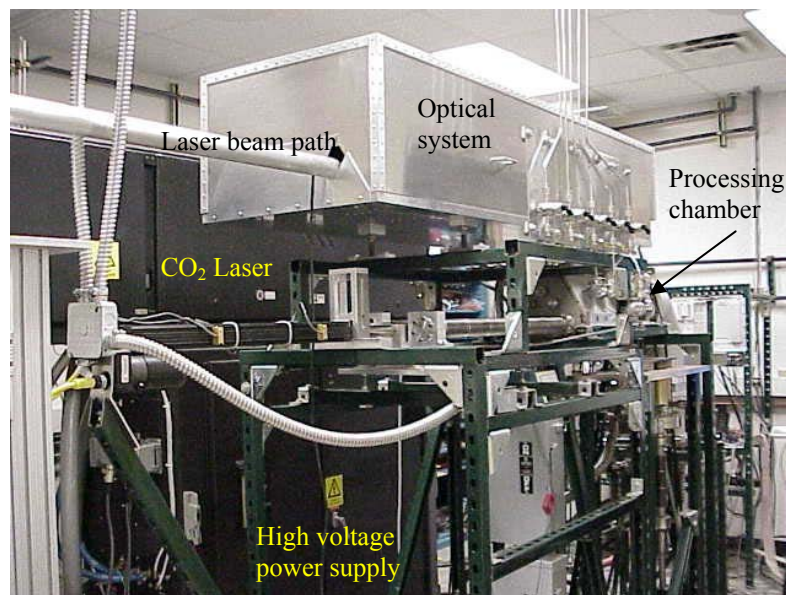


Figure 3.1. Overall view of the 1.4 kW c.w. CO<sub>2</sub> laser processing equipment.

Figure 3.2 shows a close up image of the open processing chamber, which allows introducing of motion devices to increase the degrees of freedom and thus to increase the processing flexibility of the system. The laser-processing zone is located over the right elevating piston. An observation window allows acquiring IR and color light images.

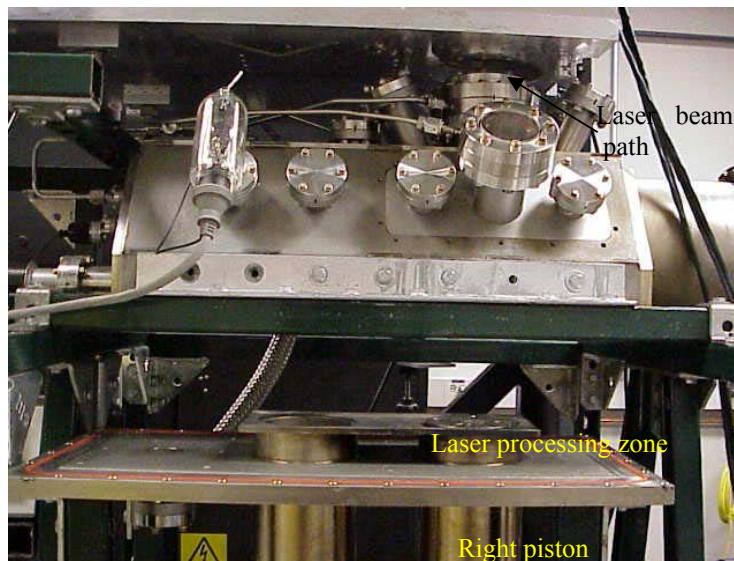


Figure 3.2. Close up view of the processing chamber.

The nominal power level of the axial flow CO<sub>2</sub> laser is 1.4 kW having a beam with TEM<sub>00</sub> mode; however, the maximum power measured at the rear mirror (RM) of the resonator cavity was 1.25 kW. The laser beam is delivered to a telescope, expansor-focusing optical system (Laser Power Optics), by means of a sealed U-shape channel consisting of a 10 cm diameter aluminum tube. There are 3 reflecting mirrors at 45° angle along the path of the beam, so that the losses by absorption of these bring down the maximum power before the telescope (BT) to 970 W as measured by an external power meter device (Coherent General Inc.). After the telescope (AT) the laser beam power is further reduced to 880 W. Because the beam is reflected by the two scanning mirrors and then crosses an approximately 5 mm thick ZnSe window an additional 10% loss must be

accounted for in order to estimate the real laser power impinging at the focal plane. This gave a maximum of 800 W at the work piece (WP) focused with a minimum spot diameter of  $0.35 \pm 0.05$  mm. Thus the maximum power density achievable in this system was  $8.32 \times 10^5$  W/cm<sup>2</sup>. The spot diameter was determined by burning several holes over an acrylic sheet, each time offsetting the z-position of the right piston. The z-coordinate for the minimum diameter hole corresponded to the focal height, and it occurred at 5 mm from the top of the piston cylinder.

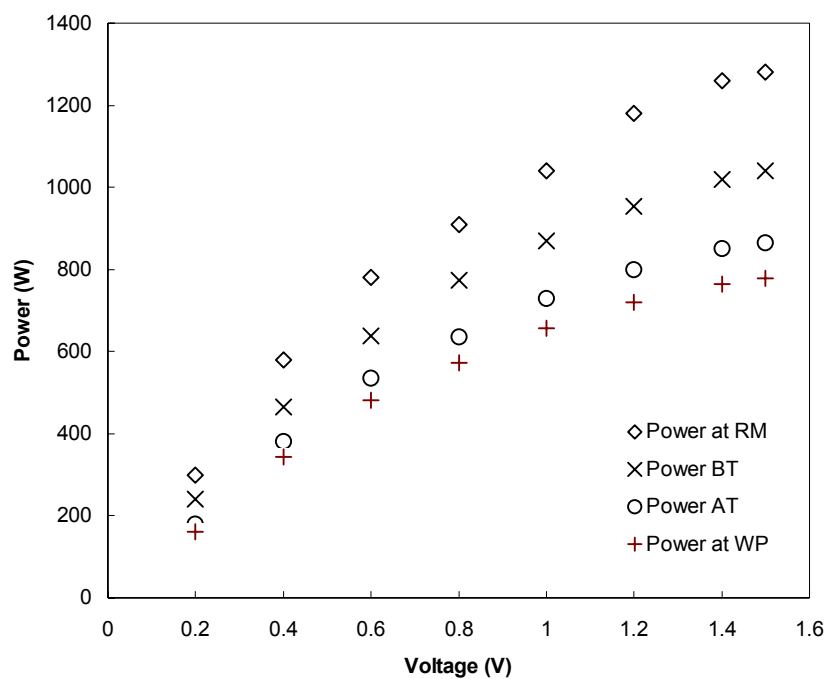


Figure 3.3. Calibration curve for CO<sub>2</sub> laser power versus input voltage.

The power output level is controlled by a computer by feeding a voltage signal through a DAQ board (National Instruments) to the laser power supply unit. In Figure 3.3, a plot of the measured power level, at different positions along the beam path, for different input voltages is shown.

The raster scanning motion of this system is provided by a dedicated controller (General Scanning Inc.) that is interfaced through a computer to the galvanometers (General Scanning Inc.) that drive the motion of the mirrors; the scan speed ranges from 0.12 to 660 mm/s. Determination of the scan speed is obtained by two parameters: the scan step (ss) and the scan period (sp); these are fed to the controller via software running in the computer. The scan speed,  $V_s$ , should be proportional to the quotient of ss and sp, the proportionality constant, k, depending on the distance between the center of the scanning mirrors and the processing surface. However, it was noticed that k also changed with the value of the sp parameter for a high ss number of 760. In Figure 3.4, a plot of the scan speed versus the sp number for a ss number of 760 is presented and a scan density of 2000 lines/inch. It can be seen that the trend of the plot follows a negative power law. The proportionality constant, k, is plotted on the same graph and it can be observed that it increases logarithmically with the sp number.



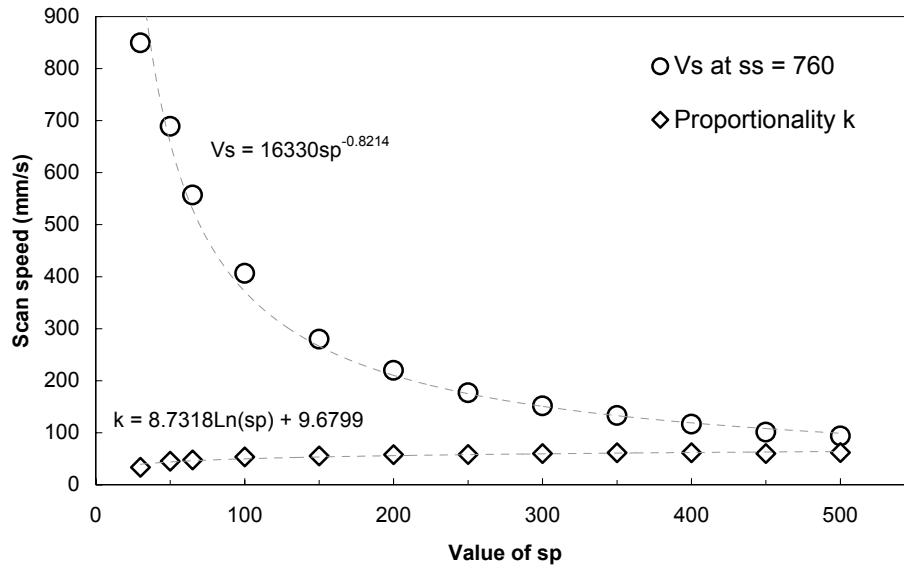


Figure 3.4. Calibration scan speed versus value of sp parameter at ss = 760.

The processing chamber can be brought down to a maximum rough vacuum level of  $10^{-2}$  Torr by means of a two stage mechanical pump. The calibration curve for the vacuum level as a function of time is shown in Figure 3.5. If further vacuum reduction is required a diffusion pump (operating with silicon oil) can be activated to achieve vacuum levels of up to  $10^{-6}$  Torr after a few hours.

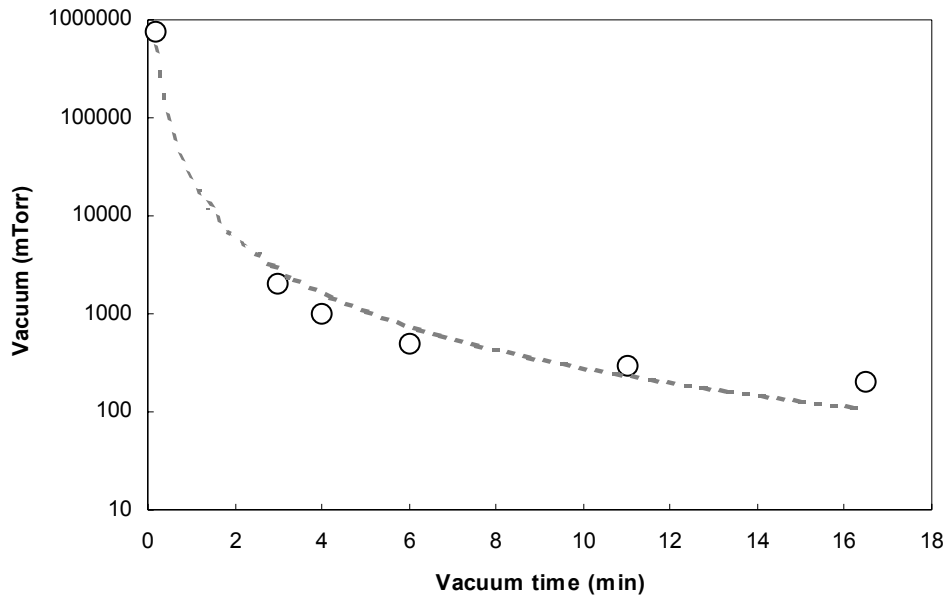


Figure 3.5. Calibration curve for rough vacuum versus time.

More detailed information about this apparatus, concerning the optical delivery system, control of scanning mirrors, z-positioning system and high vacuum capabilities can be further found in Suman Das' dissertation [1].

### 3.1.2 Nd: YAG laser based processing apparatus.

Direct laser fabrication of single-layer MAR-M 247 deposits on Inconel 718 flat substrates was explored using the Nd:YAG laser based processing apparatus located at the Department of Mechanical Engineering of the University of Texas at Austin and shown in Figure 3.6. This high temperature workstation

consists of a processing chamber that can reach vacuum levels of  $10^{-6}$  Torr by means of a mechanical pump and a diffusion pump. Additionally, it has radiation heating capabilities by a means of serpentine shaped molybdenum heating element that can withstand up to 80 amps of direct current. The temperature at the processing zone can reach up to 800°C. Gas can be purged inside the chamber to provide specific atmospheric control. The laser power level and the motion of the galvanometer scanning mirrors are controlled by a personal computer through a DAQ board (National Instruments). The laser head (U.S. Lasers) can generate up to 250 W in continuous wave mode and up to 125 W average power in pulsed mode, operated by a acousto-optic Q-switch with frequencies of up to 10 kHz and pulse length of 100 ns. The optical system consists of a beam expander-collimator, a fused silica convex focusing length, galvanometer driven mirrors and a fused silica window. A beam spot of approximately 0.25 mm  $\pm$  0.05 mm can be obtained. The maximum power density of this system corresponds to  $5.1 \times 10^{-5}$  W/cm<sup>2</sup>. By adding a similar laser head in series with the former one, up to 400 W of power can be generated; however, the beam spot width increases by more than twofold due to the presence of multi-mode structures in the beam.

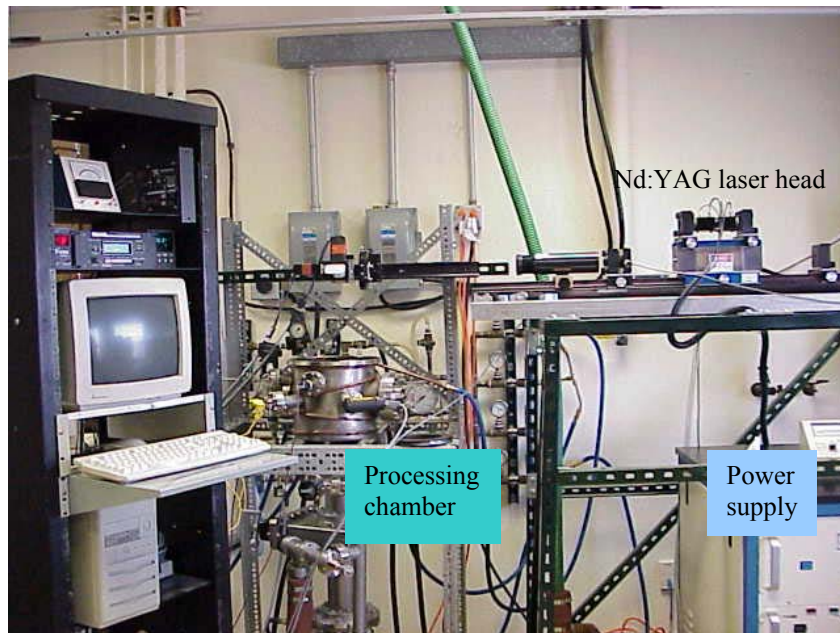


Figure 3.6. Overall view of the 250W Nd:YAG laser processing apparatus.

More information on this apparatus, regarding the optical delivery system, open loop and close loop control of laser power, scanning mirrors, in-situ temperature measurements and vacuum capabilities can be further found in Danyo, Murphy and Ahn dissertations [2,3,4].

### **3.2 LASER POLISHING OF INDIRECT-SLS METAL SURFACES**

This project was funded by the Office of Naval Research (ONR) and done together with collaborators in the Department of Mechanical Engineering of the University of Texas at Austin. In this work, the CO<sub>2</sub> laser was operated in continuous wave (c.w.) mode to polish surfaces of 420 stainless steel-40 wt.%

bronze indirect-SLS parts. Figure 3.7 shows a schematic drawing of the laser polishing process. The focused laser beam is rastered over the surface with an average scan speed along the y-axis (fast direction) and an average traveling speed along the x-axis (slow direction).

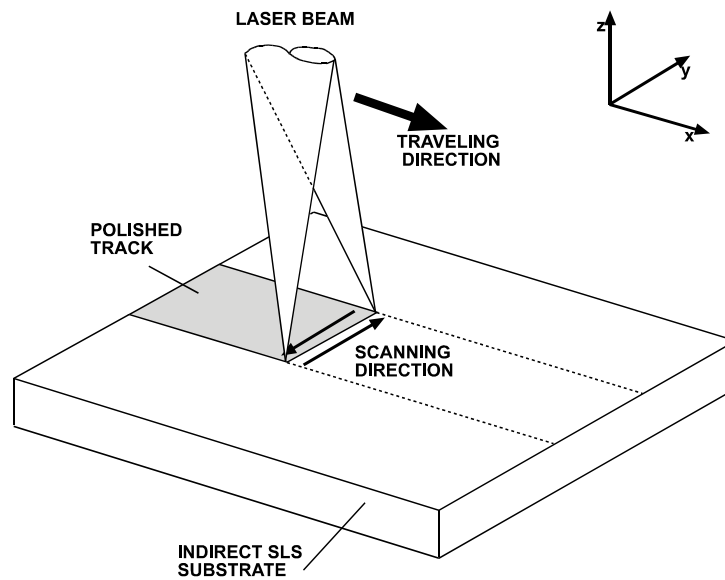


Figure 3.7. Schematic of the laser polishing process.

Four rectangular slabs (50.8 mm long x 25.4 mm wide x 12.7 mm thick) made from a material process development called LaserForm<sup>TM</sup> ST-100 (3D Systems, Inc.) were used as specimens. The slabs consisted of 420 stainless steel powder mixed with a 2 wt.% polymer binder. They were shaped into a green pre-form by means of selective laser sintering (SLS). The pre-form was buried in alumina powder and was placed inside a N<sub>2</sub> atmosphere furnace to burn off the

binder and proceed with a 40 wt.% bronze (5-10 wt.% Sn) infiltration of the part. This material system is aimed towards tool making for the injection molding industry. A recent industrial application of this process is described in Reference 5.

### **3.2.1 Surface roughness measurements**

The arithmetic surface roughness,  $R_a$ , value was employed to quantify the surface roughness of the as-received sample surfaces before and after laser polishing. This was done using a surface profile measurement system, model Dektak<sup>3</sup> (Veeco Metrology Group). It consists of a stylus tip of radius 12.5 microns that moves over the surface of interest in a straight line. The stylus is free to move in the z-direction up and down thus recording the topography of the surface within a resolution determined by the tip radius. More technical details can be found in Reference 6.

The measurement procedure in general consisted in running the surface profilometer along parallel tracks spaced every 4 mm approximately over the surface of each specimen. For each single track the  $R_a$  value was recorded and then an average was obtained among all the measured tracks. Surface roughness results of the as-received specimen before laser polishing are not vastly affected by the orientation of the profile line measurements as demonstrated by Lappo *et*

*al.* [7]. Because the sample surfaces are not exactly flat and possess curved or tilted regions (i.e., low frequency topographical features) distributed in different zone, the surface roughness value due to the real microscopy features (i.e., high frequency topographical features) can be altered if these low frequency features are considered when computing the  $R_a$  value. As these low frequency features vary randomly in degree of curvature and tilt angle, it is not appropriate to set up a cut off filter level to remove them, as some high frequency features components can be eliminated as well, underestimating the  $R_a$  value.

To solve this problem, the author decided that each profiled surface track should be inspected independently by broking it down into segments in which the variation in the  $R_a$  value is within bounds (i.e., +/- half average powder size). The  $R_a$  value of each segment is then weighted according to the length of the segment and in this manner a new and lower value of  $R_a$  is found. In cases in which a segment is short in length and shows large topographical discontinuities, it is immediately discarded from the measurement, as these features are not related to the microscopic surface roughness. Figure 3.8 illustrates the segment analysis of a surface profiled track.

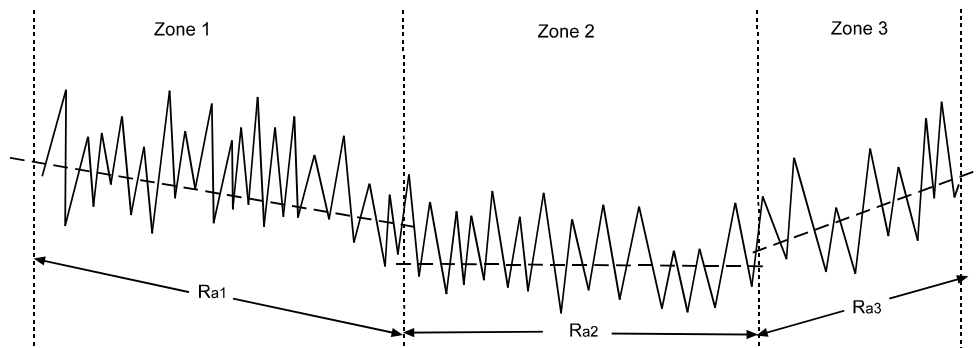


Figure 3.8. Schematic of segment analysis of a surface profiled track.

### 3.2.2 Laser polishing methodology

The aforementioned CO<sub>2</sub> laser unit was used in c.w. to laser polish thin tracks (i.e., 1.905 mm wide) on the surface of the samples along their width. The laser power used corresponded to 220 W, 334 W, 420 W and 565W and the spot beam diameter of the laser beam accounted for 0.35 $\pm$ 0.05 mm. Galvanometer driven mirrors provided laser beam speeds of up to 849 mm/s in the scan direction and 5.7 mm/s in the traveling direction with a scan density of 2000 raster-lines per inch. Each specimen was placed inside the processing chamber over the right piston and then elevated, so that the surface of the specimen matched the focal position of the beam. The chamber was sealed and evacuated down to 0.2 Torr and then back filled with an argon (industrial purity) gas up to 2 Torr. The tracks were spaced out every 5 mm and time intervals of approximately 5 minutes were allowed in between tracks for temperature field homogenization and cooling of the sample.



### 3.2.3 Surface profilometry at the laser polished tracks

After the samples were laser treated, the surface roughness at the laser polished tracks was measured following the description given in 3.2.1. In this case, parallel profiles tracks were run along the length of the laser polished track so that the width was profiled in six equidistant locations as indicated in Figure 3.9. At the each side of a polished track, where the as-received surface had not been modified, the surface was profiled once. This was done so that a better value of the local as-received surface roughness was available. The right and left side measurements were then averaged and used to normalize the resulting polished track,  $R_a$ , value thus obtaining a percent  $R_a$  variation ( $\%R_aV$ ).

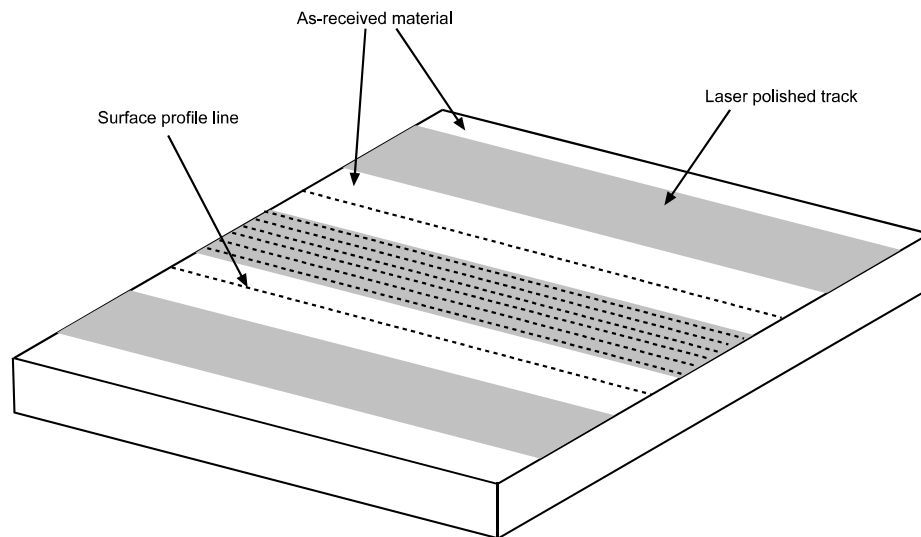


Figure 3.9. Distribution of profile measurements across polished tracks.

### **3.2.4 SEM and EDAX analysis of polished specimens**

The surface topography of the as-received specimens before and after laser polishing was examined under the scanning electron microscope (SEM) at high magnification with the purpose of observing the different topographical features that formed depending on power level and scan speed used. Semi-quantitative energy dispersive analysis of x-rays (EDAX) of these surface features was also performed to determine how the elemental distribution changed and how oxygen and other sources of contamination affected the surface morphology. For this purpose the surfaces were cleaned with de-ionized water followed by squirting over acetone and drying them with an air blower.

Cross sectioning of some of the laser polished specimens was done. The cut pieces were hot mounted in polymer resin and then coarse and fine ground in four stages. They were then polished with 6 and 15  $\mu\text{m}$  diamond suspension media and finally in a 0.25  $\mu\text{m}$  alumina polished stage in de-ionized water. The main purpose was to observe the solidification modes occurring near the surface as well as the elemental distribution of the surface and bulk of the specimen before and after processing. No etching was required for observation under SEM as the atomic contrast between the main elements (Fe and Cu) was sufficient for distinguishing them clearly.

### **3.2.5 X-ray diffraction analysis**

X-ray diffraction analysis using  $\text{CuK}_\alpha$  radiation was performed on a as-received specimen surface before being laser processed. No XRD analysis was done on polished tracks as it must be taken into consideration that the penetration of the x-rays can penetrate up to several mm from the surface, thus picking up considerable information from the unaltered bulk. Moreover, the laser polished tracks were not greater than 2 mm, making it difficult to pick exclusively information from the modified surface but also from the un-modified one.

### **3.3 COATING CYLINDRICAL C/C COMPOSITES BY “LASER INDUCED CEMENTATION”**

This project was funded and carried out with collaboration from Karta Technologies Inc., San Antonio, Texas, through a Small Business Innovation Research (SBIR Phase II) grant offered by the Missile Defense Organization (MDO) and administered by the U.S. Air Force.

In this research, the  $\text{CO}_2$  laser processing apparatus previously described in Section 3.1 was utilized; the galvanometer driven rotating mirrors provided adequate scanning rate and percentage of laser beam overlap. The cylindrical coating specimen was subjected to a rectangular heat source rather than a single moving spot. Infrared thermal mapping of the surface confirmed observation of

this rectangular heat distribution (refer to Chapter II section 2.1.2), which favors uniform and continuous coatings. These were carried out inside of the processing chamber under rough vacuum (i.e., 0.2 Torr) and then back-filled with argon gas. The slurry coated cylindrical specimen was rotated several times along its longitudinal axis while the laser beam is raster scanned to form a stationary, narrow and elongated rectangle over the length of the sample. This latter process was coined “Laser induced cementation” due to its resemblance to the pack cementation technique in which the specimen is covered by a powder mixture, packed in a crucible to be then heat treated [8]. Packing of the powder in this case was not done mechanically, but obtained by the capillary pressure exerted on the powder during drying of the alcohol based slurry. Moreover, when chloride salts are present in the slurry an oxidation reaction [9] packs the coating further.

### **3.3.1 Laser coating methodology**

A total of 74 cylindrical specimens were laser induced cementation processed. These consisted in cylindrical rounded tip 3D structural C/C composite samples machined at Karta Technologies Inc. from stock material provided by BF-Goodrich (Santa Fe Springs, CA) and C-CAT Corp. (Dallas, TX). The slurries applied onto the cylindrical specimens consisted of the following compositions in weight %:

- a) Ductile bond layer: 60Cr-40CrCl<sub>3</sub>, 50Cr-50CrCl<sub>3</sub> or 40Cr-60CrCl<sub>3</sub>
- b) Compliant diffusion barrier layer: 70Si-25Cr-5C, 65Si-25Cr-5CrCl<sub>3</sub>-5C  
or 65Si-30Cr-5C
- c) Erosion diffusion layer: 70Si-15Cr-15HfCl<sub>4</sub>

These were prepared from finely ground powders supplied by Aldrich Chemicals and Alfa-Aesar. Silicon and chromium powders had a mesh –325 particle size while graphite had a 1 to 2 μm diameter particle size. The hydrous chromium chloride salt used had a stoichiometry of [Cr(H<sub>2</sub>O)<sub>4</sub>Cl<sub>2</sub>]Cl·2H<sub>2</sub>O. The powders were weighed to the required proportions and then mixed up by grinding them using a mortar with isopropyl alcohol medium for at least 15 minutes. It was observed that the addition of metal chlorides, specifically chromium, into the slurry induced a chemical reaction with the OH<sup>-</sup> groups in the alcohol providing a molecular bridging network (i.e., gelation), increasing the viscosity and adherence of the slurry to the substrate once it has dried.

The cylindrical 3D C/C composite specimens were cleaned with acetone to remove contaminants from the surface before applying the slurry coating. The latter was deposited manually over the surface of the composite by means of a spatula or by an air-spraying technique. In both cases, the specimen was rotated mechanically as the slurry was being applied. The amount of coating mass (ACM)

deposited on the specimen before the laser process and the amount of coating mass remaining after the laser process (CMR) was recorded to determine its effects on the coating integrity and thickness. To avoid rupturing of the coating on weighing, the specimen was held vertically on a stand. Figure 3.10 illustrates the air-spray painting set up used to deposit the slurry coating onto the cylindrical samples. Figure 3.11 shows a full coverage and smooth air-sprayed coating over a cylindrical specimen.



Figure 3.10. Spray painting of cylindrical sample using a Badger™ air-spraying gun.

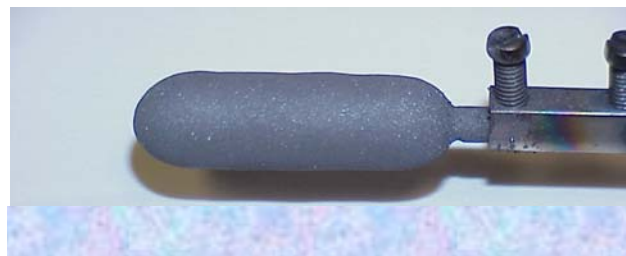


Figure 3.11. Sample #37 after the Si-40Cr slurry was air-spray coated.

The coated specimen was then located inside a rotating holder device designed by the author and collaborators and fabricated at Karta Technologies, Inc. The device was placed inside the right piston in the processing chamber. The specimen was elevated at the focal position (i.e. 0.4 mm) while suspended from one of its ends in horizontal position. The angular speed of the rotating device was then set from a voltmeter so that one complete revolution of the cylinder was done in a determined amount of time (i.e., 40 to 180 seconds) depending on the processing stage requirement. The scanning trajectory of the focused laser beam was programmed so that the beam scanned back and forth along the major axis of the cylinder over a narrow fringe of dimensions 25 mm x 0.6 mm using a geometric file with up to 4000 scanning lines/inch. This corresponded to an overlap of 99.96%. The laser beam was scanned over the specimen the same amount of time the cylindrical specimen was rotated.

Figure 3.12 illustrates the set up developed to carry out the laser induced cementation process. The coated cylindrical specimen rotated suspended from a narrow stem while the focused laser beam raster-scanned back and forth along the longitudinal length of the cylinder.

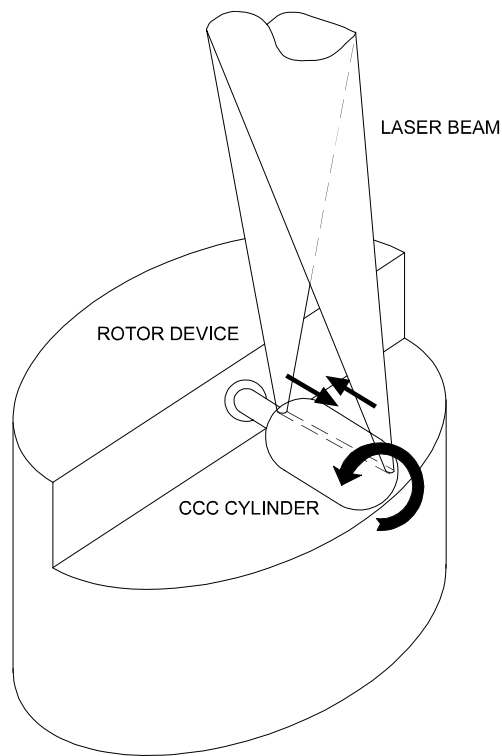


Figure 3.12. Schematic drawing of the “Laser Induced Cementation” process.

The processing chamber was vacuumed to approximately 0.1 Torr vacuum, and then purged with argon gas up to 2 Torr. A direct shroud argon gas delivery was applied over the samples by means of an annular tube ring placed on top of the sample holder. The raster-scan system was started at a given scan speed and the laser beam power was ramped up slowly to prevent scribing the sample surface. The laser raster-scan schedule consisted of 5 stages:



1. Pre-heating stage: 30-60-90 seconds scan time, no cylinder rotation, low power level to raise the temperature of the cylinder slowly and avoid detachment of coating.
2. Sintering stage: 80 to 160 seconds scan-time, i.e., one full cylinder turn, power was ramped up from low to intermediate power level to avoid thermal shock at the coating surface and minimize coating removal by sudden evaporation. Cylinder begins to glow.
3. Pre-melting stage: 60 seconds scan time, cylinder rotation, power ramp from low to intermediate level. Cylinder glows completely.
4. Melting stage: 85-165-255 seconds scan time, one full cylinder turn (+90 sec), power ramp from intermediate to high power. Intense glowing of cylinder.
5. Cooling stage: 85 to 165 seconds scan time, one full cylinder turn, power is ramped down slowly to reduce surface temperature and prevent crack formation due to thermal shock on cooling.

Figures 3.13a to 3.13c shows images of the pre-heating stage, pre-melting state and melting stages of the coating process done on a cylindrical sample.

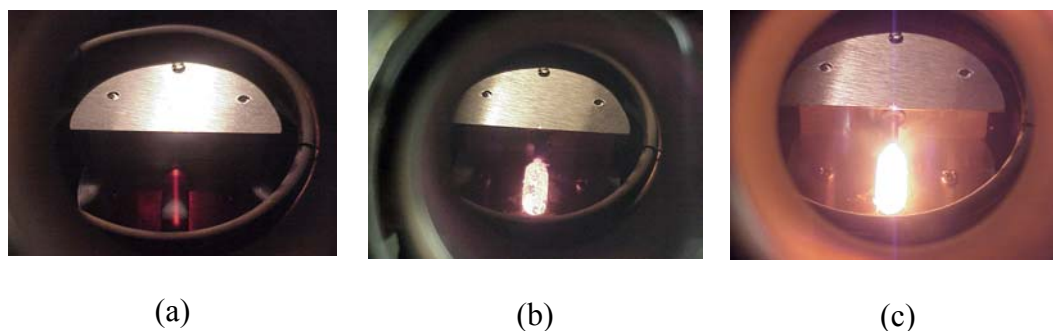


Figure 3.13. Sequence of images of Sample #47 being laser induced cemented.

### 3.3.2 Glass sealant coating methodology

Silicon dioxide modified glass type slurry was applied to some of the cylindrical specimens that were previously coated with the ceramo-refractory material described in Section 3.3.1. Specifically, the glass consisted of 50 wt.%  $\text{SiO}_2$  -325 mesh (99.5 % pure from CERAC) and 50 wt.%  $\text{Na}_2\text{CO}_3$  (anhydrous sodium carbonate from Fisher Scientific) fine mesh powders mixed in sodium silicate solution (14 vol.%  $\text{NaOH}$  – 27 vol.%  $\text{SiO}_2$  balance  $\text{H}_2\text{O}$ ) to form a sticky paste. The paste was applied manually over the coated cylinders as these were rotated mechanically. This process was tedious as the viscosity of the paste was initially low and it flowed easily. It took several minutes for moisture to evaporate thus increasing the viscosity. The specimen was first fired in a tube furnace under argon atmosphere at a temperature of 200 °C to remove moisture and decompose

the carbonate compound. A thick white porous crust was formed over the cylinder. Then the temperature was slowly raised up to 950 °C and it was held at that temperature for 30 minutes. The combination of silica and soda allowed formation of a translucent vitreous compound with low glass transition temperature (400°C) and yet high melting point (1100°C). Moreover, this glass showed low viscosity at temperatures above the melting point.

### **3.3.3 Weight loss testing to determine oxidation resistance**

After the coating process was done the stem of the specimen was cut off using a diamond saw cutter and that side was recoated with alumina cement to prevent direct exposure of the C/C to the air. Oxidation behavior of the coated and uncoated samples was evaluated by heating samples to 1000°C in a tube furnace in still air atmosphere and under an air-flow of 2ft<sup>3</sup>/hr in some cases as shown in Figure 3.14. The front rounded tip edge of the samples was also coated with alumina cement to prevent direct exposure of the C/C to the air. The samples were removed from the furnace at intervals of 30 to 90 minutes, followed by weighing until the failure of the coated specimen. A 15 minutes removal and reinsertion time was allowed for each weight measurement to prevent thermal shock on cooling and heating.



Figure 3.14. Horizontal furnace operating at 1000 °C under direct air with a coated cylindrical sample being weighted loss tested.

Simultaneously some specimens were weight loss tested at the Wright Patterson Air Force facility using a dedicated Thermo Gravimetric Analyzer that can hold the size of the cylinder. This machine allows a continuous weight measurement during the total testing time minimizing the thermal shock on heating and cooling.

#### **3.3.4 Light optical microscopy, SEM and EDAX analysis of coated specimens**

The coated specimens were cut across the longitudinal direction and hot mounted in polymeric resin. The mounted samples were subjected to 2 coarse grinding and 2 fine grinding stages followed by 2 micron diamond paste and 0.25 micron alumina polishing. A Zeiss Axiovert 405 M light optical microscope and LEO 1530 and JEOL JSM 5610 scanning electron microscopes were used to

characterize the microstructural features of the surface and cross sectional interface regions at low and high magnification, respectively. Microchemical analysis of the coating and coating/substrate interface region was conducted by using the electron microprobe and energy dispersive x-ray analysis (EDAX). No etching was necessary as good contrast of the coating phase was obtained under both light optical microscope and SEM. In the latter, the high atomic number difference among the coating elements provided good image contrast, being lighter for the heavy elements like hafnium and darker for the lighter ones such as carbon. Ceramic materials are difficult to etch due to their chemical resistance.

### **3.3.5 X-ray diffraction analysis**

Some XRD analysis using  $\text{CuK}\alpha$  radiation was performed directly on the coated cylindrical surface. The fact that it was not a flat surface is not critical for the accuracy of the results obtained. The powder mixture used for the slurry preparation was also employed to obtain XRD information. Pellets (3 mm diameter x 5 mm high) were made by pressing the powder contained inside a cylindrical die, and the pellets were then fired up to 875°C at a rate of 10 °C/min. These sintered pellets were then crushed into fine powder after being ground in mortar for 30 minutes. A small amount of fine powder was spread over a glass mount mixed with 3 drops of aromatic liquid and then allowed to dry. X-rays

diffraction analysis allowed determination of phases by matching diffraction peaks with available patterns for the possible compounds formed from the elements present in the coating. The fact that the coating thickness was of the order of 250  $\mu\text{m}$  made the penetration of the x-rays to reach down to the C/C substrate and give a strong C peak. Because the coating was rich in Si, this element could be used as the standard for calibrating peak shifts.

### **3.3.6 Indentation crack measurement for fracture toughness determination**

The thickness of the coating material delaminated from laser coated C/C composites flat surfaces was measured using a surface profilometer (see Section 3.5). The coating was cold mounted in epoxy resin and then was coarse and fine ground and finally polished with 0.25  $\mu\text{m}$  alumina in de-ionized water. A Tukon micro-hardness tester with a Vickers pyramidal indenter was used to indent the polished surface of the mounted coating. The loads used ranged from 10 to 30 Newtons, and the time of indentation was 15 seconds.

After one indentation was done, the size of the diagonals,  $d_1$  and  $d_2$ , were measured by the optical scale provided in the equipment. A Vickers hardness value (HV) was obtained from the load used and the arithmetic average of the measured diagonals. Simultaneously, the radial crack extensions that emanated from each vertex of the indenter's impression were also measured approximately

using the optical scale. In this manner an average length of the radial crack,  $C_I$ , could be obtained and used to estimate the mode I critical fracture toughness of the thin brittle coatings. Figure 3.15 provides a schematical illustration of the indentation shape and location of radial cracks.

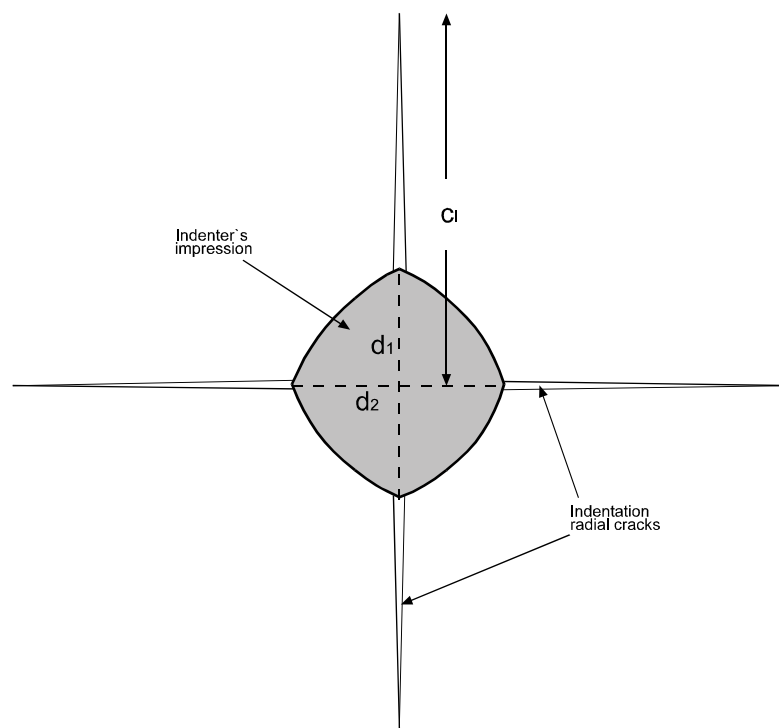


Figure 3.15. Schematic of an indenter impression and radial cracks formed.

The expression available to estimate the  $K_{IC}$  requires fitting of a non-dimensional constant,  $\xi$ . A thin coating of pure Si that was laser melted was used to measure the corresponding critical fracture toughness by the indentation

method. The constant was then obtained by making the analytical expression (Eq. 2.94) containing  $\xi_0$  equal to the literature value [10] given for the critical fracture toughness of silicon. The value of  $\xi_0$  was then fed back into the Eq. 2.94 with the indentation results for the coating material and thus a  $K_{IC}$  was obtained. More detailed information on how to perform the indentation crack measurement can be found on the ASTM standard C-1421.

### **3.3.7 Thermomechanical and differential thermal analysis**

Small cylindrical pellets (3 mm diameter x 5 mm high) were made using the same coating composition previously described in Section 3.3.1 but 2 wt. % of poly-vinyl- butyral-co-vinyl (PVB) binder was added. The mixed powders were pressed inside a steel die for a minute under a load of 1 ton/cm<sup>2</sup>. The pellets were fired in argon at 250 °C for one half hour to burn off the binder and remove chlorine gas from the decomposition of the metal salts. A Perkin-Elmer's Thermo Mechanical Analyzer (TMA) was used to obtain the thermal expansion of the pellet in the longitudinal direction under a range of temperatures of up to 875°C. This result allowed obtaining the coefficient of thermal expansion of the coating at each temperature interval by simply computing the slope of the thermal expansion versus temperature plot.



To determine the melting and solidifying points of the coating material and other possible phase transformation on heating and cooling, a small amount (approximately 5 mg) of pellet material was ground and introduced in the Differential Thermal Analyzer (DTA), which measured the change in temperature of the sample relative to an alumina standard. When a phase transformation takes place in the sample at a given temperature, it can be either exothermic or endothermic causing a positive or a negative change in the differential temperature, respectively. The coating material was tested up to a temperature of 1325 °C, which is slightly higher than the melting point of the coating mixtures.

### **3.4 “POWDER MASKING” TECHNIQUE FOR LASER DIRECTIONAL SOLIDIFICATION**

This project was funded and done in collaboration with Rolls-Royce North America, Indianapolis, Indiana, as well as the Department of Mechanical Engineering of the University of Texas at Austin.

In this research project the Nd:YAG laser equipped high temperature workstation was utilized, as it offers preheating capability of the processing zone up to 800°C. This is critical in this process, as it serves the twofold purpose of degassing the pre-placed powder as well as modifying the thermal gradient during solidification of a single layer being deposited.

The configuration of the mask-powder-substrate assembly used in this research is presented in Figure 3.16. Two pins were used to register each U-shaped mask, used to hold the powder in place, to the Mar-M 247 substrate plate.

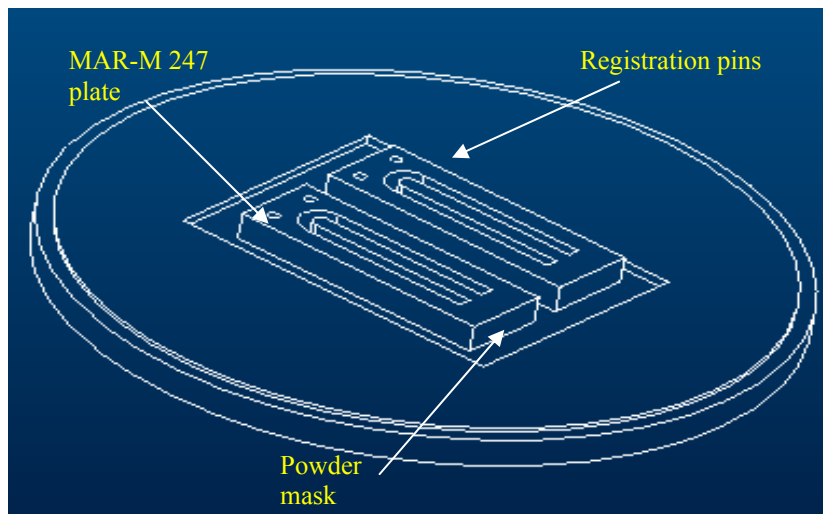


Figure 3.16. Schematic of how to register the powder masks to substrate (provided by J.Rajan).

A schematic of the laser melting process used in this work is illustrated in Figure 3.17. The laser beam raster scans back and forth laterally and travels along the mask trough, melting the entire powder depth and a small fraction of the substrate. As the melt pool advances its tail solidifies forming a sound metallurgical bond with the substrate.

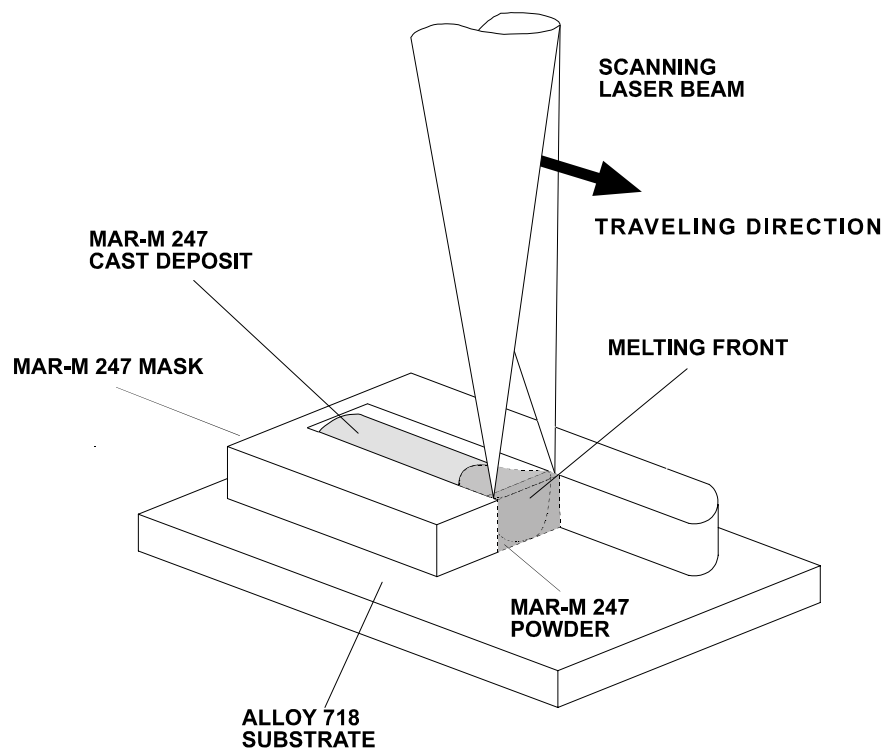


Figure 3.17. Overall schematics of the mask-powder-substrate arrangement during selective laser melting.

The substrate rests on top of a vertical wall placed immediately below the confined powder, as seen in Figure 3.18. This wall acts as one-directional heat sink so that heat extraction during the solidification is approximately one-dimensional along the z-direction enhancing solidification growth in the negative z-direction.

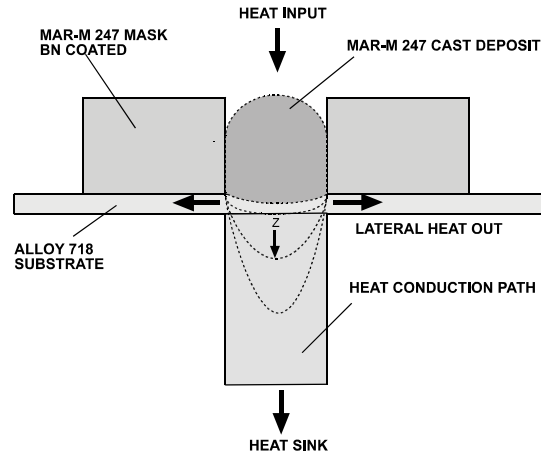


Figure 3.18. Cross-section schematic of the mask-powder-substrate arrangement indicating principal heat flow paths.

### 3.4.1 Sample preparation and process description

Sample preparation consisted of coating the 2 mm thick Mar-M 247 mask provided by Rolls Royce with boron nitride spray. The coated mask was then clamped to an Alloy 718 plate using a registration fixture designed by Murphy *et al.* and described in [3]. Mar-M 247 powder was mixed with isopropyl alcohol media to form a slurry that was deposited in the trough of the mask using a pipette and was allowed to dry. The mask-substrate registration fixture was then placed inside the processing chamber. A  $10^{-5}$  Torr vacuum was applied to the chamber before back filling with inert-reducing gas (argon - 4% hydrogen). Pre-heat by means of a radiant shield was applied to degas the powder before processing and to alter the thermal gradient in the liquid during the laser processing. The

Nd:YAG laser head was operated up to its maximum power (i.e., 250 W) in continuous mode and the laser beam was focused to a spot size of 0.25 mm. The laser beam was then raster scanned along the mask 2 mm wide trough at constant scan speed using approximately a scan density of 7000 lines/inch. The deposits were laid parallel to the rolling direction of the substrate plate.

Preliminary single-layer deposits trials were also performed on superalloy CMSX-4 5 mm thick directionally solidified plates. The deposits were laid along perpendicularly to the dendrites secondary arms.

The processes parameters used in all the single-layer deposits presented in Chapter IV Results and Discussion are included in Appendix B-III.

### **3.4.2 Characterization techniques**

After removing each mask from the corresponding substrate plate, the zone where the single layer deposits were present was sectioned across the longitudinal axis and hot mounted in polymeric resin. The mounted specimens were then fine and coarse ground using a sequence of 100, 200, 450 and 600 grit SiC paper, and then fine polished using 6 and 2  $\mu\text{m}$  size diamond suspension and 0.25 micron alumina in de-ionized water. Marble's reagent (50 vol.%  $\text{H}_2\text{O}$  + 50 vol.% HCl and 10 g  $\text{CuSO}_4$ ) was used to etch the specimens and reveal the microstructural features by dipping them in the etching solution for 30 to 60

seconds and then rinsing with running water and drying. Macro optical images were taken of the overall shape of the deposits. The resulting microstructure was observed using a Zeiss STEMI SV8 and a Zeiss Axiovert 405M light optical microscopes up to a magnification of 1000x.

### **3.5 ADDITIONAL LASER SURFACE ENGINEERING PROJECTS**

Other projects in which the author participated together with research collaborators were carried out using the CO<sub>2</sub> laser based high temperature station already described and a laser cladding facility located in Houston, Texas. These projects consisted of: Ni-Cr and TiC/TiC-Ni coatings of 347H stainless steel flat samples, Si-Cr-Hf-C coatings of thin flat C/C composites, casting of NiTi shape memory alloy rod-like structures by laser melting and laser cladding of C/C composite tubes. A brief experimental description of each project is presented to facilitate understanding and implementing future research that might be of a similar laser processing nature.

All but the last of these projects shared the same processing scheme; that is, the focused laser beam was raster scanned along a rectangular area, so that a pseudo-energy line source was moved over a pre-placed slurry coating. By altering the density of scan lines, the width and length of the scan pattern, the scan step and scan period multiple, combinations of scan speed and traveling speed

were achieved. Figures 1.1, 2.1 and 2.2 are schematic diagrams of these setups. In all these processes, the chamber was brought to a rough vacuum of approximately 0.2 Torr, and argon gas was then purged directly to the processing zone.

### **3.5.1 Coating of 347H stainless steel slab specimens**

The Cr-Ni coatings were done with collaborators from Karta Technologies Inc., San Antonio, Texas, while the TiC/TiC-Ni coatings were executed in conjunction with investigators from Kanpur Institute of Technology, Kanpur, India.

The specimens consisted of 347H annealed cold finished stainless steel slabs of size 50.8 mm x 12.7 mm x 6.35 mm. The composition of the steel in weight percent was: 17.30 Cr, 10.20 Ni, 1.65 Mn, 0.64 Si, 0.024 P, 0.020 S, 0.41 Mo, 0.31 Cu, 0.041 N, 0.63 Co, 0.63 CB + Ta, balance Fe.

Figure 3.19 illustrates an schematic diagram of the laser raster-scan configuration used over the TiC/TiC-Ni pre-coated 347H stainless steel surface.

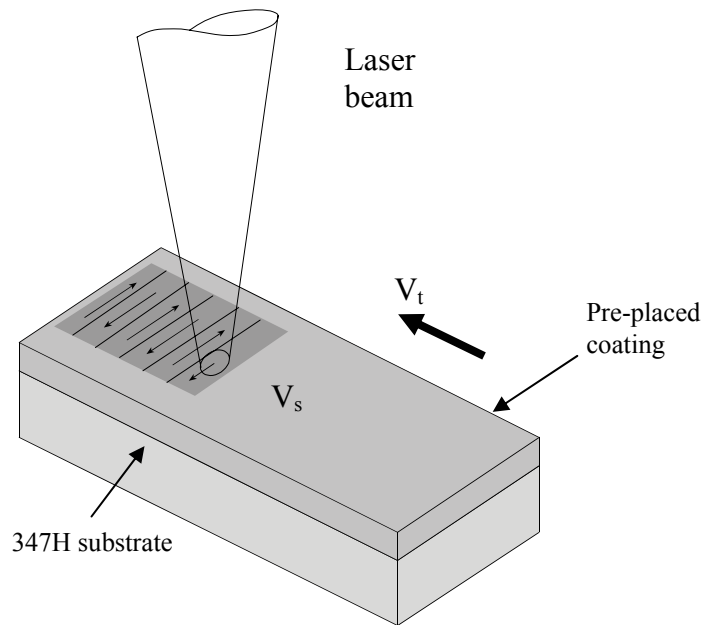


Figure 3.19 Schematic diagram of laser coating of TiC/TiC-Ni on 347H steel.

The slabs that were coated with the 50 wt.% TiC - 50 wt.% Ni powder mixture were previously coarse-fine ground and then fine polished to remove roughness and oxides from the surface. Slurry coatings of 50Cr-50Ni, TiC and 50TiC-50Ni in weight % were prepared by mixing commercially available fine powders (mesh -325) in isopropyl alcohol media in a ratio of 1 g of solid mixture per 10 ml of alcohol. These were applied to the surface by means of a spatula or by an air-spray gun. After applying one layer of slurry, it was allowed to dry and weighed to determine the mass deposited. By means of the theoretical density of the powders and assuming a packing density of 30%, the coating height was



approximated. If more material was needed on the surface, then a second layer was applied and so on.

After the laser coating process was done, the specimens were sectioned across the longitudinal axis and polished according to the standard metallographic preparation procedure. Marbles and aqua-regia (50 vol.% HCl and 50 vol.%  $\text{NH}_3\text{O}_4$ ) reagents were used to etch and reveal the microstructural features of the Cr-Ni and TiC-Ni coated specimens, respectively. The polished mounts were dipped in the corresponding etching solution for 30 seconds. A Zeiss Axiovert 405M optical microscope was used to observe the microstructural features of the coating and interface at magnification lower than 1000x. A LEO 1530 and JEOL JSM 5610 scanning electron microscope each equipped with an EDAX probe were used, respectively, to study surface morphology and chemical composition of the single layer deposits. X-ray diffraction using  $\text{CuK}_\alpha$  radiation of the coated surfaces was also done to determine the presence of amorphous phases and particular intermetallic compounds.

### **3.5.2. Coating of planar C/C composites**

This research was carried out with collaboration from Karta Technologies Inc., San Antonio, Texas. The results obtained on the flat C/C composites were not encouraging as most of the coating delaminated partially or completely after

the process for several combinations of laser power, scan speed and scan density as well as coating composition and sequence. Therefore, no further research was attempted with this type of specimen and the research efforts were instead centered on the coating of C/C cylinders with much better results. Explanation to the observed interface debonding phenomenon can be found in Chapter II Section 3.3. The most critical feature of the laser coating of a ceramic substrate by a ceramic coating is the lack of laser-substrate interaction time so that temperature at the substrate and coating are neither sufficiently high nor established for long enough times to allow complete wetting and diffusion chemical species. A weak discontinuous bond layer at the interface forms when wetting is incomplete and diffusion is sluggish. On cooling from the fabrication temperature a biaxial strain state of tensile character develops on the coating due its high CTE relative to that of the C/C composite substrate. These high tensile stresses drive existing cracks on the coating to growth towards the interface, where the cracks bow following the weakest path, thus causing delamination. Even if the laser-substrate interaction time is increased, a too high temperature at the substrate below the coating may weaken the substrate facilitating spallation. Determination of the correct operating windows that provided good interface bonding keeping the integrity of the coating and substrate sound proved to be a difficult if not impossible task to achieve with flat C/C composite specimens.

Nonetheless the delaminated coatings were used for indentation crack measurement purposes to generate fracture toughness data as well as to make pellets for TMA and DTA testing. The latter tests were performed to determine the CTE of the laser fused coating as well as its melting and solidification points.

### **3.5.3. Casting of a shape memory alloy by laser melting**

This research was done together with investigators from Kinki University in Hiroshima, Japan. Rod-like structures were cast by laser melting of a mechanically alloyed Ti-Ni powder. The powder was compacted inside a rectangular trough of dimensions 25.4 mm x 12.7 mm x 6.35 mm carved out in an aluminum holder of dimensions 50.8 mm x 76.2 mm x 25.4 mm and placed inside of the right piston in the CO<sub>2</sub> laser processing chamber. The trough was previously sprayed coated with graphite to prevent melting of the aluminum and ease the removal of the cast material. The powder surface was then leveled so that it matched the focal position of the laser beam; the powder was allowed to degas for 24 hours under a vacuum of 0.06 Torr. Figure 3.20 illustrates the laser raster-scan processing set up employed in this research to cast shape memory alloy structures.

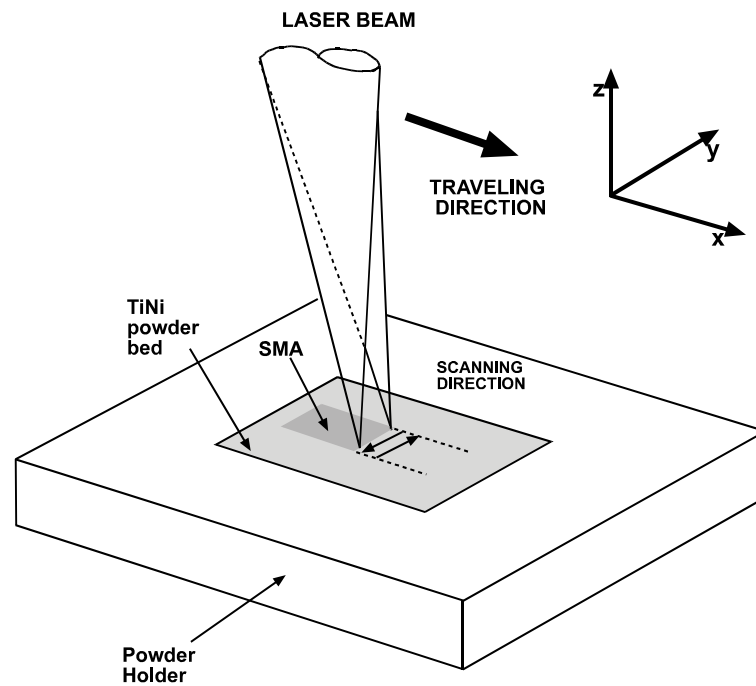


Figure 3.20 Schematic diagram of laser melting of a shape memory alloy powder.

Rod-like structures were obtained. They had an average diameter of 2-3 mm and a length of 10-15 mm. These were sent to Kinki University in Japan for shape memory property assessment, oxygen content and solidification microstructure.

### 3.5.4 Laser cladding of C/C composite tubes

This research was done at the Laser Cladding Services (LCS) in Houston Texas in collaboration with Karta Technologies Inc., San Antonio, Texas.

LCS is an industrial bureau owned by Gremada Industries, Inc. (USA) and Technogenia (France). It provides coating services for large metal parts such as drilling crowns used in oil-well exploration. The coating is primarily done using the laser cladding technique by blowing coating material in powder form coaxially with the laser beam together with shielding gas. The laser beam is generated from a 6.0 kW TEA CO<sub>2</sub> laser (Rofin-Sinar) and is delivered to the work piece by an x-y-z computer controlled gantry (Siemens). A lathe is available when the work piece needs to be rotated along its longitudinal axis. Powders can be mixed to a specific composition ratio and delivered by a dedicated fine powder dispenser unit (Sulzer Metco) connected to the cladding nozzle.

C/C composite tubes were provided by Lockheed Martin having a 10 mm inner diameter and 12 mm outer diameter. These were cut into 25 mm long tubular specimens and mounted on a rotary shaft connected to a lathe. A total of 7 specimens were laser clad with SiC-30Cr and Cr-30SiC (in weight %) fine powder mixtures following a spiral deposition pattern. The main objective sought after for the coating was to decrease the permeability of the tube wall. The SiC-30Cr powder mixture was prepared by dry ball milling for 24 hours, the Cr-30SiC was mixed manually at LCS. The laser power used ranged from 1000 to 2000 W, the beam size was varied from 5 to 8 mm and the traveling speed was set to 33.3 mm/s. The step size is the track overlap required to match the longitudinal motion

of the laser beam with the rotation motion of the shaft so that the complete surface is coated; it varied from 4 to 6 mm. Powder mass flow ranged from 7 to 10 g/min. Figure 3.21 shows an image taken at LCS of the cladding head over a C/C composite tubular specimen before the laser process started.

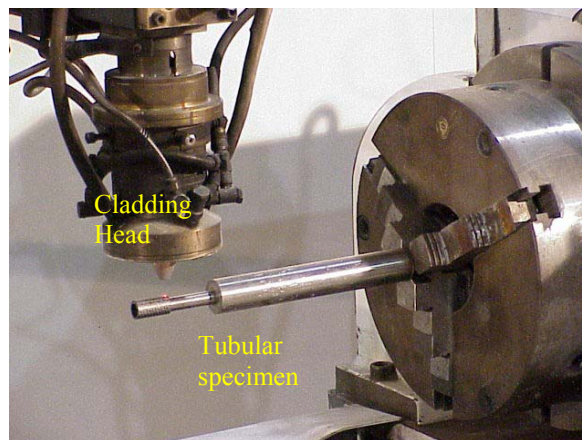


Figure 3.21 Typical rotary shaft sample holder and laser cladding head.

After the tubular specimens were coated, three of them were sectioned across and along the longitudinal direction. The cut pieces were cold mounted in epoxy resin and allowed to set for 24 hours. They were then fine and coarse ground followed by 0.25  $\mu\text{m}$  alumina polishing with de-ionized water. A JEOL JSM 5610 scanning electron microscope was used to observe at high magnification the integrity of the coating and substrate at the interface as well as cracks and porosity of the coating. An EDAX probe was used to map the elemental composition of the surface of the tubes.

The remaining four tubes were subjected to a preliminary water permeability test. It consisted in gluing one end of the tubular specimen to a metal flat surface using silicone sealant; a glass tube 65" high having its outer diameter slightly less than the inner diameter of the C/C composite tube was inserted at the opposite end of the specimen and sealed, too. Then, once the sealant was totally dried, water was poured inside of the specimen and glass tube up to 30" from the flat surface; a bung was used to close the other end of the glass tube and avoid water loss by vaporization. This column of water provided approximately a hydrostatic pressure of 7.5 kPa. This set up was left for up to 72 hours and the height of the water column was recorded several times during this period. As no water permeation was observed at this height, the water column was doubled, so the pressure acting on the tube walls corresponded to 15 kPa, the column height was recorded again during a 72 hours period.

### **3.5.5 Linear motion device for coating slab specimens**

This device was specifically designed to be used for the coating of thin C/C composites; however, it was also employed for some trials of the TiC-Ni coatings on stainless steel 347H, as it allowed change of the motion speed of the specimen relative the laser beam during the coating processing. Figure 3.22 shows the linear translator designed by the author and collaborators that was

manufactured at Karta Technologies Inc. This device allowed linear motion displacement of flat samples of length up to 6 inches at a speed of up to 1.5 mm/sec. The rotary device used in coating the cylindrical C/C composite samples drove the stage. In this manner if pre-heating of the sample was necessary it was achieved by having the sample stationary with respect to the scanning laser beam, a feature difficult to obtain with the scanning mirrors alone.

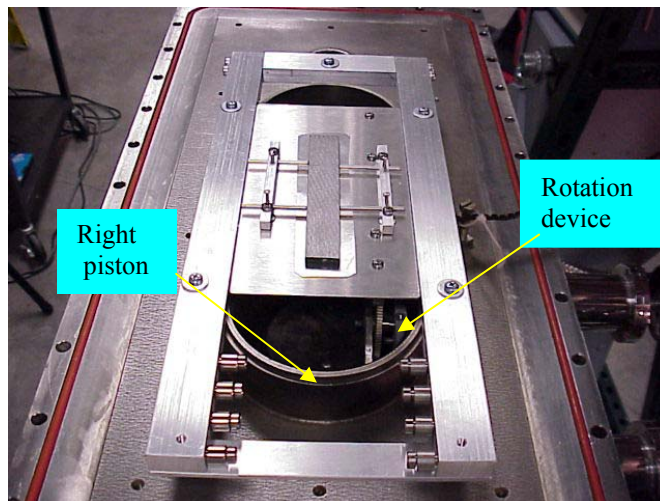


Figure 3.22. Linear translation stage mounted inside of CO<sub>2</sub> laser processing chamber.

The speed of the linear device was controlled by a voltmeter and the device had a linear dependence shown in Figure 3.23.



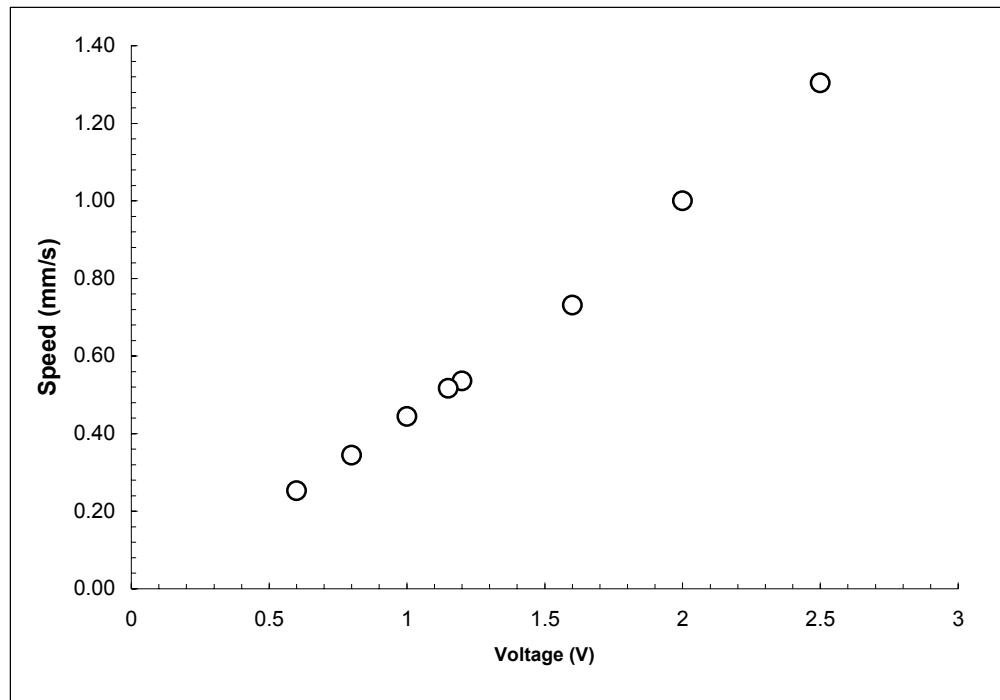


Figure 3.23. Calibration curve for the speed of linear motion stage versus voltage.

### 3.6 REFERENCES

1. S. Das, Ph.D. Dissertation Thesis, University of Texas at Austin, December 1998.
2. G. Danyo, M.Sc. Thesis, University of Texas at Austin, 1998.
3. J. Murphy, M.Sc. Thesis, in progress, University of Texas at Austin, 2003.
4. S. Ahn, Ph.D. Dissertation Thesis, in progress, University of Texas at Austin, 2003.

5. DTM-Corporation, "Housings for hearing aid transmitter created within two month window", *Horizons Q3*, 5-7 (2001).
6. Veeco Metrology Group, Dektak<sup>3</sup> Operating and technical manual.
7. K. Lappo, J.A. Ramos, J. Murphy, K. Wood, D.L. Bourell, J.J. Beaman in *Rapid Prototyping of Materials*, edited by F.D.S. Marquis and D.L. Bourell, (TMS, Warrendale PA, 2002), 185-190.
8. C.A.A. Cairo, M.L.A. Graca, C.R.M. Silva, J.C. Bressiani, *Journal of the European Ceramic Society*, 21, 325-329 (2001).
9. J.C. Bailar, H.J. Emeleus, R. Nyholm and A.F. Trotman-Dickenson, Eds., Comprehensive Inorganic Chemistry, v.3, (Elmsford, N. Y., 1973).
10. G.R. Anstis, P. Chantikul, B.R. Lawn, D.B. Marshall, *Journal of the American Ceramic Society*, v. 64, No. 9, 533-538 (1981).

## **CHAPTER IV. RESULTS & DISCUSSION**

### **4.1 LASER POLISHED FE - CU INDIRECT-SLS PARTS**

Comprehensive characterization results of the laser polished tracks on four Fe-Cu slab specimens are presented and discussed in this section. Measurement of the arithmetic surface roughness  $R_a$  by means of linear profilometry of the as-received and laser treated surfaces revealed the behavior of the percent  $R_a$  variation ( $\%R_aV$ ) with laser power and traveling speed. Scanning electron micrography (SEM) and semi quantitative energy dispersion analysis of x-rays (EDAX) results of the cross-section and surface of the as-received and laser treated material are presented. X-ray diffraction analysis done on a generic as-received surface is presented as well. Additionally, numerical results of the surface temperature evolution model as well as results of the models for predicting the  $R_a$  under the different melting mechanisms are presented. A full description of the parameters used to process these specimens can be found on Appendix B-I.

#### **4.1.1 LaserForm ST-100<sup>TM</sup> surface morphology**

LaserForm ST-100<sup>TM</sup> is a material system aimed towards tool making for the injection molding industry. As described in Chapters II and III, this material

system is made by selective laser sintering a green part from stainless steel grade 420 precursor powder that is then fired and post-infiltrated with liquid bronze (approximately 5 wt.% tin). The firing process is done inside a vertical furnace under a N<sub>2</sub> atmosphere, and the green part is submerged in fine alumina powder to reduce surface oxidation. Final part composition is 60 wt.% 420 stainless steel and 40 wt.% bronze. The surface roughness of these as-received parts typically ranges from 9.0 to 2.4 μm depending on the SLS process parameters and stainless steel powder particle diameter used.

Figure 4.1 shows the surface morphology of an as-received indirect-SLS sample having a surface roughness value between 7-9 μm. This surface may be described as close-packed arrangement of liquid phase sintered spherical particles of about 100 μm radius. On the other hand, Figure 4.2 shows the morphology of the surface of an as-received sample having a lower surface roughness between 2-5 μm. The surface is covered with patches of solidified infiltration liquid with a spatial frequency of approximately 50 μm. It is not clear how those patches form; however, they appear to be the result of bead blasting or similar post-operation done over the bronze surface.

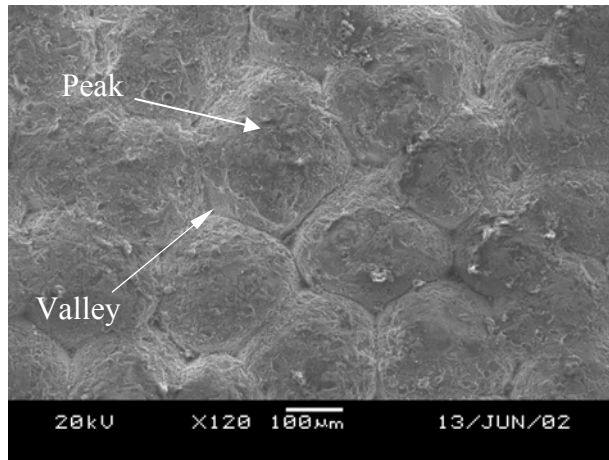


Figure 4.1. SEM image of the surface of indirect-SLS part having an  $R_a = 7-9 \mu\text{m}$ , 120x.

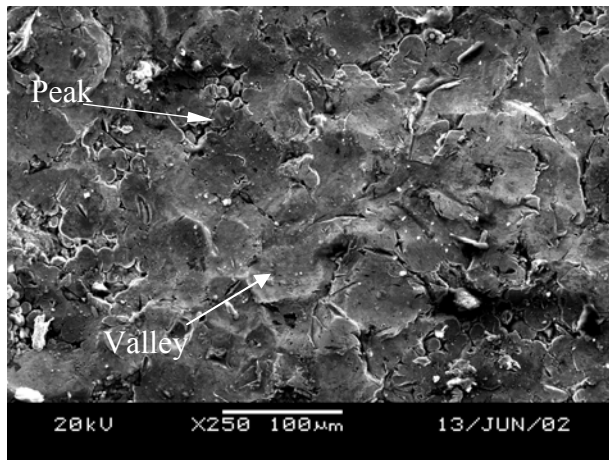


Figure 4.2. SEM image of the surface of indirect-SLS part having an  $R_a = 2-5 \mu\text{m}$ , 250x.

#### 4.1.2 Processing parameters

Table 4.1 shows the operation window used in the  $\text{CO}_2$  laser polishing trials of indirect-SLS slabs. The laser spot beam diameter  $D$  was approximately 0.4 mm. Figure 4.3 indicates that this operation window falls inside the melting-

welding zone of a power density versus interaction time log-log processing map [1].

	Maximum Value	Minimum Value
Laser beam power P [W]	565	225
Scan speed $V_s$ [mm/s]	850	100
Power density $P/D^2$ [W/mm <sup>2</sup> ]	$3.53 \cdot 10^3$	$1.41 \cdot 10^3$
Interaction time $D/V_s$ [s]	$4.0 \cdot 10^{-3}$	$4.7 \cdot 10^{-4}$
Energy Density $P/D/V_s$ [J/cm <sup>2</sup> ]	1413	66

Table 4.1. Operational window used in CO<sub>2</sub> laser polishing trials of indirect-SLS parts. The material system considered is 60 wt.% 420 stainless steel-40 wt.% bronze.

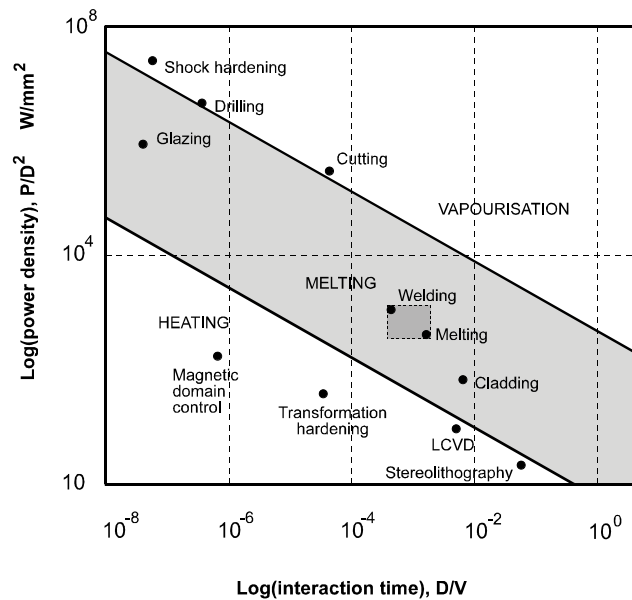
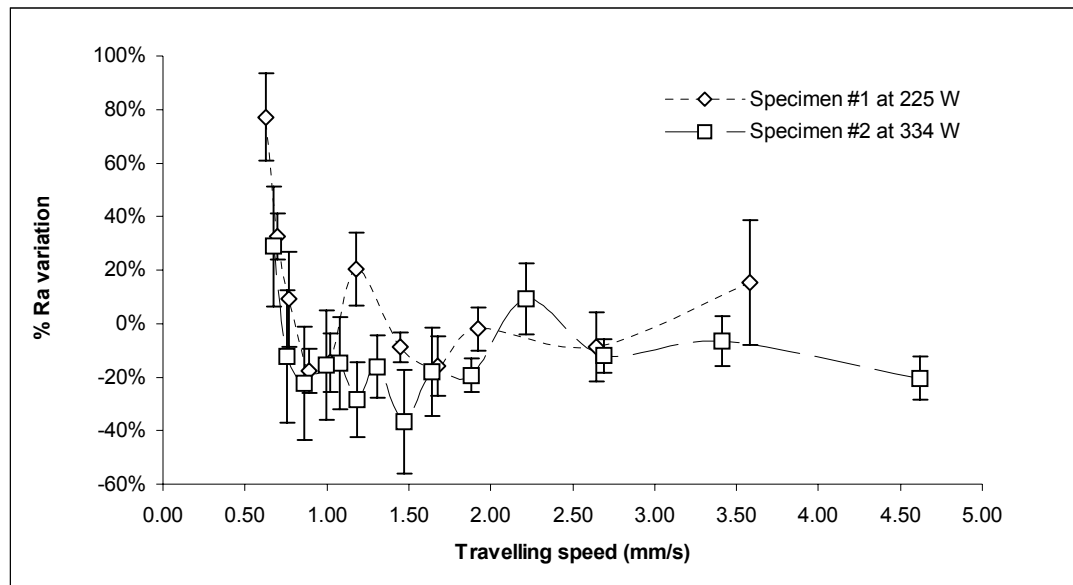


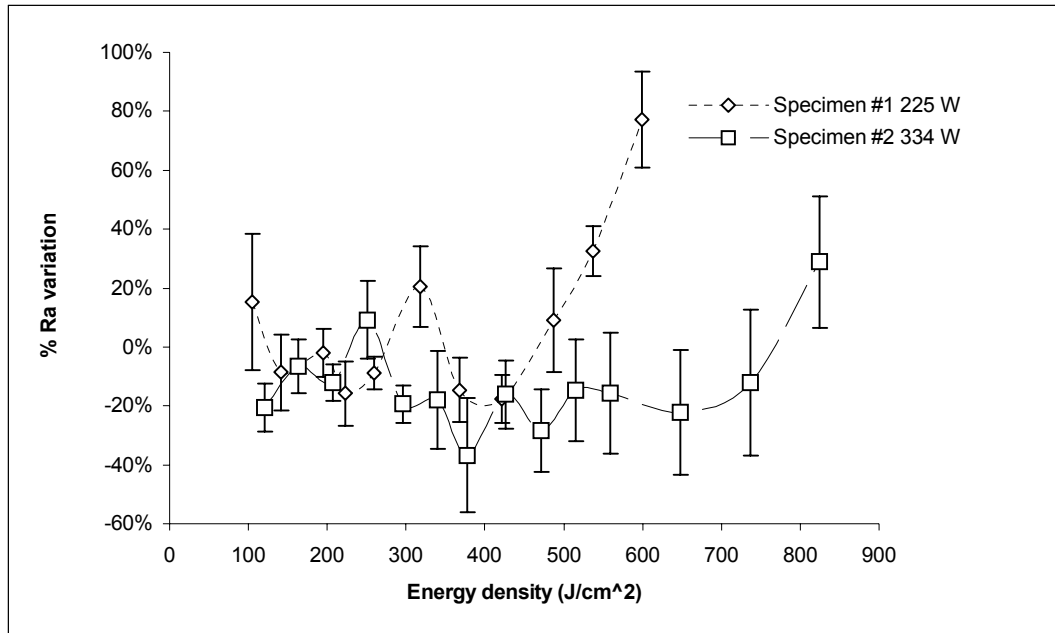
Figure 4.3. Operational window for several laser processes. Adapted from Steen [1]. The dark box near “Welding” and “Melting” indicates the utilized CO<sub>2</sub> laser polishing operational window.

### 4.1.3 Surface roughness measurements

In Figure 4.4a, the percent variation in  $R_a$  roughness (normalized) for each laser polished track relative to the as-received  $R_a$  value adjacent to the track is plotted as a function of the traveling speed used to modify the surface. The plot corresponds to specimens #1 and #2, laser treated at 225 W and 334 W, respectively. Figure 4.4b is the plot of the same percent variation in  $R_a$  roughness data but expressed in terms of the energy density (i.e., Andrews number) used in processing the surfaces.



(a)



(b)

Figure 4.4. Percentage normalized  $R_a$  roughness variation of indirect-SLS stainless steel grade 420–40 wt.% bronze infiltrated versus (a) increasing traveling speed (b) increasing energy density.

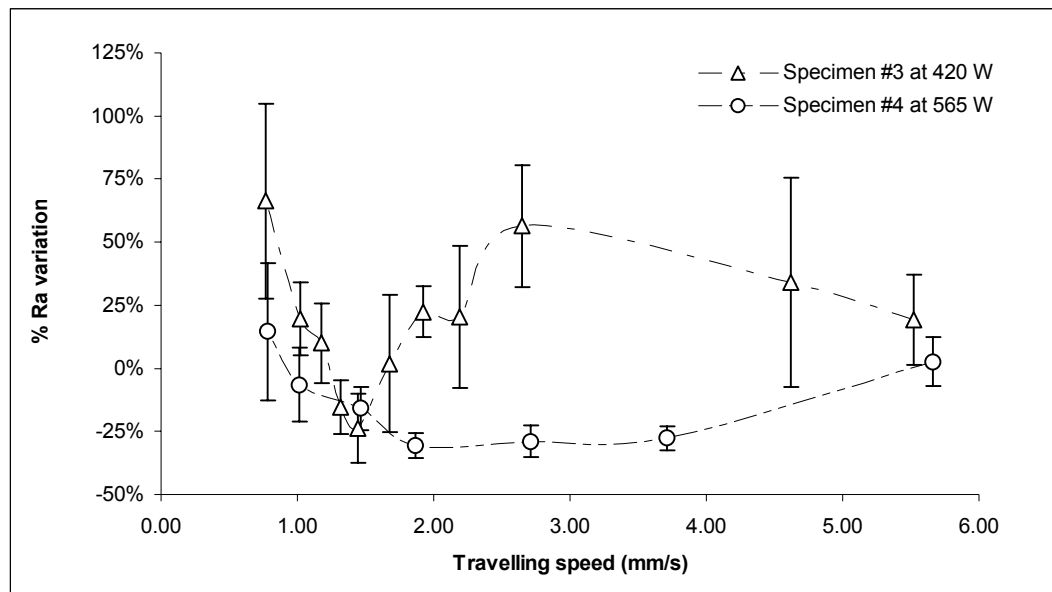
From Figure 4.4 it can be observed that for a laser power of 225 W, a maximum 18%  $\pm$  8% reduction in  $R_a$  roughness was achieved, while for 334 W it corresponded to 37%  $\pm$  19%, occurring at traveling speeds of 0.89 (i.e., 421.9 J/cm<sup>2</sup>) and 1.47 mm/s (i.e., 378.1 J/cm<sup>2</sup>), respectively. When the traveling speed was further decreased, the percent variation was reduced to almost zero at 0.7 mm/s for both specimens, becoming a positive percentage variation for even lower traveling speeds. That observation is in agreement with the surface-over-melt mechanism that occurs at low traveling speeds [2]. However, in the speed range of 1 to 1.5 mm/s, Specimen #1 showed a localized positive variation of 20%



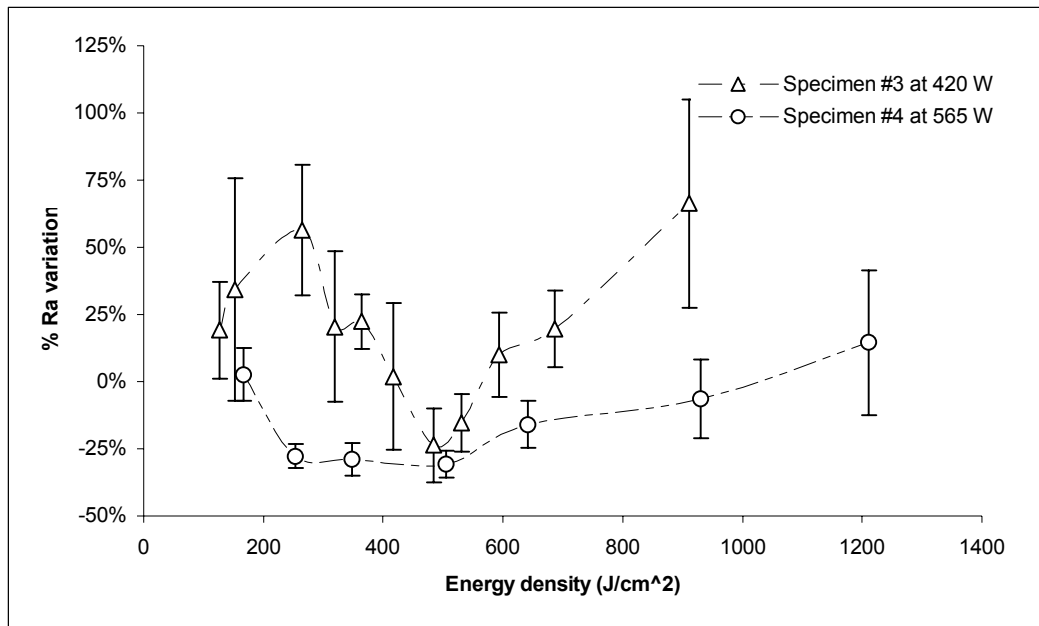
+/-14% at approximately 1.18 mm/s (i.e., 318.2 J/cm<sup>2</sup>). On the other hand, traveling speeds higher than 1.5 mm/s gave a percent reduction between 20% to 7% in Specimen #2, except for a speed of 2.25 mm/s (i.e., 250.9 J/cm<sup>2</sup>) that gave an anomalous and local 9% +/-13% R<sub>a</sub> increase. For the same range of traveling speeds, Specimen #1 showed percent R<sub>a</sub> reduction oscillating around 16% to 2%, but at 3.58 mm/s (i.e., 104.7 J/cm<sup>2</sup>) it turned anomalously into a positive variation of 15% +/-23%, too. Except for the described local anomalies, the percent R<sub>a</sub> reduction behavior obtained at high-speeds agrees with the mechanism of surface-shallow-melting and early onset of surface-over-melt [2,3]. The localized erratic percent R<sub>a</sub> variation behavior observed can be attributed more to the presence of alumina particle streams as well as the formation of iron oxide platelets, rather than a systematic error associated with the surface modification processes and measurement. These two hypotheses will be further discussed later in this section together with the empirical evidence of their existence.

Similar type of plots for Specimens #3 and #4, polished with 420 W and 565 W, respectively, were constructed and are presented in Figure 4.5. From these graphs, it can be observed that approximately a 24% +/-14% R<sub>a</sub> reduction was obtained for Specimen #3 at 1.45 mm/s (i.e., 483.9 J/cm<sup>2</sup>) and a 31% +/-5% reduction for Specimen #4 at 1.87 mm/s (i.e., 504.6 J/cm<sup>2</sup>). Additionally, for both specimens, it was seen that lower traveling speeds or equivalently higher energy

densities monotonically increased the percent  $R_a$  variation up to a 66% +/-39% and 15% +/-27% increase, respectively. For traveling speeds higher than the ones providing the maximum percent  $R_a$  reduction, a significant trend contrast was observed. In the Specimen #3, the percentage variation anomalously reverted from negative to positive past 1.5 mm/s. In Specimen #4, the trend showed a negative percent variation, yet its absolute value decreased with increasing speed, becoming slightly positive (3% +/-10%) at 5.66 mm/s (166.3 J/cm<sup>2</sup>). The percent variation should never be positive unless the SOM regime is fully developed; however, the laser processing of this particular material system appears to be highly sensitive to oxygen partial pressure as well as the presence of contaminants embedded in the part surface (i.e., alumina particles).



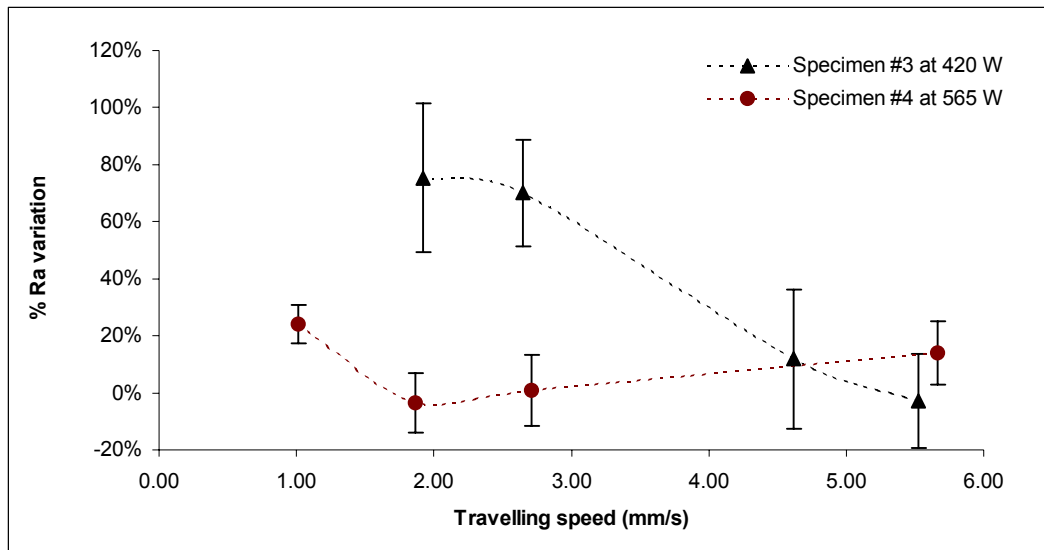
(a)



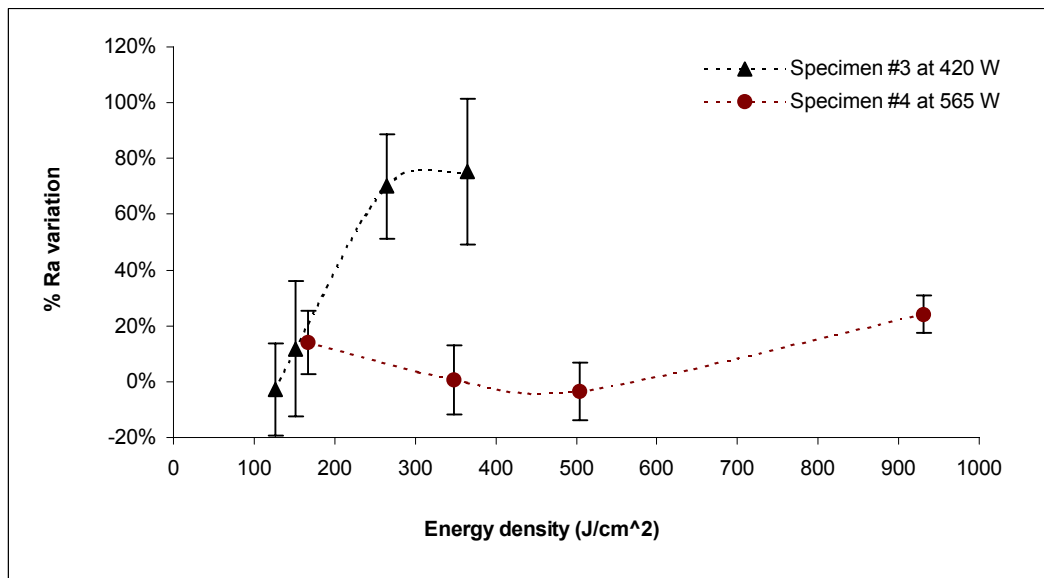
(b)

Figure 4.5. Percentage normalized  $R_a$  roughness variation of indirect-SLS stainless steel grade 420–40 wt.% bronze infiltrated versus (a) increasing traveling speed (b) increasing energy density.

Because of the pronounced contrast in roughness variation behavior between Specimen #3 and #4, it was decided to repeat some of the laser polishing tracks using the same parameters and measuring the percent variation in  $R_a$  again to see how sensitive the results were to the repeatability of the process. These data was averaged with the corresponding previous data and the new results are presented in Figure 4.6. For the process carried out at 420 W, the trend shape did not change considerably, and it remained a positive variation for most of the traveling speed range.



(a)



(b)

Figure 4.6. Percent normalized  $R_a$  roughness variation of indirect-SLS stainless steel grade 420–40 wt.% bronze infiltrated versus (a) increasing traveling speed (b) increasing energy density.

For the process done at 565 W the trend was similar to the first set of trials, but it shifted upwards considerably signaling a positive character in the roughness variation. In this specimen, the maximum percent reduction in roughness of 4% +/-10% occurs also at 1.87 mm/s (504.6 J/cm<sup>2</sup>). These results centered the research efforts into analyzing the surface of the laser polished tracks and cross section below them to elucidate an explanation to the anomalies presented.

#### **4.1.4 SEM and EDAX cross sectional analysis**

Cross section observation and analysis of indirect-SLS laser polished tracks done in Specimens #1, #2 and #4 at different speeds are presented in the following set of figures. Figure 4.7 shows the layered structure of Specimen #1. Typical features of the SLS process appear, in this case the sintering of the 420 stainless steel precursor powder. Figure 4.8 shows how the precursor steel particles, ranging between 10 – 25 microns in diameter, appear embedded in the Cu-rich phase after the liquid sintering processes. A ratio of 60 wt.% 420 stainless steel to 40 wt.% bronze can be verified from the image, by estimating the percent area of light-gray color (Cu-rich phase) and of dark-gray color (Fe-rich phase). Darker-gray spots within the Fe-rich phase consist of Cr-rich phase. A small amount of porosity, accounting for less than 1% is also observed as black spots.

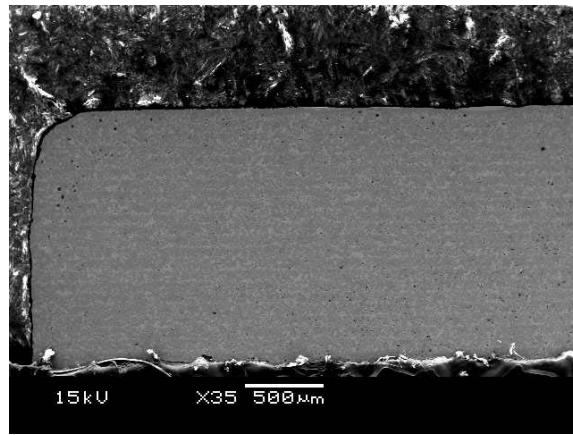


Figure 4.7. As-received layered cross section of Specimen #1, 35x.

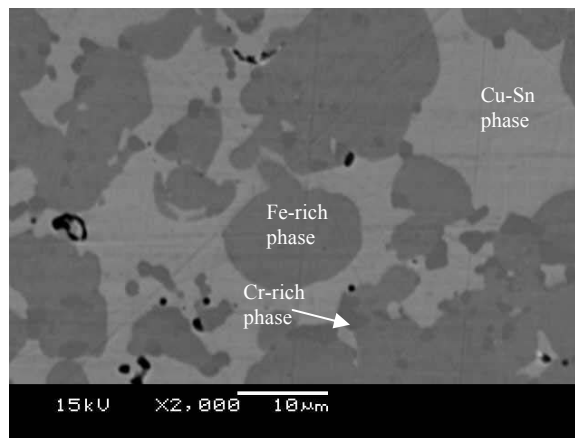


Figure 4.8. As-received bulk region of Specimen #1, 2000x.

Figure 4.9 shows a close up image near the surface region, indicating that most of surface of the as-received material (i.e., not laser treated) is covered by a thin layer of Cu-rich phase. This a very important observation as it determines the type of surface-over-melt regime mechanism that might take place depending on whether or not the penetration of the melt is deep enough to start melting the Fe-rich phase simultaneously.

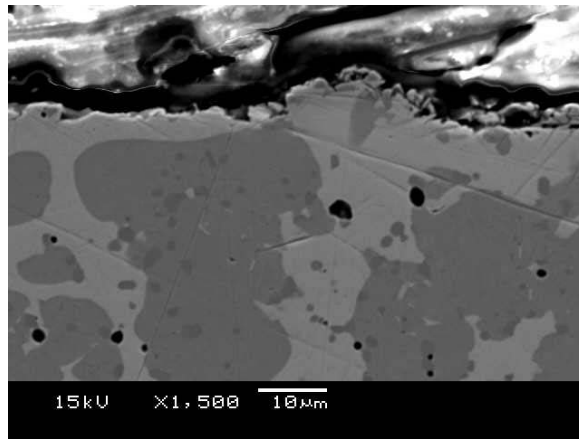


Figure 4.9. As-received surface region of Specimen #1, 1500x.

Figure 4.10 shows a sequence of element maps of Fe, Cu and Cr for the cross section of Specimen #2 near a non laser treated surface region in between laser polished tracks # 6 and # 7. The dark colored phase on the SEM image corresponds to the Fe-rich phase whereas the light colored phase corresponds to the Cu-rich phase which extends almost entirely over the surface. The Cr-rich phase appears as clusters within the Fe-rich phase indicating that during the liquid-phase sintering this phase has segregated out from the steel phase. This phase is also present in small quantities at the surface of the specimen. Tin was equally distributed as the Cu map signaling that the bronze phase has not undergone any compositional changes.

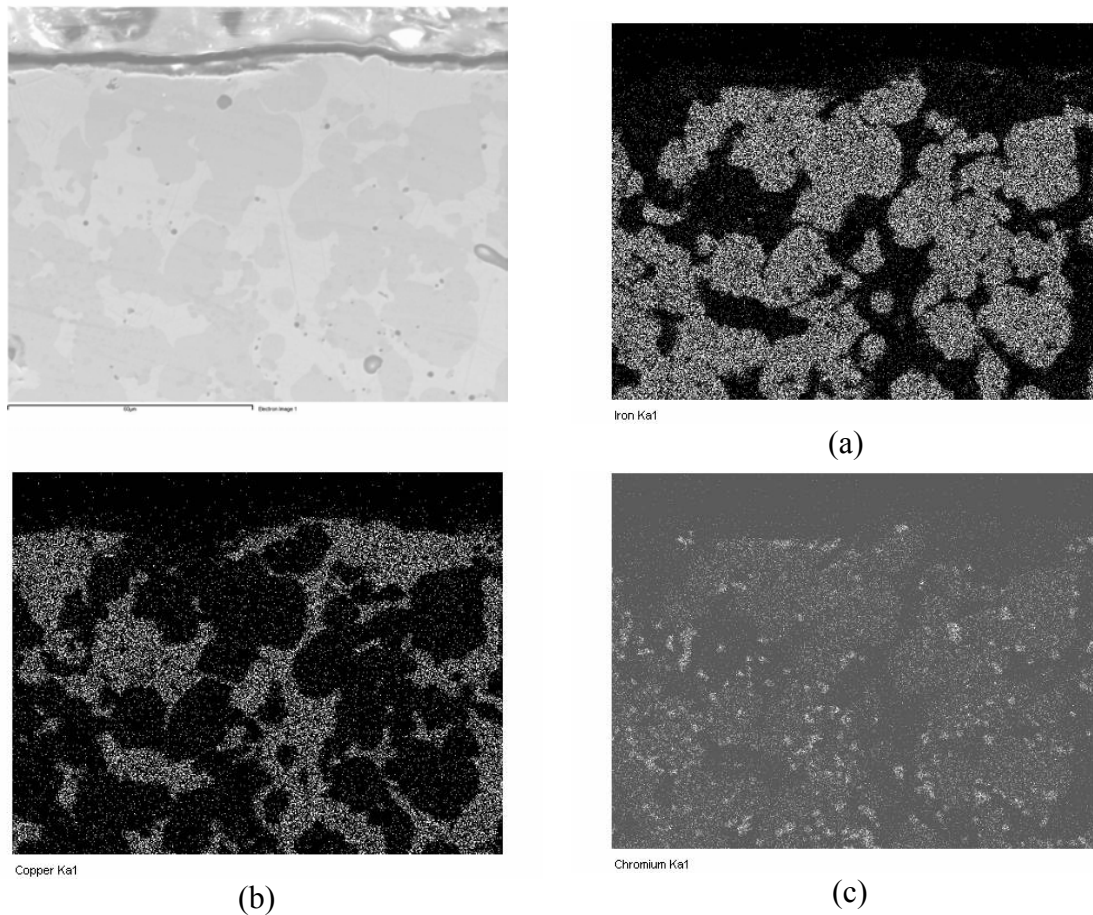


Figure 4.10. Elemental mapping of (a) Fe composition, (b) Cu composition and (c) Cr composition of the as-received surface region in between laser polished tracks of Specimen #2.

Figure 4.11 shows the cross section of a surface region in specimen #1 that underwent the laser polishing treatment at 225 W at 1.68 mm/s (i.e., 223.4 J/cm<sup>2</sup>). A melt depth of approximately 20  $\mu\text{m}$  was achieved and solidification occurred first as a Fe-rich phase that extended up to 10 microns from the bottom of the pool



in direct contact with the un-melted solid. The solidification of a Cu-rich phase then followed and extended up to the surface. However, at the center of this image, the Fe-rich phase solidified all the way to the surface as if it were pushing the Cu-rich phase laterally. From the Fe-Cu phase diagram (see section 2.2.3), the Fe-rich phase must solidify first as it has a considerably high melting point than the Cu-rich phase. Moreover, the shape of the liquidus line of the Fe-Cu system favors solidification of the  $\gamma$ -Fe phase, and, as the temperature is lowered, Cu is segregated out into the liquid until the peritectic line is reached (1080°C). At that point, a peritectic reaction,  $L + \gamma\text{-Fe} \rightarrow (\text{Cu})$ , should take place if enough time for diffusion in the solid were allowed. As this is not the case, the Cu-rich liquid remaining solidifies as Cu directly without consuming the already solidified  $\gamma$ -Fe phase. On further cooling down to room temperature, the phase diagram indicates that the  $\gamma$ -Fe phase will transform into  $\alpha$ -Fe phase and the (Cu) phase will not undergo any transformation. As both phases will reduce their solubility limit any excess Fe or Cu in the respective phase will precipitate out until the maximum solubility limit is reached, respectively. This solidification results in the observed layering of the Cu-rich phase at the surface followed by the Fe-rich phase immediately below.

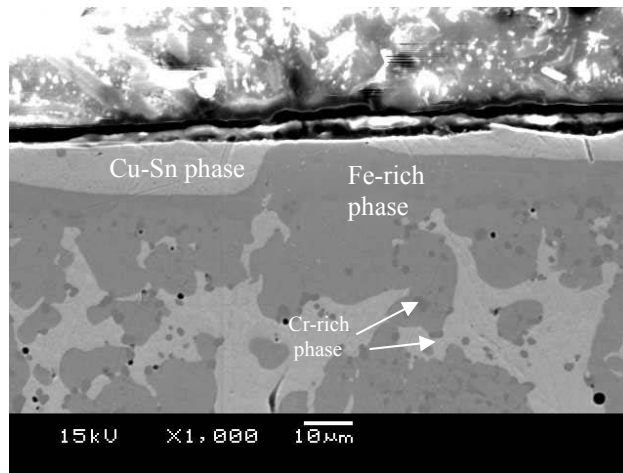


Figure 4.11. Laser polished surface region in Specimen #1, track 4 done at 225 W and 1.68 mm/s speed, 1000x.

The sequence of elemental maps of Fe, Cu, Cr, and Sn corresponding to a magnification of the cross section previously shown in Figure 4.11 are illustrated in Figure 4.12. The Fe-rich phase is homogenous in composition both at the remelted and bulk zones. However, the Cr-rich clusters have been dissolved and reincorporated in the solidified phase as these did not appear in the solidified zone Figure 4.12c. In the case of Sn, it remained well homogenized in the Cu-rich solid solution after solidification. Second phase precipitates in the Cu-rich and Fe-rich phases due to the narrowing of the solubility limit on cooling cannot be resolved in these maps.

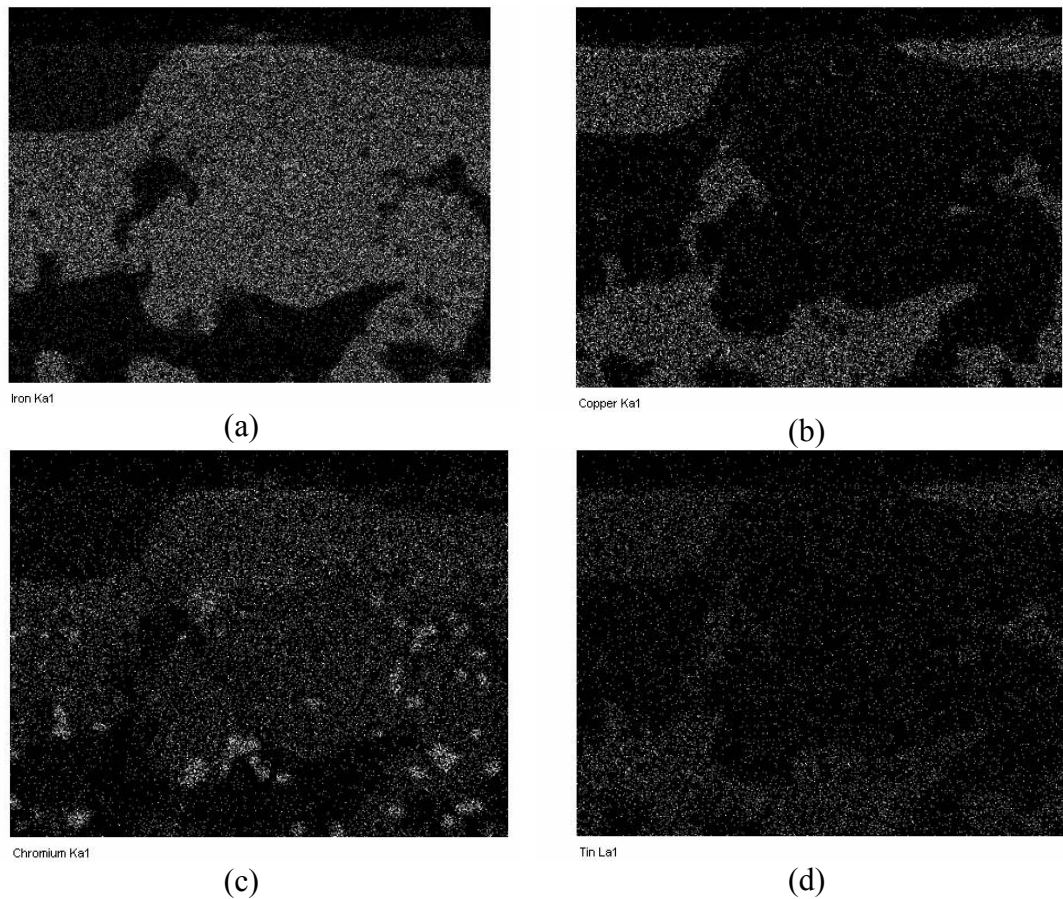


Figure 4.12. Elemental mapping of laser polished track surface of Specimen #1 shown in Figure 4.11. (a) Fe distribution, (b) Cu distribution, (c) Cr distribution, (d) Sn distribution.

Figure 4.13 shows another two-layered solidification pattern, in this case a power level of 565 W and a speed of 5.66 mm/s (i.e., 166.3 J/cm<sup>2</sup>) were used to obtain an overall melt depth of 25  $\mu\text{m}$ . The Cu-rich layer is not discontinuous, however only measured 5  $\mu\text{m}$ . Figure 4.14 illustrates the same type of solidification obtained in this case at 334 W and 4.62 mm/s, but at lower

magnification (150x) to show the uniformity and continuity of the two-layered solidification pattern.

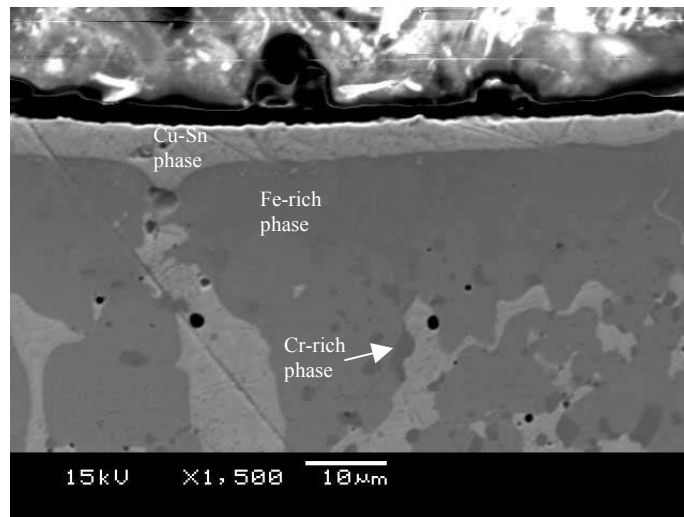


Figure 4.13. Laser polished surface region in Specimen #4, track 1 done at 565 W and 5.66 mm/s speed, 1500x.

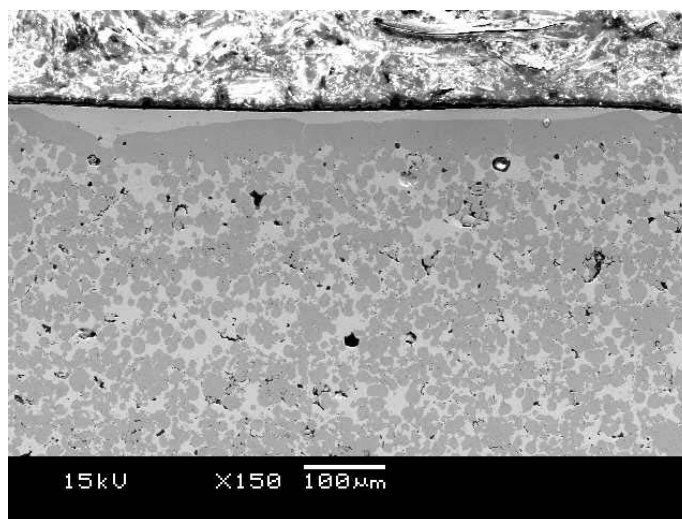


Figure 4.14. Laser polished surface region in Specimen #2, done at 334 W and 4.62 mm/s, 150x.

#### **4.1.5 SEM and EDAX Surface analysis**

The surface morphological and compositional analysis was divided into two ranges, one corresponding to low laser power, 225 W to 334 W, and the other to a high laser power, 420 W to 565 W.

##### ***4.1.5.1 Low laser power range***

Figures 4.15-4.17 show SEM images of laser raster-scan tracks done on specimen #2, having widths of 1.42 mm, 1.61 mm, and 1.93 mm, respectively. The difference in resulting track widths is due to the different power level and scan speed combinations used, rendering in this particular case energy densities of 251, 340 and 648 J/cm<sup>2</sup>, respectively. However, the programmed scan width corresponded to 1.9 mm. The as-received roughness value  $R_a$  of the specimen was 2.42  $\mu\text{m}$  +/- 0.29  $\mu\text{m}$ , while the obtained  $R_a$  values of the tracks after laser polishing were  $R_a = 2.69 \mu\text{m} \pm 0.33 \mu\text{m}$  (track #4), 1.93  $\mu\text{m}$  +/- 0.39  $\mu\text{m}$  (track #6) and 1.89  $\mu\text{m}$  +/- 0.52  $\mu\text{m}$  (track #12). From Figure 4.15 it can be seen that the resulting surface of the polished track #4, created at a traveling speed of 2.22 mm/s, appears covered with a pattern of narrow ripples, all parallel to the scanning speed direction.

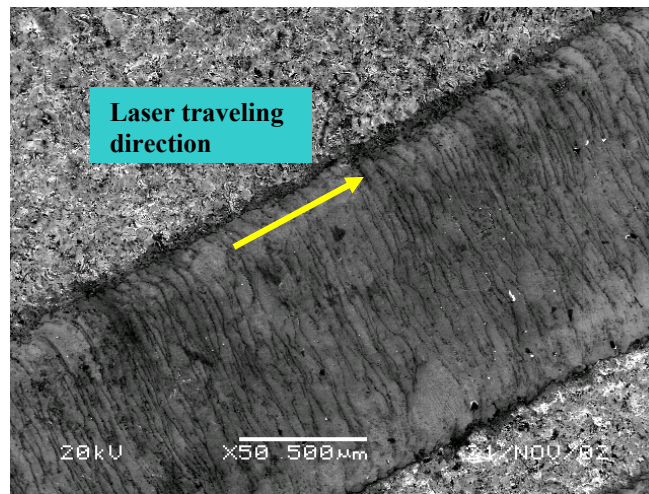


Figure 4.15. Laser polished track #4, 50x. Processing parameters, resulting % roughness  $R_a$  variation and track width: 334 W,  $v_t = 2.22$  mm/s,  $v_s = 333$  mm/s,  $\%R_aV = +9\%$ ,  $w = 1.42$  mm.

Figure 4.16 shows the resulting surface of laser polished track #6, created at a traveling speed of 1.64 mm/s. This surface appeared smoother but it had an oblique pattern of depressions at an angle of approximately  $30^\circ$  with respect to the scanning direction, resembling cracks instead of the narrow ripples observed in track #4. These surface depressions should correspond to undulations induced after the onset of a surface-over-melt regime. The lighter zone observed towards the right of the track indicates that charging is higher there, caused perhaps by some polymer binder residue left from the sintering stage and that emerged at the surface after the solidification process.

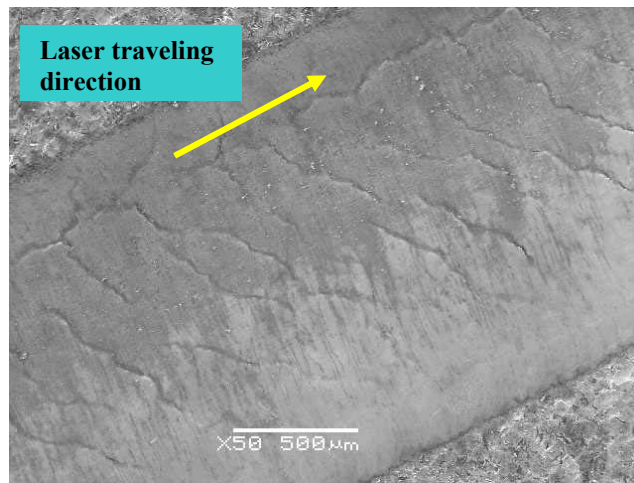


Figure 4.16. Laser polished track #6, 50x. Processing parameters, resulting % roughness  $R_a$  variation and track width: 334 W,  $v_t = 1.64$  mm/s,  $v_s = 246$  mm/s,  $\%R_aV = -18\%$ ,  $w = 1.61$  mm.

Figure 4.17 shows the surface of laser polished track #12, created at a traveling speed of 0.86 mm/s. A pattern of oblique linear features can also be observed forming again an angle of approximately  $30^\circ$  with the scanning direction; this pattern is spaced out periodically. As observed at higher magnification these features are not surface cracks but rather surface undulations. Nonetheless at some of the apexes cracks have nucleated and extended.

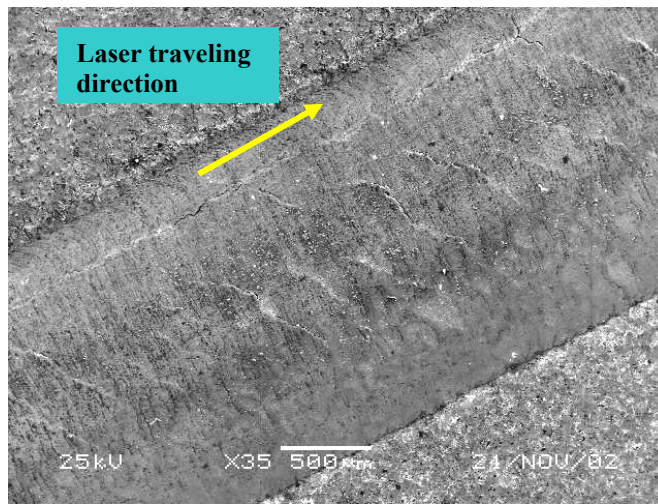


Figure 4.17. Laser polished track #12, 35x. Processing parameters, resulting % roughness  $R_a$  variation and track width: 334 W,  $v_t = 0.86$  mm/s,  $v_s = 129$  mm/s,  $\%R_aV = -22\%$   $w = 1.93$  mm.

Figure 4.18 shows a higher magnification SEM image of the surface of the laser track #12 (Figure 4.17) illustrating two consecutive pattern apexes which are spaced apart by a distance  $\lambda$  approximately 300  $\mu\text{m}$ . They are clearly parallel to each other. It can be verified that these correspond to wave peaks rather than cracks, but in some of these peaks cracks have nucleated. Another feature seen on this image is the appearance of a second and much finer periodic pattern closely spaced forming a 30° angle with the former. This pattern however, seems discontinuous by comparison.



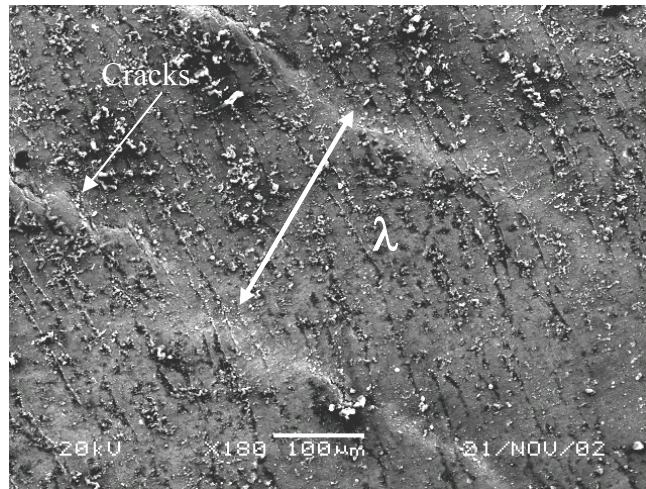


Figure 4.18. High magnification image showing two consecutive periodic peaks in track #12, 180x.

Cracking of the treated surface along the wave apexes may be associated with a slight difference in coefficient of thermal expansion between the Cu-rich phase and Fe-rich phase [4], but sufficient to drive a pre-existing crack especially due to the high cooling rate experienced by the surface after the laser has traversed that region.

The surface-shallow-melting mechanism may have operated in track #4, but the embedded particles increased the resulting  $R_a$  value of the surface. The onset of surface-over-melt has undoubtedly commenced in tracks #6 and was more developed in track #12, as indicated by the surface waviness observed.

The sequence of images shown in Figure 4.19a to 4.19d correspond to magnified inner portions of the laser polished track previously shown.

Additionally, laser track #1 is included. The latter was created using an energy density of  $121 \text{ J/cm}^2$  and a maximum  $\%R_aV = -21\%$  was achieved. From Figure 4.19a, it can be observed that considerable surface planarization occurred when compared to the as-received surface topology (Figure 4.2). However, approximately 20% of the area is covered by dispersed and long-streamed particles parallel to the beam scanning direction. The fact that these features appeared in bright white color is indicative of their insulating nature, suggesting these to be oxide particles, as later revealed by EDAX analysis. These features unquestionably contributed to the increase in measured resulting  $R_a$  value.

The narrow ripples observed in Figure 4.15 are now resolved at high magnification in Figure 4.19b. These corresponded also to long streams of particles of oxides of aluminum and silicon as revealed by EDAX analysis. They account for approximately 25% coverage of the laser smoothed surface.

Figure 4.19c shows a magnified inner portion of the laser scanned track #6 previously illustrated in Figure 4.16. A depression on the surface signaled the onset of low frequency waves. Approximately 25% of the surface area was covered by long-streamed alumina and silica particles.

Closer examination of the surface illustrated in Figure 4.19d, taken at a magnification of 800x, revealed that the second periodic pattern observed in Figure 4.18 was dispersed and it had a spacing of 10-20  $\mu\text{m}$ . Approximately 40%

of the surface area is covered by this debris-like deposition. It was perpendicular to the traveling direction of the laser beam thus parallel to the scanning direction. It consisted of multiple agglomerated particles (1-5  $\mu\text{m}$  in size), mostly oxides.

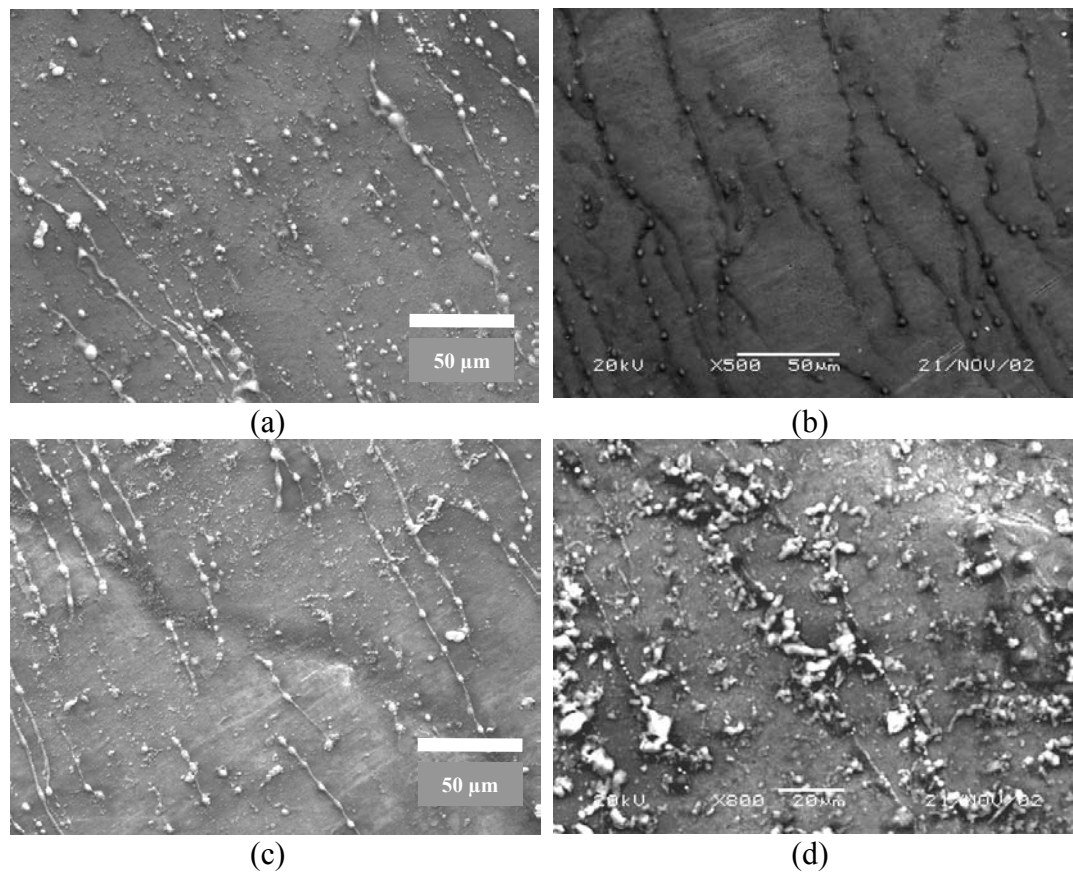
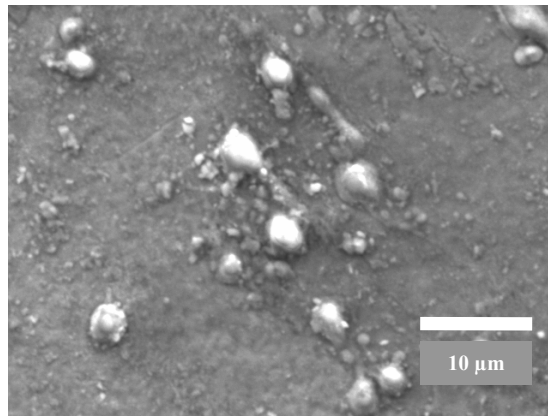
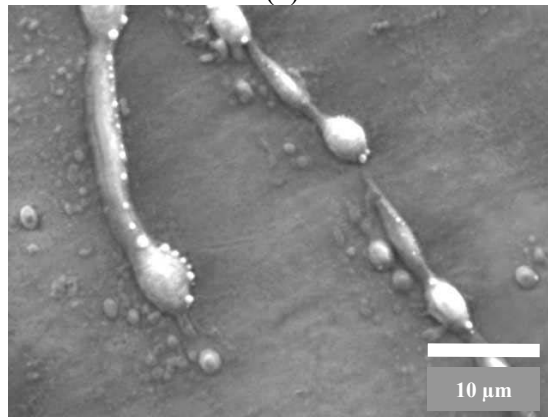


Figure 4.19. Magnified inner zone of different laser scanned track processed at 334 W (a) track #1:  $v_s = 693$  mm/s and  $v_t = 4.6$  mm/s at 500x, (b) track #4:  $v_s = 333$  mm/s and  $v_t = 2.2$  mm/s at 500x, (c) track #6:  $v_s = 246$  mm/s and  $v_t = 1.6$  mm/s at 500x, (d) track #12:  $v_s = 129$  mm/s and  $v_t = 0.86$  mm/s at 800x.

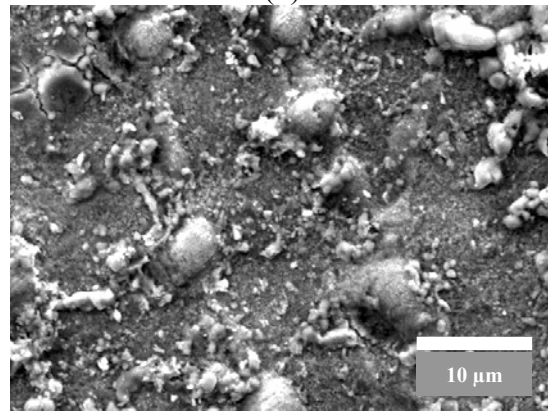
Figure 4.20a to 4.20c illustrates the morphology of the embedded particles on the laser polished surfaces of tracks #1, #6 and #12 respectively. On track #1 these are independent single spherical particles, 3 to 4  $\mu\text{m}$  in diameter and correspond to clusters of oxides particles (e.g.,  $\text{Al}_2\text{O}_3$  or  $\text{SiO}_2$ ) embedded within a resolidified sessile drop of substrate material. From Figure 4.20a these particles cover up to 15% of the smoothed surface. In the case of track #6, the drop-like particles (5 to 6  $\mu\text{m}$  in diameter) are fewer in number and they are interconnected by a stream of resolidified material; the surface tension has caused necking of the material connecting the particles. These long-streamed features cover up to 20% of the smooth surface. Sub-micron bright white spherical particles, i.e., Al and Si oxides, are attached to the sides of these resolidified features. Finally, on track #12 a different pattern covered the surface, consisting now of 5 to 10  $\mu\text{m}$  lumps of resolidified material mixed with oxides particles. These features may cover up to 25% of the surface area; however, in between lumps a form of debris also covers the smoothed surface.



(a)



(b)



(c)

Figure 4.20. Magnified inner zone of different laser scanned track processed at 334 W, 2500x (a) track #1:  $v_s = 693$  mm/s and  $v_t = 4.6$  mm/s (b) track #6:  $v_s = 246$  mm/s and  $v_t = 1.6$  mm/s (c) track #12:  $v_s = 129$  mm/s and  $v_t = 0.86$  mm/s.

As indicated by a semi-quantitative energy dispersive analysis of x-rays (EDAX) done on specimen #3 and #4 and described in the next section, the minuscule white particles observed in Figure 4.20a to 4.20c are Al and Si oxide compounds. The presence of aluminum oxide particles finds its origin on the alumina powder used to cover the green parts during infiltration process. On the other hand, silicon oxide particles arise from oxidation of elements present in the stainless steel grade 420 precursor powder. The latter two oxides are thought to form because of surface adsorbed molecular oxygen and the not so low partial pressure of oxygen used during the polishing process (i.e.,  $10^{-5}$  atm). Additionally, silica particles may have also become embedded in the as-received surface during a sand blasting operation after infiltration. The presence of such oxide agglomerates explains the deviation in  $R_a$  value encountered after the profilometry measurements.

#### ***4.1.5.2 High laser power range***

Specimens #3 and #4 were laser polished with 420 W and 565 W at different traveling speeds, respectively. The as-received surface  $R_a$  roughness of each specimen corresponded to  $2.06 \mu\text{m} \pm 0.25 \mu\text{m}$  and  $2.33 \mu\text{m} \pm 0.22 \mu\text{m}$ . Comparison of polished track #3 on specimen #3 done at 420 W at 2.65 mm/s (i.e.,  $264.6 \text{ J/cm}^2$ ) with track #3 on specimen #4 done at 565 W at 2.71 mm/s (i.e.,  $347.6 \text{ J/cm}^2$ ) showed a drastic change in measured  $R_a$  value after the laser

polishing. This corresponded to  $3.13 \mu\text{m} \pm 0.48 \mu\text{m}$  for specimen #3 and  $1.71 \mu\text{m} \pm 0.15 \mu\text{m}$  for specimen #4, which accounted for %R<sub>a</sub>V of +56% and -29% respectively. The main hypothesis to explain this difference is that at a high laser power for a fixed traveling speed, the surface temperature is higher and the melting pool is deeper, so more Fe is incorporated in the melt until the nominal composition is reached. These factors together with the high oxygen partial pressure used in the process increased the probability of oxidizing the Fe-rich phase at a much higher rate than the Cu-rich phase (see Ellingham diagram section 2). The Fe-oxide phase can provide a smoothing mechanism over the mechanisms that increase roughness such as oxide stream-particle line up and formation of surface waves from the Cu-rich phase. From Figure 4.21 it can be seen that laser-treated surface showed rippling spaced out every 100  $\mu\text{m}$ , a common signature of the SOM at high power and relative low speeds. At the apexes of these waves a darker color phase gathers containing long-streamed particles. Surface cracks were also present. In the case of Figure 4.22 the polished surface showed also a waviness character but it is covered with larger areas of a darker color phase. Interconnected streams of particles were also present.

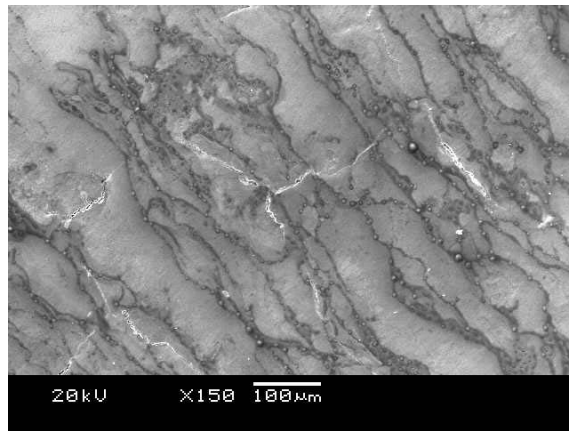


Figure 4.21. Laser polished track #3 in specimen #3, 150x. Processing parameters, resulting %  $R_a$  roughness variation: 420 W,  $v_t = 2.65$  mm/s,  $v_s = 396$  mm/s, % $R_aV = +56\%$ .

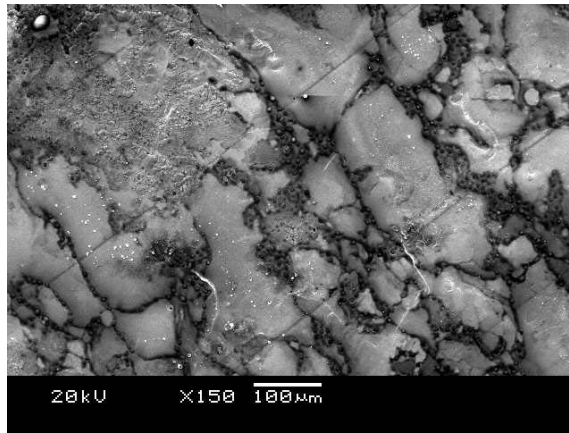


Figure 4.22. Laser polished track #3 in Specimen #4, 150x. Processing parameters, resulting %  $R_a$  roughness variation: 565 W,  $v_t = 2.71$  mm/s,  $v_s = 406$  mm/s, % $R_aV = -29\%$ .

Figure 4.23 illustrates at higher magnification the stream of interconnected spherical particles as well as surface cracks. In Figure 4.24 the polished surface is covered with a dark colored phase having a grainy and flaky appearance.



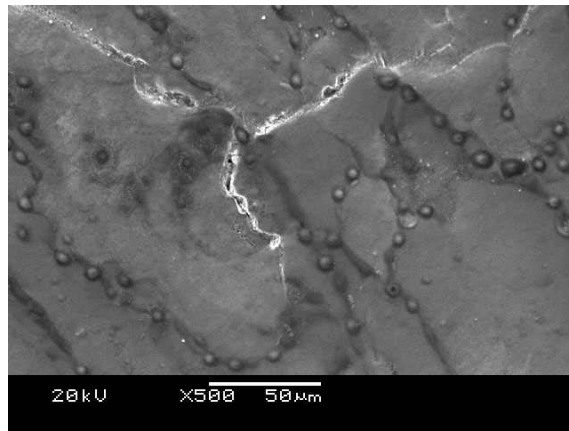


Figure 4.23. Magnified inner zone of Specimen #3 laser scanned track #3, 500x. Processing parameters : 420 W,  $v_t = 2.65$  mm/s,  $v_s = 396$  mm/s.

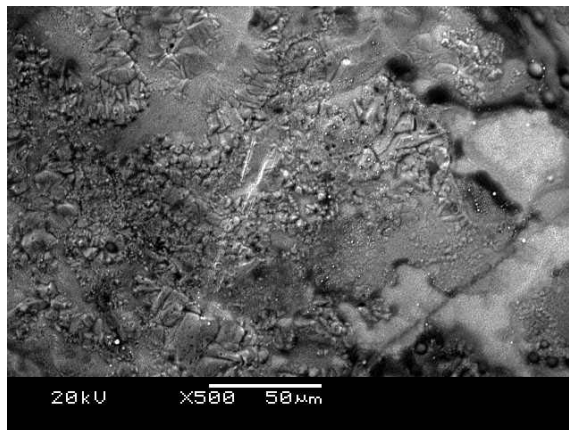


Figure 4.24. Magnified inner zone of Specimen #4 laser scanned track #3, 500x. Processing parameters: 565 W,  $v_t = 2.71$  mm/s,  $v_s = 406$  mm/s.

A close up image of a stream of embedded particles shown in Figure 4.23 can be clearly observed in Figure 2.25. The particle looked halfway buried on the smoothed substrate with sizes ranging from 4 to 8  $\mu\text{m}$  in diameter. Semi-quantitative EDAX indicated that these particles consisted of an Al-rich oxide phase, presumably  $\text{Al}_2\text{O}_3$ , while the matrix surrounding them corresponded to a

Cu-rich phase. These spherical particles occupied approximately 25% of the image. Each particle contributed at least to 1-2  $\mu\text{m}$  in roughness increase, so that the noise introduced by these particles can reach up to 0.25-0.50  $\mu\text{m}$ . This is a minimum of 10-20% increase in as-received roughness.

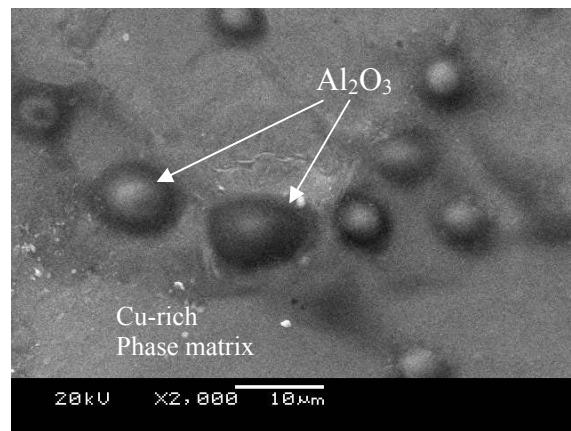


Figure 4.25. Magnified inner zone of Specimen #3 laser scanned track #3, 2000x. Processing parameters: 420 W,  $v_t = 2.65$  mm/s,  $v_s = 396$  mm/s. Al-rich oxide particles embedded on a Cu-rich phase matrix.

From Figure 4.26 a layer of Fe-rich phase has emerged over the Cu-rich phase smooth substrate. The Fe-rich layer consists mostly iron, iron oxide and alumina, silica and copper oxide, and as such provides a smoothing of the surface waves caused by the SOM mechanism, even though its surface roughness appears less smooth than the polished substrate.

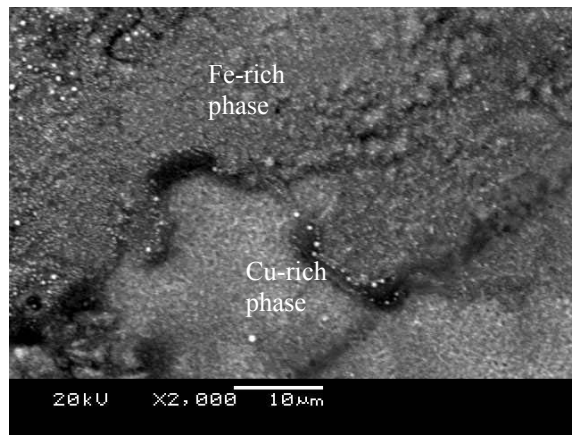


Figure 4.26. Magnified inner zone of Specimen #4 laser scanned track #3, 2000x. Processing parameters: 565 W,  $v_t = 2.71$  mm/s,  $v_s = 406$  mm/s. Showing a layer of Fe-rich phase on top of Cu-rich phase.

Semi-quantitative spectrochemical analysis of the as-received material of Specimen #3 near the border of laser polished track #3 as shown in Figure 4.27 indicated that the surface was rich in Cu (62 at.%) and Sn (5 at.%) followed by C (20 at.%) and oxygen (10 at.%). The high amount of C is not attributed to adsorbed  $\text{CO}_2$  solely, but rather to the polymer binder present in the green part. During the burn-off stage of the sintering process the polymer formed carbonaceous compounds that may be collected near the surface of the green part. Fe is present in 2 at.% followed by Cr with a composition less than unity. Figure 4.28 is the energy dispersive chemical spectrum of the as-received zone, showing the Cu and Sn peaks to be more pronounced. A similar composition is found on the as-received material of Specimen #4 near the border of the laser polished track #3.

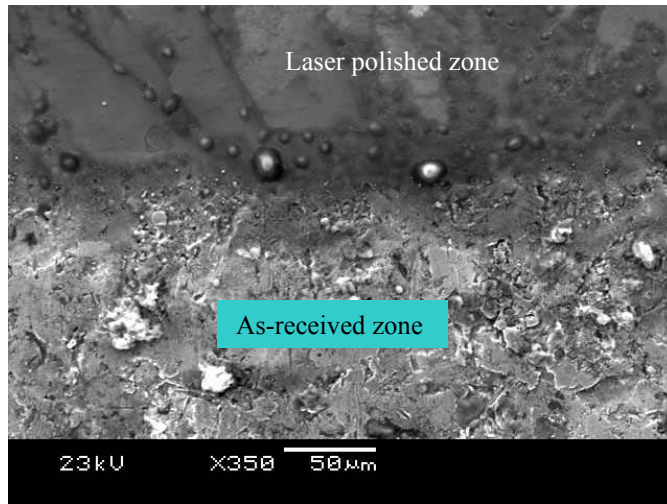


Figure 4.27. Border region of Specimen #3 between as-recieved and laser polished track #3, 350x. Processing parameters: 420 W,  $v_t = 2.65$  mm/s,  $v_s = 396$  mm/s.

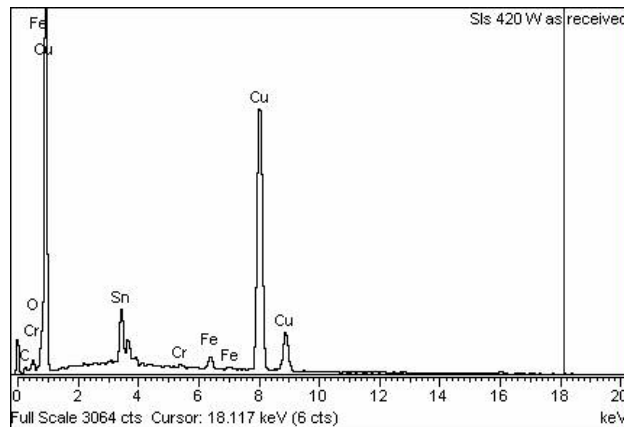


Figure 4.28. Energy dispersive chemical spectrum of as-received zone near border of laser polished track #3 in Specimen #3.

Again Cu (39 at.%) and Sn (3 at.%) are followed by C (22 at.%) and oxygen (34 at.%). Fe is present at 1 at.% together with a small atomic percentage of Si (less than unity).

The composition analysis of the spherical particle on Specimen #3 shown at the center of Figure 4.29 and found in the laser polished track #3, corresponded primarily to Al (28 at.%) and oxygen (57 at.%), as indicated in the chemical spectrum graphed in Figure 4.30. Cu and Fe are present in an atomic percent below unity. A Ca peak is also distinguished in this spectrum with a composition of 6 at.%; however, this peak may correspond to that of Sn. Alumina fine particles were trapped at the surface during the infiltration stage and emerged to the surface during the laser treatment.

The composition of the dark-colored phase surrounding these particles is rich in Cu (20 at.%), Fe (2 at.%), Cr (less than 1 at.%) and Sn (2 at.%). Al and Si are also present but in lower amounts of 6 at.% and 10 at.%, respectively. Cu, Fe, Al and Si are present in oxide form as the oxygen content is very high, 52 at.%. The amount of C (6 at.%) present in the dark colored phase is considerably lower compared to the as-received indicating that the polymer residues may have been burned off during the laser treatment.

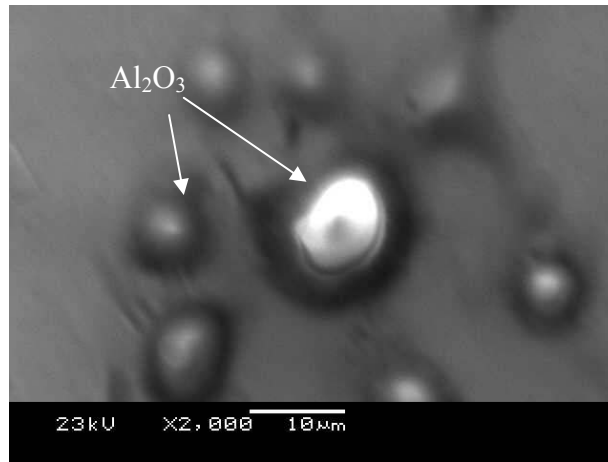


Figure 4.29. Magnified inner zone of Specimen #3 laser scanned track #3, 2000x. Showing a cluster of spherical particles embedded in a dark-colored phase.

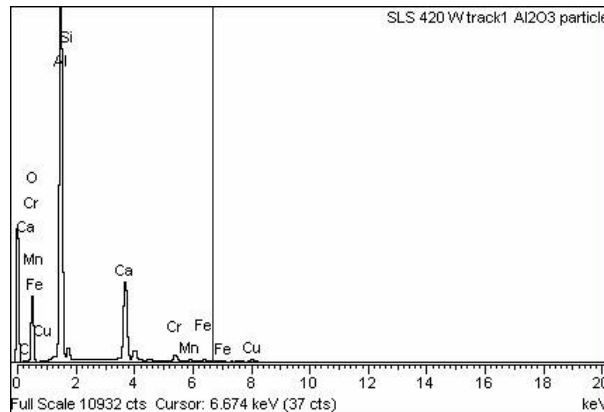


Figure 4.30. Energy dispersive chemical spectrum of spherical particle in laser polished track #3 in Specimen #3.

In Figure 4.31, a light-colored phase can be observed at the center of the image. The EDAX analysis indicates that it is rich in Cu (43 at.%) but the amount of oxygen present is relatively small (34 at.%) signaling that not all the Cu at the surface has been oxidized. There is also a higher content of Fe (5 at.%) compared with the as-received and dark colored phase. Again the C content (8 at.%) in this

phase is lower much lower than the as-received material. A light-colored phase can be associated with compositions having large fractions of a higher atomic number element likes Cu, relative to other elements of lower atomic numbrer, like Si, Cr and Fe in this particular case. The latter, when present at large fractions, will favor the formation of a dark-colored phase.



Figure 4.31. Magnified inner zone of specimen #3 laser scanned track #3, 1500x. Showing a light-colored phase.

A magnified inner zone of the surface of Specimen #4 corresponding to the laser polished track #3 is presented in Figure 4.32. In this image a dark-colored phase and a light-colored phase can be clearly distinguished as well as the presence of a cluster of spherical particles embedded in the latter phases. From a compositional point of view the main difference between the dark and light colored phases lies in the Cu content relative to the oxygen content. For the dark colored phase Cu is present at a 16 at.% and oxygen at 53 at.% indicating that all the Cu should be oxidized. On the other hand, the light colored phase has a higher

Cu content of 49 at% and a lower oxygen content of 20 at% signalling this time that a fraction of the Cu will be present as an oxide only. In both cases the amount of Fe was similar (6 at.%) and for the rest of the elements the only striking difference is a higher amount of Si in the dark-colored phase of 8 at.% compared to a 1 at.% of the light-colored phase. These compositions are in agreement with the quantities obtained from the semi-quantitative spectrochemical analysis done on Specimen #3 at the laser polished track #3 and #1.

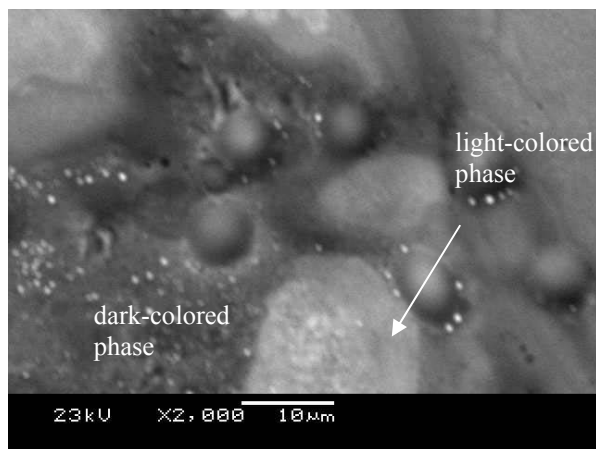


Figure 4.32. Magnified inner zone of Specimen #4 laser scanned track #3, 2000x. Processing parameters: 565 W,  $v_t = 2.71$  mm/s,  $v_s = 406$  mm/s. Showing a dark-colored phase and light-colored phase.

Figure 4.33 shows a spectrum pattern for one of the spherical particles seen in Figure 4.32. The pattern is similar to the one seen before in Figure 4.30, depicting the same strong Al, Si and oxygen peaks. These peaks again indicate that the spherical particles are composed mostly of alumina and silica. It is also likely that oxides of Cr and Fe were formed and that due to the low surface energy



of these oxides, they were not wet by molten copper and instead balled at the surface [5].

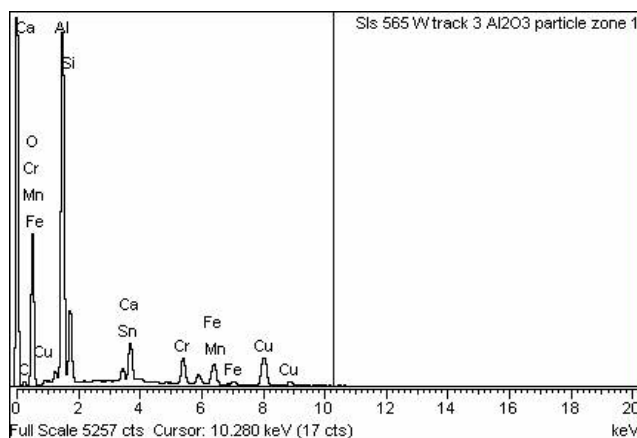


Figure 4.33. Energy dispersive chemical spectrum of spherical particle in laser polished track #3 in Specimen #4.

Finally, an interesting observation is presented in Figure 4.34. It consists of a phase not observed before, showing a flake-like-plate morphology having a main composition rich in Fe (41 at.%), oxygen (27 at.%) and Cr (13 at.%). The Cu content in this phase is low equal to 4 at.% and Sn was not detected. Al and Si are also present but in lower contents of 1 and 4 at.%, respectively. Because of the fact that Al and Si were already present as oxides and Cr is a stronger oxide former than Fe, there is no oxygen content left available for Fe to become oxidized after discounting the oxygen associated with  $\text{Al}_2\text{O}_3$ ,  $\text{SiO}_2$  and  $\text{Cr}_2\text{O}_3$ . This does not discard the possibility of Fe being oxidized.

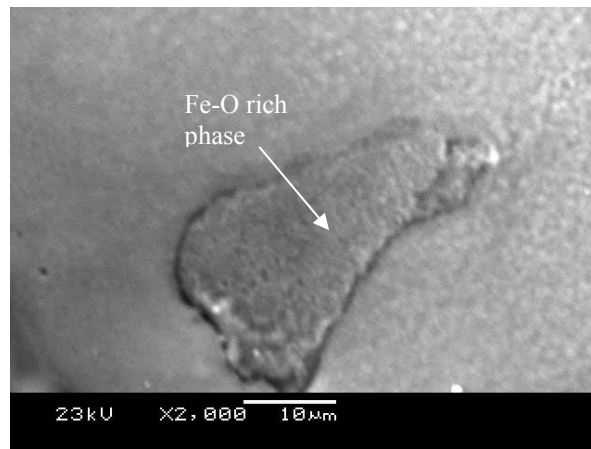


Figure 4.34. Magnified inner zone of specimen #4 laser scanned track #3, 2000x. Showing a Fe-rich phase.

Figures 4.35 and 4.36 show the energy dispersive chemical spectra of the Fe-rich phase and the surrounding phase, respectively. These two diagrams differ significantly in the intensity of their Fe and Cu peaks. From Figure 4.36, can be confirmed that the surrounding phase is rich in Cu (46 at.%) and oxygen (31 at.%). Al, Si, Cr and Fe were also present, however in lesser quantities. It is likely that these elements were present in the form of oxides such as  $\text{Al}_2\text{O}_3$ ,  $\text{SiO}_2$ ,  $\text{Cr}_2\text{O}_3$  and  $\text{Fe}_3\text{O}_4$ . Considering all the oxygen required to form these oxides, Only a 16 at.% would be available to oxidize Cu. This indicates that at least a 30 at.% of the Cu at the surface is oxygen free.

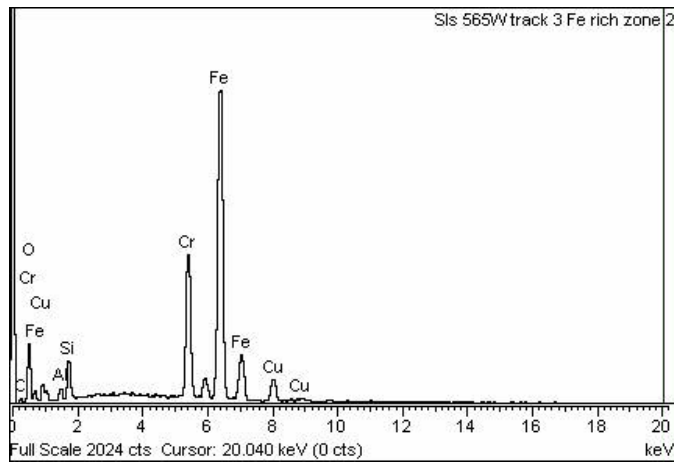


Figure 4.35. Energy dispersive chemical spectrum of Fe-rich phase in laser polished track #3 in Specimen #4.

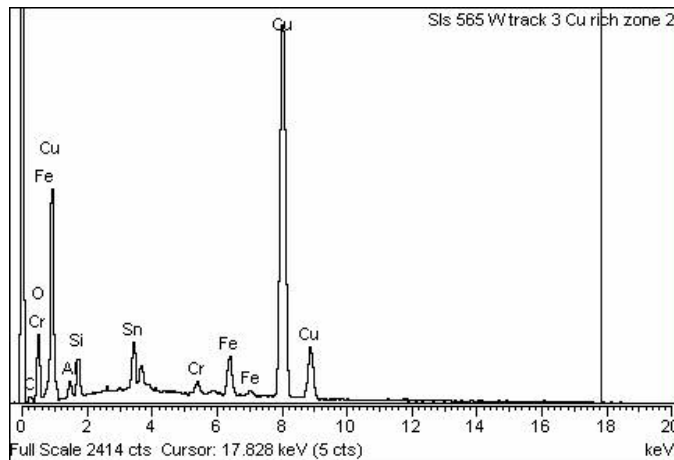


Figure 4.36. Energy dispersive chemical spectrum of Cu-rich phase in laser polished track #3 in Specimen #4.

Table 4.2 summarizes the chemical composition, in atomic percent, of the as-received surface, light-color and dark-color phases of Specimens #3 and #4. Moreover, the composition of the spherical particles is also included together the composition of the Fe-rich and Cu-rich phases observed in Specimen #4.

Table 4.2. Semi-quantitative chemical analysis (atomic %) of the surface of as-received and laser polished surface parts.

Element	As-received Spec. #3	As-received Spec. #4	Light phase Spec. #3	Light phase Spec. #4	Dark phase Spec. #3	Dark phase Spec. #4	Cu-rich phase Spec. #4	Fe-rich phase Spec. #4	Spherical particle Spec. #3 Figure 4.29
<b>C</b>	20	21	8	18	7	9	12	9	6
<b>O</b>	10	34	34	20	52	53	31	27	57
<b>Al</b>	-----	-----	1	<1	6	2	2	2	28
<b>Si</b>	-----	<1	4	1	10	8	3	4	2
<b>Cr</b>	<1	-----	1	1	<1	3	<1	13	<1
<b>Fe</b>	2	1	5	6	2	6	3	41	<1
<b>Cu</b>	62	39	43	49	20	16	46	4	<1
<b>Sn</b>	5	3	3	3	2	1	2	-----	-----

#### 4.1.6 X-ray diffraction analysis

Figures 4.37 shows the x-ray diffraction patterns of a generic indirect-SLS as-received surface. It shows the presence of the expected Cu-Sn phase corresponding to the bronze and the Cr-Fe phase corresponding to the stainless steel grade 420. An Al-Si-Cr phase probably formed as a result of the infiltration process was also indexed. However, it is known that the penetration of the x-rays can reach up to a couple mm from the surface, thus picking up most of the information from the bulk.

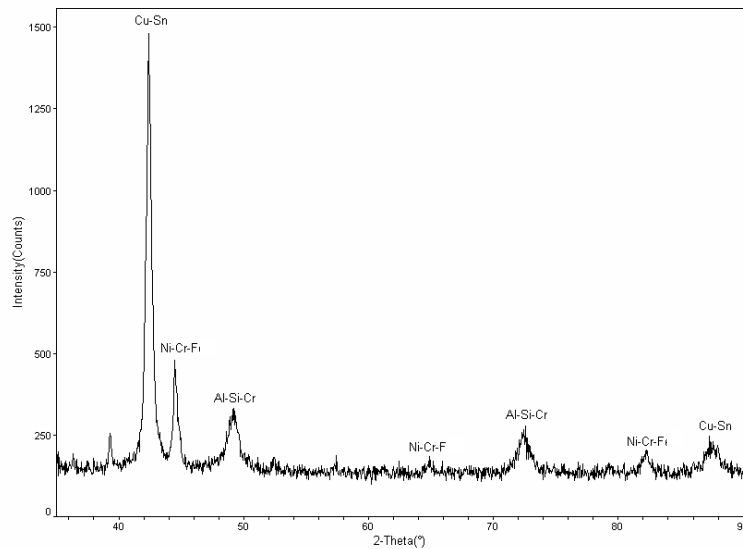


Figure 4.37. X-ray diffraction pattern of generic as-received indirect-SLS surface.

The fact that the laser polished tracks obtained were less than 2 mm in width and taking into account the large penetration of the x-rays in the material, determined that doing x-ray diffraction analysis on the polished tracks would not contribute to the understanding of the surface phenomena occurring. The diffraction of the x-rays would take place largely on the adjacent as-received surface and from the unaltered bulk making it difficult to interpret the results correctly.

#### 4.1.7 Modeling results

Numerical results of the different models that were previously described in Chapter II, Sections 2.1 and 2.2 are presented in this section. These results allow

in certain cases explanation of some of the behavior observed from the empirical data.

#### ***4.1.7.1 Surface temperature evolution***

The surface temperature at the middle position of the track width (1.9 mm) as a function of the interaction time for a raster-scan energy source and a line-energy source, is shown in Figure 4.38. The power level, and traveling speed in both cases is the same and equal to 565 W and 3.71 mm/s, respectively; the scan speed for the raster-scan source is 557 mm/s. It can be seen that for a line-source the peak temperature is approximately 40% higher than in the case of the raster-scan source at the end of the heating cycle. This is after the beam has traversed its own diameter. In terms of the overall energy conservation, this observation suggests that the substrate experiences a larger thermal load when a raster-scan source is used rather than a line source. Moreover, the heating cycle peak temperature due to the raster-scan source oscillates from 950 to 1100 °C, whereas for the line-energy source it increases monotonously up to the peak value.

However, during the cooling cycle, the amplitude of the temperature oscillation due to a raster-scan source is approximately 20% higher than the one corresponding to the line-energy source, but this difference decreases with cooling time until both temperatures become equal. The amplitude of the

temperature oscillation also decreases with cooling cycle time, until it becomes a single temperature.

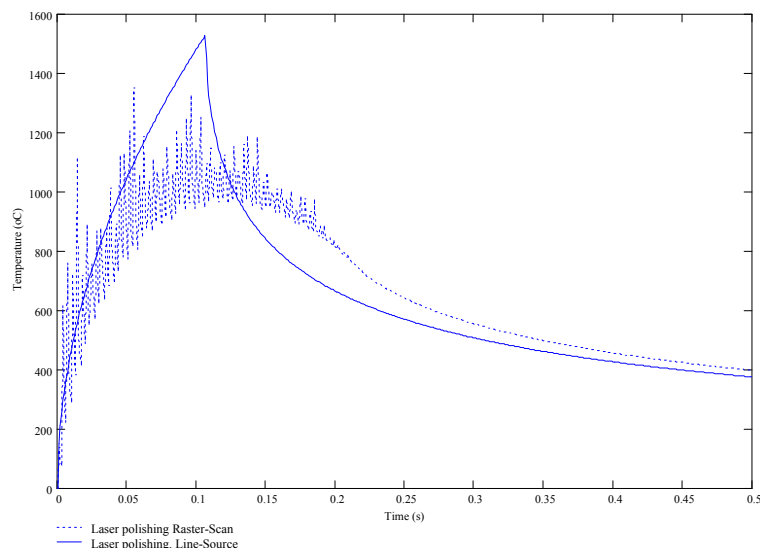


Figure 4.38. Surface temperature profile of raster-scan-spot energy source and line-energy source at 565 W laser power and 3.71 mm/s traveling speed (85 % heat losses accounted for in the model).

To set the peak temperature range above the peritectic temperature of the Fe-Cu material system used (i.e., 1094 °C), the losses by reflection of the laser beam, convection and radiation has to be accounted for up to 85% of the input laser energy. Figure 4.36 shows the actual space temperature distribution at the laser-material interaction zone obtained with a real-time capture infrared imaging system. The processing parameters used to make this laser polishing track were the same ones used to calculate the plot of Figure 4.39. The white inner zone in the image has an average temperature of 1040 °C for an emissivity parameter of

0.9, signaling that an even higher temperature was reached at the center of that ring.

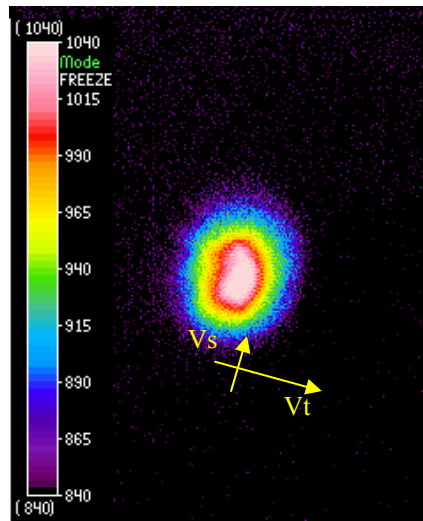


Figure 4.39. Infrared thermal image of interaction zone for a 565 W raster-scan laser beam traveling at 3.71 mm/s and scan speed 557 mm/s. Emissivity parameter was set to 0.9.

Two surface temperature profiles for a laser raster-scan polishing process are plotted in Figure 4.40 for two different power levels and a closely similar scan speed of 401.5 mm/s  $\pm$  4.5 mm/s. In the same graph, the peritectic temperature of 1094 °C and the liquidus temperature of 1440 °C corresponding to the Fe-Cu material system are plotted as well. This plot illustrates that for a laser power level of 420 W, melting of the Cu-rich phase occurs only as it does not go above the liquids temperature, whereas for a high power level of 565 W complete melting of the Fe-rich phase takes place. These temperature profiles were



obtained considering that the losses due to reflectivity of the laser beam by the surface, as well as conductive and radiation heat transfer to the surroundings accounts for an 80% of the incident beam energy.

From the same graph, it can also be observed that at 420 W the resident time of the melt is approximately 100 ms shorter than for 565 W. Those two factors indicate that the molten Fe-rich phase is more likely to be enriched with oxygen at 565 W rather than at 420 W. This could explain the marked contrast between the percent roughness  $R_a$  variation ( $\%R_aV$ ) obtained under this two sets of processing parameters (see Figure 4.5). At 420 W the  $\%R_aV$  measured was 56% while at 565 W it corresponded to -29%. Under these two processing conditions the surface over melt regime was established increasing the surface roughness above the as-received level. Particularly, at 565W the probability of forming a Fe-rich phase enriched with oxygen at the surface is higher, thus potentially diminishing the resulting roughness.

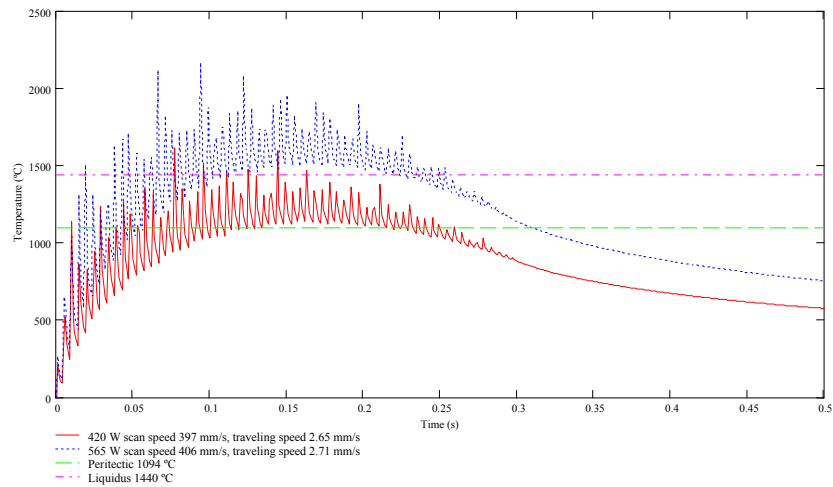


Figure 4.40. Surface temperature profile of two raster-scan energy sources of laser power 420 W and 565 W and 397 mm/s and 406 mm/s scan speed, respectively (80 % total energy losses accounted for).

Figure 4.41 shows another plot of two surface temperature profiles this time having approximately similar energy density values of  $948 \pm 11 \text{ J/cm}^2$ , but different processing parameters: 420 W and scan speed 115 mm/s, 565 W and 151 mm/s, respectively. The profile corresponding to 565 W shows a 600 °C higher bottom-peak temperature than the one obtained using 420 W, which shows a bottom-peak temperature of 1900 °C. However, the residence time above the liquidus temperature (1440 °C) is 100 ms longer for the profile evaluated at 420 W. The two profiles converge to the same temperature after 1.5 s have elapsed, reaching the peritectic temperature of the alloy system simultaneously.

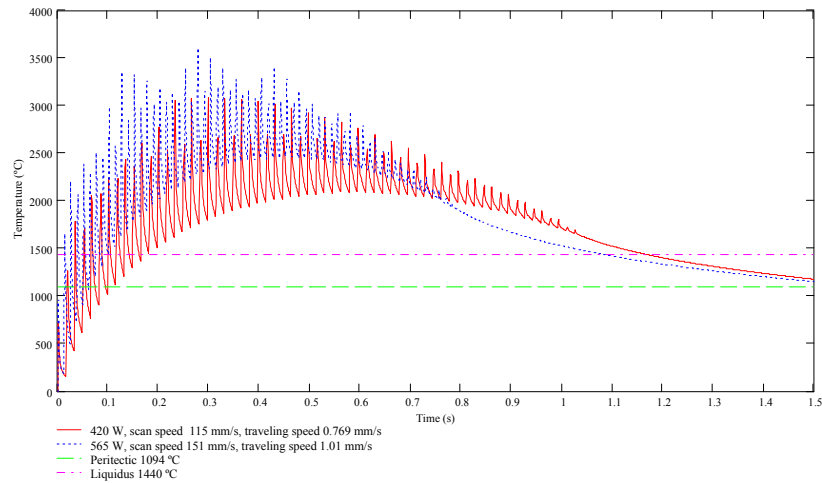


Figure 4.41. Surface temperature profile of raster-scan-spot energy source at constant energy density for different laser power of 420 W and 565 W and 115 mm/s and 151 mm/s scan speed, respectively (80 % total energy losses accounted for).

#### 4.1.7.2 Surface shallow melting

Table 4.3 provides the definition of the variables used and their approximate values obtained from [5,6] for bronze, used in generating the following numerical results. In principle, the surface-shallow-melting regime does not involve considerable melting depth as it is imposed that melting can not go beyond the precursor particle radii. The modeling then considered that a Cu-rich phase would be melted only, as this phase appeared primarily at the surface of the as-received specimens as shown in Figure 4.9. Therefore, this model assumes that the precursor powder at the surface consists mostly of a Cu-rich phase. The precursor powder used to produce the green part was assumed to have an average

particle radius of 10  $\mu\text{m}$ . The laser power levels considered in the model were 220, 334 W, 420 W and 565 W while the traveling speeds varied from 5.5 to 8 mm/s. The assigned width of the polished tracks was 1.9 mm and their length was 25 mm.

Figure 4.42 is a plot of the percent roughness variation ( $\%R_aV$ ) as a function of scanning speed based on Eq. 2.24-2.30 and 2.35 (see Chapter II). To obtain the percent variation in surface roughness, the as-received  $R_a$  value was also computed from Eq. 2.35, but in this case using a zero filled height and a melted sphere radius equal to 10  $\mu\text{m}$ . This yielded an as-received  $R_a$  value of 9.6  $\mu\text{m}$ , which is larger than the measured as-received  $R_a$  value. However, when plotting the  $\%R_aV$ , the data were normalized and the scaling effect from the model was then removed. Table 4.3 presents the variables included in the model as well as their values and units.

It is observed that the proposed model renders a  $\%R_aV$  that behaves accordingly with the description of the surface-shallow-melting mechanism. That is, the resulting  $R_a$  value (below the as-received value) decreases with decreasing traveling speed. In terms of the  $\%R_aV$ , the model predicts that a negative percent variation is obtained for all the power levels used. The percent variation was larger as power increased and the traveling speed decreased. As the power level is

increased it can be seen also that the relative change in  $\%R_aV$  is less, indicating the mechanism becomes less sensitive to processing speed at high power.

Additionally, the percent energy losses associated with each power level was varied from 8% at 225 W to 55% at 565 W, so that the average temperature of the melt was at least equal or higher than the peritectic temperature of the Fe-Cu system (i.e., 1094 °C) but not higher than the vaporization temperature of the alloy (approx. 2500 °C). The increase in percent energy losses with increasing power level may be explained by the fact that a higher superheating of the melt means larger losses by radiation heat transfer.

Table 4.3 Definition of variables used in modeling the SSM mechanism.

Variable	Definition	Value
P	Laser power	225-565 W
$\mathcal{R}$	Reflective and convective losses	0.08-0.55
$\rho$	Density of solid and liquid	8887 kg/m <sup>3</sup>
$C_{p_s}$	Heat capacity of solid phase	383 J/kg°C
$C_{p_l}$	Heat capacity of liquid phase	647 J/kg°C
L	Latent heat of fusion	205363 J/kg
k	Heat conductivity of solid	370 W/mK
$D_L$	Laser spot diameter size	0.390 mm
$R_p$	Powder particle radius size	10 $\mu$ m
$\delta$	Thickness of substrate	7.0 mm
$v_s$	Laser beam scan speed	5.6 - 7.8 mm/s
$T_{MAX}$	Maximum surface temperature	> 1094 °C
$T_m$	Melting temperature	1094 °C
$\eta$	Viscosity of the liquid	4.3 mPa/s
$\gamma_{LV}$	Surface tension of liquid-vapor	1.385 J/m <sup>2</sup>
$r_m$	Radius of hemisphere after melting	
$z_f$	Filled height	

From the model it was also possible to observe that traveling speeds lower than 5.5 mm/s would cause melting of the hemispherical caps beyond the limits of the surface- shallow-melting mechanism, and the onset of the surface-over-melt would occur. Thus, a different mechanism was required (see next section). For traveling speeds higher than 8 mm/s, the temperature of the surface was lower than 1094 °C meaning that no melting should occur with no roughness reduction. The first observation indicates that as the experimental laser polishing trials were all done with speeds lower than 5.5 mm/s, the probability of the SSM mechanism dominating the process is low, and it is more likely that an early onset of the SOM had taken place.

The plotted values in Figure 4.42 were obtained after increasing the  $f_2$  parameter (Eq. 4.26) within 2% of its original value. Two percent more energy was required to go into the substrate by heat conduction to balance the energy equation (Eq. 2.24) adequately. This adjustment implies that the temperature profile imposed on the substrate given by Eq. 2.27 differs from the real substrate temperature.

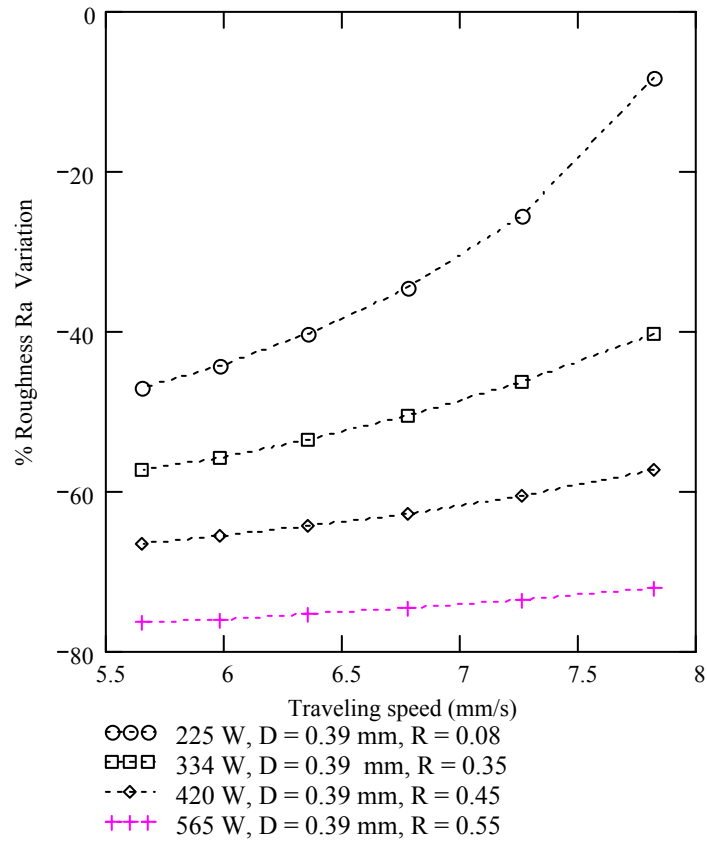


Figure 4.42. Plot of modeled percent roughness  $R_a$  variation versus high traveling speeds for average particle radius size of  $10 \mu\text{m}$ .

A necessary condition for the energetic model to be valid is the average solidification time for each scan speed must be longer than the corresponding average spreading time. From Figure 4.43 it can be observed that the time for solidification at 565 W is larger than the spreading time by several orders of magnitude for all scan speeds. This is a good indication for the validity of the

model considering the crudeness of the kinetic model implemented (see Chapter II Eq. 2.31-2.33).

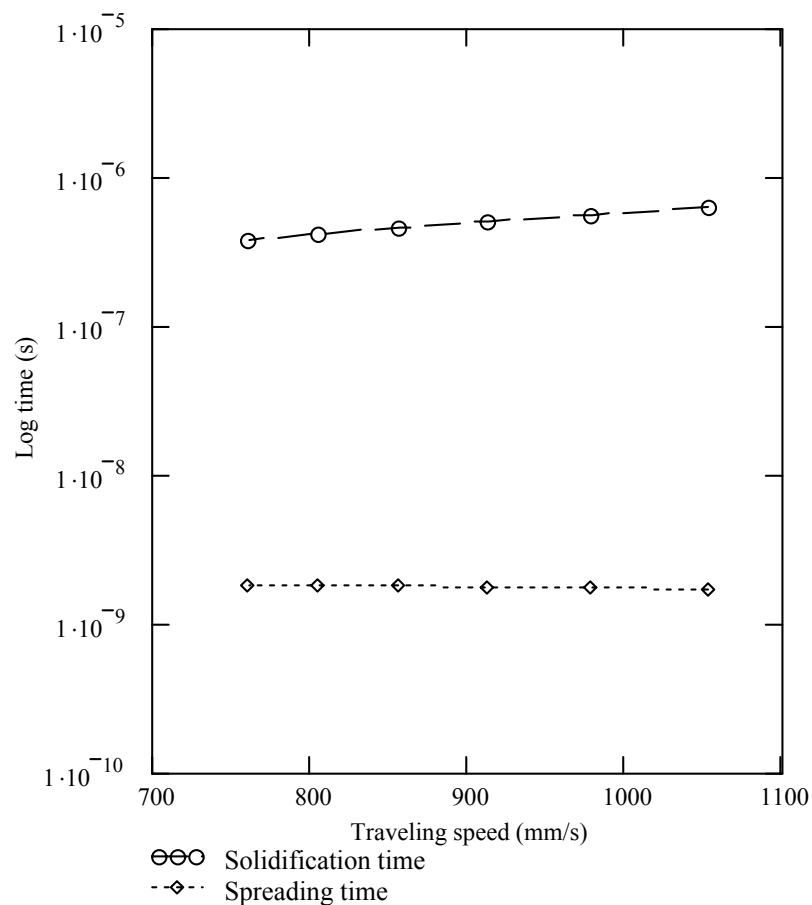


Figure 4.43. Plot of the modeled solidification and spreading average times versus scan speed for  $R_p = 10 \mu\text{m}$  at 565 W.

The spreading time appears to decrease slightly as the scan speed increases, in agreement with the decrease in melted volume and decrease in filled trough height. However, the solidification time oddly increases with increasing



scan speed. One possible explanation is that the superheating of the melt decreases more in relative terms to the decrease in radial depth of melt of the hemispherical caps at high scan speeds than at low scan speeds (see Eq. 2.33). This again may be associated with the expression given by Eq. 2.27 used to obtain the surface temperature.

#### **4.1.7.3 *Surface over melting***

The results of the thermo-physical model for surface over melting (SOM) described previously in Chapter II Section 2.2.2, are plotted in Figure 4.41 as percent roughness  $R_a$  variation data ( $\%R_aV$ ) together with experimental data measured from several laser polished tracks performed on LaserForm-ST100<sup>TM</sup> specimens. The as-received  $R_a$  value of the surface was  $2.48 \mu\text{m} \pm 0.25 \mu\text{m}$ . The laser power was kept fixed at 334 W and the scanning speed was varied from 692.7 to 101.3 mm/s. However, only the  $\%R_aV$  results for traveling speeds ranging from 1.06 mm/s (177.2 scan speed) to 0.61 mm/s (101.3 mm/s scan speed) are plotted below, as this is thought to be part of a fully developed surface-over-melt regime. Table 4.4 presents the variables included in the model as well as their values and units. As the melt depth encountered in the SOM mechanism is vastly larger than the depths found in the SSM mechanism, the physical properties

in this model corresponded to a 60 wt.% stainless steel grade 420 - 40 wt.% bronze (5 wt.% tin) alloy mixture instead of the pure bronze properties.

Table 4.4. Definition of variables used in modeling the SOM mechanism.

Variable	Definition	Value
P	Laser power	334 W
R	Reflective and convective losses	0.35
$\rho$	Density of solid phase	8199 kg/m <sup>3</sup>
$\alpha$	Thermal diffusivity of solid phase	4.663*10 <sup>-5</sup> m <sup>2</sup> /s
L	Specific latent heat of solidification	233600 J/kg
K	Heat conductivity of solid	162.9 W/mK
K <sub>MOD</sub>	Modified heat conductivity	226 W/mK
v <sub>SCAN</sub>	Laser beam traveling speed	0.61-1.06 mm/s
T <sub>M</sub>	Melting temperature	1440 °C
T <sub>O</sub>	Initial temperature	25°C
$\mu$	Viscosity of the liquid	5.531 mPa/s
$\sigma$	Surface tension of liquid-vapor	1.62 J/m <sup>2</sup>
d $\sigma$ /dT	Surface tension temperature coefficient	-0.252 mJ/m <sup>2</sup>

From the plot in Figure 4.44, it can be seen that the modeled data showed a sign reversal in the %R<sub>a</sub>V value with decreasing scan speed, going from a negative percent variation to a positive percent variation. This indicates that an early onset of the SOM mechanism could provide roughness reduction if the processing parameters are such that the depth of melt is large and the superheating achieved is low, thus reducing the wave amplitude [7]. The experimental %R<sub>a</sub>V values show the same trend as the modeled values within the same order of magnitude in percent variation, except for a larger scattering associated with the

presence of long-streamed oxide clusters previously illustrated as well as the surface roughness measurement procedure.

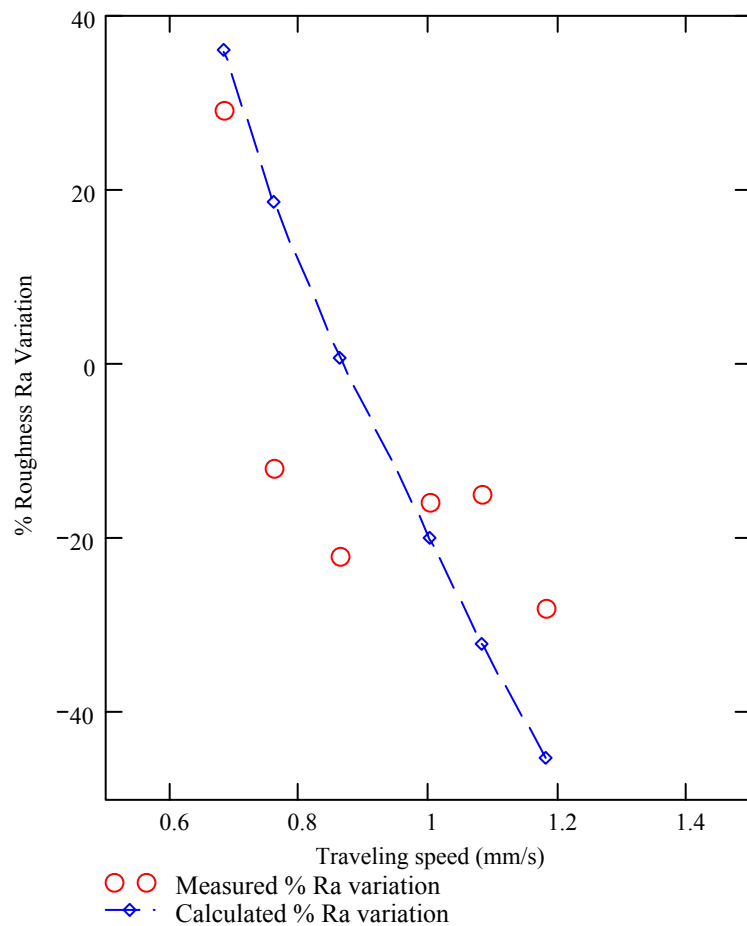


Figure 4.44. Plot of experimental and modeled percent surface roughness  $R_a$  variation data versus traveling speed for Specimen #2.

The experimental  $\%R_aV$  values corresponding to a laser power of 220 W, 420 W and 565 W shown in Figure 4.4 and 4.5, also show a similar sign reversal trend in the percent roughness variation with decreasing traveling speed. This suggests that the ratio between the degree of superheating of the melt to the depth

of melt does not vary significantly with power in the case of a laser raster-scan process.

From the model results, it can also be inferred that as the scan speed is lowered, the surface temperature immediately under the center of the laser beam increases, increasing the amplitude of the surface wave, but simultaneously the depth of melt is increased and so is the solidification time. These latter two variables tend to decrease the relief amplitude; however, the effect of surface temperature overwhelms them. Moreover, the effect of adding a surface curvature term (Eq. 2.43) brings the amplitude down to a reasonable order of magnitude. The latter term and the viscous damping term depend on the characteristic wavelength  $\lambda$  of the solidified surface periodic structure (refer to Chapter II).

A plot of the measured average characteristic wavelength  $\lambda$  for each laser track is presented in Figure 4.45. Its trend is much the same as that of the modeled  $\%R_aV$  values. Therefore, we can infer that this parameter plays a significant role in the determination of the amplitude of the surface relief. As for the second periodic pattern observed under the SEM (Figures 4.18 and 4.19d), this model does not take into account its additive effect on the modeled surface roughness. However, it can be considered as part of the noise when measuring the  $R_a$  value of the treated surfaces experimentally.

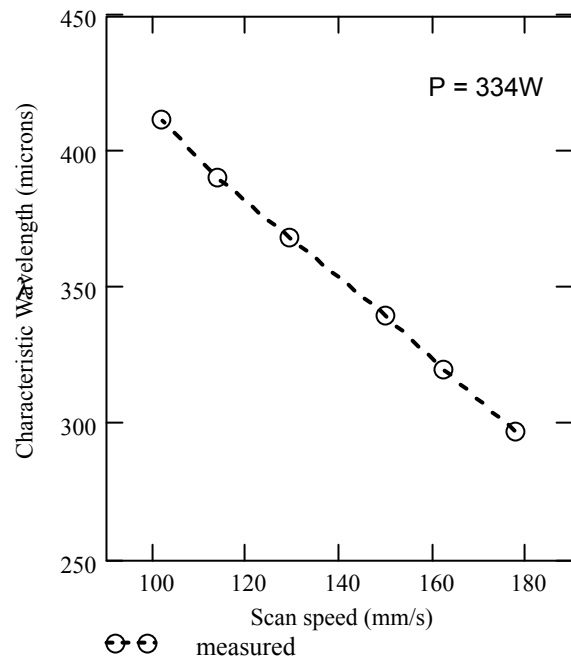


Figure 4.45. Plot of the measured average surface wavelength  $\lambda$  versus scan speed in Specimen #2.

## 4.2 LASER INDUCED CEMENTATION OF CYLINDRICAL C/C COMPOSITES

Presented in this section are the characterization results of the laser fusion coated flat carbon-carbon (C/C) composite and laser induced cementation coated cylindrical carbon-carbon (C/C) composite specimens. A full description of the parameters used to process these specimens can be found on Appendix B-II. Optical and Scanning electron micrography (SEM) as well as semi-quantitative energy dispersion analysis of x-rays (EDAX) results of the cross-section and surface of the coated C/C composites are discussed with regard to coating thickness and continuity achieved, interface bond type, stabilized phases, and defect formation. X-ray diffraction analysis done on some of the coated specimens as well as on the final coating material is presented too. Determination of the coefficient of thermal expansion (CTE) of the coating material as well as the its phase transformation was done by means of thermo-mechanical analysis (TMA) and differential temperature analysis (DTA), respectively. The latter results are plotted for the laser fused slurry material and compared to the furnace heat treated slurry material. The critical stress intensity factor  $K_{Ic}$  of the final coating material after being the laser treated was measured by the indentation fracture technique. The cylindrical coated C/C composites were heat treated at 1000°C in air for several hours to determine the oxidation resistance performance of the coating sequence. The results are presented as a percent weight reduction

versus heat treatment time. From these results a percent weight reduction rate was estimated. Additionally, numerical results of the cooling temperature evolution inside a bi-layer cylindrical body as well as of the magnitude of plane stress and plane strain state in cylindrical coordinates within the coating layer are presented. These results allowed better understanding of the conditions that drove crack extension in the cylindrical coatings as a function of their radial thickness and cooling time.

#### **4.2.1 Preliminary results: planar C/C composite surfaces**

At the initial stage of this research, multiple 3D weaved flat carbon-carbon composites (C/C composites) of different sizes (provided by Karta Technologies, Inc.) were laser fused coated at The University of Texas at Austin using different coating mixtures and laser raster-scan schemes to determine the parameters that could provide complete and homogenous coating of the overall surface with minimal cracking and no delamination after the fabrication process. Figure 4.46 shows the appearance of an as-machined flat 3D C/C composite before it was laser fused coated.

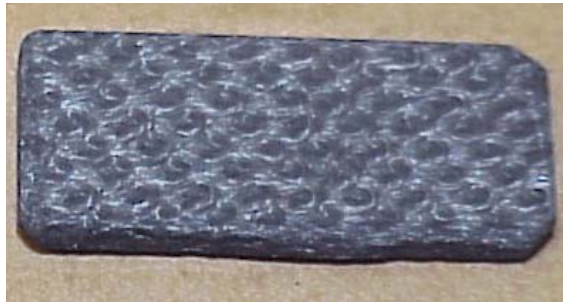


Figure 4.46. As-machined C/C composite sample.

Figure 4.47 shows a close up image of the surface texture of an as-received rectangular C/C composite specimen similar to the specimen shown in Figure 4.46. It is observed that the surface is inherently rough, providing a larger interface area for mechanical interlocking. However, it is known that for certain geometries, surface roughness hinders wetting and formation of a continuous reactive bond due to the presence of sharp grooves [8].

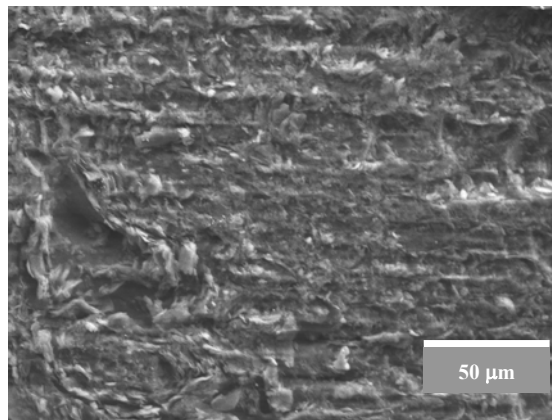


Figure 4.47. SEM image of 3D weaved C/C composite rough surface, 1000x.



Figure 4.48 shows an SEM image of the surface of one of the first C/C composite specimens (#6) that was coated with a pure silicon layer by means of the laser raster-scan fusion process. The process was done at 240 W and a traveling speed of 5 mm/min. Complete wetting of the surface with pure silicon was not achieved, most probably due to the presence of surface adsorbed oxygen resulting in the formation of a silica ( $\text{SiO}_2$ ) layer. Presence of a silica layer on the surface also alters the surface tension balance and favors solidification with higher wetting angles. A  $\beta$ -SiC continuous interfacial layer at the substrate is most likely to form, apparently independently of time, as soon as the molten silicon wets the surface [9]. The thickness and extent of this interfacial layer will be a function of the laser dwell time during which time the silicon remains at or above its melting temperature. According to Shewmon [10], for C atoms to diffuse 1 micron into silicon at least 10 seconds of diffusion time are needed.

Longer dwell times involve slower scanning speed and larger beam overlap. However, longer dwell times will lead to longer exposure times of the slurry to contaminants such as oxygen that hinder the wetting of the composite surface. This suggests that an optimum dwell time exists that minimizes the wetting angle caused by exposure to impurities and maximizes the reaction layer thickness which is controlled by atomic diffusion.

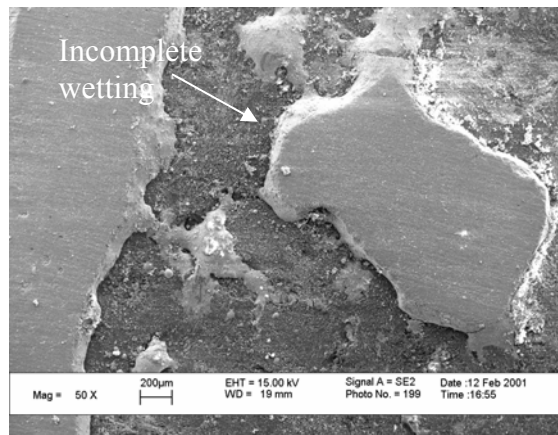


Figure 4.48. Surface of Specimen #6, Si coating indicating signs of incomplete wetting of the surface, 50x. The surface has been coarse polished.

To improve wetting of the C/C composite surface by silicon, the composition of the chemical slurry was modified by adding 10 wt.% of hafnium carbide. HfC is a refractory compound that melts at about 3900°C. The high heat capacity of this carbide [11] is thought thermally to stabilize the melting front and aid in even spreading of the molten slurry possibly by a dragging mechanism, as the melt region is stirred by Marangoni's type flow [1,12].

The formation of a hypereutectic pattern can be observed at higher magnification in Figure 4.49 corresponding to the surface of coated Specimen #16. The Hf-Si phase diagram shows that a eutectic point is present at approximately 70 wt% Si and that the eutectic temperature corresponds to 1330°C [13]. The white microconstituents correspond to Hf which appears with that contrast due to hafnium high atomic number. Eventually, HfC may have dissolved and carbon atoms may have dissociated from it and may have diffused towards

the surrounding Si. The eutectic phase lowers the melting point of the mixture and therefore increases the level of superheating, which in turn reduces the viscosity of the molten slurry allowing it to flow with less difficulty. This coating was consolidated at 1020 W and a traveling speed of 0.28 mm/s.

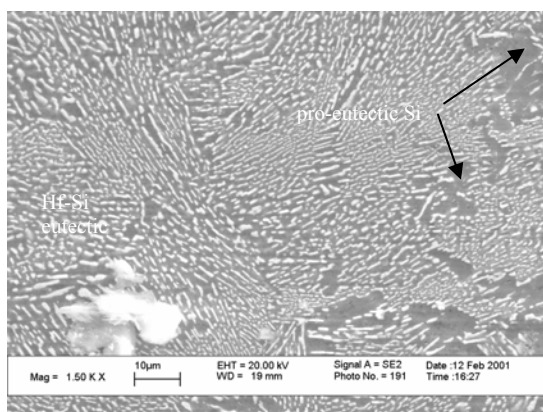


Figure 4.49. Surface of Specimen #16, 1500x of Si-10wt.%HfC coating indicating a eutectic-like morphology.

As illustrated in Figure 4.50, a network of long cracks can be seen on the surface of Specimen #16. These have probably originated due to the large CTE mismatch between the Si-HfC coating and the C/C substrate. These cracks are deleterious to the oxidation protection of the substrate by the coating.

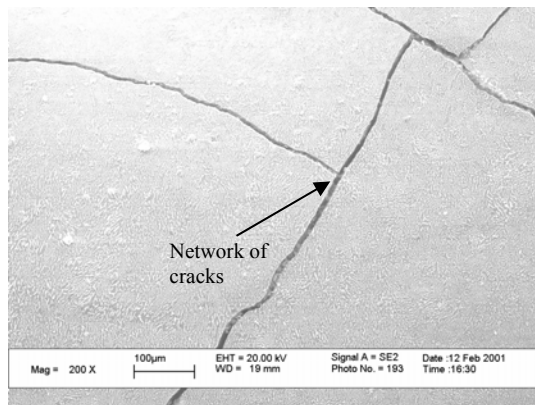


Figure 4.50. Surface of the coated surface of Specimen #16, showing a network of cracks, 200x.

Figure 4.51 and 4.52, show photos of two different 3D C/C composite specimens that have been laser fused coated. In both these specimens the laser has raster-scanned the surface from left to right. Figure 4.51 shows a 28 mm x 10 mm x 3 mm rounded edge specimen coated with a first layer of Si-20SiC-5Ti-5Al mixture (wt.%). Good spreading of the coating is seen but balling is still present. Figure 4.52 shows a tapered specimen coated with a Si-15HfC-10Ir-5Ti mixture (wt.%) along its entire length. The taper was used to increase the substrate mass as the laser beam reached the end of the specimen. This compensated for the heat accumulation and therefore inhibited excessive temperature increase as the laser advanced. In both specimens the temperature at the beginning of the sample up to 1/5 of its length is not high enough to melt the coating and produce good spreading and bonding to the substrate. There were three remedies to this problem: use thinner specimens, scan the specimen from right to left during a

second coating step, or to start the laser with the highest power possible and ramp the power down as the laser advanced to the opposite end. The last option was implemented when coating the specimens that followed.

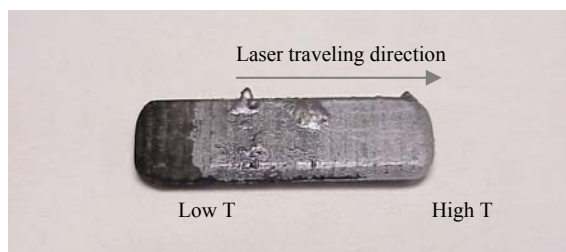


Figure 4.51. Specimen #71, first coating layer consisting of Si-20SiC-5Ti-5Al.

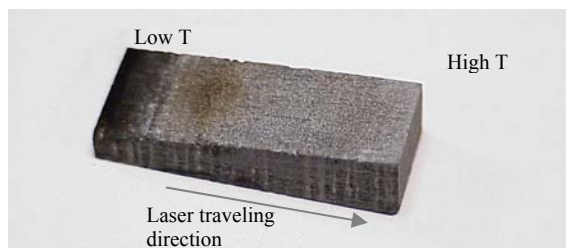


Figure 4.52. Specimen #67. Tapered specimen showing first coating layer consisting of Si-15HfC-10Ir-5Ti.

Figure 4.53 shows a high density of networking cracks in Specimen #71. To mitigate the deleterious effect of the numerous cracks seen, an overcoat layer was applied on the specimen. This final coating step consisted of dipping the specimen into an ethyl-silicate agent (SILBOND™) for 10 minutes followed by curing at room temperature in air for 24 hours. The sealant agent was observed to

penetrate the cracks due to its extremely low viscosity, and it formed a glassy layer on the sample surface.

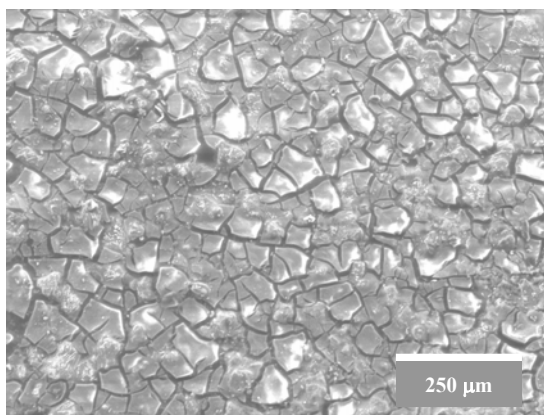


Figure 4.53. Surface of Specimen #71 illustrating surface of final layer of Si-15HfC-10Ir-5Ti (wt.%) laser fused coating, 200x.

Figure 4.54 shows Specimen #261 prepared for oxidation performance testing. Its coating sequence consisted of two layers per side of a mixture of Si-10SiC-10CrCl<sub>3</sub>-30HfC (wt%). The coating mass deposited was approximately 400 mg, the laser power was ramped down from 780 to 300 W, and the traveling speed was kept constant at 0.15 mm/sec. Vacuum pressure of 1mTorr (obtained by a diffusion pump) and a direct argon shroud were used. The overall laser fusion coated surface appeared to be well spread and no signs of delamination were seen. However, surface pitting was present. After the laser fusion process, the specimen was also dipped into SILBOND™ (ethyl silicate solution) for 10 minutes and cured at room temperature in air for 24 hours. Infiltration of the

surface grooves was observed to occur driven by a capillary pressure providing a possible crack sealing mechanism. Alumina cement was then applied manually around its perimeter as this zone showed signs of incomplete coating.



Figure 4.54. Specimen #261 prepared for weight loss testing, coating consisted of Si-10SiC-10CrCl<sub>3</sub>-30HfC (wt.%) and SILBOND<sup>TM</sup> overcoat layer.

Specimen #270 is shown in Figure 4.55 after the laser fusion coating sequence was applied at both sides, consisting of a first layer of pure Cr followed by a second layer of Si-10SiC-10Cr-20HfC-6Ir layer. The total coating mass deposited was approximately 800 mg, the laser power was ramped down from 840 to 400 W, and the traveling speed was kept constant at 0.15 mm/sec. Vacuum pressure of 200 mTorr and a direct argon shroud were also used. The overall surface of the specimen appeared to have been completely coated with a homogenous layer of coating material. Ripple-like features were observed over the surface of the specimen. The coated specimen was then dipped in SILBOND<sup>TM</sup> solution.



Figure 4.55. Specimen #270, after being laser fusion coated at both sides.

The percent weight reduction test results performed at Karta Technologies, Inc. on flat C/C composite specimens # 259, 261, and 270, at 1000° C in flowing air (2 cfh) for up to 7 hours are plotted in Figure 4.56. For comparison purposes, a bare flat specimen was also tested and showed a 87% weight reduction after 1 hour of oxidation test. It can be noticed that Specimen #259 (coating sequence: Ti-20HfC, Si-67HfC-14Ti, (wt.%) and SILBOND™) experienced a 64% weight reduction after seven hours of exposure, while Specimen #270 had undergone a 38% weight reduction after only two hour of exposure. These results indicate that the rate of percent weight reduction of Specimen #259 was almost a third that of Specimen #270 and a tenth of the bare specimen. The enhanced performance of Specimen #259 could be explained by the higher coating mass (1.03 grams) applied to this cylinder and the addition of Ti in the coating mixture. Titanium promotes formation of a TiC reaction layer at the interface while reducing the effects of oxygen contamination by dissolving oxygen in the Ti( $\alpha$ ) phase. On the other hand, Specimen #261 showed an 80% weight reduction after 4 hours of



oxidation exposure. This oxidation rate is comparable to that of Specimen #270. However, the coating mass of Specimen #261 (400 mg) was half that of Specimen #270 (800 mg). It is possible that HfC and iridium when mixed together can undergo a Lewis Acid-Base type exothermic reaction that creates an Hf-Ir intermetallic compound [14], which could lead to a further increase in the CTE mismatch between the coating and substrate. This could increase crack formation during fabrication and testing.

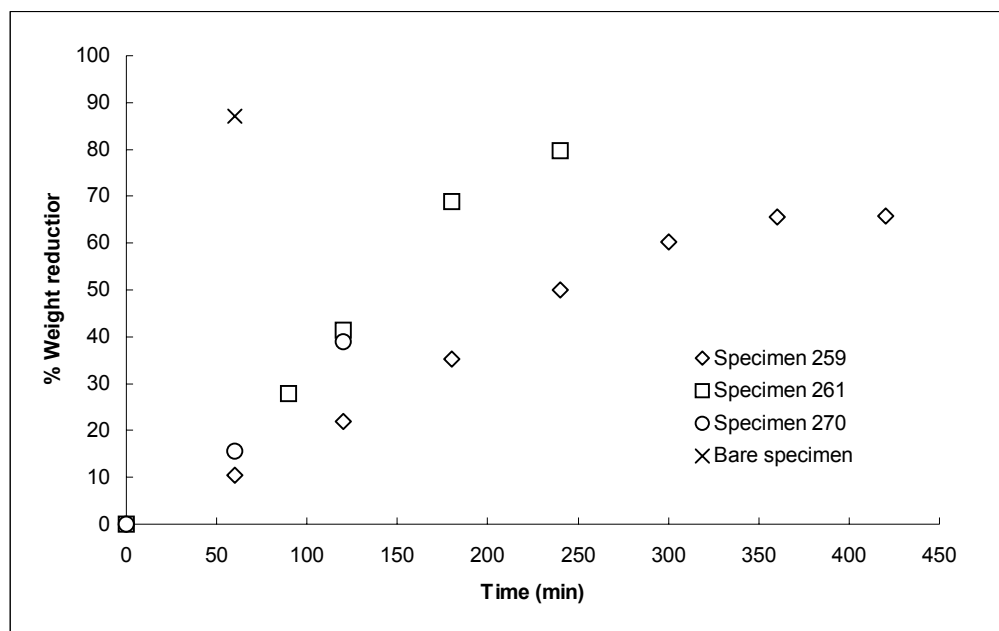


Figure 4.56. Percent weight reduction versus heating time at 1000 °C in flowing air 2 cfh for different planar specimens.

At the end of the weight loss tests, the C/C composite substrate of each specimen was highly consumed leaving only the coating shell signaling that air was able to penetrate the shell through the pre-existing cracks. It appeared as

though the SILBOND™ overcoat did not provide an effective crack sealant mechanism. SEM revealed severe cracking of the coating shell, while EDAX indicated a strong Si and oxygen peaks at the surface possible due to the applied SILBOND™ overcoat. The surface of Specimen #270, as shown in Figure 4.57, revealed the presence of a network of cracks formed during the fabrication process plus severe fracture of the coating occurring during the weight loss test. Most of the composite matrix material was oxidized leaving only the carbon fibers.

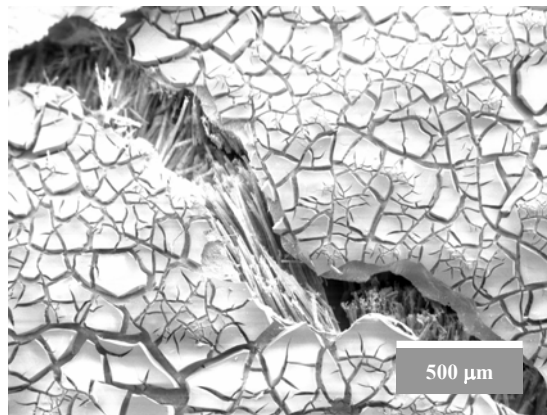


Figure 4.57. Surface of Specimen #270 after weight loss testing for 2 hours, 100x.

Later on, it was confirmed that the ethyl silicate solution underwent severe cracking after drying allowing air to penetrate through the crack troughs. It was found afterwards that for SILBOND™ to work effectively as a crack sealant, it required a specific furnace curing cycle to form a continuous glassy phase. No further attempts were made to use SILBOND™ as a final overcoat due to the

difficulty in finding public information regarding the proper curing cycle to form a continuous glass phase from this agent.

## 4.2.2 Refractory coatings achieved on C/C composites cylinders

### 4.2.2.1 Overall shape and appearance of refractory coatings

Figure 4.58a illustrates a rendered CAD image of the geometry of the C/C cylinders used in the Laser Induced Cementation process indicating its dimensions. Figure 4.58b shows the image of an actual bare as-machined 3D weaved C/C composite cylinder provided by Karta Technologies, Inc. The average overall surface area of these specimens not considering the stem added for handling purposes corresponds to 785.4 mm<sup>2</sup>.

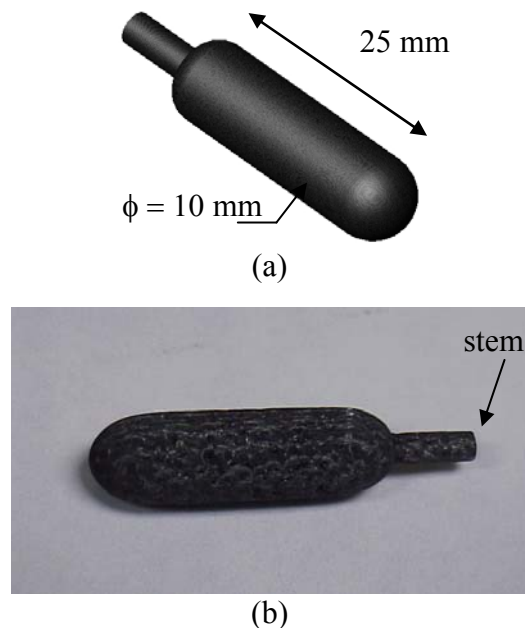


Figure 4.58. (a) Rendered CAD image of C/C composite cylinder. (provided by West [15]) (b) Bare as-machined 3D C/C composite cylinder.

Figure 4.59 illustrates the theoretical temperature at the surface of the coating material during a preheating stage and a melting stage in the LIC process (see Chapter II Section 3.3). For comparison purposes the temperature profile from a equivalent line-energy source process is also included. The thermal/physical properties considered in this example corresponded to an equal mixture of coating layers #2 and 3# corresponding to Si-25Cr-5C (wt.%) and Si-15HfCl<sub>4</sub>-15Cr (wt.%), respectively. Because hafnium chloride decomposes into Hf<sup>+</sup> and Cl<sup>-</sup> ions, the latter were assumed to recombine into chlorine gas Cl<sub>2</sub> and leave the coating so its contribution to the physical properties could be obviated. For the preheating stage the laser power was set to 200 W and the angular speed of the cylinder to 0.0785 rad/s. On the other hand, for the melting stage the power was set to 800 W and the angular speed to 0.0349 rad/s. In both cases the scan speed was set to 565 mm/s and the number of scan lines per inch to 4000 for a total scan period of 3 minutes. A 40% energy loss was considered for the preheating stage and 80% was used for the melting-stage. As in the latter, the temperatures are higher and the process lasted almost twice the time. From the obtained temperature plots at the center of the cylinder, it can be observed that for the melting stage the melting temperature of the coating material is reached after 1.5 seconds and the melt residence time lasted for 2 seconds.

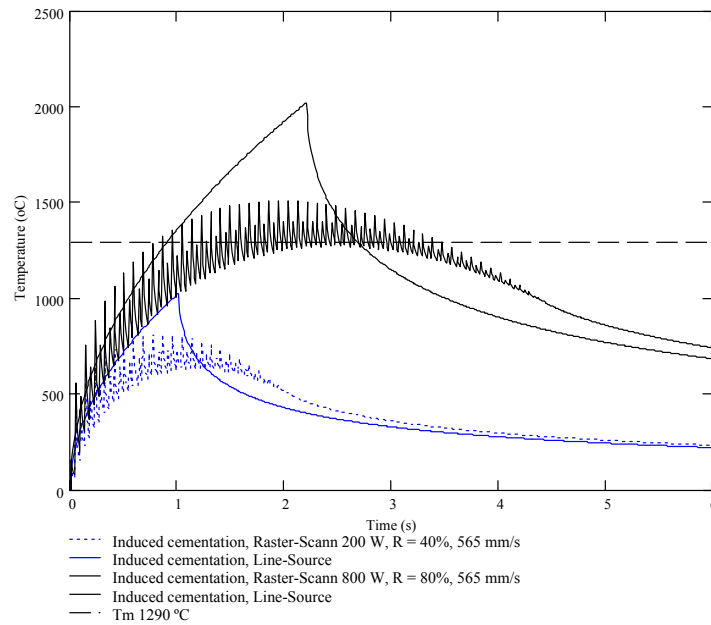


Figure 4.59. Theoretical temperature profile obtained at the surface of a coated C/C composite cylinder during the LIC process.

Considering the temperature profile for the corresponding line-energy source, it can be seen that the melting temperature is reached after 1 second, but it lasted less than 2 seconds. A larger peak temperature of almost 2000 °C is achieved followed by a steep cooling rate. These features are undesirable for the LIC process and can cause vaporization of the coating material and induced cracking, respectively. During the preheating stage the maximum temperature achieved in the raster-scan process did not go above 700°C, and it lasted for about 1 second above 500°C, followed by gradual cooling. In the case of the line-energy source, the peak temperature reaches 1000°C, and it is also followed by a very steep rate of cooling.

In Figure 4.60 it can be observed that an overall homogenous surface coating was achieved on a C/C composite specimen (# C2) after the LIC process. The coating sequence in this case included a first layer of pure Cr followed by a layer of Si-10SiC-10Cr-20HfC-6Ir (wt.%). Alumina cement was applied at the side of the cylinder where the stem once was, as the stem had to be removed leaving an exposed carbon zone. The horizontal depression line seen at the middle of the cylinder is where the laser beam began scanning when the rotation of the cylinder had not yet started. Because of the low oxidation resistance performance of this coating scheme, caused by the reaction between HfC and Ir, it was decided to exclude Ir in the following coatings and also replace HfC by HfCl<sub>4</sub> as this salt could dissociate and leave the Hf<sup>+</sup> ions free to react with Cr and Si in the slurry during the LIC process. Availability and economic reasons also favored the removal of Ir and the use of HfCl<sub>4</sub> instead of pure Hf.

It was also noticed that a mixture of pure Cr with CrCl<sub>3</sub> hydrous salt gave better coating results than a pure Cr coating. Metals chloride salts tended to undergo an olation-polymerization reaction when combined with isopropyl alcohol [16]. This provided better adhesion of the slurry to the C/C composite slurry during the LIC process.



Figure 4.60. Specimen # C2 as coated and prepared for weight loss testing.

Figures 4.61 and 4.62 show LIC as-processed cylindrical specimens #17 and #18. These specimens consisted of a four stage coating sequence, precisely:  $\text{CrCl}_3$ -30Cr, Si-25Cr-5C, Si-30HfCl<sub>4</sub>-15Cr, and Si-15HfCl<sub>4</sub>-5Cr-5SiC all in wt.%. The overall amount of mass deposited was 648 mg and 490 mg, respectively. The exterior appearance was homogenous, smooth and of a “silver-bullet” color appearance.



Figure 4.61. Specimen #17 after the LIC coating process. Surface is covered completely and appears smooth, homogenous and silver in color.



Figure 4.62. Specimen #18 after the LIC coating process. Surface is covered completely and appears smooth and uniform.

This type of coating scheme presented an enhanced oxidation resistance performance at a 1000°C in air relative that experienced by the coating type used for Specimen # C2. When tested in an inert atmosphere (argon gas) at the same temperature, the stability of the coating was outstanding as revealed by SEM observation and EDAX analysis.

Figures 4.63 and 4.64 show LIC as-processed cylindrical Specimens # 24 and #29. These two specimens consisted of a coating sequence, precisely: CrCl<sub>3</sub>-35Cr, Si-25Cr-5CrCl-5C, Si-30HfCl<sub>4</sub>-15Cr, and Si-15HfCl<sub>4</sub>-7Cr-7SiC all in wt.%. The overall amount of mass deposited was 1069 mg and 606 mg, respectively. The exterior appearance was not as smooth and homogenous as that obtained with Specimens #17 and # 18 for the same coating composition sequence. The color of the surface was also dull and grayish. Nonetheless, the oxidation resistance performance of Specimen # 24 was similar to that of Specimen #15. The latter



specimen was coated with the same layer sequence used to coat Specimen #17 and #18 and resulted also with a similar exterior appearance.



Figure 4.63. Specimen # 24 as LIC processed, surface is covered completely but lumps are spread over the coating. Stem has been removed.



Figure 4.64. Specimen # 29 as LIC processed before final coating, surface is fully covered and uniform. Metal stem holder is shown at the right hand side.

In terms of the coating composition the main differences between the latter two specimens with Specimen #17 and #18 lies in the replacement of 5 wt.% of  $\text{CrCl}_3$  for pure Cr in the second layer and 2 wt.% more Cr and SiC in the final layer. Another factor that may play a role in the coating surface quality is the powder purity at the time the slurries were prepared. In the case of Specimens #24 and #29, the slurries were prepared with the same chemicals batch used in coating

specimens #17 and #18, but eight weeks later. Micron size powders can easily pick up contaminants and moisture from the atmosphere as they are handled and stored.

Figure 4.65 shows LIC as-processed cylindrical Specimen #32. This specimen was coated with the same layer composition and sequence used in Specimens #17 and #18. The overall amount of mass deposited was 448 mg. The powders used for preparing the slurries were from the same “old” batch. However, the surface exterior appearance was smoother than Specimen #24, probably due to the lower amount of mass added per layer, but not as smoother and shiny as Specimens #17 and #18.



Figure 4.65. Specimen # 32 as LIC processed, surface is covered totally and appears smooth.

To obtain better oxidation resistance performance it was decided to remove the fourth coating layer previously used, as SiC particles were suspected to nucleation surface cracks during the fabrication process, which on one hand may be beneficial to prevent delamination of the coating [17], but on the other hand allows oxygen to penetrate into the C/C substrate. It was also decided to remove 5 wt.% of Cr from the third layer and instead increase the relative amount

of pure Cr in the first layer. This was done to increase the probability of achieving a chromium carbide interface product layer during consolidation of the first layer. Thermodynamically, it was verified that when silicon and chromium carbide (e.g.  $\text{Cr}_2\text{C}_3$ ) are reacted together, formation of SiC and  $\text{CrSi}_2$  reaction products is achieved. This suggests that when the second coating layer (which contains 65 wt.% Si) is made to react with the previously deposited chromium carbide product layer, a SiC/ $\text{CrSi}_2$  product layer should be formed over the C/C composite.

Figures 4.66 and 4.67 show LIC as-processed cylindrical Specimen # 40 after the first and second composition layer, respectively. This Specimen was covered with a three coating sequence consisting of the new selected compositions all in wt.%:  $\text{CrCl}_3$ -50Cr, Si-25Cr-5 $\text{CrCl}_3$ -5C and Si-30HfCl<sub>4</sub>-10Cr. The total amount of mass deposited was 212 mg. Figure 4.66 shows the resulting  $\text{CrCl}_3$ -50Cr layer coating while Figure 4.67 shows the resulting Si-25Cr-5 $\text{CrCl}_3$ -5C layer coating. Both coatings are well spread and uniform.



Figure 4.66. Specimen # 40 after first  $\text{CrCl}_3$ -50Cr (wt.%) layer has been LIC applied. Almost a 100% coating coverage has been obtained.



Figure 4.67. Specimen # 40 after the second Si-25Cr-5CrCl<sub>3</sub>-5C (wt.%) layer has been laser fused. A smooth coating has been obtained all over the surface.

The oxidation resistance performance of this type of coating layer composition and sequence, as measured using a dedicated thermogravimetric analyzer equipment available at the Wright-Patterson AFB Materials Laboratory, was comparable to the performance achieved by the previously shown specimen coatings. Therefore, variations in coating layer composition did not have a vast impact in the oxidation resistance performance, as it mainly depended on the pre-existence of cracks before the testing. However, the performance was considerably improved when a glass-modified sealant overcoat was applied to the refractory coating as it allowed crack sealing, so extending the endurance of the specimen by almost threefold.

#### ***4.2.2.2 Light optical microscopy of bulk microstructure of refractory coatings***

In Figure 4.67 it can be seen that a coating thickness of approximately 50  $\mu\text{m}$  was achieved in Specimen #2. A three coating layer sequence was applied consisting of: CrCl<sub>3</sub>, Si and SiO<sub>2</sub>-30Si-10SiC all in wt.%. The formation of an

interface reaction product (most likely SiC) between the composite surface and the coating bulk was observed. This reaction product is probably a SiC/CrSi<sub>2</sub> layer that grew at the expense of the previously deposited Cr carbide layer as indicated by an equilibrium thermodynamic computation (Thermo-Calc<sup>TM</sup>). In fact, this specimen was subjected to a sequence of 5 two-minute heating processes, each one reaching temperatures between 1000 °C to 1500 °C. Three of these heating cycles provided enough time and temperature to grow a SiC layer several microns thick.

The white phase seen in Figure 4.68 consists of a Si-rich matrix that contains a fraction of the Cr that was deposited in the first layer. A large SiC particle of about 20 μm in diameter can be seen at the right hand side of the image. At the top of the coating a different layer consisting probably of silica and SiC particles is observed, too.

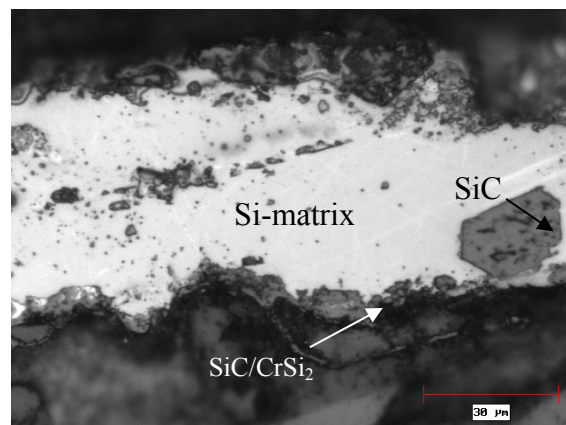


Figure 4.68. Cross-section of Specimen #2, 500x. A reaction layer has formed at the interface.

Figure 4.69 shows that a good wetting reaction has taken place over Specimen #2 and that even the inner cavities of the composite are filled with coating material. These provide an additional interlocking mechanism in addition to that of the reaction bond.

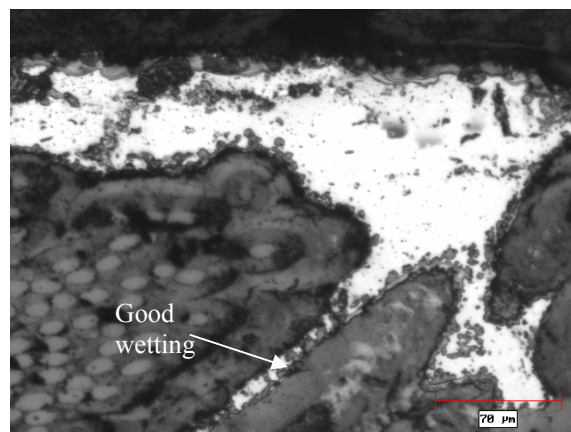


Figure 4.69. Cross-section of Specimen #2, 200x. Indicating that good wetting is achieved over the surface of the C/C composite aided by capillarity.

From Figure 4.70, a continuous Cr/Cr-carbide layer was formed over the surface of the composite when the  $\text{CrCl}_3$ -30Cr (wt.%) layer chemically reacted with it during the laser induced cementation process. The thickness of this layer ranged from 5 to 10  $\mu\text{m}$ .

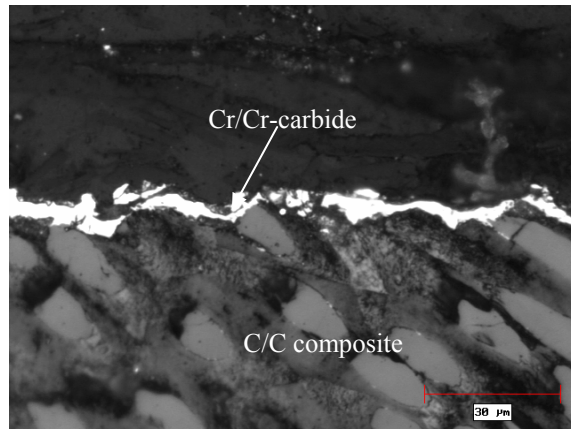


Figure 4.70. Cross-section of Specimen #3, 500x. Showing a Cr/Cr-carbide thin layer.

Figure 4.71 illustrates how a SiC/CrSi<sub>2</sub> layer, 2-3 μm thick, had replaced the previously deposited Cr/Cr-carbide layer in Specimen #5. This specimen underwent a first layer coating of CrCl<sub>3</sub>-30Cr, followed by a Si-50HfC layer and a final overcoat of SiO<sub>2</sub>-30Si-10SiC all in wt.%. This specimen was also subjected to an overall 6 minute process at a temperature between 1000 °C to 1500 °C, that assisted growth of the SiC layer by diffusion of carbon atoms from the substrate. The matrix seen in Figure 4.71 consists of a Si-rich phase which contains a fraction of the Hf and graphite from the dissociated HfC, as revealed later by EDAX. The darker faceted particles correspond to HfC particles that did not decompose during the reaction and perhaps to some SiC particles applied in the overcoat. Moreover, according to Favre [9], when SiC forms at the interface of a

carbon substrate in contact to molten silicon, it tends to fracture and the broken fragments get trapped in the coating above the SiC product layer.

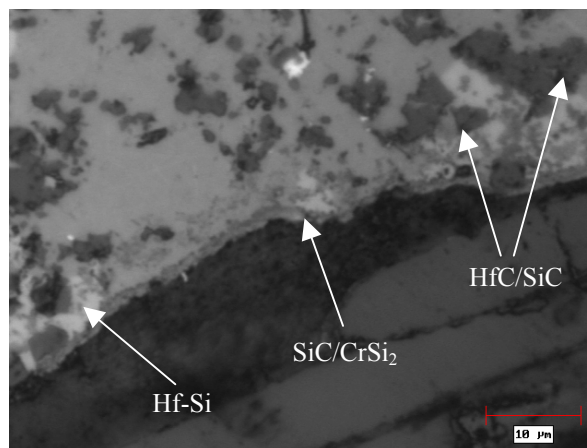


Figure 4.71. Interface of Specimen #5, 1000x. A reaction product layer at the interface is clearly seen along the surface of the C/C composite.

From Figure 4.72, the presence of a reaction product layer at the interface can be reconfirmed at another region of Specimen #5. The “light” phase embedded on the Si-rich matrix is well spread all over the coating thickness as revealed in Figure 4.72, resembling a eutectic lamellar structure. This phase corresponds to a Hf-rich phase containing a fraction of Si and C as well as Cr from the previous chromium carbide coating as revealed by EDAX analysis. Dark faceted particles are thought to consist primarily of HfC and to a minor extend SiC.



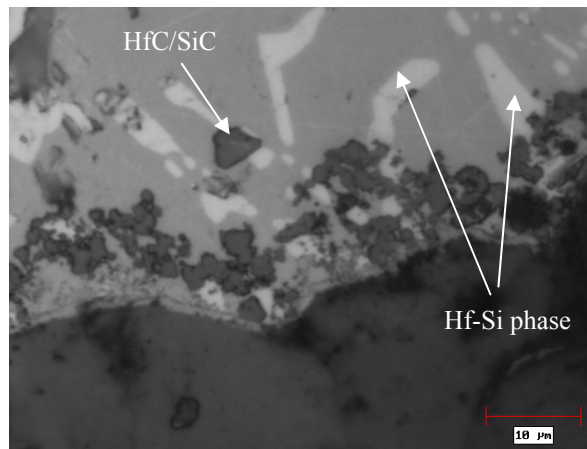


Figure 4.72. Interface of Specimen #5, 1000x. Illustrating the light-phase embedded in the Si-rich matrix.

#### ***4.2.2.3 Scanning electron microcopy of surface and bulk microstructure of refractory coatings***

##### ***Cr-CrCl<sub>3</sub>, Si, SiO<sub>2</sub>-Si-SiC coating sequence***

In Figure 4.73 the surface of the overcoat layer deposited in Specimen #2, consisting of SiO<sub>2</sub>-30Si-10SiC (wt.%) is shown. A glassy phase is present consisting of SiO<sub>2</sub> islands embedded in a matrix having a chemical composition equal to 67 wt.% Si, 26 wt% oxygen, 3 wt% Hf and 3 wt% Cr as revealed by semi-quantitative EDAX. The composition of this matrix phase indicates that the overcoat layer has blended with the previous layer. Embedded SiC fragments, 25 μm in length, are also present as faceted features. This chemical analysis also demonstrates how chromium that was deposited originally in the first layer was removed from the surface of the composite and dissolved into the coating,

reaching to the top of it. This corroborates that intermixing among all the layers deposited has occurred.

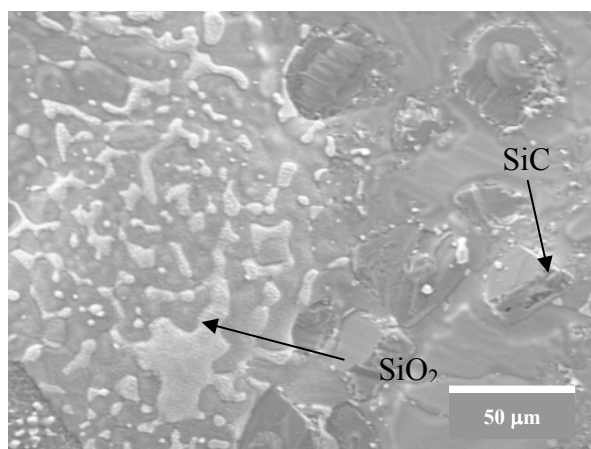


Figure 4.73. Surface of Specimen #2, 1000x. Showing  $\text{SiO}_2$  phase and SiC embedded particles in the Si-rich matrix phase.

Figure 4.74 shows the Cr/Cr-carbide ( $\text{Cr}_x\text{C}_y$ ) layer, 5  $\mu\text{m}$  thick, that was deposited over the surface of the composite (Specimen #3) when  $\text{CrCl}_3$ -30Cr was chemically reacted during the laser induced cementation process. The composition of this layer as determined by EDAX analysis corresponds to 61 wt% Cr, 27 wt.% C and 12 wt.% O. The high graphite content can be attributed to the C/C substrate, whereas the oxygen content may indicate that oxidation of the chromium surface has taken place. Additionally, the surface of the composite was soundly reaction wet by chromium.

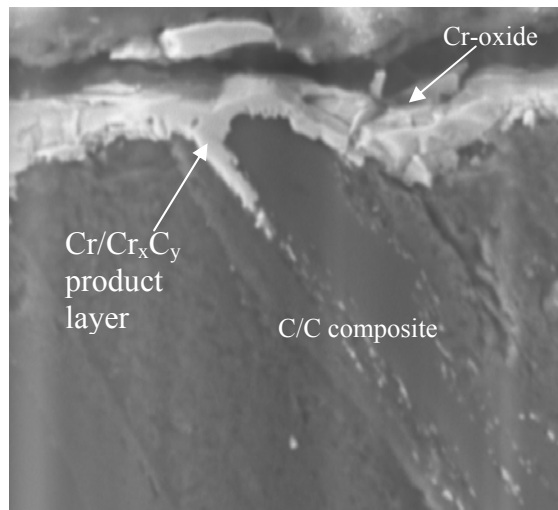


Figure 4.74. Cross-section of Specimen #3, 2500x. Showing the Cr/Cr<sub>x</sub>C<sub>y</sub> product layer over the composite surface.

**Cr-CrCl<sub>3</sub>, Si-HfC, SiO<sub>2</sub>-Si-SiC coating sequence**

From Figure 4.75 it can be observed that a coating of approximately 300 to 400  $\mu\text{m}$  thick with good wetting characteristics of the coating material over the substrate was obtained in Specimen #5. Some porosity is present throughout the coating layer. This specimen was coated with a sequence of three distinct layer compositions consisting of: CrCl<sub>3</sub>-30Cr, Si-50HfC and SiO<sub>2</sub>-30Si-10SiC all in wt.%.

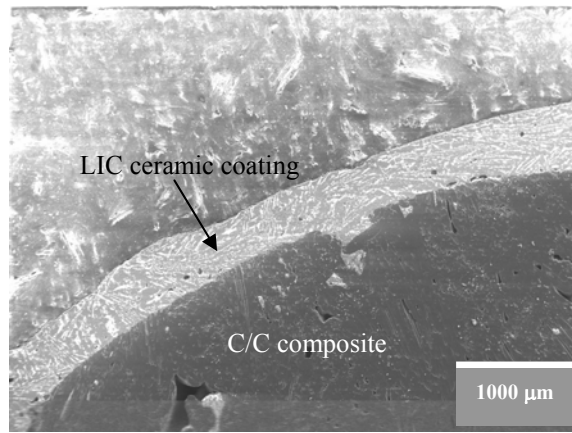


Figure 4.75. Cross-section of Specimen #5, 50x. Showing thickness uniformity and good coating spreading over C/C substrate.

In Figure 4.76 the “gray” phase has an elemental composition of 94 wt.% Si, 3 wt.% Hf, 2 wt.% graphite and less than 1 wt.% Cr and it should correspond to the  $\alpha$ -Si phase. On the other hand, the “white” (previously labeled “light” phase on Figure 4.72) phase has an elemental composition of 48 wt.% Hf, 41 wt.% Si, 7 wt.% graphite, 3 wt.% oxygen and less than 1 wt.% Cr. It should then correspond to a eutectic phase having  $\text{HfSi}_2$  and  $\alpha$ -Si as microconstituents. At the interface between the composite and coating semi-quantitative EDAX gave a composition of 53 wt.% Si, 43 wt.% C, 2 wt.% Hf and 1 wt.% Cr. Such composition suggests that a mixture of  $\text{SiC}$ ,  $\text{CrSi}_2$  and  $\text{HfC}$  phases are present at the interface. The large C and Si weight percent can be attributed to the C/C substrate and surrounding  $\alpha$ -Si matrix, respectively.

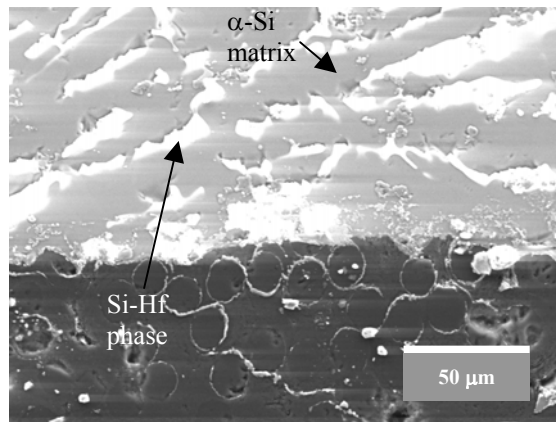


Figure 4.76. Cross-section of Specimen #5, 1000x. Indicating the  $\alpha$ -Si matrix and the Si-Hf “white” phase.

Figure 4.77 illustrates the cross section of Specimen #8. The coating was done using a three distinct layer sequence: the first layer corresponded to the previous  $\text{CrCl}_3$  based layer applied to Specimen #5, the second layer corresponds to Si-35HfC and the third layer to  $\text{SiO}_2$ -10Si-5SiC all in wt.%. The powder mixture used in the second layer was previously heat treated at 750 °C in air to oxidize the HfC and form  $\text{HfO}_2$ , as confirmed by the XRD analysis done on the powders before and after the heat treatment (see Section 4.2.2.5); it was inevitable that some of the silicon may have been oxidized, too, but to a lesser extent.

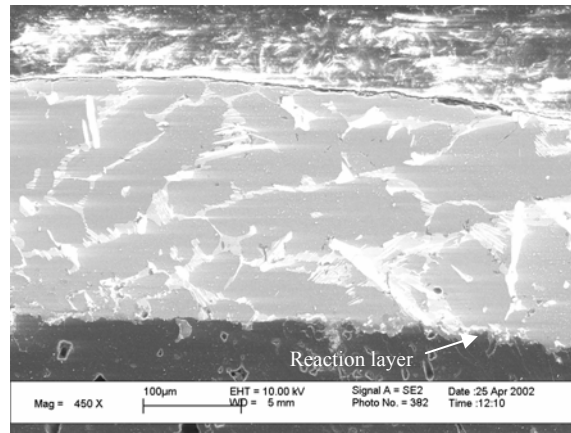


Figure 4.77. Cross-section of Specimen #8, showing a uniform coating 200  $\mu\text{m}$  thick, 450x. A micron size reaction layer at the interface can be observed.

This heat treatment was done to determine the effects in the coating integrity when using an oxide of hafnium instead of its carbide as the precursor material. From thermal expansion measurements using a thermomechanical analyzer it was observed that when HfC becomes oxidized into  $\text{HfO}_2$ , a first order transition occurs at 590°C, with an associated large volume expansion, as illustrated in Figure 4.78. This transition causes a positive variation in the CTE of the material of up to two orders of magnitude. This may induce deleterious cracking of the consolidated coating during weight loss tests if a fraction of the HfC remained in the LIC coating. The preheat-treated powder prevents this reaction to some extent by limiting residual HfC, thus avoiding an oxidation reaction of this kind from taking place during the weight loss testing.

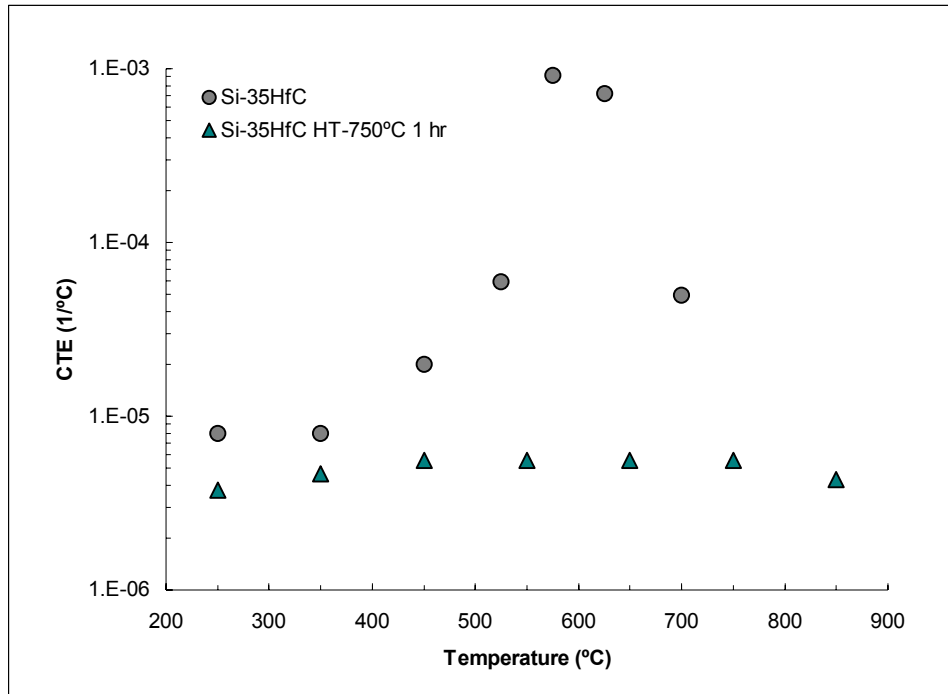


Figure 4.78. Coefficient of thermal expansion of the Si-35HfC (wt.%) powder mixture before and after heat treatment at 750°C, measured at different temperatures in air up to 850 °C. A first order transition occurs when the HfC becomes oxidized at 590°C.

Figure 4.79 shows a close up image of the microstructure of the bulk coating of Specimen #8. The “gray” phase away from the white phase consists of 97 wt.% Si, 2 wt.% graphite and 1 wt% Cr indicating that  $\alpha$ -Si phase has formed. The matrix near the white phase has a composition of 32 wt.% Si and 68 wt% Hf, signaling that it should corresponds to a eutectic phase consisting of  $\text{HfSi}_2$  and  $\alpha$ -Si microconstituents. The “white” phase has a different composition of 18 wt.% Si, 81 wt.% Hf and 1 wt.% oxygen, suggesting that it should correspond to a phase having  $\text{HfSi}$  and  $\alpha$ -Si. The third phase “light-gray” that grew adjacent to

the latter phase has a composition of 63 wt.% Si, 28 wt.% Cr, 6 wt.% C and 3 wt.% oxygen; thus, it may correspond to a phase consisting of  $\text{CrSi}_2$  and  $\alpha\text{-Si}$  microconstituents. The white color of the hafnium-rich phase is due to the high atomic number of this element that results in bright contrast relative to the silicon, as the latter element has a low atomic number. From the composition of these phases it can be seen that most of the  $\text{HfO}_2$  and possibly some residual  $\text{HfC}$  have dissociated into hafnium cations that recombined with silicon and chromium to form the observed silicide compounds.

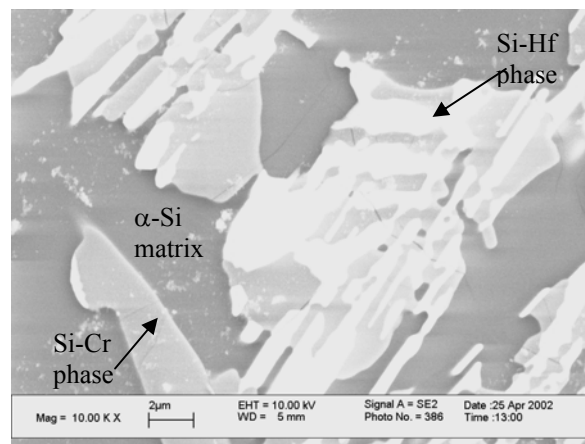


Figure 4.79. Magnified microstructure of Specimen #8, 10000x. Si-rich phase (gray), Si-Hf phase (white) and Si-Cr (light-gray) phase are seen.

**Si-Cr-C, Si-HfCl<sub>4</sub>-Cr, Si-HfCl<sub>4</sub>-Cr-SiC coating sequence**

The microstructure of the cross section of Specimen #18 is shown in Figure 4.80. A three coating composition sequence was applied consisting of: Si-25Cr-5C, Si-30HfCl<sub>4</sub>-15Cr and Si-15HfCl<sub>4</sub>-5Cr-5SiC all in wt.%. A uniform



coating with a thickness of approximately 350  $\mu\text{m}$  having low porosity can be seen. The applied coating has wet most of the surface grooves indicating proper spreading and strong bonding by mechanical interlocking.

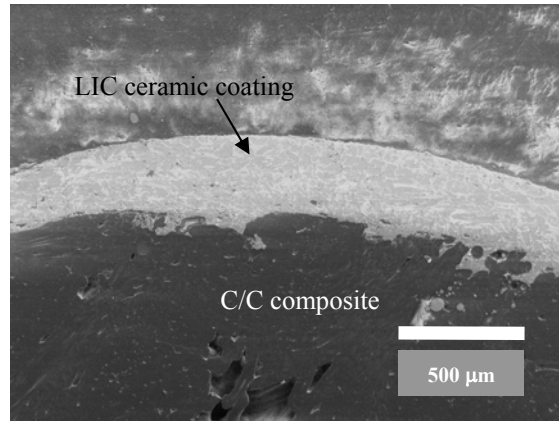


Figure 4.80. Cross-section of Specimen #18, no heat treatment, 100x. A coating thickness of approximately 350  $\mu\text{m}$  is shown.

Figure 4.81 shows that a wetting reaction has taken place and that even the inner cavities of the composite are filled with coating material. This provides an additional bonding mechanism. The microstructure resembles that of a eutectic alloy, where in this particular case the pro-eutectic phase would be the  $\alpha$ -Si phase, and the hafnium and chromium silicides would correspond to the eutectic phase.

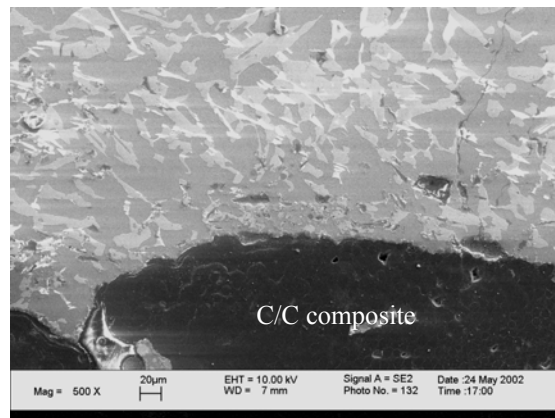


Figure 4.81. Cross-section of Specimen #18, no heat treatment, 500x. Reacting wetting is achieved over the surface.

The formation of a SiC product at the interface between the C/C composite surface and the coating bulk can be observed in Figure 4.82. It corresponds to a SiC layer of composition: 37 wt.% C and 63 wt.% Si. The excess graphite can be attributed to nearby C/C substrate. The thickness of this layer ranges from 4 to 8  $\mu\text{m}$ . When comparing the observed SiC reaction layer of this specimen with the SiC/CrSi<sub>2</sub> reaction layer observed in Specimen #5, it can be concluded that the presence of CrSi<sub>2</sub> in the reaction layer of Specimen #5 was a direct consequence of the Cr/Cr-carbide layer that had been initially deposited on it. Finally, the gray phase in the microstructure corresponds to the  $\alpha$ -Si matrix, while the white phase corresponds to a Hf silicide compound.

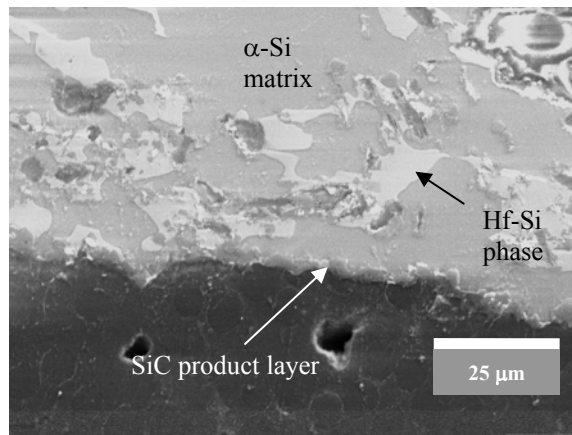


Figure 4.82. Cross-section of Specimen #18, no heat treatment, 2000x. A Si carbide layer 4-8  $\mu\text{m}$  thick is observed at the interface.

Figure 4.83 shows that the coating microstructure of Specimen #18 resembles that of Specimen #8. The  $\alpha$ -Si phase (99 wt.% Si and 1 wt.% oxygen) is present as the matrix, a white phase corresponding to a  $\text{Hf}_2\text{Si}$  (92 wt.% Hf, 7 wt.% Si, and less than 1 wt.% graphite) is observed as well as a light-gray phase consisting of  $\text{HfSi}$  and  $\text{CrSi}_2$  microconstituents (69 wt.% Hf, 19 wt.% Si, 11 wt.% Cr and 1 wt.% oxygen). Between the white phase layers a  $\text{CrSi}_2$ -Si phase is also present having a composition of: 55 wt.% Si, 36 wt.% Cr, 6 wt.% oxygen and 2 wt.% graphite. These phases show a lamellar type morphology with a length scale of the order of 1 to 10  $\mu\text{m}$ .

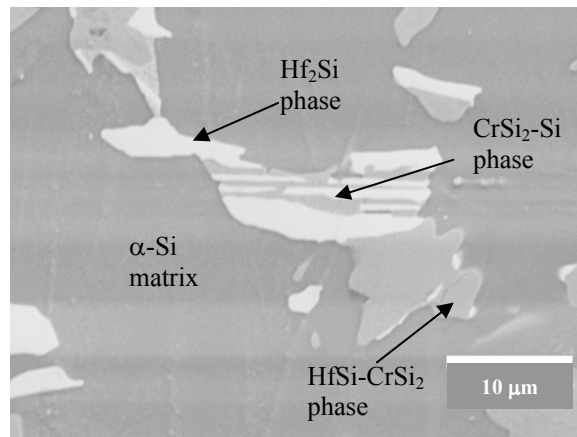


Figure 4.83. Cross-section of Specimen #18, no heat treatment, 5000x. The  $\alpha$ -Si matrix contains three distinct embedded phases.

Figure 4.84 show the cross-section of the Specimen #18 after 2 hours 30 minutes of heat treatment in argon at 1150 °C. The thickness of the coating shown measures approximately 300  $\mu\text{m}$  and no major cracks are observed within that magnification range. The distribution of second phase inside the Si-rich matrix remains macroscopically unchanged.

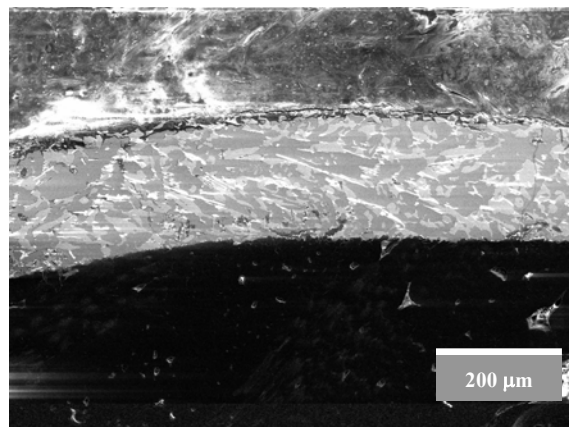


Figure 4.84. Cross-section of Specimen #18, after 2 hours and 30 minutes of heat treatment, 250x. Coating thickness is approximately 300  $\mu\text{m}$ .

Cracking along the phase boundaries is observed in Figure 4.85. The  $\alpha$ -Si matrix (gray phase) has almost the same composition of the un-heat-treated specimen, i.e., 99 wt.% Si and less than 1 wt.% oxygen. A reduction in Si content and an increase in C and O content were measured in this phase after the heat treatment. On the other hand, the white phase now consists of 91 wt.% Hf, 5 wt.% graphite, 4 wt.% oxygen, and less than 1 wt.% Si, indicating the presence of  $\alpha$ -Hf phase. The light gray phase surrounded by the white phase now consists of 58 wt.% Si and 37 wt.% Cr and 4 wt.% oxygen, which is similar to the composition of the untreated specimen except for the absence of graphite and a lower oxygen content. It is concluded that the silicon present in the original  $\text{Hf}_2\text{Si}$  phase has diffused out and that graphite and oxygen atoms have diffused from the surrounding phases towards the white phase.

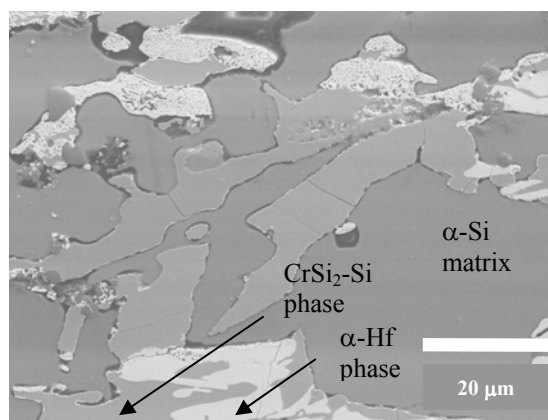


Figure 4.85. Cross-section of Specimen #18, after 2 hours and 30 minutes of heat treatment, 2500x. Detachment along phase boundaries is observed.

Figure 4.86 shows a magnified image of the cross section of Specimen #18, at the interface between the C/C composite and the coating. The composition of the original product layer is stoichiometric SiC, i.e., 39.6 wt.% C and 60.4 wt.% Si. A crack is also seen at the upper right hand side of the image cutting through the different phases.

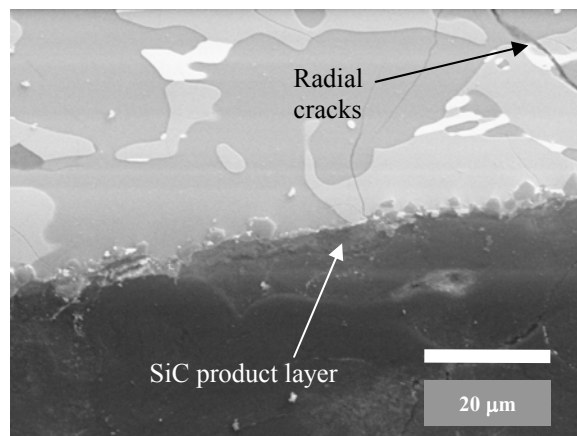


Figure 4.86. Cross-section of Specimen #18, after 2 hours 30 minutes of heat treatment, 2500x. The SiC product layer at the interface remained compositionally unchanged after the treatment.

Figure 4.87 shows a low-magnification cross-section of Specimen #18 after 2 hours and 30 minutes of heat treatment in argon at 1150 °C. The thickness of the coating after the heat treatment remained at approximately 350 μm and showed no change in uniformity along the perimeter of the cylinder. Only a few vertical cracks were observed, spaced out almost equally every 1-2 mm. These are

likely to have been formed on removal of the specimen from the heat treating furnace. However, no delamination of the coating was noted.

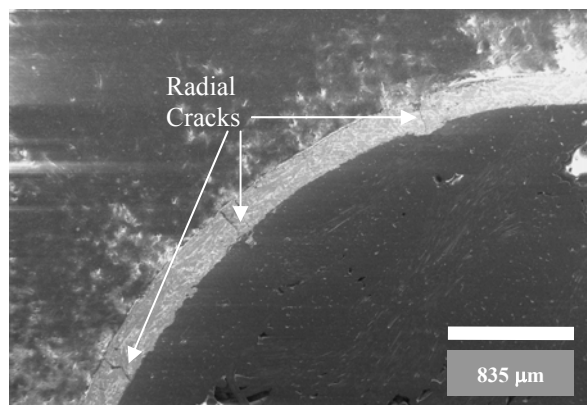


Figure 4.87. Cross-section of Specimen #18 after 2 hours and 30 minutes at 1150 °C in argon, 60x.

**Ethyl Silicate (SILBOND™) and Sodium Silicate overcoats**

In an attempt to deposit an overcoat sealant layer over some of the refractory coatings previously described, Specimen #31, was dipped in SILBOND™ solution three times, 15 minutes each, and left to cure between dips at room temperature. The main purpose was to provide a sealing mechanism for the radial cracks that formed on the refractory coating during fabrication (e.g., Figure 4.87). The total mass of SILBOND™ applied to this specimen corresponded to 160 mg. The specimen was then fired at 300 °C in air for 10 minutes. Figures 4.88 and 4.89 show the appearance of the SILBOND™ overcoat before and after the firing, respectively. In both cases cracks developed due to the volume contraction of the overcoat on curing. The firing process densified further the overcoat, and, as it

crystallized the crack expanded, exposing the refractory surface to the atmosphere.

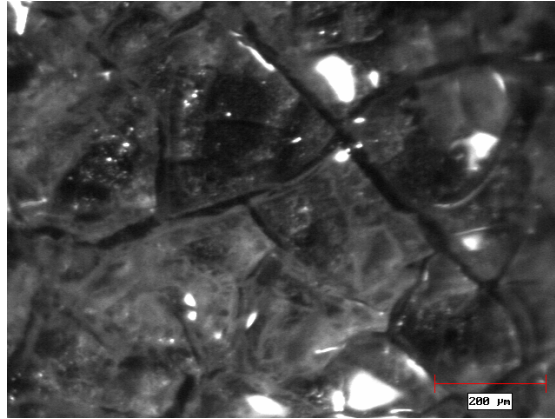


Figure 4.88 Surface of Specimen # 31, after coated with SILBOND™. Multiple cracks are present due to the shrinkage of the ethyl-silicate solution on curing.

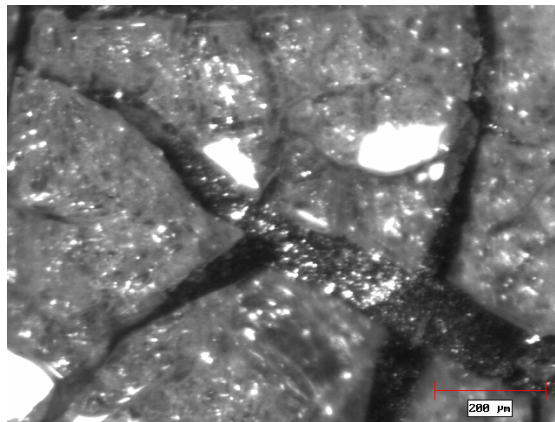


Figure 4.89. Surface of Specimen # 31, after coated with SILBOND™ and cured at 300°C for 10 minutes. Previously shown cracks have not healed, instead crack openings are wider.



Because of these unsatisfactory results, the use of SILBOND™ as an overcoat layer to seal cracks was discarded. A sodium silicate solution commonly known as “waterglass”, combined with silica and sodium carbonate powder was attempted instead.

Figures 4.90 and 4.91, show the surface of a glass-modified overcoat based on pure sodium silicate solution and a mixture of silica and sodium silicate solution, respectively. The overcoats were consolidated on Specimens #41 and #42, respectively, using the LIC process. In both cases a network of surface cracks was observed; however, it was expected that these cracks will seal themselves when the overcoat is exposed to high temperature.

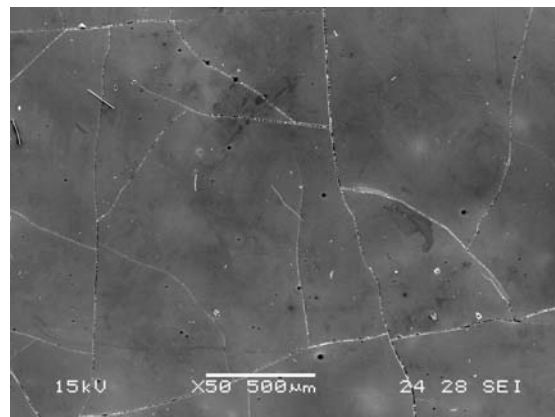


Figure 4.90. Surface of Specimen #41, showing the glass-modified overcoat obtained from the sodium silicate using the LIC process, 50x.

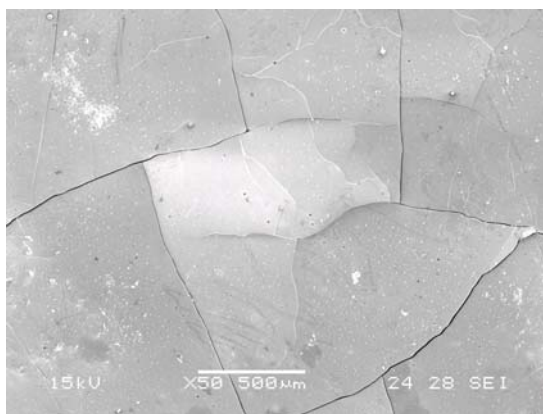


Figure 4.91. Surface of Specimen #42, showing the glass-modified overcoat obtained from silica and sodium silicate using the LIC process, 50x.

It was finally decided to produce an overcoat having a low glass transition temperature  $T_g$  and a high enough melting point  $T_m$  to withstand the weight loss tests. A glass-modified compound consisting of a  $\text{Na}_2\text{CO}_3+\text{SiO}_2$  powder mixture in sodium silicate solution was selected. This soda type modified-glass has a  $T_g$  in the vicinity of  $450\text{ }^\circ\text{C}$  and a  $T_m$  of about  $1100^\circ\text{C}$ . After application of this overcoat composition on Specimen #43 by means of the LIC process, it was decided to form the glass-modified overcoat by conventional furnace firing. The results are shown in the next section.

#### ***CrCl<sub>3</sub>-Cr, Si-Cr-C, Si-HfCl<sub>4</sub>-Cr, Na<sub>2</sub>O-SiO<sub>2</sub> coating system***

The refractory coating applied to Specimen #45 by the LIC technique consisted of a 3 layers sequence, namely:  $\text{CrCl}_3\text{-40Cr}$ ,  $\text{Si-25Cr-5C}$  and  $\text{Si-}$

15HfCl<sub>4</sub>-15Cr in wt.%. The glass-modified overcoat, which was applied by a furnace firing process at 950 °C for 30 minutes in argon, consisted of a mixture of 1 gram of Na<sub>2</sub>CO<sub>3</sub> - 2SiO<sub>2</sub> (at.%) diluted in 10 ml of sodium silicate solution (14% NaOH and 27% SiO<sub>2</sub> balance H<sub>2</sub>O). Both coatings and the C/C substrate can be clearly differentiated from one another in Figure 4.92.

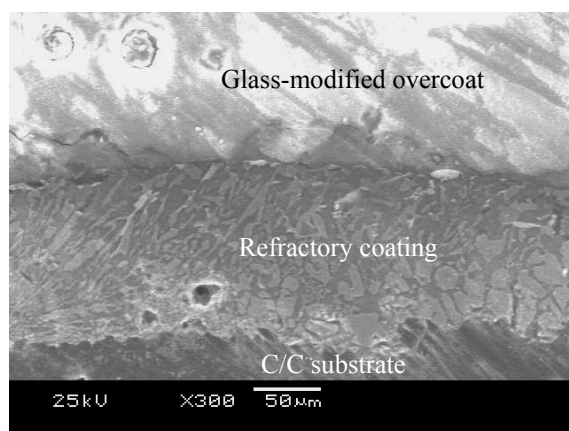


Figure 4.92. Cross-section of Specimen #45, 300x. Shown are the glass modified overcoat, the refractory coating and the C/C substrate.

Figure 4.93 illustrates a close up of the interface between the glass-modified overcoat and the refractory coating layer. The glass-modified phase has a composition of 53 wt.% oxygen, 12 wt.% Na and 35 wt.% Si, which is richer in oxygen and lower in sodium relative to the stoichiometry of the powder mixture used. The addition of sodium silicate solution and the firing process have altered the composition from that of the precursor powders according to what was measured by semi-quantitative analysis. From Figure 4.93 it can be also seen that

the glass-modified overcoat has wet completely and uniformly the surface of the refractory coating.

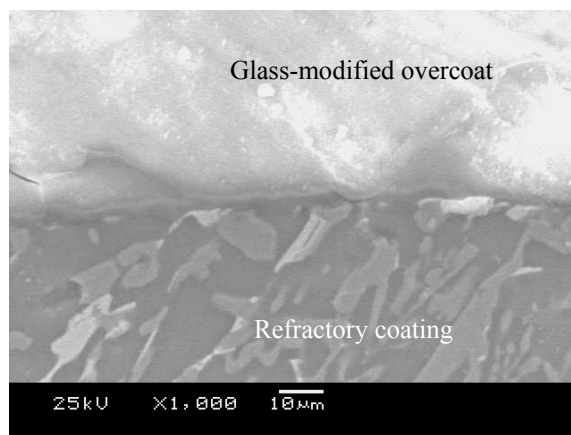


Figure 4.93. Cross-section of Specimen #45, upper interface at 1000x. Good wetting of the refractory coating by the glass-modified overcoat has been achieved.

From Figure 4.94, three distinct phases can be observed: “gray”, “light-gray” and “white”. According to the semi-quantitative EDAX results, the gray phase consists mainly of 73 wt.% Si and 19 wt.% Cr (possibly a phase made of  $\alpha$ -Si with  $\text{CrSi}_2$  microconstituents). The presence of a small amount of graphite, 6 wt.%, may be due to SiC and an oxygen level of 2 wt.% was also detected. The light-gray phase has a composition of 52 wt.% Si and 49 wt.% Cr indicating that a  $\text{CrSi}_2$  has formed. The white phase consists of 70 wt.% Hf, 29 wt.% Si and 1 wt.% Cr (possibly a ternary phase consisting of  $\text{HfSi}_2$ ,  $\alpha$ -Si and  $\text{CrSi}_2$  microconstituents). It must be taken into consideration that the accuracy of the semi-quantitative analysis is limited, as the electron beam probe used to excite the

different elements at a specific location can excite neighboring elements and thus pick up signals that do not correspond to the observed phase. Therefore, it is possible that the gray phase is simply  $\alpha$ -Si, that the light gray phase corresponds to  $\text{CrSi}_2$  and that the white phase corresponds to  $\text{HfSi}_2$ .

Thermodynamic equilibrium calculation results were obtained using Thermo-Calc<sup>TM</sup> software [18] for the different coating mixtures applied for comparison with the semi-quantitative data. From the third coating layer (Si-15HfCl<sub>4</sub>-15Cr in wt.%) at 1210 °C, a chromium silicide phase,  $\text{CrSi}_2$  (Si 52.3 wt.% and Cr 47.7 wt.%), should form. A  $\text{Hf}_{3.43}\text{Si}$  (95.6 wt.% Hf, 4.4 wt.% Si) phase having the hcp A3 structure is predicted by Thermo-Calc<sup>TM</sup>. Because this phase is not reported in the Hf-Si binary phase diagram, it is thought to consist of a eutectic phase having  $\text{Hf}_2\text{Si} + (\alpha\text{-Hf})$  microconstituents. A pure silicon phase is also predicted by Thermo-Calc<sup>TM</sup>.

On the other hand, from the second coating layer (Si-25Cr-5C in wt.%) at 1299°C, Thermo-Calc<sup>TM</sup> results indicates that a similar  $\text{CrSi}_2$  (52.5 wt.% Si and 47.5 wt.% Cr) phase should be present. The  $\alpha$ -Si (99.8 wt.% Si and 0.2 wt.% C) phase having the diamond A4 structure is predicted as well as the presence of SiC (Si 70 wt.% and C 30 wt.%).

From the SEM image shown in Figure 4.92, the second and third layers of the refractory coating appeared to have blended. Therefore, a coating composition

corresponding to the average composition between these layers was fed into Thermo-Calc<sup>TM</sup> to predict the phases present under equilibrium conditions at 1210 °C. Again, the CrSi<sub>2</sub>, SiC and α-Si phases were present, the latter with a slight reduction in graphite content (0.15 wt.% C). Once more, a Hf<sub>3.44</sub>Si phase (95.6 wt.% Hf and 4.4 wt.% Si) having a hcp A3 structure was predicted. As mentioned before, the composition of this phase should correspond to a eutectic phase having (α-Hf) and Hf<sub>2</sub>Si microconstituents. This eutectic phase forms at a hafnium composition larger than 92 wt.%, signaling that chromium and graphite have reacted first with silicon. Whatever small amount of silicon is left then reacts with hafnium.

Comparing the resulting phases from the semi-quantitative analysis and the theoretical analysis an agreement is reached for the existence of the CrSi<sub>2</sub> and the α-Si phases. A controversy is present between the existence of a measured HfSi<sub>2</sub>+α-Si eutectic and a predicted Hf<sub>2</sub>Si+α-Hf eutectic. Because of the reduced time available for formation of these phases (order of minutes), it is sensible to assume that the white phase corresponds to the former.

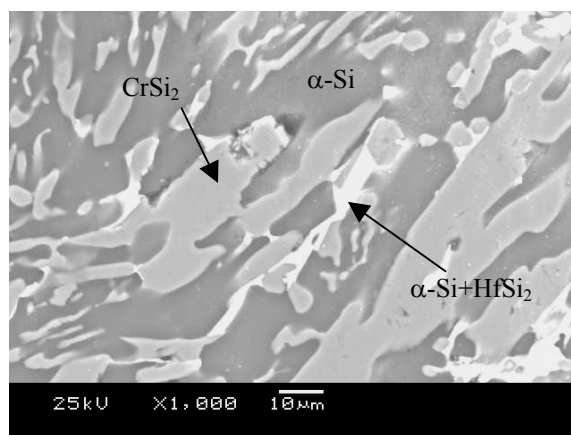


Figure 4.94. Cross-section of Specimen #45, refractory coating at 1000x. Three distinct phases can be observed: gray, light gray and white.

In Figure 4.95, the product layer at the interface between the C/C substrate and the refractory coating is shown. A light gray phase consisting of 53 wt.% Si and 47 wt.% Cr (5 wt.% C was not considered) can be observed and it corresponds to the already identified  $\text{CrSi}_2$  phase. However, according to the result given by Thermo-Calc<sup>TM</sup> when the reaction between  $\text{Cr}_3\text{C}_2$  and Si is considered at the interface, a phase with a composition of 75.5 wt.% Cr and 24.5 wt.% Si should have formed, i.e., a  $\text{Cr}_5\text{Si}_3$  phase. Additionally, SiC (70 wt.% Si and 30 wt.% C) and  $\text{Cr}_3\text{C}_2$  (86.7 wt.% Cr and 13.3 wt.% C) should be present. Originally, it was assumed that the first deposited  $\text{CrCl}_3$ -Cr layer formed a  $\text{Cr}_3\text{C}_2$  product layer over the surface of the C/C composite that consecutively reacted with silicon from the second coating layer, Si-25Cr-5C, to form a SiC layer.

However, Figure 4.95 has revealed that a  $\text{CrSi}_2$  forms more readily than  $\text{SiC}$  as the latter requires longer times for graphite to diffuse from the substrate.

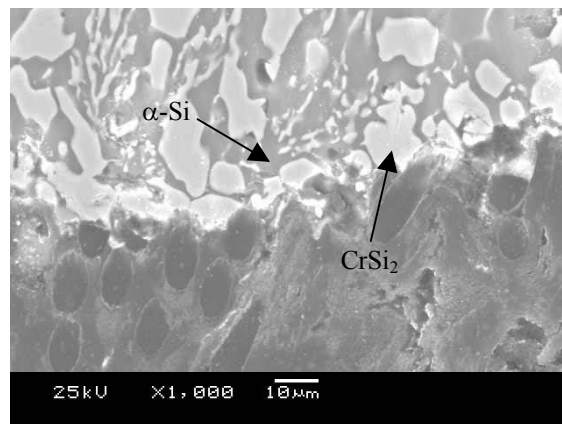


Figure 4.95. Cross-section of Specimen #45, interface with substrate at 1000x. Two distinct phases can be observed: gray and light gray.

The reactive wetting of the  $\text{CrSi}_2$  phase over the C/C substrate is clearly observed in Figure 4.96. Grooves between fibers are wet completely by this phase, but a large wetting angle has resulted at the triple points.

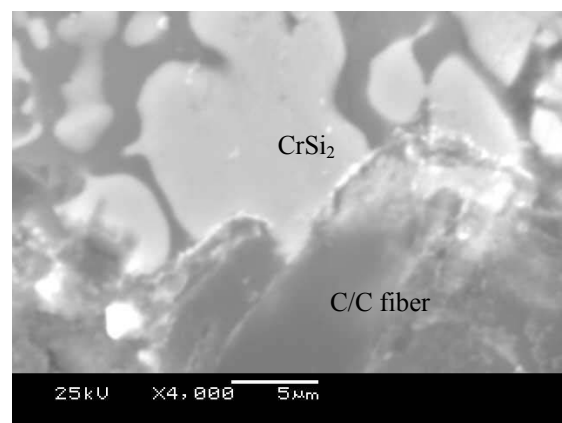


Figure 4.96. Cross-section of Specimen #45, interface at 4000x. Reactive wetting of  $\text{CrSi}_2$  phase over C/C fiber.



The cross section of Specimen #41 after a weight loss test at 1000°C in air for 3 hours is shown in Figure 4.97. The glass-modified overcoat has developed pores along the interface; however, it can be seen that cracks within the refractory coating were covered by the glass-modified overcoat. It can also be seen that no radial cracks run completely from the surface of the glass overcoat into the substrate. Coating thickness of the refractory layer is approximately 150 μm while the glass-modified coating is 250 μm. Both upper and lower interfaces appear to be continuous and well attached.

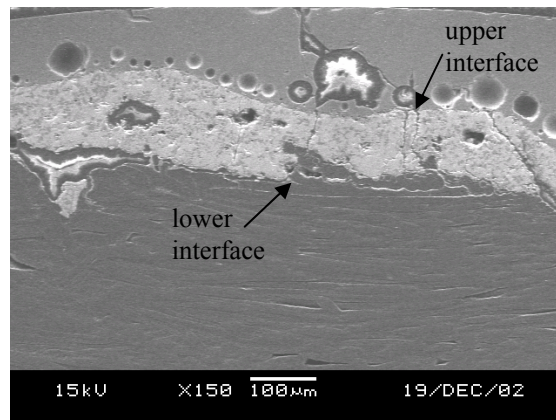


Figure 4.97. Cross-section of Specimen # 41, after weight loss tests at 1000 °C for 3 hours in air, 150x.

Figure 4.98 indicates that decohesion of some of the 10 μm diameter carbon fibers from the carbonaceous matrix has taken place near the coating interface in Specimen #42 after being weight loss tested for 3 hours at 1000 °C in

air. This may suggest that some oxygen diffused into the C/C substrate and oxidized the matrix forming a gaseous product.

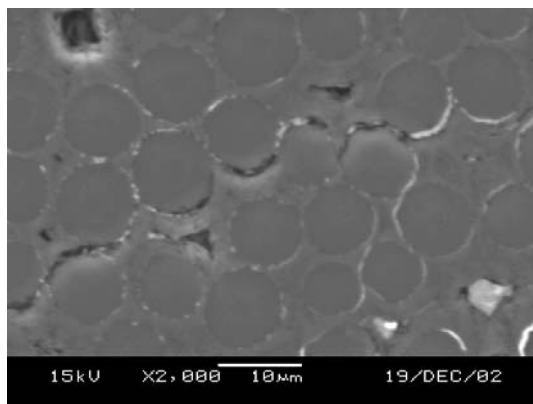


Figure 4.98. Cross-section of Specimen #42, after weight loss test, 2000x. A close up of the C/C fibers and carbonaceous matrix near the interface is shown.

Figure 4.99 shows the cross section of Specimen #43, after it was subjected to a weight loss test for over 20 hours at 1000 °C in air. After that testing period it was found that the specimen had lost 28% of its original weight. This was one of the best oxidation performance results obtained in a C/C cylinder coated with a refractory layer and a glass-modified overcoat. No cracks formed along this portion of the coating. However, a large pore is seen as well as and some interfacial substrate grooving. The glass-modified sealant overcoat shows good adherence to the refractory coating. The refractory coating has undergone severe pitting. Specimen #43 possesses a similar refractory coating sequence as Specimens #41 and #42.

Due to the low  $T_g$  of the sodium glass-modified overcoat, the temperature range available for thermal shock to occur is lower than, for example, a pure silica glass based sealant overcoat had been used. The lower  $T_g$  minimized crack formation in the overcoat when exposed to rapid cooling rates. Moreover, the CTE of the refractory coating ( $1.5 \cdot 10^{-5}$  1/K as measured) is higher than the CTE of the soda glass overcoat ( $9 \cdot 10^{-6}$  1/K [19]). Therefore, only compressive stresses should be induced in this layer. This may eventually cause delamination by buckling.

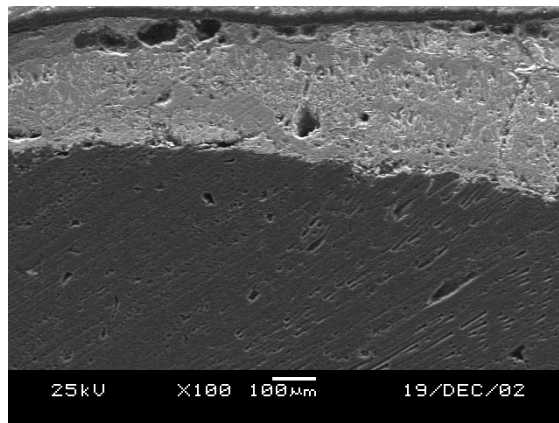


Figure 4.99. Cross-section of Specimen #43, after weight loss test for 20 hours at 1000 °C in air, 100x.

From Figure 4.100 it can be observed that the microstructure and phase distribution in the bulk of the coating has not been altered vastly during the 20 hour weight loss test at 1000°C. This indicates the Hf and Cr silicide phases formed are stable in oxidizing environments at even higher temperatures than

1000°C. This also suggests that for these phases to have formed, the temperature of the specimen during the LIC process must have been higher than the testing temperature. Especially under the laser beam, temperatures may have reached well above 1500 °C. These temperatures were sufficient to form the corresponding metal-silicide compounds. Comparing the interface of this specimen to that shown in Figure 4.95, it can be observed that the CrSi<sub>2</sub> product layer has disappeared from the interface in this case. This phase may have dissolved into the Si-rich phase during the high-temperature exposure allowing the growth of the SiC phase at the interface.

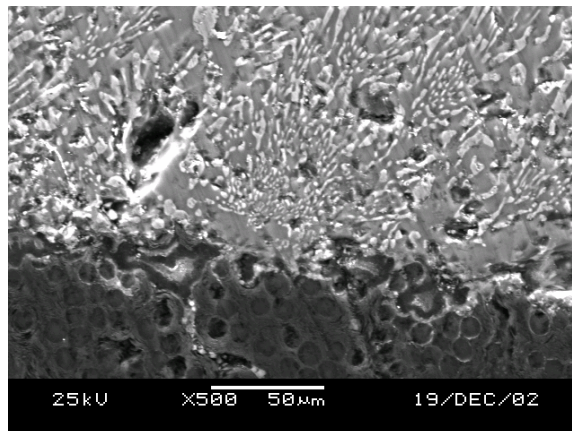


Figure 4.100. Cross-section of Specimen # 43, after weight loss test, 500x. A sound microstructure integrity near the interface with the C/C substrate is shown.

In Figure 4.101, the microstructure below the glass-modified interface seems similar to that of the un-tested Specimen #45, but apparently the white phase appears to have diffused towards the upper interface. The gray phase in this

case corresponds to 92 wt.% Si and 8 wt.% C, while the light-gray phase corresponds to 52 wt.% Si and Cr 48 wt.% (6 wt.% C was not considered) consisting in the  $\text{CrSi}_2$  phase. The white phase below the interface shows now a composition of 79 wt.% Si, 15 wt.% Cr, 4 wt.% Hf and 1 wt.% oxygen (6 wt.% C was not considered), while at the interface the white phase had a different composition consisting of 31 wt.% Si, 31 wt.% Hf, 32 wt.% oxygen and 6 wt.% Cr. This suggests that Hf has diffused toward the glass-modified overcoat during the high temperature exposure. Finally the composition of the glass-modified consisted of 70 wt.% oxygen, 29 wt.% Si and 1 wt.% Na. This indicates that the original sodium content has been depleted, probably due to vaporization of this chemical specie.

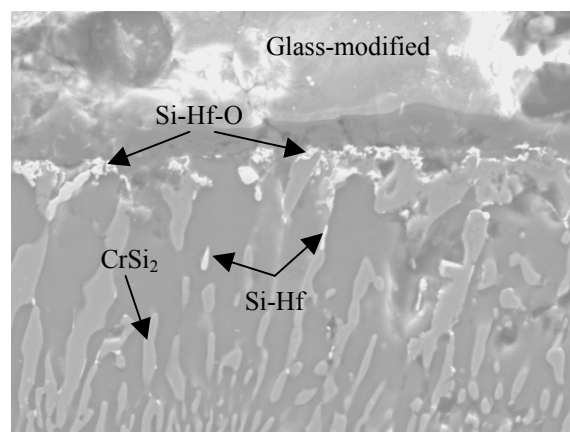


Figure 4.101. Cross-section of Specimen # 43, after weight loss test, 500x. A sound microstructure integrity near the interface with the glass modified overcoat is shown.

Figure 4.102 shows the surface of Specimen #46 after being weight loss tested at 1000 °C in air for 5 hours. This specimen was coated with a similar coating sequence as the previous specimens. The weight lost testing was done this time using a dedicated thermo-gravimetric balance in the Wright-Patterson AFB. The overcoat observed corresponded to a modified glass made out of silica and sodium carbonate precursor powders. The integrity of the overcoat has been altered dramatically as compared to the surface of untested specimens (Figures 4.90 and 4.91). Cavities have formed on the surface perhaps due to the reactivity of sodium ions present on the glass-modified overcoat. These may have reacted with elements in the refractory coating underneath.

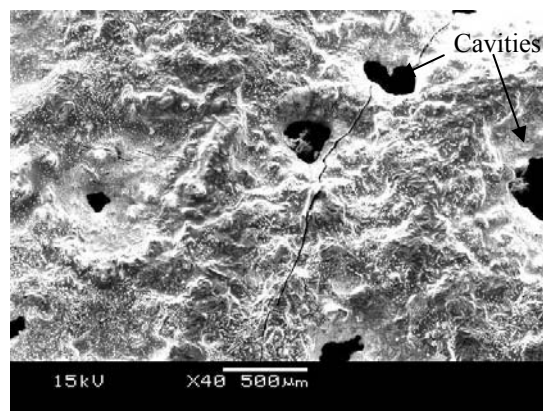


Figure 4.102. Surface of Specimen #46, after weight loss test for 5 hours at 1000 °C in air, 40x. Porosity has developed on the surface of the sodium glass-modified overcoat.

From Figure 4.103 it can be seen that a network of cracks is present; nevertheless, at high temperatures these cracks should heal as the glass-modified overcoat can flow at lower temperatures. The light speckles, 5  $\mu\text{m}$  in size, had similar composition as the glass-modified matrix, but contained they additionally a 3 wt.% Cr as indicated by semi- quantitative EDAX.

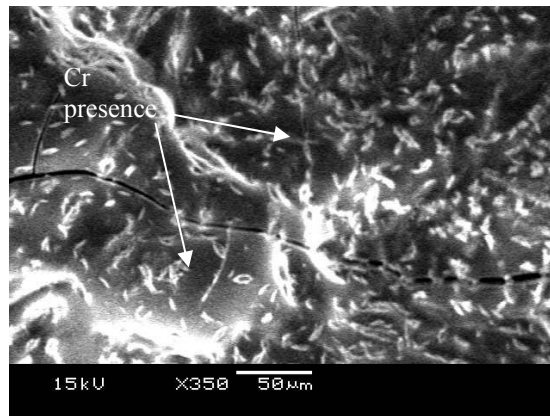


Figure 4.103. Surface of Specimen #46, after weight loss test, 350x. Channeling cracks are present at the surface.

#### 4.2.2.4 EDAX spectra and mapping of coating phases

Figure 4.104 illustrates the EDAX spectrum obtained from the reaction product layer that was formed when coating Specimen #3 with  $\text{CrCl}_3\text{-30Cr}$ . Refer to Figures 4.70 and 4.74 to observe the described reaction product coating over the C/C substrate. Intense peaks corresponding to Cr and C are present. These may signal the formation of a Cr carbide compound. An oxygen peak is also present indicating that chromium oxide might have formed at the layer surface.

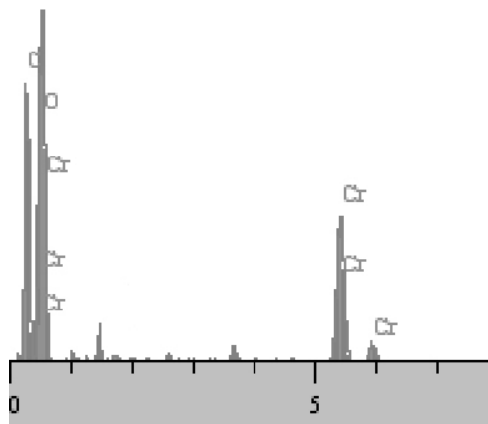
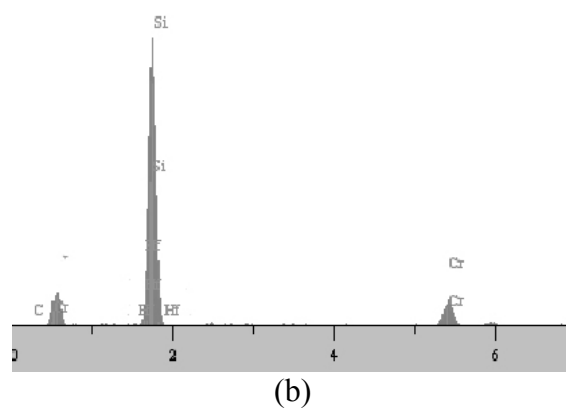
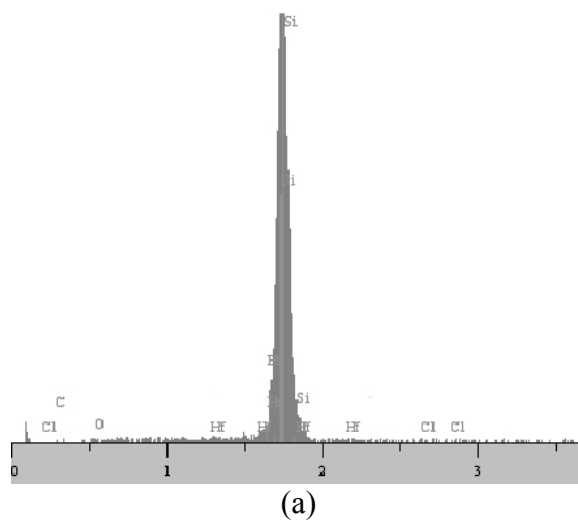


Figure 4.104. EDAX spectrum of reaction product layer at the interface of Specimen #3 showing intense Cr and C peaks.

Figures 4.105 (a) to (c) show the EDAX spectra of the three different phases observed in the refractory coating applied to Specimen #18 after a 2 hr and 30 minutes weight loss test. Refer to Figure 4.85 to observe the presence of three distinct colored phases. From Figure 4.105 (a), a single intense peak of Si is present confirming the existence of the  $\alpha\text{-Si}$  phase. From Figure 4.105 (b) the presence of Si and Cr peaks indicate that a chromium silicide may have formed,



such as  $\text{CrSi}_2$ . Finally, Figure 4.105 (c) verifies the presence of a hafnium silicide compound from the intense Hf and Si peaks. Less intense peaks of oxygen and carbon may be due to surface adsorbed  $\text{CO}_2$  and  $\text{O}_2$  molecules.



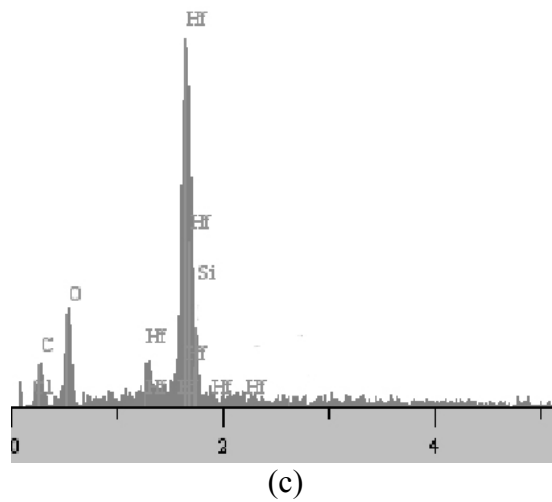
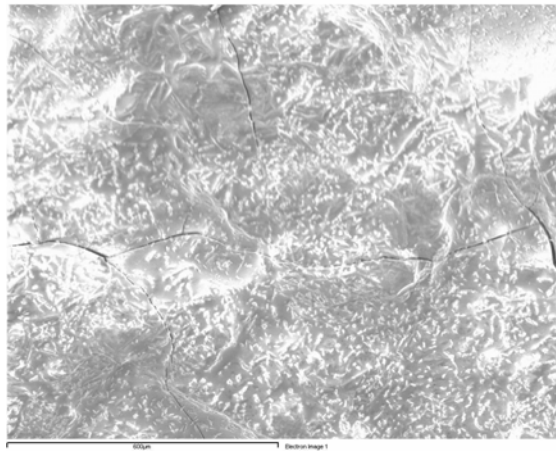
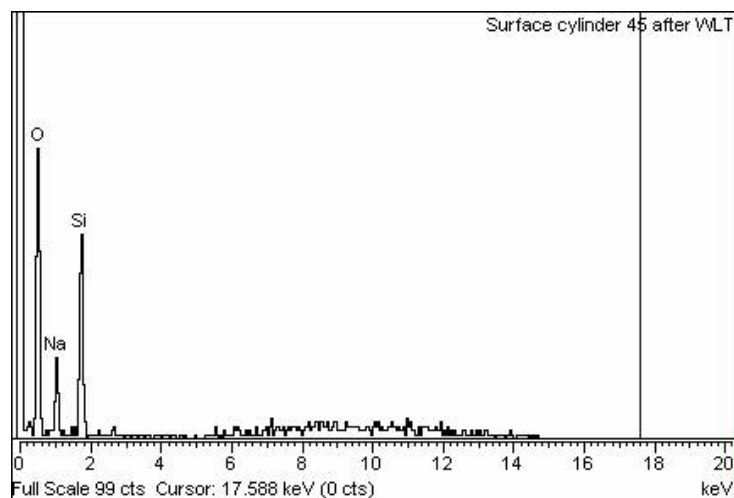


Figure 4.105. EDAX spectrum of Specimen #18, after weight loss test for 2 hr 30 minutes. (a) Gray phase showing a strong Si peak, (b) light gray phase showing strong Si peak and less intense Cr, Hf and C peaks, (c) white phase showing strong Hf and Si peaks.



(a)



(b)

Figure 4.106. (a) Surface of glass-modified overcoat in Specimen #46 (b) EDAX spectrum of a surface spot.

Figure 4.106a shows the SEM image of the surface of the glass-modified overcoat applied to Specimen #46 after being weight loss tested for up to 5 hours. In Figure 4.106b the illustrated EDAX spectrum from that surface indicates the presence of Si, Na and oxygen peaks as expected.

Figure 4.107 shows the SEM image of the surface area of the glass-modified overcoat applied to Specimen #47 after being weight loss tested. This area was selected for EDAX elemental mapping. Figures 4.107 (b) to (d) show the distribution of Si, oxygen and Na, respectively. These distributions appear rather similar, indication that the composition of the glass-modified overcoat was significantly homogenous. Dark zones in the maps indicate that the surface is not

flat but with emerging features, thus blocking the path of the emitted signal from the material to the detector [20].

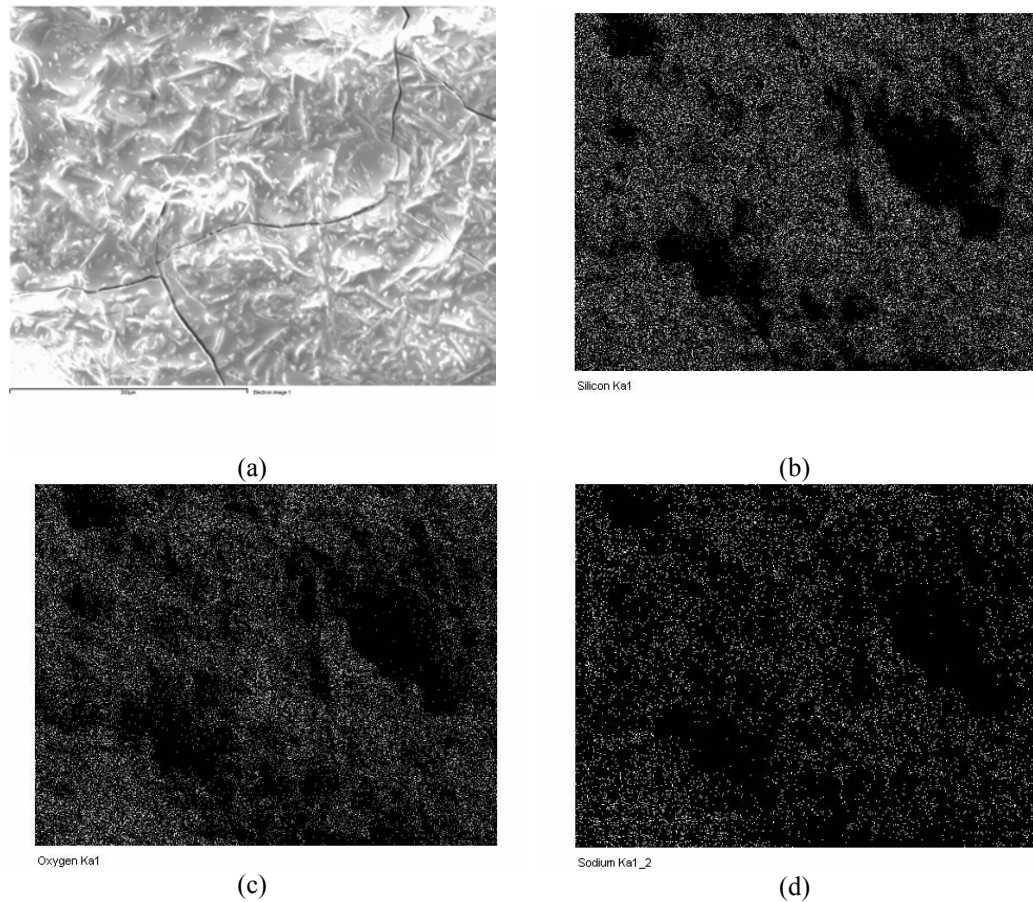
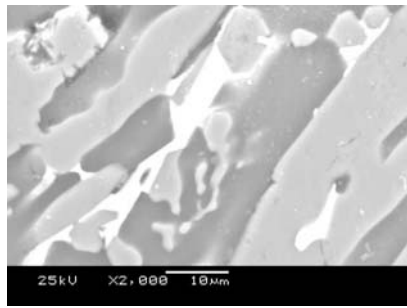
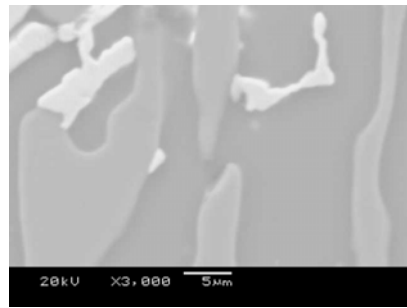


Figure 4.107. (a) Surface of glass-modified overcoat on Specimen #47 selected for elemental mapping (b) Si distribution (c) oxygen distribution (d) Na distribution.

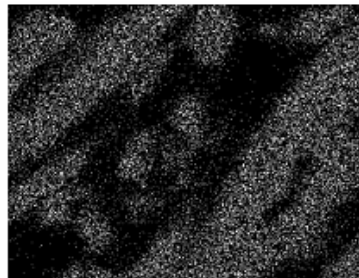
In Figure 4.108 an elemental mapping comparison between the refractory coating phases of Specimens #45 (not weight loss tested) and #43 (weight loss tested) is presented.



(a<sub>1</sub>)

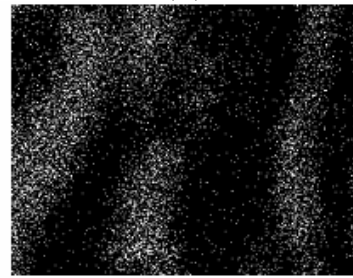


(a<sub>2</sub>)



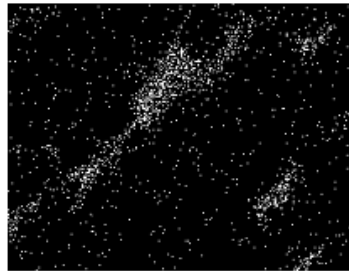
Chromium Ka1

(b<sub>1</sub>)



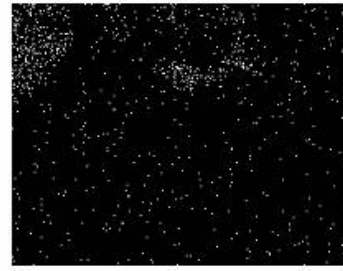
Chromium Ka1

(b<sub>2</sub>)



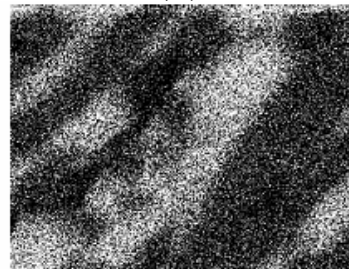
Hafnium La1

(c<sub>1</sub>)



Hafnium La1

(c<sub>2</sub>)



Silicon Ka1

(d<sub>1</sub>)



Silicon Ka1

(d<sub>2</sub>)

Figure 4.108. (a<sub>1</sub>) Specimen #45 (not weight loss tested) (b<sub>1</sub>) Cr distribution (c<sub>1</sub>) Hf distribution (d<sub>1</sub>) Si distribution (a<sub>2</sub>) Specimen #43 after weight loss test (b<sub>2</sub>) Cr distribution (c<sub>2</sub>) Hf distribution (d<sub>2</sub>) Si distribution.

It can be seen that the Si and Cr distributions are similar, but hafnium is less concentrated after the weight loss test. This suggests that hafnium experiences a tendency to migrate out of the white phase, as already mentioned. From Figure 4.109 it can be seen that there is a difference in the spectrum of the Hf-Si phase (white colored phase) in the specimen that has not undergone weight loss testing relative to the phase in the specimen that was tested. It appears as though as the stability of hafnium in this phase is not significant at high temperatures.

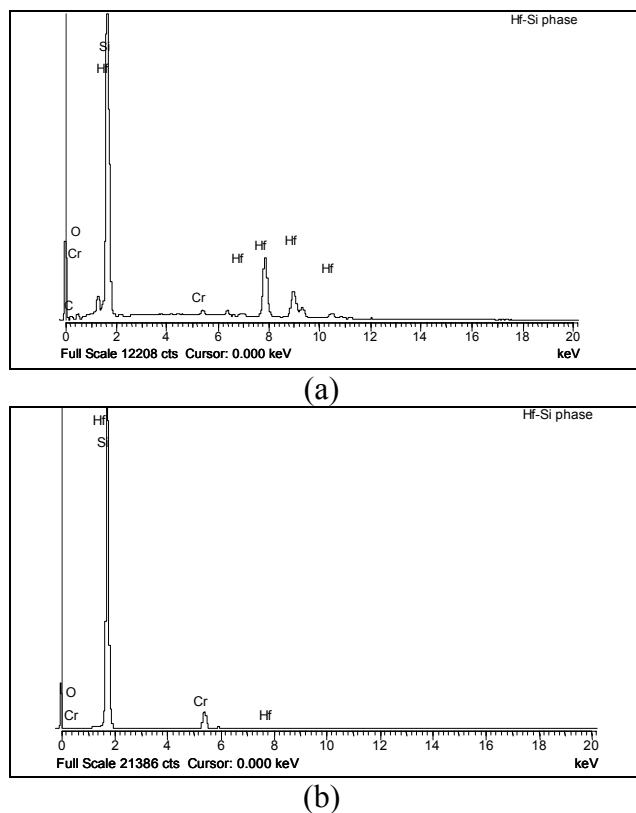


Figure 4.109. Comparison of EDAX spectra of the Hf-Si "white" phase (a) before and (b) after heat treatment due to weight loss testing.

In Figure 4.110 the mapping analysis at the upper interface between the refractory coating and the glass-modified overcoat in Specimen #45 shows that all the elements are homogenously distributed in their respective phases and that no interdiffusion has occurred during the fabrication of the specimen coatings.

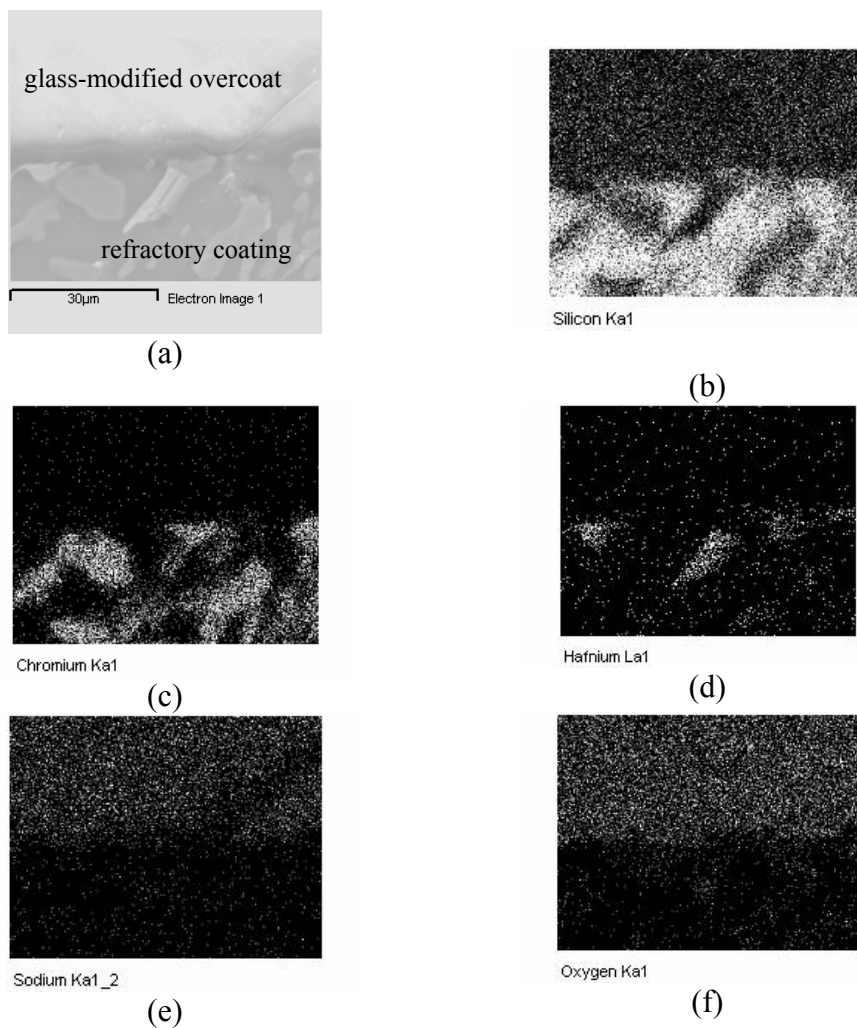


Figure 4.110. (a) Specimen #45, upper interface showing glass-modified overcoat (b) Si distribution (c) Cr distribution (d) Hf distribution (e) Na distribution (f) oxygen distribution.

From Figure 4.111 the mapping of the various elements at the lower interface between the refractory coating and the C/C composite substrate reveals that chromium diffusion towards the C/C region has occurred at a higher rate compared to observed silicon interdiffusion. On the other hand, diffusion of carbon from the C/C substrate into the coating has not occurred. Bright spots in Figure 4.111d correspond to the C added deliberately in the second layer, but it could also be a signal noise.

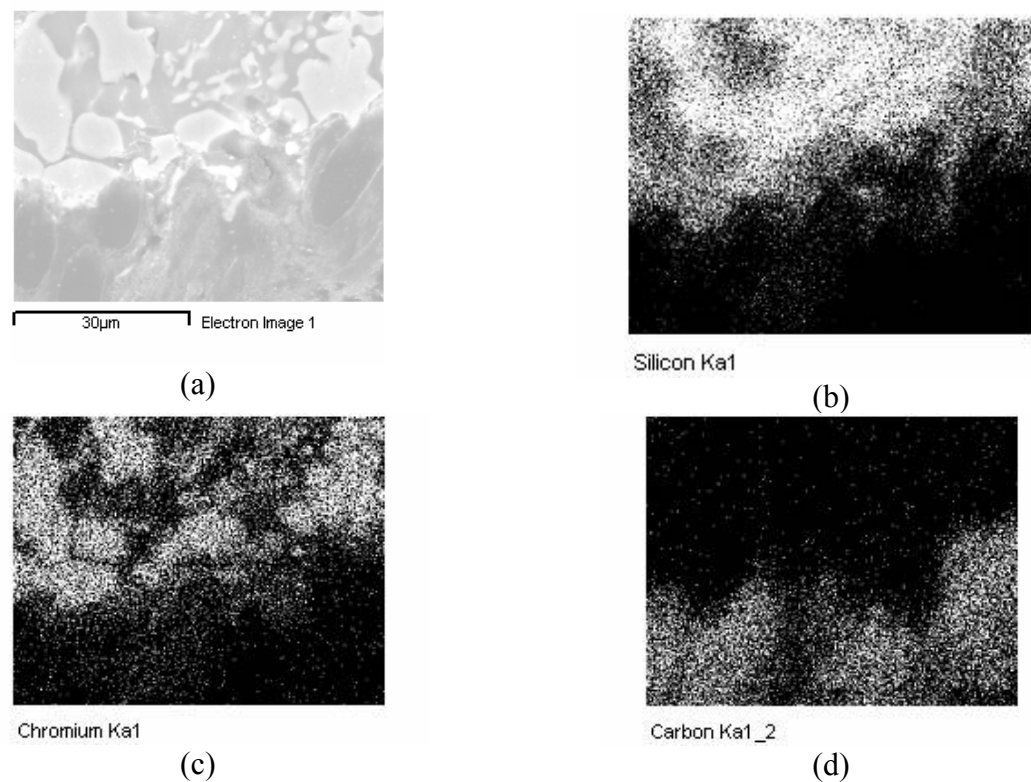
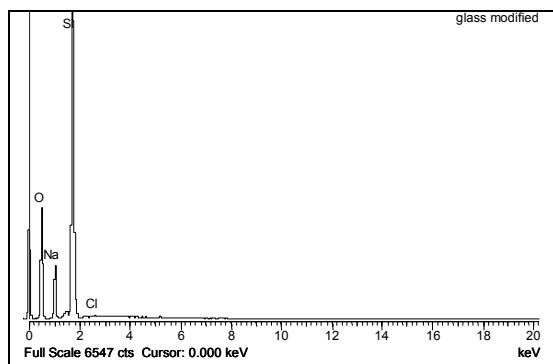


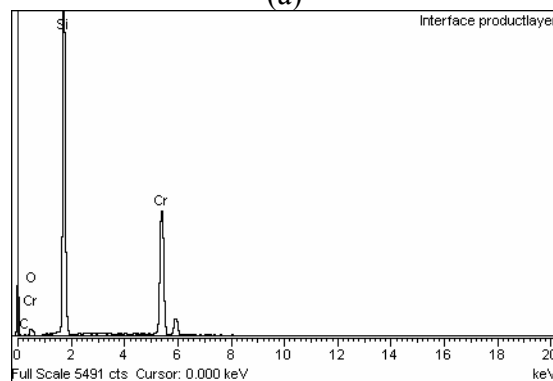
Figure 4.111. (a) Specimen #45, lower interface with C/C composite (b) Si distribution (c) Cr distribution (d) C distribution.



Finally, EDAX spectra of the interfacial region at both the upper and lower interfaces is illustrated in Figure 4.112 (a) and (b). In spectrum (a), all the expected peaks are present (i.e., Si, Na and oxygen), but additionally an almost negligible chlorine peak is revealed. This signals that traces of  $\text{Cl}^-$  ions remained in the refractory coating after the laser processing and migrated towards the upper interface during the overcoat formation. During the weight loss test, the high reactivity of  $\text{Cl}^-$  ions and the elevated temperature is perhaps one of the reasons for the pitting and cavity formation in the overcoat surface.



(a)



(b)

Figure 4.112. EDAX spectra of the (a) upper interface region in Specimen #45 and (b) lower interface region in Specimen #45.

In spectrum (b), strong Cr and Si peaks indicate the formation of a  $\text{CrSi}_2$  reaction product layer; however, the presence of a C peak indicates the presence of SiC, too.

#### 4.2.2.5 X-ray diffraction analysis

From Figure 4.113, the x-ray diffraction (XRD) pattern of a Specimen # 3, coated with a chromium product layer, is shown. An intense chromium oxide ( $\text{Cr}_5\text{O}_{12}$ ) peak was indexed as well as the graphite peaks and a chromium carbide ( $\text{Cr}_{22}\text{C}_6$ ) peak. The graphite peak originates from the C/C substrate. Oxidation of the resulting chromium layer is feasible as the coating process was done at high temperature and under rough vacuum conditions. Moreover, the peaks are broad indicating that the coating formed had a significant fraction of an amorphous structure.

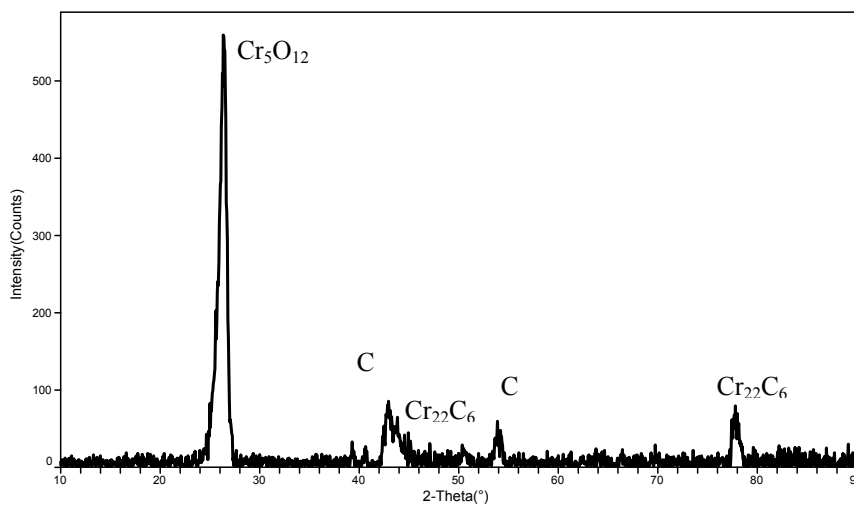
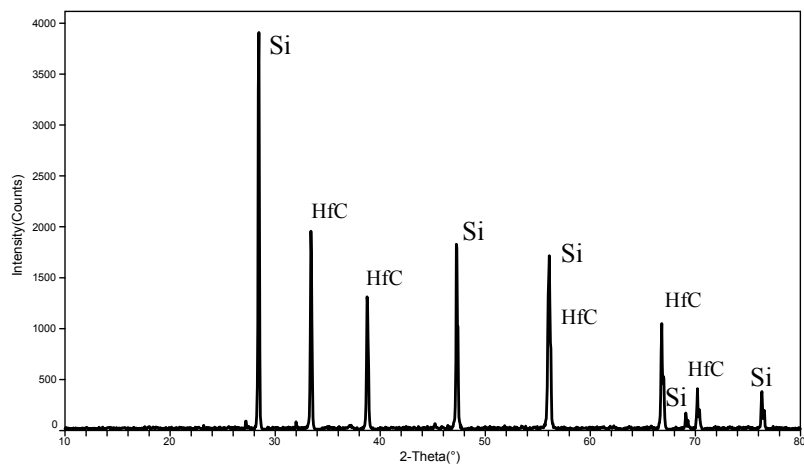
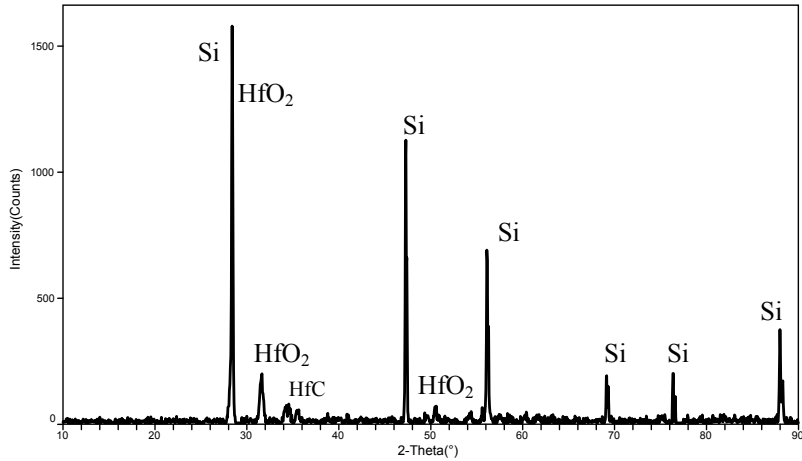


Figure 4.113. XRD pattern of chromium coated surface of Specimen #3.

The XRD pattern shown in Figure 4.114 (a) corresponds to the Si-35HfC powder mixture used to coat Specimen #8. From this diffraction pattern all the Si and HfC peaks are indexed and the ratio of the low angle peaks corresponds approximately to 35:65. This powder mixture was then heat treated at 750°C for 1 hour in air to oxidize the HfC to form HfO<sub>2</sub>. From Figure 4.114 (b), the XRD pattern of the powder after the heat treatment shows all the Si peaks plus those corresponding to the HfO<sub>2</sub> phase, a small peak of HfC is seen. No presence of SiO<sub>2</sub> peaks is observed indicating that the temperature was too low for silicon to oxidize.



(a)



(b)

Figure 4.114. X-ray diffraction pattern of the Si-35HfC (wt.%) powder mixture used in Specimen #8 (a) before and (b) after a heat treatment at 750°C for 1 hour in air. It can be observed that the HfC has been almost completely oxidized to HfO<sub>2</sub> while no presence of SiO<sub>2</sub> is indicated.

Figure 4.115 shows the XRD pattern of the silicon coated surface of Specimen #C15. From this pattern, the presence of SiC is not verified but only that of Si and C. This means that only a very thin SiC interface might have formed. However, the extent of this interface over the composite surface is not known.

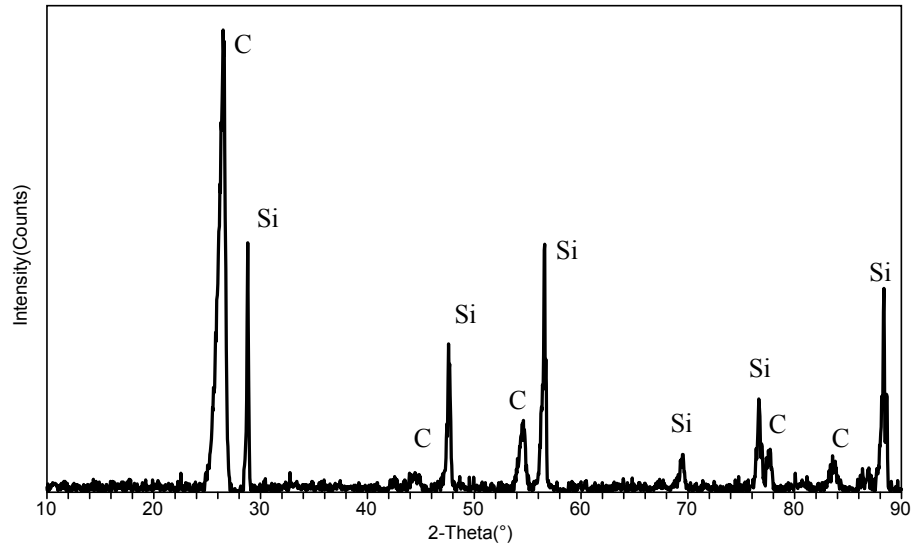


Figure 4.115. XRD pattern of the surface of silicon coated Specimen #C15.

Figures 4.116 and 4.117 show XRD patterns of the powder mixtures corresponding to second and third coating layers, this is Si-25Cr-5C and Si-15HfCl<sub>4</sub>-15Cr all in wt.%, respectively. The powders were ground separately and shaped into pellets that were heated continuously up to 875°C in air at a rate of 10°C/min and then allowed to cool. The heat treated pellets were then ground again and the powder formed was used to determine the composition of each mixture. In Figure 4.116 the sharp Si, Cr and C peaks are clearly indexed and the Cr to Si peak ratio corresponds to 25:70 while the C to Si ratio corresponds to 5:70. This indicates that 875°C was not a high enough temperature and there was not sufficient time for expected compounds like CrSi<sub>2</sub> and SiC to form. Moreover,

no oxide phases are indexed, signaling once more that the temperature and time of heating were not sufficient for oxidation and other chemical reactions to take place.

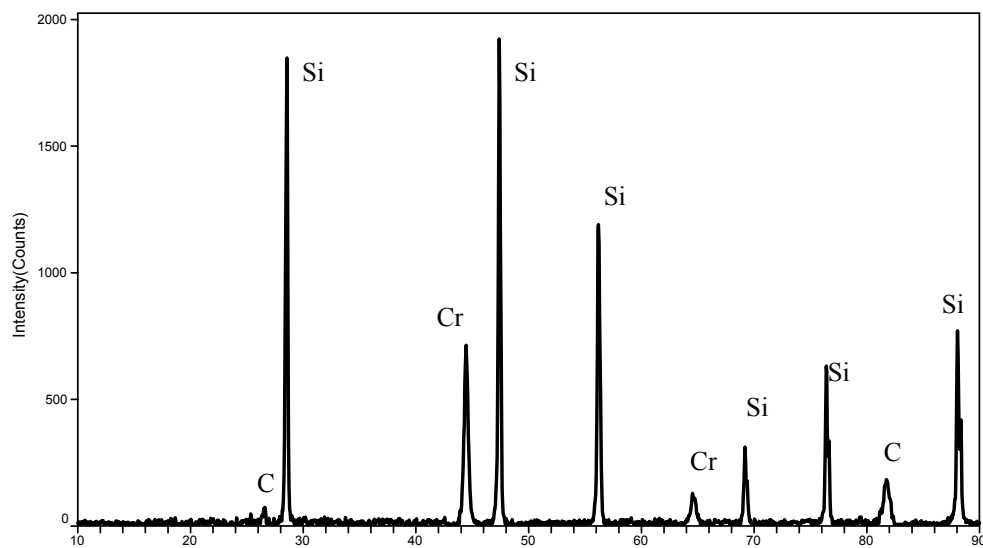


Figure 4.116. XRD pattern for Si-25Cr-5C (wt.%) mixture heated up to 875°C in air.

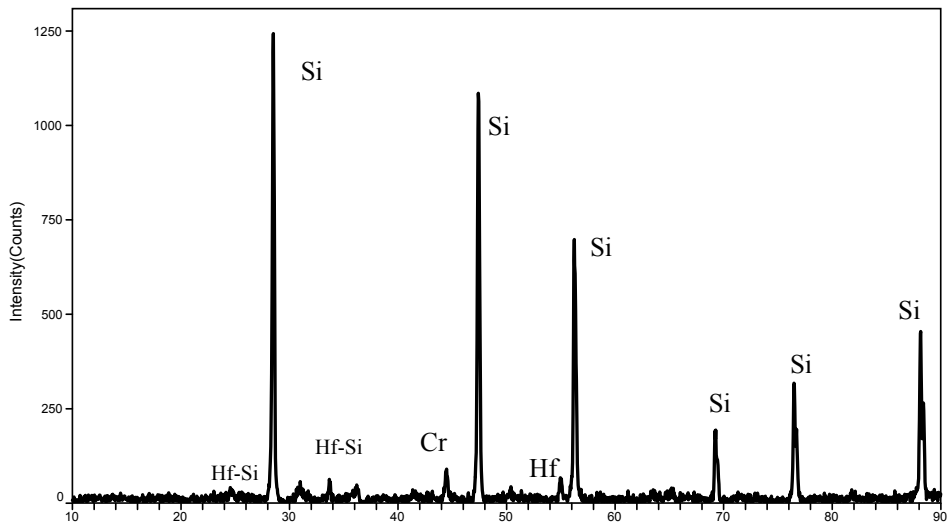


Figure 4.117. XRD pattern of Si-15HfCl<sub>4</sub>-15Cr (wt.%) mixture heated up to 875°C in air.

The same can be said from Figure 4.117, as the sharp diffraction pattern for Si, Cr and Hf are clearly indexed. However, the hafnium salt has decomposed and most of the Cl<sup>-</sup> ions have evolved from the powder. Low intensity peaks corresponding to hafnium silicide (HfSi<sub>2</sub> and Hf<sub>2</sub>Si) are present indicating that the reactivity of this mixture was higher than for the previous coating material mixture, as expected from the presence of hafnium.

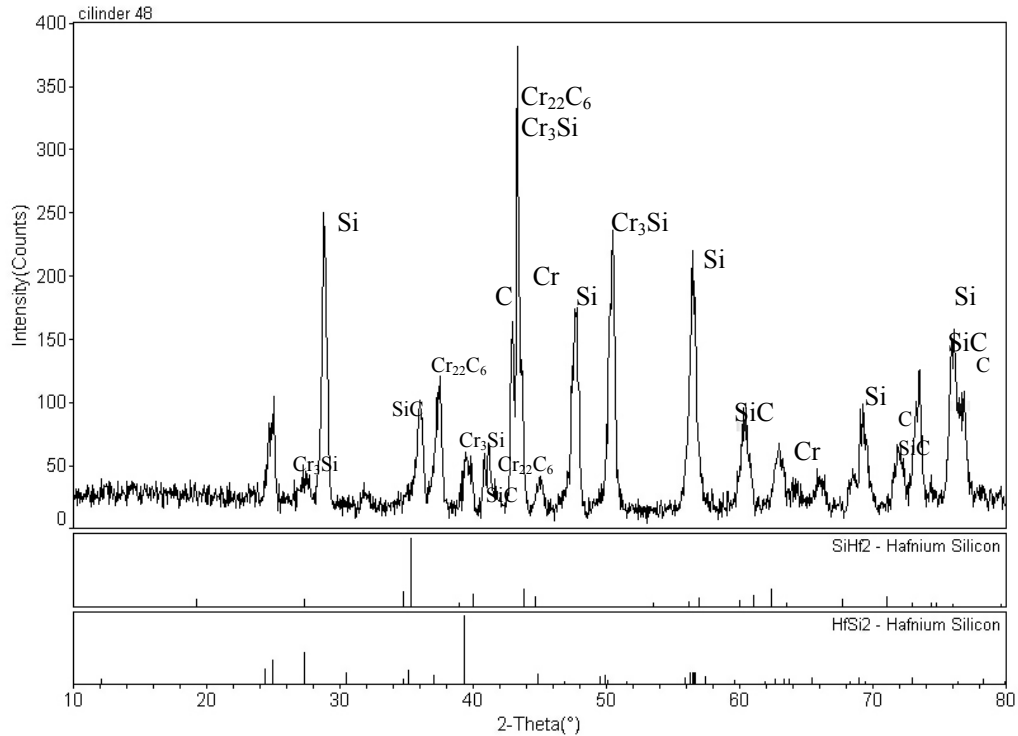


Figure 4.118. XRD pattern of Specimen #48 coated with a  $\text{CrCl}_3$ -30Cr, Si-25Cr-5C and Si-15HfCl<sub>4</sub>-15Cr layers (all in wt.%) by the LIC process.

Lastly, from Figure 4.118 a complex diffraction pattern was obtained from the surface of Specimen #48. This C/C composite cylinder was coated using the LIC process with a three layer sequence consisting of :  $\text{CrCl}_3$ -30Cr, Si-25Cr-5C and Si-15HfCl<sub>4</sub>-15Cr in wt.%. The peaks are broad signaling that the laser processed material has a high fraction of amorphous structure. The Si, Cr and C peaks can be indexed together with SiC,  $\text{Cr}_{22}\text{C}_6$  and  $\text{Cr}_3\text{Si}$  peaks. Some of the



peaks from the hafnium-silicide phases,  $\text{SiHf}_2$  and  $\text{HfSi}_2$ , can be matched to those recorded.

#### ***4.2.2.6 Determination of the coefficient of linear thermal expansion***

Thermo-mechanical analysis (TMA) results of two coatings, having similar composition, are presented in Figure 4.119 and 4.120 as plots of the linear expansion of a cylindrical pellet made from the coating materials versus temperature variation on heating and cooling. The heating rate corresponded to 10 °C/min and the atmosphere used was still air. The TMA results for a coating segment previously laser fused, of composition Si-20Cr-7HfCl<sub>4</sub>-3C in wt%, is presented in Figure 4.74. From this plot, it can be seen that on heating the linear expansion increases up to 450 °C to then become stalled until 650°C and to increase again at a higher rate until 875 °C. During the cooling stage the linear contraction is homogenous and well behaved down to room temperature.

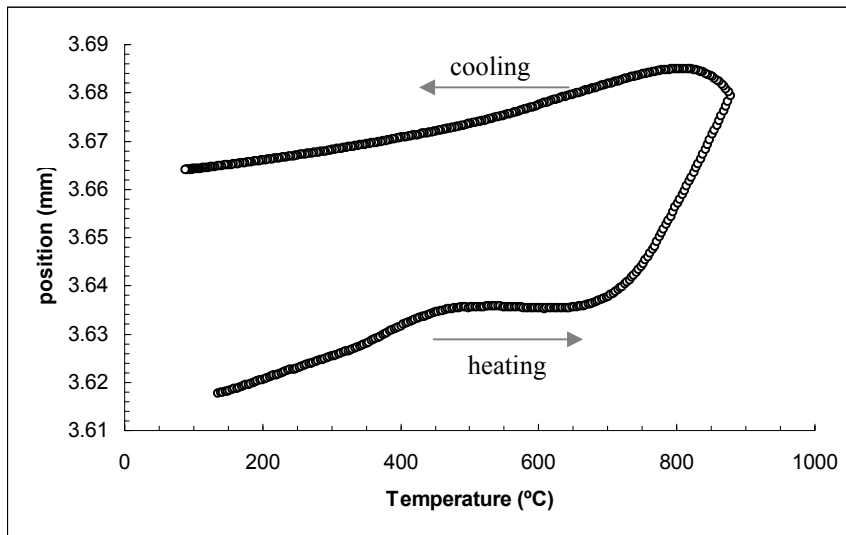


Figure 4.119. TMA plot of laser processed coating material pellet consisting of Si-20Cr-7HfCl<sub>4</sub>-3C in wt.%.

In Figure 4.120 the TMA results of a non-laser treated precursor powder, of composition Si-20Cr-7.5HfCl<sub>4</sub>-2.5C in wt%, are plotted. It can be observed that during the heating stage the linear expansion increases monotonously up to 875 °C and during the cooling stage the linear contraction decreases in the same manner down to room temperature.

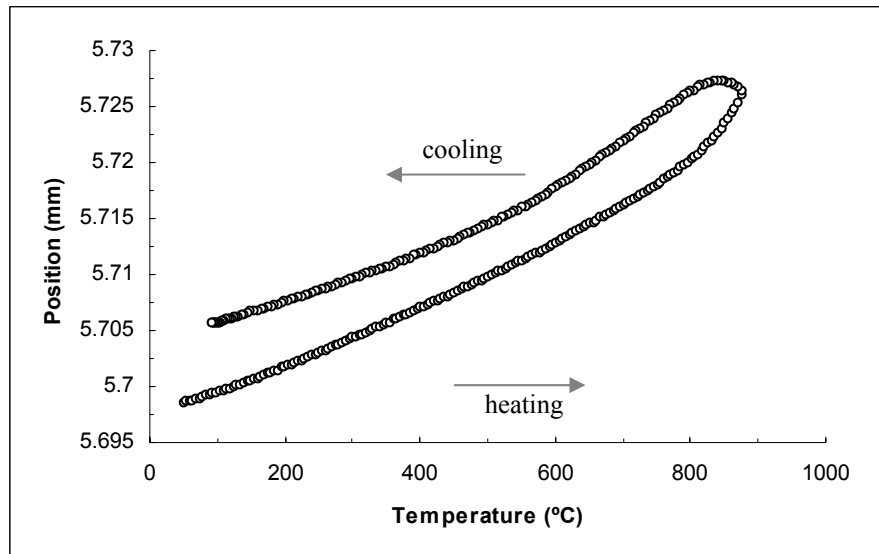


Figure 4.120. TMA plot of precursor powder mixture pellet consisting of Si-20Cr-7.5HfCl<sub>4</sub>-2.5C in wt.%.

The coefficients of thermal expansion were then obtained from these plots by numerically computing the first derivative at each point by a finite difference scheme and dividing the result by the original length of the pellet. The results are plotted in Figures 4.121 and 4.122, respectively. From the first plot, it can be seen that the CTE below 400°C corresponds to an average value of  $1.8 \times 10^{-5} \text{ K}^{-1}$  and then decreases to zero until 650°C. It then increases up to  $7 \times 10^{-5} \text{ K}^{-1}$  at 850 °C.

In Figure 4.123, the CTE values are much better behaved and the average value for the CTE within a range of 180 °C to 700°C corresponds to  $5 \times 10^{-6} \text{ K}^{-1}$ . The estimated average value of the CTE from a rule of mixtures for the pure elements that make up the coating corresponds to  $3.85 \times 10^{-6}$ . This result is almost an order of magnitude smaller than the CTE values seen on the laser processed

material, Figure 4.121, except for the 400 to 650 °C range where the former shows anomalously low CTE values.

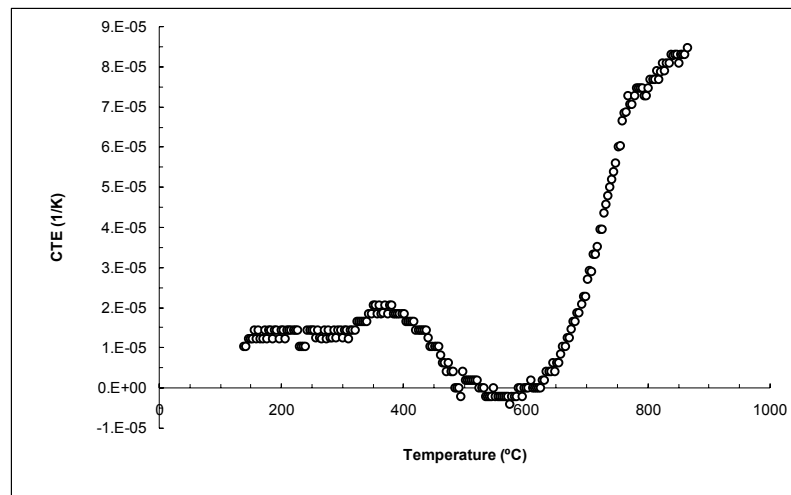


Figure 4.121. CTE plot during heating stage of laser processed coating material consisting of Si-20Cr-7HfCl<sub>4</sub>-3C in wt.%.

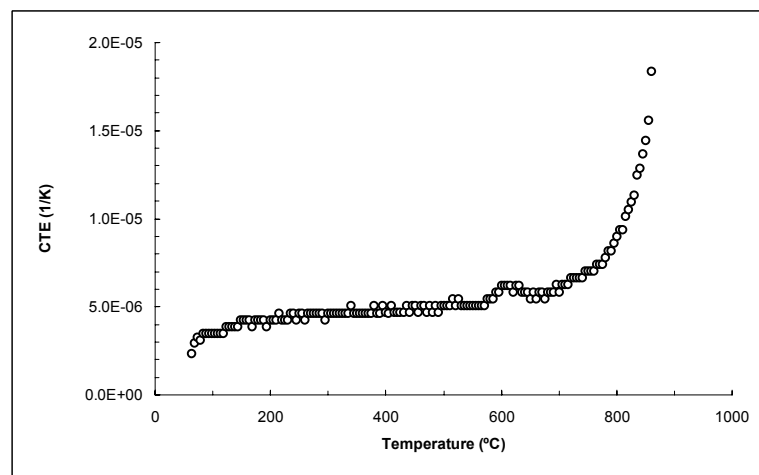


Figure 4.122. CTE plot during heating stage of precursor powder mixture consisting of Si-20Cr-7.5HfCl<sub>4</sub>-2.5C wt.%.

#### 4.2.2.7 Differential thermal analysis

Differential thermal analysis (DTA) was done on the same coating materials that were tested for TMA in the previous section to determine the melting and solidifying temperatures of the coating material applied to the C/C composites as well as any other kind of phase transformation that may have taken place during laser processing. These results are presented in Figure 4.123 and 4.124 for laser processed and non-processed coating materials, respectively. From the first plot, the principal feature on the heating stage is the endothermic peak due to the solid-liquid phase transition at 1290 °C. A smaller peak at 1260°C can be seen.

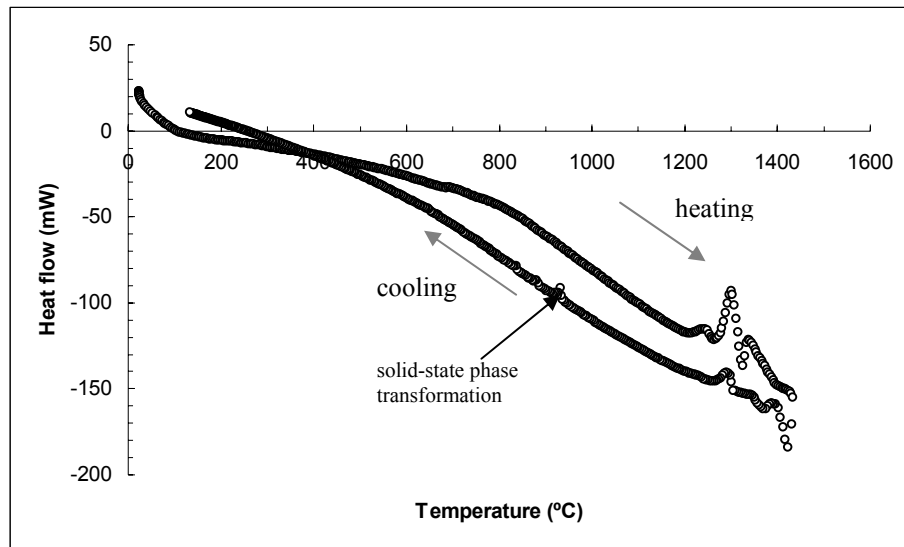


Figure 4.123. DTA plot of laser processed coating consisting of Si-20Cr-7HfCl<sub>4</sub>-3C wt.%.

On cooling, the liquid-solid phase transition (exothermic peak) occurs at the temperature of approximately 1290°C. An additional exothermic peak occurs at 890°C signaling the occurrence of a solid state transformation. This may be the transformation of trydamite into quartz provided some of the silicon has been oxidized to SiO<sub>2</sub>.

The DTA results for the precursor powder mixture non-processed are very similar to those of the laser processed coating. On heating a single endothermic peak occurs at 1300°C signaling the solid-liquid phase change. On cooling two small exothermic peaks are seen at 1310°C and 790°C. The first signals the liquid-solid phase transformation while the second peak suggests that a solid state phase transformation has occurred, presumably a trydamite to quartz transformation.

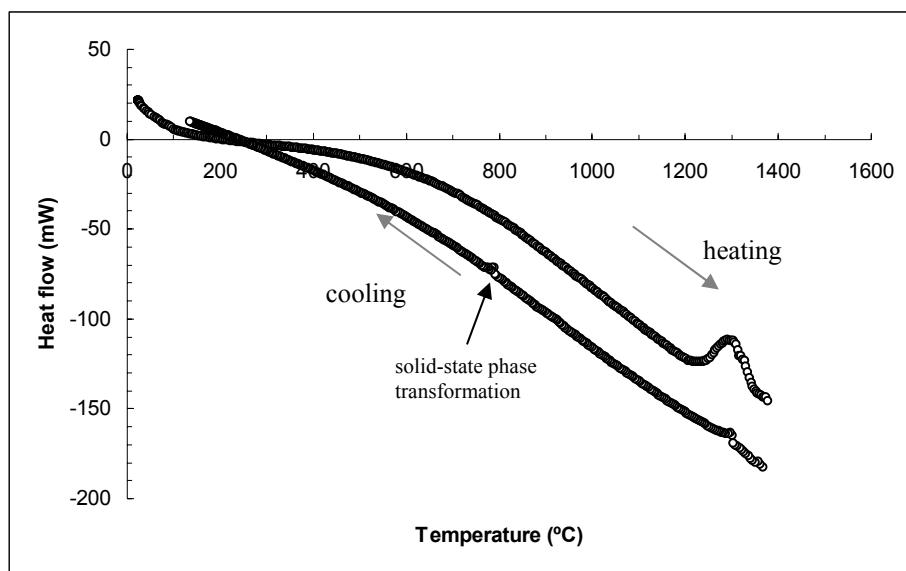


Figure 4.124. DTA plot of powder mixture consisting of Si-20Cr-7.5HfCl<sub>4</sub>-2.5C wt.%.

#### ***4.2.2.8 Determination of the fracture toughness of a laser processed coating***

The results from the indentation fracture methods used to determine an approximate value of the mode-I critical fracture toughness ( $K_{Ic}$ ) for a laser processed coating material with an average composition of Si-20Cr-7HfCl<sub>4</sub>-3C (wt.%) is presented in Figure 4.125. The half indentation average diagonal  $d/2$ , the semi-crack length  $c$ , the hardness Vickers  $H$ , and the computed  $K_{Ic}$  are all plotted as function of the applied indenters load  $P$ . The nondimensional fitting constant used to obtain the value of the fracture toughness was obtained from [21] and it corresponded to 0.016. To verify the accuracy of this constant the procedure was repeated with a directionally solidified silicon polished slab; the constant fit the empirical data well in relation to the publish data for silicon, i.e.,  $8 \cdot 10^5 \text{Pa} \cdot \text{m}^{0.5}$  [21]. The  $K_{Ic}$  value for the coating material in this case had an average value of  $3.9 \text{MPa} \cdot \text{m}^{0.5}$ . If the fracture toughness were to be calculated from a rule of mixtures of the pure elements present in the coating its value would correspond to  $16.43 \text{MPa} \cdot \text{m}^{0.5}$ , indicating that a considerable overestimation of the coating fracture toughness would be incurred.

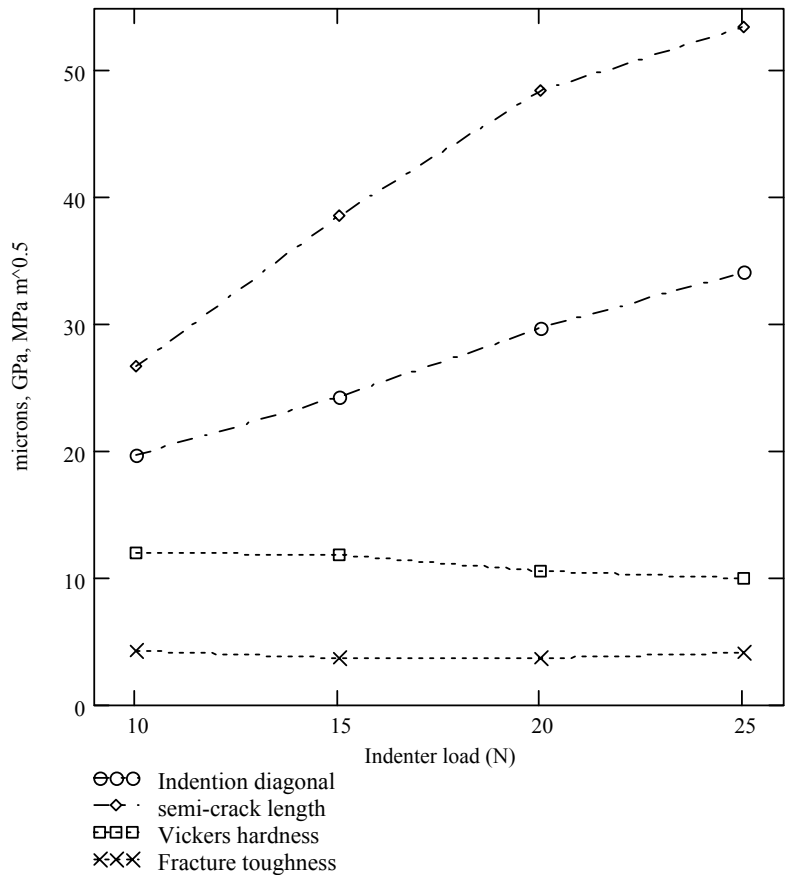


Figure 4.125. Plot of the indentation half diagonal, semi-crack length, Vickers hardness and fracture toughness as a function of applied load.

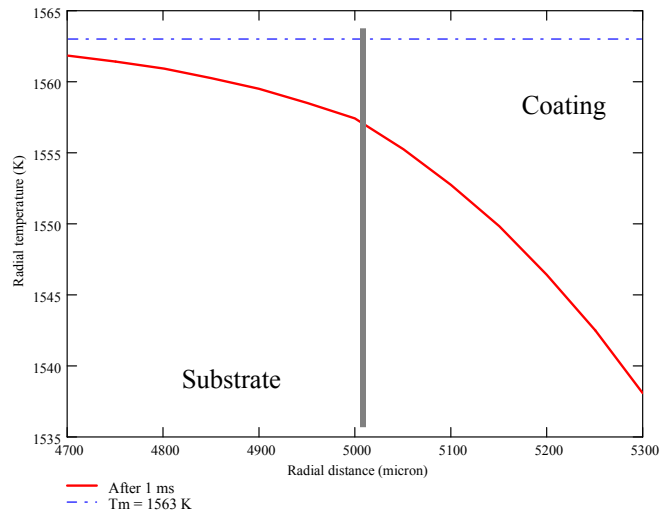
#### 4.2.2.9 Coating fracture analysis

To better explain the observations of coating fracture and delamination in some of the coated cylinders, it is convenient to understand the primary factors that drive the cracks, primarily: temperature field and the stress states on cooling.

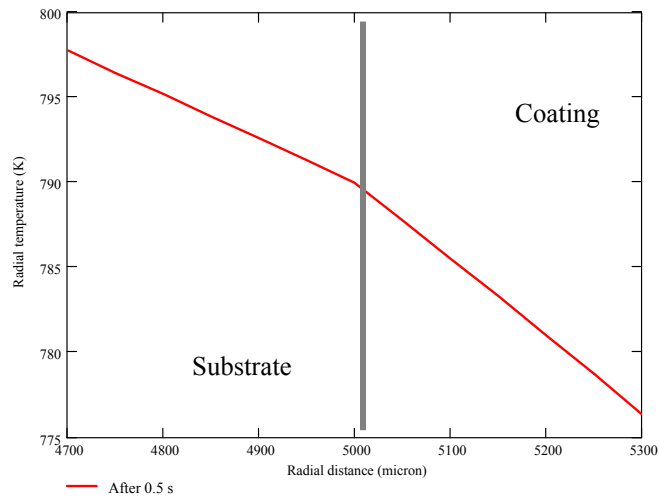


### **Thermal analysis**

From Figure 4.126, the calculated radial temperature profile during cooling of a coated C/C composite having a uniform initial temperature equal to the melting point of the coating (i.e., 1563 K) is plotted. Figures 4.126 (a) and (b) correspond to different cooling times of 1 ms and 0.5 s, respectively. These plots were obtained by implementing the two-layer cylinder model presented in Chapter II Section 2.3.4.2. It can be observed that the temperature gradient at the coating-side is steeper than at the substrate-side even though the heat flow crossing the interface must be equal. As heat evolves from the center of the cylinder towards the surface of the coating during cooling, the thermal conductivity of the C/C substrate must be higher than that of the coating to balance the thermal gradient difference. From the second plot, the thermal gradient in the neighborhood of the interface increases in magnitude at the substrate-side with increasing cooling time, while it decreases at the coating-side. This is verified when plotting the first derivative of temperature with respect to the radial direction as shown in Figure 4.126 for 1 ms and 0.5 s.



(a)



(b)

Figure 4.126 Simulated radial temperature distribution during cooling of a coated cylinder from an initial temperature of 1563 K (a) after 1 ms (b) after 0.5 s.

As cooling time increases, the thermal gradient becomes uniform along the radial direction, but at the interface the difference in thermal gradient remains almost constant and equal to 2 K/mm. The difference in thermal gradient between

the coating and substrate contributes together with the CTE mismatch of the two materials ( i.e.,  $5.6 \cdot 10^{-5} \text{ K}^{-1}$ ) to the development of a tensile stress state in the coating.

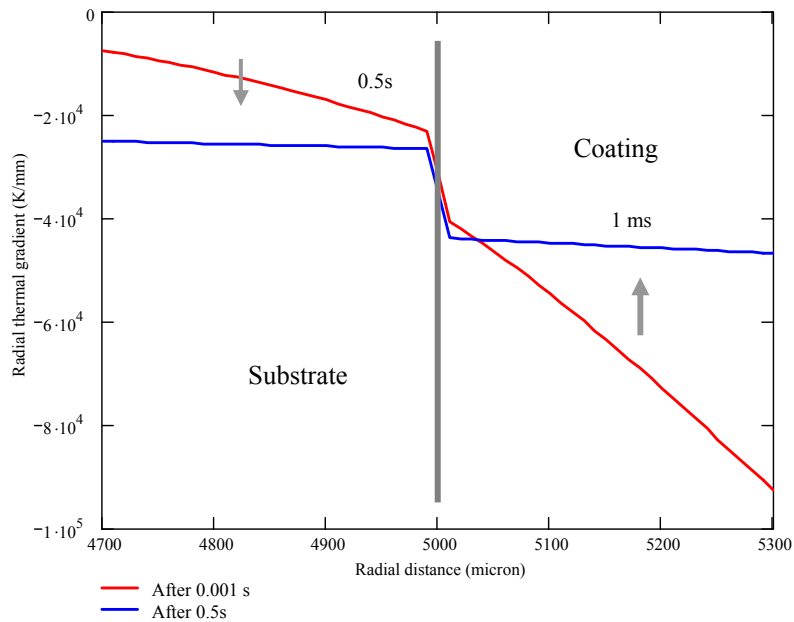


Figure 4.127. Simulated thermal gradient distribution during cooling of coated cylinder (a) after 1 ms (b) after 0.5 s.

### **Stress state analysis**

In Figure 4.128 the plane stress state,  $\sigma_r$  and  $\sigma_\theta$ , along the radial direction of the coated cylinder is plotted against radial distance from the center of the cylinder. The stress state plotted corresponds to a cooling period of half a second

for cylinder radius of 5 mm, a coating thickness of 300  $\mu\text{m}$  and an initial temperature equal to the melting point measured by means of DTA.

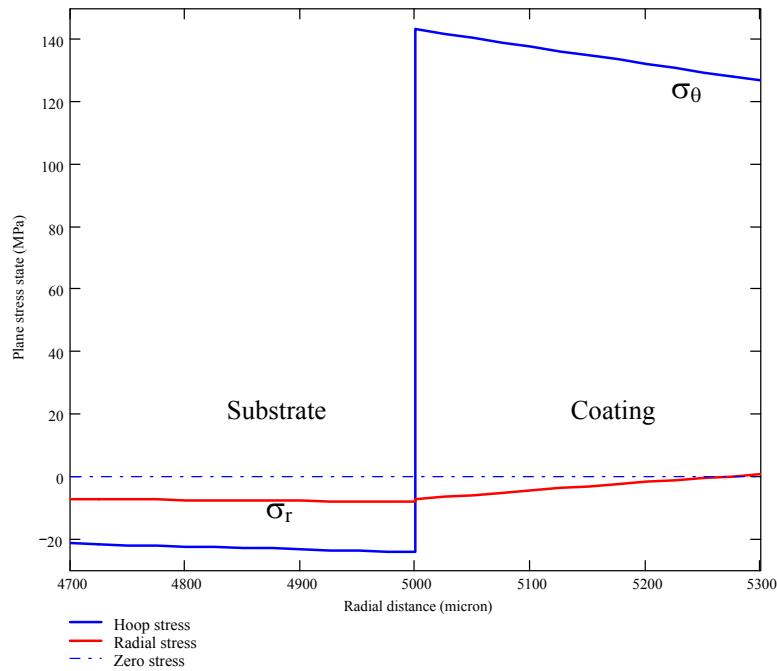


Figure 4.128. Plot of the plane stress state,  $\sigma_r$  and  $\sigma_\theta$ , along the radial direction from the center of the substrate to the coating surface.

The coating is under a tensile distribution of the hoop stress ( $\sigma_\theta$ ) and a compressive distribution of the radial stress ( $\sigma_r$ ), with the latter being two orders of magnitude smaller than the former. The radial stress on the coating approaches a zero value at the surface, due to the imposed boundary condition in the model proposed in Chapter II Section 2.3.4.1. The substrate on the other hand, is under both a radial and tangential compressive stress state distribution of equal order of

magnitude. The radial stress at the interface between the substrate and coating must have the same magnitude from either side, in accordance to the second boundary condition imposed in the model.

These numerical results indicate that the magnitude difference of the tensile hoop stress at the coating and substrate is the main driver for the propagation of pre-existing cracks. The compressive radial stress shows low magnitude and may not play a significant role on crack extension. On the other hand, the substrate is under compression and the magnitude of the stresses is low compared to the fracture stress of the C/C composite (1.85 GPa), so no spallation of the C/C composite would be expected unless considerable weakening of the graphite fiber has occurred due to oxidation at high temperature.

From the plot shown in Figure 4.129, it can be noticed that the hoop and axial stresses under plane strain condition throughout the coating are larger than the hoop stress under plane stress condition by almost a 20%. In all three cases the maximum value of the stress occurs at the interface between coating and substrate, suggesting that cracks that have originated at the surface of the coating will tend to expand radially through the coating all way to the substrate. The hoop and axial stresses converge to the same value at the surface of the coating, as in this location the radial stress is zero.

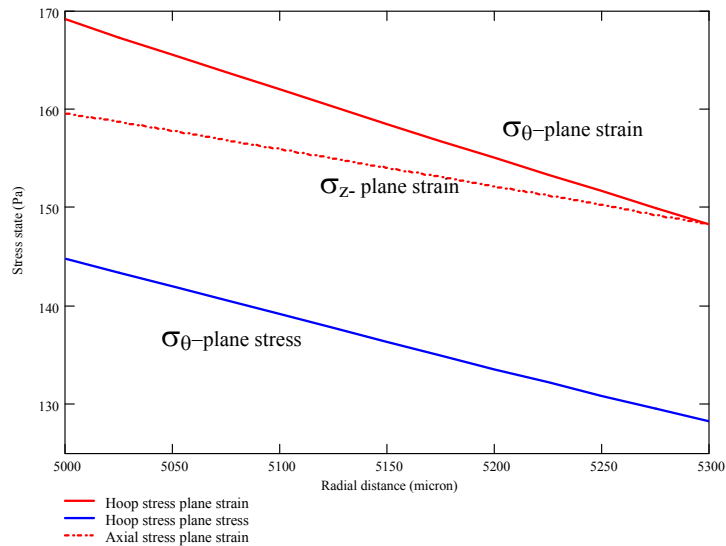


Figure 4.129. Plot of the plane stress and plane strain hoop stress,  $\sigma_{\theta}$ , as well as the axial stress in plane strain,  $\sigma_z$ , along the radial direction from the interface to the coating surface.

In Figure 4.130 the calculated radial stresses under plane strain and plane stress state condition in the coating are plotted within the radial length of the coating layer. It can be seen that both are compressive stresses and have their maximum value at the interface between the coating and the substrate (5000  $\mu\text{m}$ ), but of low magnitude. Both radial stresses tend towards a zero stress value at the surface of the coating according to the boundary condition applied at that location when modeling the problem of thermal stresses of a coated cylinder.

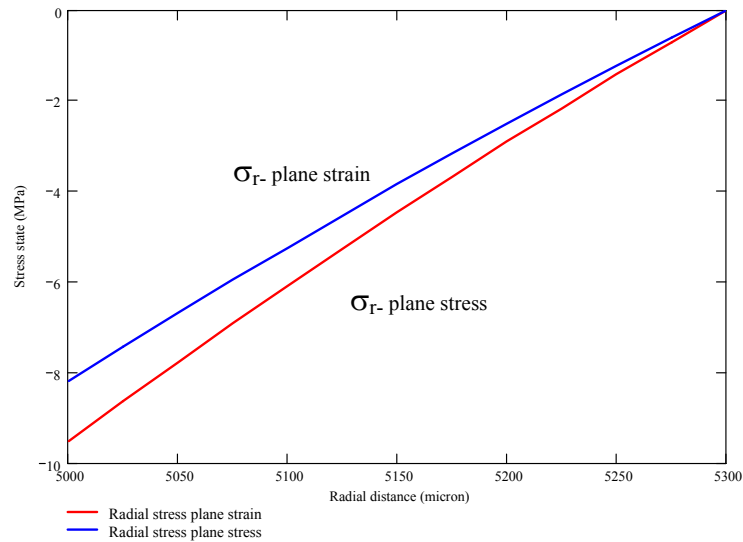


Figure 4.130. Plot of the plane stress and plane strain radial stress,  $\sigma_r$ , along the radial direction from the interface to the coating surface.

These last two plots were computed for a cooling period of 0.5 seconds. The criterion established by Hutchinson *et al.* [22] to determine whether surface cracks, channeling cracks or delamination would develop according to the thickness of the coating was applied to obtain Table 4.5. Three coating thickness of 100, 200 and 300  $\mu\text{m}$  and four cooling periods equal to 0.1 s, 0.5 s 1 s and 2 s were considered in building up this table. For each combination of parameters, a minimum and maximum coating thickness was obtained from Hutchinson's criterion, for each of the three cracking patterns. The minimum coating thickness corresponds to the criterion evaluated at the interface (coating-side) while the

maximum coating thickness corresponds to the criterion evaluated at the coating surface.

From Table 4.5 it can be seen that for a coating thickness of 300  $\mu\text{m}$  surface and channelling cracks would develop after a cooling time of 0.5 s, but no delamination of the coating from the substrate should occur. For the case of 1 s cooling time, only surface cracks should develop. For longer cooling periods none of the latter should occur as the critical coating thickness exceed the values achieved in the process (i.e., 500  $\mu\text{m}$ ). This suggests that most of the crack propagation should take place within one second cooling from the highest processing temperature, as indicated in Table 4.5 by the highlighted numbers. The criterion was evaluated with the hoop stresses under condition of plane strain at the interface and surface of the coating and in this manner a coating thickness range was determined as criteria.

Table 4.5 Crack propagation criterion based on coating thickness and time of cooling.

Coating thickness Cooling time	Surface cracking			Crack channelling			Coating debonding		
	100 ( $\mu\text{m}$ )	200 ( $\mu\text{m}$ )	300 ( $\mu\text{m}$ )	100 ( $\mu\text{m}$ )	200 ( $\mu\text{m}$ )	300 ( $\mu\text{m}$ )	100 ( $\mu\text{m}$ )	200 ( $\mu\text{m}$ )	300 ( $\mu\text{m}$ )
0.1 (s)	6	22-26	50-65	11-12	45-51	99-129	21-23	86-99	191-248
0.5 (s)	16-17	64-73	137-178	33-35	127-147	274-357	63-282	244-281	527-686
1 (s)	64-67	240-276	499-649	128-135	479-552	998-1298	245-259	921-1062	1919-2495
2 (s)	973-1029	3398-3918	6612-8599	1946-2057	6793-7835	13220-17190	3740-3954	13060-15060	25410-33050



### Fracture observation

In Figure 4.131 the surface of the overcoat layer deposited in Specimen #2, consisting of SiO<sub>2</sub>-30Si-10SiC in wt.% can be observed. A network of long channeling cracks are clearly seen and are a product of the CTE mismatch and thermal gradient difference between substrate and coating as well as the fast cooling rates at which the specimen is exposed during coating consolidation.

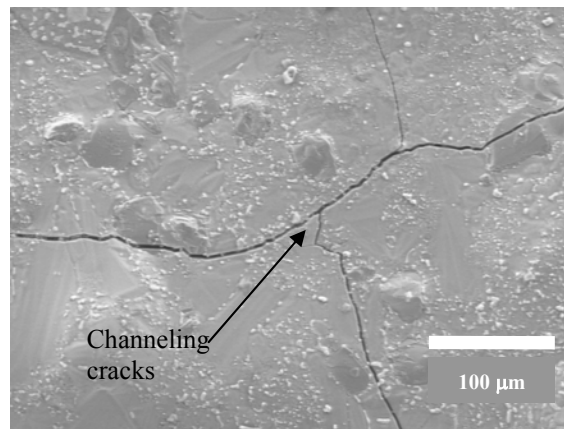


Figure 4.131. Surface of Specimen #2, 500x. Crack channeling has occurred.

From Figure 4.132, a radial crack (in opening mode) runs from the top of the surface all through the thickness of the coating of Specimen #5, cutting through the different phases and extending into the composite substrate at a certain angle with the interface. This indicates that a shear fracture mode coexists with the opening mode at the substrate and that the fibers have weakened during the LIC process. The extension of this crack was driven by the mismatch in coefficient of thermal expansion (CTE) between the overall coating mixture and

the C/C composite substrate. This in turn sets a large tensile thermal hoop stress in the coating during cooling of the specimen. The coating thickness of this specimen was approximately 300  $\mu\text{m}$ . From Table 4.5, it can be seen that channeling cracks had probably developed within the very early stages of cooling (0.5 seconds) as no interface debonding was observed. The critical energy release rate of the coating material as a whole is surpassed and extension of a pre-existing crack occurs.

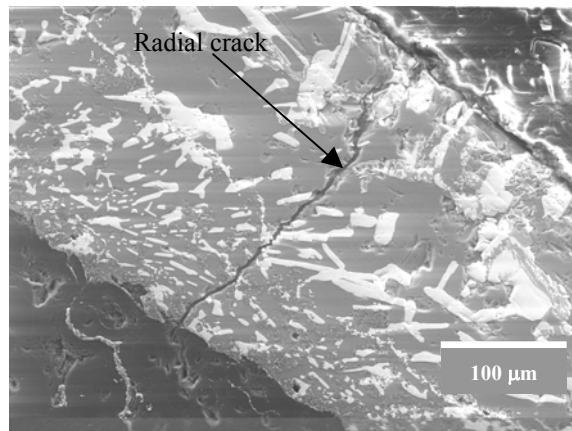


Figure 4.132. Cross-section of overall coating layer in Specimen #5, 500x. A radial crack has extended completely towards the C/C substrate.

Another radial crack is shown in Figure 4.133 that developed in Specimen #8 during the cooling stage of the LIC process. The coating thickness of this specimen, where the crack propagated, reached approximately 130  $\mu\text{m}$ .

According to Table 4.5 the crack extension should have occurred within one second of cooling time to validate the criterion. No debonding had originated. However, a spalling crack can also be observed running perpendicular to the sample in the C/C composite substrate. Weakening of the substrate fiber-matrix bonding must have taken place to allow for a crack to propagate in that region. This region is supposedly under compression stresses and C/C composites possess high fracture toughness.

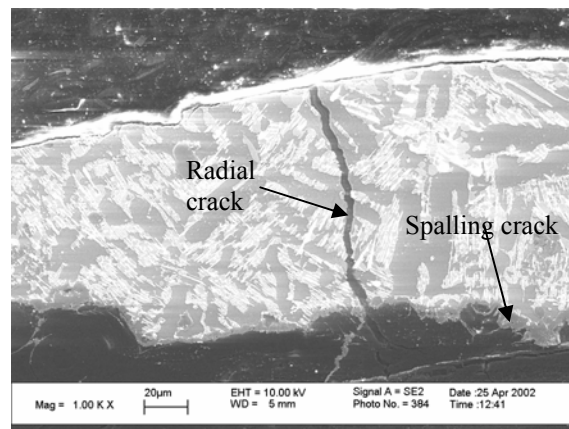


Figure 4.133. Cross-section of Specimen #8, 1000x. A radial crack through the coating and a spalling crack along the substrate can be observed.

From Figure 4.134 the propagation of a radial crack is seen that probably originated at the refractory coating layer during the fabrication of Specimen #42. During the weight loss test the crack deflected along the interface between the coating and the modified-glass overcoat, but it also continued along the radial

path, being arrested at a void. It can also be see that a crack has branched off from the debonding crack and has extended towards the radial crack, as it were attracted by the latter. This indicates the activation of a shear mode II component of the stress intensity factor. The coating thickness where the crack extended in opening mode I is of the order of  $70\ \mu\text{m}$  while the overcoat thickness up to the large pore measures approximately  $110\ \mu\text{m}$ . No delamination of the coating from the C/C substrate is seen. It is worth pointing out that the presence of an overcoat layer of different fracture toughness requires modification of the criterion defined in Table 4.5 for it to be accurate.

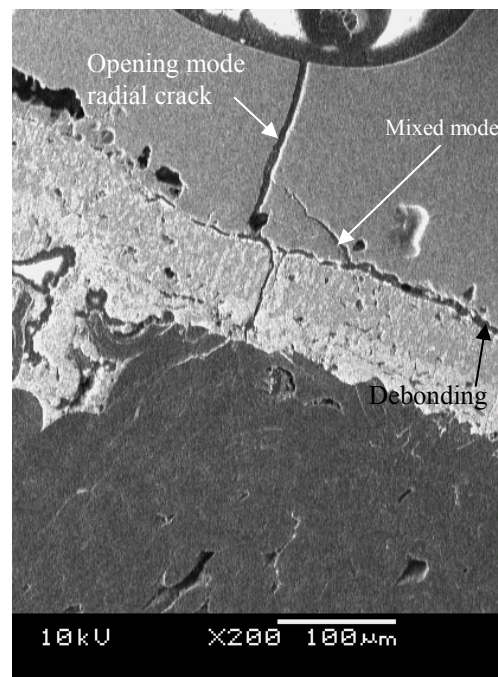


Figure 4.134. Cross-section of Specimen # 42, after weight loss test, 200x. Delamination of the overcoat from the refractory coating has occurred.

The refractory coating in Figure 4.135 shows a mixed-mode crack having a half penny shape; this crack has not propagated into the glass-modified overcoat. In this location the specimen refractory coating corresponds to 200  $\mu\text{m}$  while the glass- modified overcoat extends to 140  $\mu\text{m}$ . The specimen had gone through 20 hours of weight loss testing at 1000°C in air. During the test it has been removed from the furnace on several occasions for weight measuring purposes and then reinserted back. Interface debonding is also seen at the left hand side of the image.

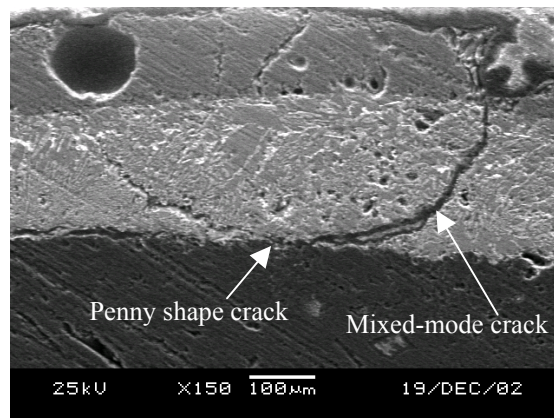


Figure 4.135. Cross-section of Specimen #43, after weight loss test for 20 hours at 1000 °C in air, 150x. A penny shape crack is seen in the refractory coating.

#### 4.2.2.10 *Weight loss oxidation testing*

Figure 4.136 shows the remains of Specimen #C2 after being weight loss tested at 1000 °C in air. Delamination of the coating has occurred during the test, reducing the oxidation protection performance. From the results shown in Figure

4.90, this specimen has experienced a 47.5 % weight reduction after 2 hours 20 minutes of exposure at 1000 °C in flowing air (2 cfh). The percent weight reduction behavior of this specimen is almost linear with exposure time, while the oxidation endurance is twice that of a blank cylindrical specimen.



Figure 4.136. Specimen # C2 after weight loss test at 1000 °C in flowing air.

From Figure 4.137 it can be seen that the oxidation protection endurance at a temperature of 1150°C achieved by Specimen #15, after 9 hours and 10 minutes corresponded to a 42 % weight reduction. Its coating mass was 744 mg. This specimen performed similarly to Specimen #24 which showed a 23.5% weight reduction at a temperature of 1000°C after 5 hours. Specimen #24 had a total coating mass of 1069 mg and it contained a SILBOND™ overcoat. Specimen #15 had the same coating sequence as Specimen #24 but not a last SILBOND™ overcoat.

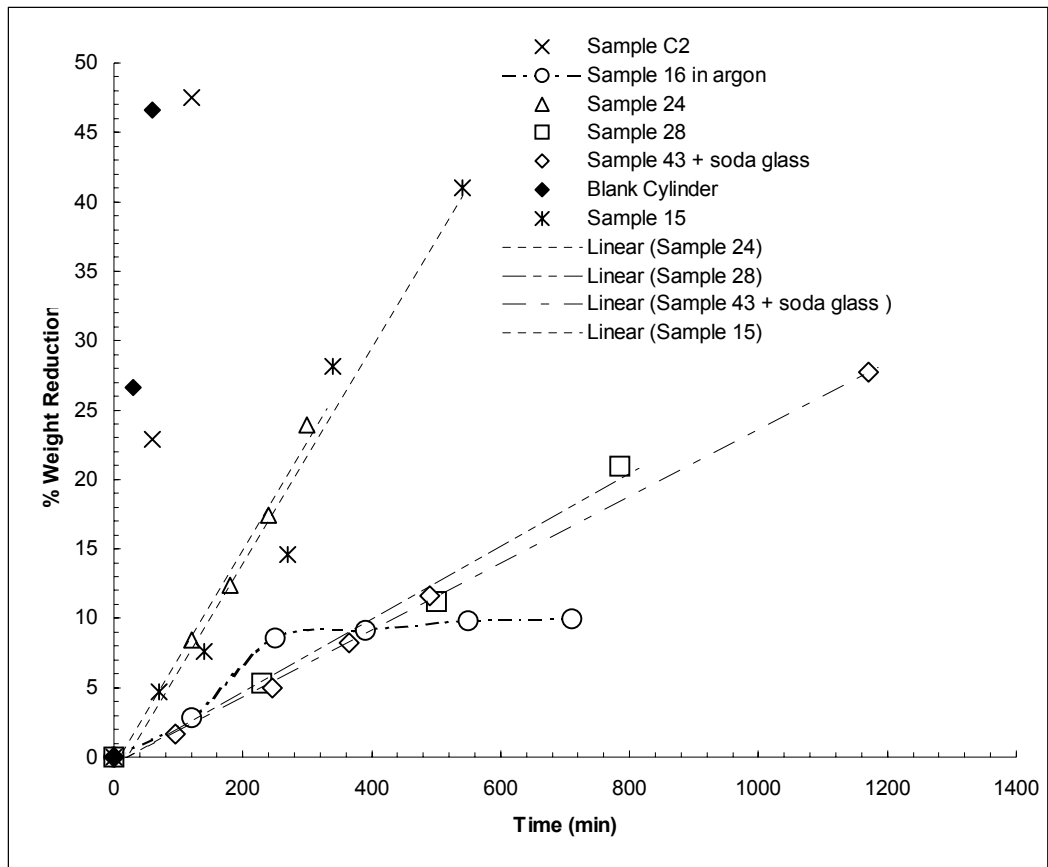


Figure 4.137. Percent weight reduction versus heating time of several specimens tested within a 1000-1150°C temperature range in still and flowing air and argon.

Specimen #16 was tested for temperature coating stability under flowing argon gas. From Figure 4.90, it can be observed that a 10 % weight reduction after 12 hours at 1150 °C was measured. This mass loss is probably due to surface oxidation happening during the removal of the specimen from the furnace for weighing purposes as well as the presence of moisture in the coating.

From the plots shown in Figure 4.137, one of the best oxidation protection endurance at a temperature of 1000°C in still air was achieved by Specimen # 28. After 13 hours of exposure time, a 21% weight reduction was recorded. This specimen had a total deposited coating mass of 266 mg and its surface was smooth. Under the optical magnification, no cracks were present before the weight loss test began. After the first 4 h interval test only a 5.4 % weight reduction had occurred. By then a few small cracks had developed on the surface. Specimen #28 showed a two fold increase in oxidation resistance compared with Specimens # 15 and # 24, the coating sequence among them being quite similar. Moreover, its coating mass was less than a half of the mass of Specimen #15.

Finally, Specimen # 43 consisting of a refractory coating and a glass-modified overcoat showed a 28% weight reduction after almost 20 hours of testing. This result corresponded to the best performance achieved in this research work. The glass-modified overcoat was able to flow at low temperatures over the surface of the refractory coating and fill up pre-existing cracks. However, the specimen was removed from the furnace five times for weighing purposes on several instances. At the third removal, it was noticed that two cavities had developed at the overcoat eroding the refractory coating. These cavities (approximately 3 mm in diameter) were patched with alumina cement, the new weight was recorded and the experiment continued.



From the plots illustrated in Figure 4.138, it can be seen that the oxidation effects on the substrate started at a temperature of 650 °C. When the temperature had reached 1000 °C the specimens had already lost approximately 4 % of their original weight. The percent reduction in weight followed a linear trend, meaning that a fraction of the surface area of the composite was in direct exposure to the atmospheric air at 1000 °C through the network of channeling cracks that extended to the substrate. After almost 5 hours at 1000 °C Specimen #40 lost 32.5 % of its original weight, while Specimens #44 and #46 lost approximately 15 % of their original weight and Specimen #47 underwent an 11 % weight reduction only.

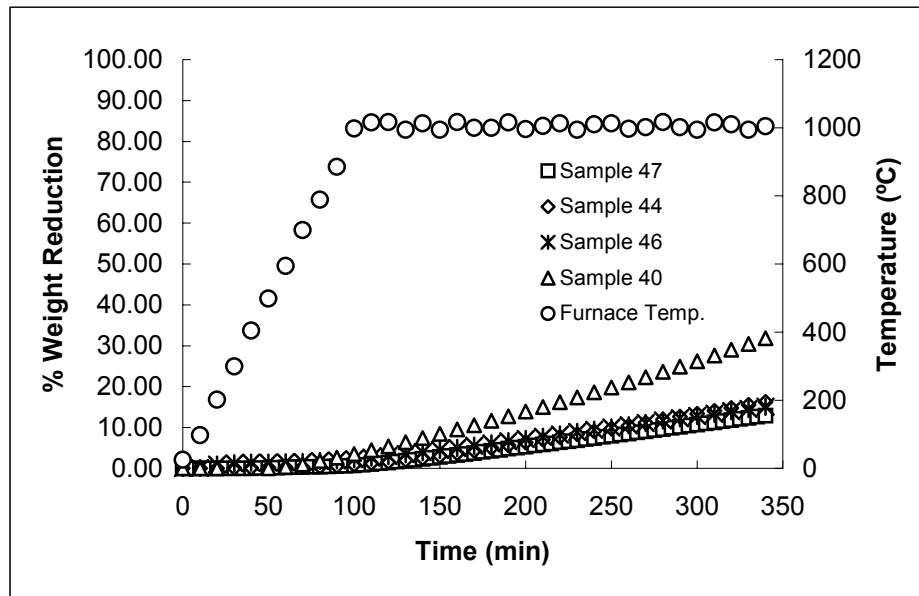


Figure 4.138. Percent weight reduction versus heating time at 1000 °C in air. Tests performed at Wright-Patterson AFB Materials Laboratory, using a dedicated TGA unit.

These last three specimens had a glass-modified overcoat applied over the refractory coating that extended the oxidation protection by more than twofold compared with Specimen #40; the latter had only a bare refractory coating applied. The hardware used for testing these specimens did not need removal of the specimen during the complete testing. Cavity formation was also observed on the overcoat surface of these specimens. However, no patching of the cavities was done during the testing period.

### **4.3 SINGLE LAYER SUPERALLOY DEPOSITS BY POWDER MASKING TECHNIQUE**

Optical microscopy characterization results of the single layer laser deposited Mar-M 247 masked powder on Alloy 718 polycrystalline and over CMSX-4 directionally grown substrates are presented and discussed in this section in the light of solidification theory. A solidification mode growth map for the dendritic and equiaxed growth regions was constructed for the Mar-M 247 alloy over which the local thermal gradient (G) and local solidification growth rate (R) at the surface of the solidifying rear front of each specimen was plotted. Processing parameters used in creating the single layer Mar-M247 deposits are presented on Appendix B-III. The parameters corresponding to single layer Mar-M 247 deposits over CMSX-4 directionally grown substrates cannot be released due to a non-disclosure agreement with Rolls-Royce North America.

#### **4.3.1 Optical macrographs and micrographs of deposits**

From Figure 4.139 it can be seen by the overall shape of Specimen #21 that a low wetting angle occurred at the deposit-substrate interface. The width of the deposit at the interface is 1191  $\mu\text{m}$  and its height, measured at its center, corresponds to 1244  $\mu\text{m}$ . The upper surface of the deposit is round after solidification due to the non-wetting mask surface as well as a high surface tension at the center compared to the lateral sides. This indicates that high

temperatures in the melt are experienced towards the sides rather than the center of the melt pool.

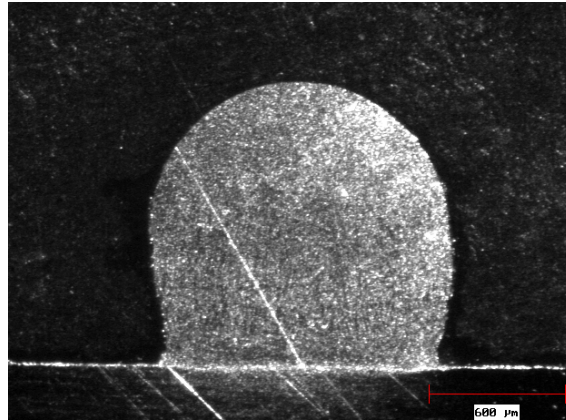


Figure 4.139. Stereo macrograph of the cross-section of a Mar-M 247 deposit over Alloy 718 substrate corresponding to Specimen # 21, 25x.

In Figure 4.140, the etched cross-section of Specimen #22 is illustrated. This specimen was fabricated under identical processing parameters as Specimen #21. However, in this case etching of the specimen reveals that polycrystalline dendrites have grown quasi-parallel to the [100] direction up to 40% of the maximum height of the specimen. Next to it, there is a region that extends up to 60% of maximum height in which almost half of the dendrites continue to grow along that direction, but the remaining dendrites have tilted their preferential growth orientation towards the [001] direction. From half the height up to 90% of it, more dendrites appeared to be oriented along the [001] direction, but also some equiaxed structure can be identified. Finally, within the top 10% of the height the

structure becomes fully equiaxed due to a low thermal gradient in the liquid free surface and a high solute saturation favoring a large constitutional undercooling. Broken dendrite arms, unfused powder as well as oxide inclusion can be potent heterogeneous nucleation agents for equiaxed grains.

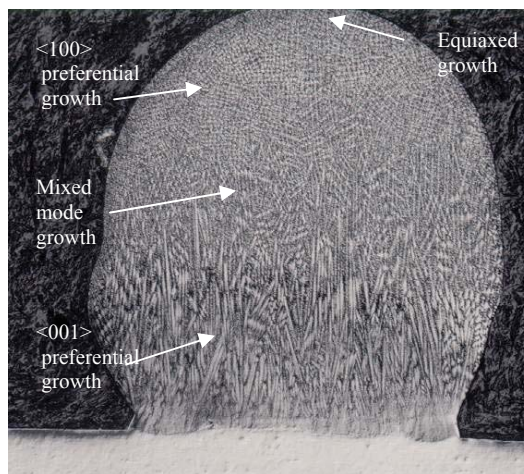


Figure 4.140. Macrograph of the etched cross-section of a Mar-M 247 deposit over Alloy 718 substrate corresponding to Specimen #22, 50x (Courtesy of Rolls-Royce America).

Figure 4.141 shows the narrow metallurgical bond achieved between the deposit and substrate corresponding to Specimen #21. Cellular growth extends 264  $\mu\text{m}$  perpendicularly upwards from the interface and is then followed by a fine columnar dendritic growth along the [001] direction up to 471  $\mu\text{m}$ . Some polycrystalline columnar dendrites show a certain degree of misorientation from

the [001] direction. The approximate primary dendrite arm spacing is 22  $\mu\text{m}$  and some porosity is also observed.

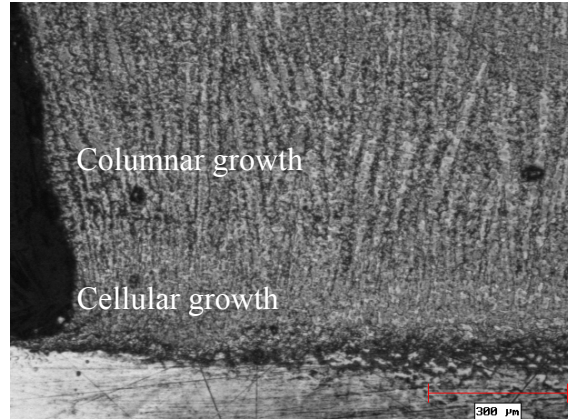


Figure 4.141. Micrograph of the cross-section of Specimen #21, 100x. Shown is the deposit-substrate interface.

From Figure 4.142, above half the height of the deposit the dendritic [001] growth tilts towards the [100] orientation. This may be caused by a change in direction of the maximum thermal gradient at the fusion boundary during solidification of the spherically shaped melt pool. However, in this particular specimen, at the center line of the deposit, columnar dendrites can be seen to grow up to 80% of the maximum height. The processing parameters used on the deposits obtained on CMSX-4 substrates cannot be revealed due to a proprietary agreement with Rolls-Royce North America.

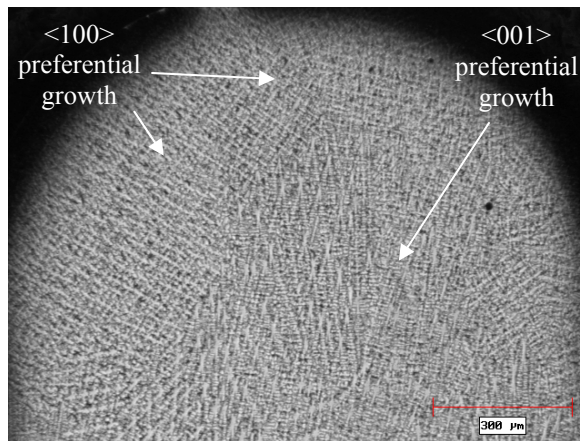


Figure 4.142. Micrograph of the cross-section of a Mar-M 247 deposit over CMSX-4 alloy substrate, 50x. The upper region of the deposit.

#### 4.3.2 Optical micrographs of dendritic structure

From Figure 4.143, it can be seen how a group of columnar dendrites have grown parallel to the [001] direction up to 70% of the height of the deposit. The structure around them corresponds to dendrites that have changed their growth orientation towards a [100] direction.

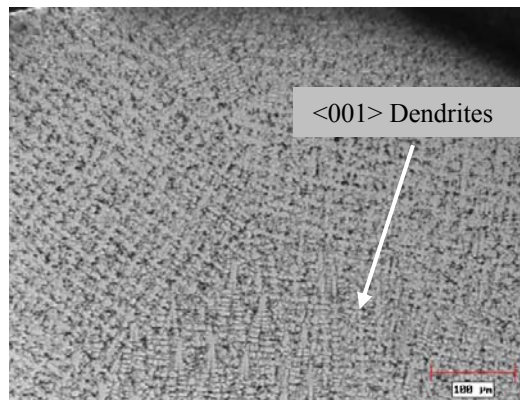


Figure 4.143. Micrograph of the cross-section of a Mar-M 247 deposit over directionally grown CMSX-4 alloy substrate, 100x. The upper middle region of the deposit.

In Figure 4.144 polycrystalline dendrites are clearly observed growing in the [001] direction up to an extension of 721  $\mu\text{m}$  above the substrate surface. The primary dendrite arm spacing corresponds to approximate 21.5  $\mu\text{m}$ .

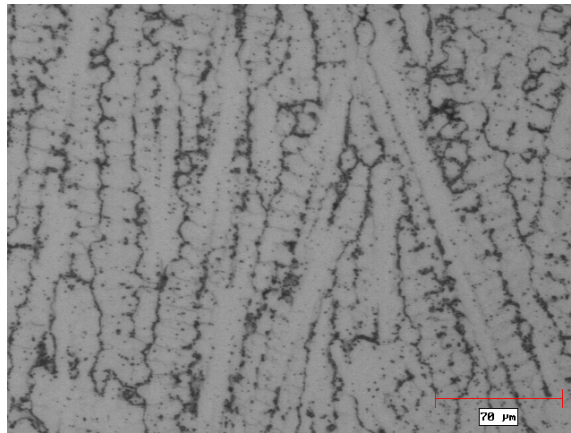


Figure 4.144. Micrograph of the columnar dendritic region above the cellular region in Specimen #51, 200x.

Figure 4.145 shows a dendritic structure having dendrites aligned along different directions. One group of dendrites are oriented along a certain angle with the [001] direction (in plane) while the other dendrites are oriented along a certain angle with the [100] direction (out of plane), i.e., contained in the plane of the micrograph and perpendicular to it, respectively.



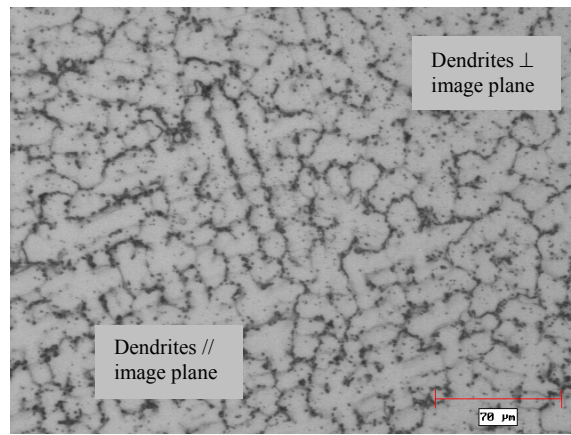


Figure 4.145. Micrograph of the cross-section of a Mar-M 247 deposit over 718 alloy substrate corresponding to Specimen #52, 200x, showing the dendritic structure.

The transition from a dendritic growth aligned quasi-parallel to the [001] direction to a growth direction aligned quasi-parallel to the [100] direction can be clearly observed in Figure 4.146.

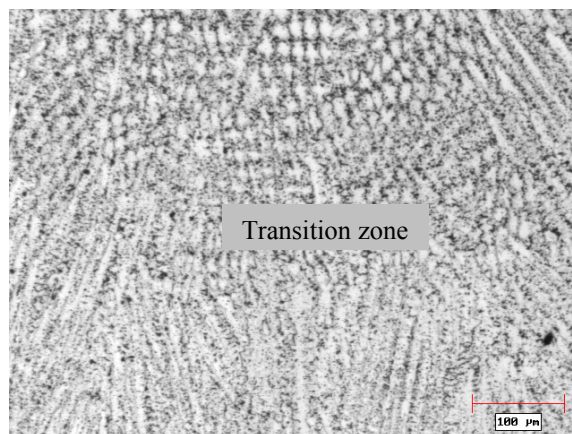


Figure 4.146. Micrograph of middle region of Specimen #53, 100x. Transition from [001] (below) to [100] (above) polycrystalline dendritic orientation.

From Figure 4.147 it can be observed that at the cellular/dendrite interface of Specimen #55, a solidified polycrystalline dendritic structure region was achieved having a primary arm spacing of 16  $\mu\text{m}$ . Some porosity is also present.

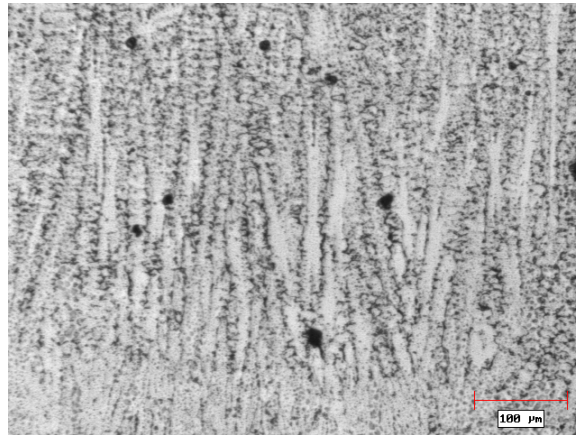


Figure 4.147. Micrograph of the cross-section of Specimen #55, 100x. Showing polycrystalline dendrites above the cellular region.

From Figure 4.148 it can be observed how the polycrystalline dendrites experience a reorientation from the [001] direction towards direction of maximum thermal gradient at the fusion boundary.

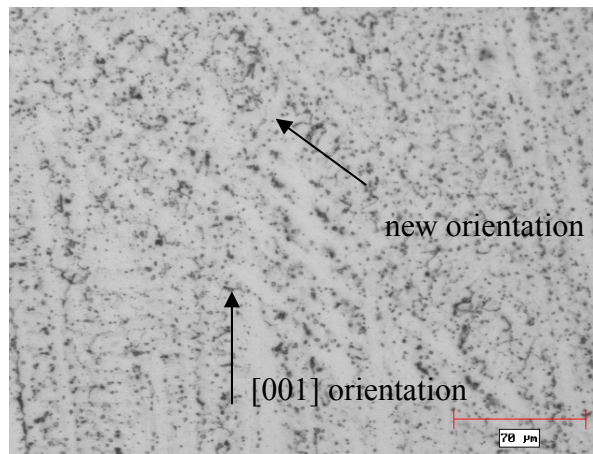


Figure 4.148. Micrograph of the longitudinal-section of Specimen #55, 200x. Showing reorientation of dendrites.

#### 4.3.3. Plot of maximum growth rate (G) versus maximum rate of solidification (R)

Figure 4.149 shows a  $\log R_L$  versus  $G_L$  plot where a  $G_L/R_L$  ratio of 38000  $^{\circ}\text{Fs}/\text{in}^2$  has been graphed (continuous line). This  $G_L/R_L$  ratio value is of most interest as it determines the columnar to equiaxed transition zone for all nickel base alloys [23]. The values of  $G_L$  were obtained from Equation 4 described in Chapter II Section 2.4.1 using the heat conductivity and melting point of Mar-M 246 from Ref. 24, i.e.,  $K = 0.4225 \text{ W}/\text{in}/^{\circ}\text{F}$  @ 2000  $^{\circ}\text{F}$  and  $T_m = 2450 \text{ }^{\circ}\text{F}$ . The laser coupling efficiency  $\eta$  was taken as 100%.

According to this plot it can be seen that all specimens fall inside the columnar dendritic growth region away from the columnar to equiaxed transition boundary. Therefore, they should not have nucleated and grown equiaxed grains at the surface of the deposit. However, this observation does not hold as revealed

by optical microscopy. This model does not include the variation in thermal gradient at the surface of the deposit due to the loss of heat primarily by radiation heat transfer.

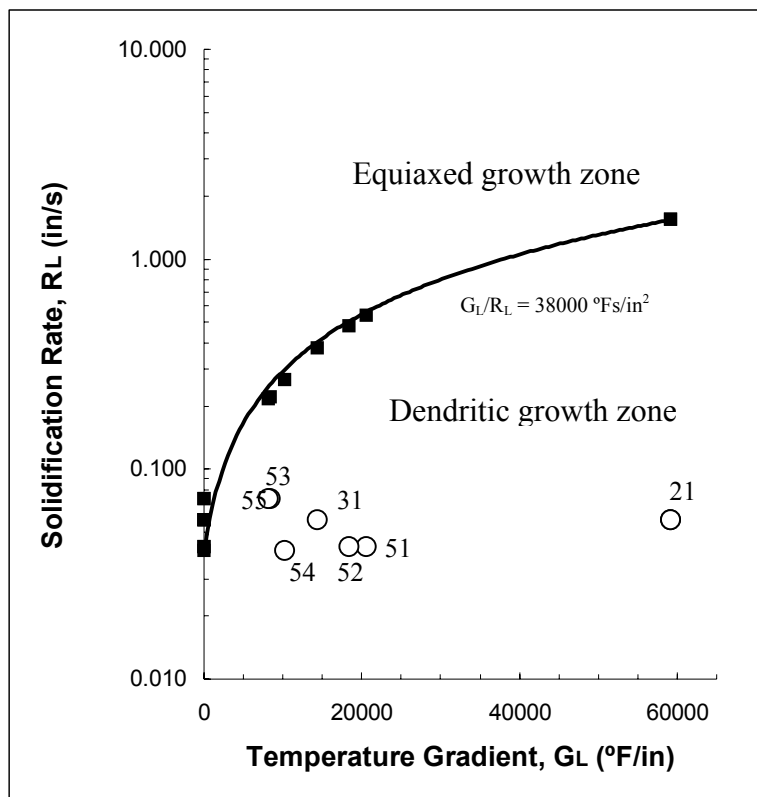


Figure 4.149. Solidification processing map for the SLLD of Ni-base superalloy powder (Ref. 23 and Appendix B-III).

#### 4.4 REFERENCES

1. W.M. Steen, Laser Material Processing, 2<sup>nd</sup> ed., (Springer Verlag, 1994).
2. J.A. Ramos, D.L. Bourell and J.J. Beaman, Proceedings of the 2002 MRS Spring Meeting, Symposium LL, A. Piqué; A.S. Holmes; D. Dimos Eds., 53-61 (2003).
3. J.A. Ramos, D.L. Bourell in Rapid Prototyping of Materials, F.D.S. Marquis; D.L. Bourell Eds., TMS, Warrendale PA, 191-201 (2002).
4. M.F. Ashby, Materials Selection in Mechanical Design, (Butterworth Heinemann, 1992).
5. N. Eustathopoulos, M.G. Nicholas and B. Drevet, Wettability at High Temperatures, Pergamon Materials Series Volume 3, (Pergamon, 1999).
6. ASM Metals Handbook, 9<sup>th</sup> edition, v.1 and 2, (Metals Park, Ohio).
7. T.R. Anthony and H.E. Cline, *J. Applied Phys.*, 48, 9, 3888-3894 (1977).
8. X.B. Zhou and J.Th.M. De Hosson, *J. Matter. Res.*, v.10, 8, 1984-1992 (1995).
9. A. Favre, H. Fuzellier and J. Suptil, *Ceramics International*, 29, 235-243 (2003).
10. P. Shewmon, Diffusion in Solids, 2<sup>nd</sup> edition, (TMS, 1989).
11. J. F. Shackelford, W. Alexander, Eds. CRC –Materials Science and Engineering Handbook, 3<sup>rd</sup> ed. (CRC Press, 2001).
12. D. Schuocker, High Power Lasers in Production Engineering, (Imperial College Press, World Scientific, 1999).
13. M. Hansen and K. Anderko, Constitution of Binary Alloys, (McGraw Hill, 1958).

14. Leo Brewer, "Chemical Bonding Theory Applied to Metals", Alloying, J.L. Walter, M.R. Jackson, and C.T. Sims Eds., (ASM International, 1988).
15. S. West, private communication.
16. J.C. Bailar, H.J. Emeleus, R. Nyholm and A.F. Trotman-Dickenson, Eds., Comprehensive Inorganic Chemistry, v.3, (Elmsford, N. Y., 1973).
17. R.C. Rossi, *Ceram. Bull.* 48(7), 736, (1969).
18. ThermoCalc™ Software AB.
19. M.W. Barsoum, Fundamental of Ceramics, (McGraw Hill, 1997).
20. M. Schmirling, private communication.
21. G.R. Anstis, P. Chantikul, B.R. Lawn and D.B. Marshal, *J. Amer. Ceram. Soc.* , 64, 9, 533-538 (1985).
22. J.W. Hutchinson, Z. Suo, "Mixed Mode Cracking in Layered Materials", in Advances in Applied Mechanics, (Academic Press, 1992).
23. M. McLean, Directionally Solidified Materials for High Temperature Service, (The Metals Society, London, 1983).
24. ASM Metals Handbook, 9<sup>th</sup> edition, v.3 (Metals Park, Ohio).

## **CHAPTER V. CONCLUSIONS AND SUGGESTIONS**

### **5.1 LASER POLISHED FE - CU INDIRECT-SLS PARTS**

A two-layer solidification pattern has been observed after surface laser remelting of the Fe-Cu indirect-SLS material system in agreement with a non-equilibrium phase transformation typical for a fast cooling process. First, a Fe-rich phase is solidified until the peritectic temperature is reached, followed by the solidification of the Cu-rich phase.

Five possible melting mechanisms can operate during the non-tactile laser polishing of a Fe-Cu indirect-SLS material system, namely: surface shallow melting of a single-phase, surface over melting I (onset single-phase melting), Surface over melting II (fully developed single-phase melting), surface over melting III (onset dual-phase melting with oxide formation) and surface over melting IV (fully developed dual-phase melting with oxide formation).

Small clusters consisting of aluminium and silicon oxides are spread over the smoothed surface thus increasing its surface roughness. Presence of alumina and silica has its origin from the infiltration step.

Low frequency high amplitude ripples were formed periodically over the melted surface produced by the surface over melting mechanism. A high frequency low amplitude dispersion of Al, Si, and possibly Cr oxides particles is also found over these ripples. These artefacts increase the roughness of the laser polished surface.

At 225 W and 334 W, laser polishing provided percent reductions in surface roughness  $R_a$  of up to -18% and -37%, respectively. The type of mechanism responsible in both conditions is thought to be surface-over-melting mode I; nonetheless, a certain fraction of surface shallow melting could also be present. Presence of alumina particles in the as-received material increased considerably the resulting  $R_a$  variation.

At 420 W and 565 W, laser polishing provided a percent reduction in surface roughness  $R_a$  of up to -24% and -31%, respectively. The type of mechanism responsible in both conditions is thought to be surface-over-melting mode III. However, for the same speed, at 420 W laser power the melt depth is not as deep as for 565 W and similarly superheating of the melt is relatively less. Deep melts and high superheating favor formation of a Fe-rich phase at the surface that is also rich in oxygen and has the appearance of a flat platelet thus



potentially reducing the roughness due to induced surface waviness of the Cu-rich phase.

### **5.1.1 Surface roughness modeling**

#### **5.1.1.2 *Surface shallow melting***

An analytical model for predicting the surface roughness  $R_a$  of a laser polished indirect-SLS surface has been formulated successfully assuming that a SLS surface is made up of close-packed hemispherical particles of given radii size.

Decoupling of the laser polishing physical phenomena into an energetic and a kinetic stage aided the implementation and solution of the analytical model. The energetic step was represented by two cubic polynomial functions whereas the kinetic step required integration of a first order ODE.

The model was solved numerically to determine the maximum and minimum heights of the newly established surface morphology of melted caps and filled valleys after laser polishing to predict the resulting surface roughness.

#### **5.1.1.2 *Surface over melting***

Optical and SEM observation of the surface of the laser polished tracks under the SOM regime confirm the formation of two periodical structures, one of high

frequency low amplitude and the other of low frequency high amplitude. Both contribute to the surface roughness achieved after the laser polishing process, but the latter is thought to be more critical in increasing the  $R_a$  value above the as-received level.

A modified thermo-physical model based on previously reported models [1,2] is presented, signaling good agreement with roughness  $R_a$  and characteristic surface wavelength results obtained for a fixed laser power and varying laser beam scan speeds. Increment in roughness  $R_a$  value with decreasing scanning speed is predicted by the present model. The main contribution of the present model is the incorporation of the surface curvature effects as a restoring force aiding gravity to bring the amplitude of the surface wave down to zero. The main assumption here is that the surface relief behaves as it if were a sinusoid of fixed propagation vector.

### **5.1.2 Suggestions for future work**

This process appears to be an effective technique for reducing the surface roughness of planar sample parts as made by indirect-SLS technology. Higher order surfaces (concave or convex) should provide similar enhancing results provided the processing parameters, laser beam power, spot beam diameter and scan speed, are dynamically adjusted so that the energy density is kept within

processing bounds. Surface oxidation is an issue that can be avoided by the usage of improved vacuum level and high purity back-filled inert gas. Removal of embedded silica and alumina particles from the as-received surface is recommended as well. The rod-like surface artifacts seen at high magnification could be removed from the planar surface by a subsequent laser ablation process.

Enhancing the accuracy of the Surface Shallow Melting model can be further obtained by analytically determining an expression for the curve representing the surface of the molten liquid once it has settled inside of the trough between three close-packed hemispheres. Calculus of variations must be resorted to find such a analytical solution.

Laser polishing by melting is a promising technique to achieve reduction in surface roughness of freeform-fabricated parts at a fast processing rate. It should be further explored in articles made from a single-phase material system without surface contaminants.

## **5.2 OXIDATION PROTECTION BARRIER COATINGS FOR C/C COMPOSITES**

Laser induced cementation process (LIC), a new laser based technique, is capable of depositing uniform coatings over cylindrical samples of carbon-carbon composites. The overall laser processing time to achieve this coating was no longer than 10 minutes and it was divided in three coating steps of approximately

3 to 4 minutes each. No ultra high-vacuum conditions were needed for the coating process.

A three-coating composition sequence based on  $\text{CrCl}_3\text{-C}$ ,  $\text{Si-Cr-C}$  and  $\text{Si-HfCl}_4\text{-Cr}$  showed the best coating results in terms of coating adhesion to the substrate prior to LIC process, as well as surface integrity, coating thickness uniformity and strong bonding to the substrate after the LIC process. Si, Cr and Hf provide a good combination for oxidation resistance at intermediate temperature (i.e. 1000-1150°C) as demonstrated before by other authors [3]. Their relative composition should be within the range of the eutectic points of the Cr-Si, Hf-Si and Hf-Cr binary phase diagrams. This reduces the melting temperature of the ternary alloy as well as provides metal-silicide formation and a resulting eutectic lamellar structure.

Initially, it was thought that a first Cr layer added to the composite should act as a crack bridging agent, however the second coating based on Si wet the composite at the expense of that CrC-rich layer and instead a  $\text{SiC/CrSi}_2$  thin layer was formed. The bonding of the latter was stronger and it should prevent delamination during testing. However, as it was seen by the SEM analysis, cracks were able to propagate all way through the SiC-rich layer into the composite surface.

The coatings demonstrated mechanical interlocking, low porosity, and uniform thickness of up to approximately 350  $\mu\text{m}$ . The coatings showed phase stability at high temperature when heated at 1150°C for two hours 30 minutes in argon. Minimal delamination of the coating was observed.

Crack extension during the fabrication of the coating is a problem that still needs to be solved to increase the oxidation resistance performance at high temperatures in air. The coating layer experienced a plane strain tensile stress state. The hoop stresses are caused primarily by the CTE mismatch and thermal gradient difference between the substrate and the coating during cooling from the melt. The difference in thermal gradient at the interface also increases the magnitude of the tensile hoop stress. The tensile stress state is high enough to provide the pre-existing cracks with enough energy to overcome the critical energy release rate of the coating.

The indentation fracture method appeared to be a suitable technique for determination of the value of the opening mode fracture toughness of the LIC coating material.

Combination of silica and sodium carbonate in sodium silicate solution allows formation of a glass overcoat with low glass transition temperature (400°C) and yet high melting point (1100°C). Moreover, a low viscosity glass is achieved at temperatures above the melting point. This overcoat can flow at low

temperatures and seal the cracks present in the refractory coating and solve the problem associated with presence of cracks. Due to the low glass transition temperature value, the temperature range available for thermal shock is also lower than when using, for example, a pure silica glass sealant, thus minimizing cracking of the glass-modified overcoat.

A 11% weight reduction after a five hours testing at 1000°C in still air (a -2.2 wt.%/hr rate of percent weight reduction) was achieved using a dedicated TGA equipment (at the Wright-Patterson AFB) with no removal of the specimen during the complete test.

A 28% weight reduction after a 20 hours testing at 1000°C in still air (a -1.4 wt.%/hr rate of percent weight reduction) was achieved using a conventional horizontal furnace and a microbalance (at The University of Texas at Austin). These required repeated removal of the specimen from the furnace during the complete test, allowing however to patch two cavities formed on the glass-modified overcoat.

Metal chlorides as precursor powder to create the refractory coating show good adhesion properties before the processing due to an olation reaction on mixing with isopropyl alcohol. During the laser fusion process chlorine evolves from the coating and leaves the metal ions free to react with Si and Cr. However,

its use should be avoided due to the high reactivity of the  $\text{Cl}^-$  ion; rather metal compounds from less reactive elements such as metal nitrides should be used.

This research demonstrated that ceramic coatings consolidated over a ceramic substrate by high-speed raster-scanning of a high power  $\text{CO}_2$  laser beam is a versatile technique. However, the success of the technique depends on the availability of adequate heating time, which is needed to spread the coating and drive the reactive-diffusion bonding. This is only possible if the heat from the laser beam is confined into the substrate by minimizing heat conductivity from the specimen to its surroundings.

The LIC technique is a viable and controllable alternative to conventional vacuum fusion and packed cementation processes used for ceramic coatings. The process can also be used to cast thin-walled ceramic patterns using, for example, a sacrificial ceramic substrate material like carbon.

### **5.2.1 Suggestions for future work**

A glass-modified overcoat having with the lowest possible value of its glass transition temperature and the highest melting point possible must be developed, bearing in mind that its component should have the lowest chemical reactivity to prevent cavity formation.

### 5.3 DIRECTIONALLY GROWN SUPERALLOY DEPOSITS

Deposition of single layer – single track Mar-M 247 over Alloy 718 polycrystalline sheet was achieved successfully by laser raster scanning. Sound metallurgical bonds were observed between the substrate and the deposit. A narrow cellular front solidified due to the high thermal gradient in the liquid and slow local growth rate.

Polycrystalline dendrites grew perpendicular to the substrate along the  $\langle 001 \rangle$  orientation up to half the height of the deposits as also reported in Reference 4. It appears that the dendritic front then experienced bowing as the maximum thermal gradient at the fusion boundary rotated towards a  $\langle 100 \rangle$  direction associated with the approach to the free surface of the melt pool. This indicates that the shape of the melt pool must have a spherical shape rather than a comet shape.

The measured primary dendrite arm spacing was found to be in the 16-22  $\mu\text{m}$  range. It had the same order of magnitude as the primary dendrite spacing found in laser claddings of Ni-base superalloy deposits reported in Reference 4.

Near the free surface, columnar-to-equiaxed solidification transition occurs, likely due to the  $G_L/R_L$  ratio decrease. Solute is also rejected from the fusion boundary and its concentration builds up, increasing the degree of constitutional undercooling in the melt ahead. Radiation heat transfer from the



surface of the deposit also alters the local thermal gradient favoring solidification of melt by nucleation and growth of equiaxed grains.

### **5.3.1 Suggestions for future work**

It appears desirable to perform electron back scattered diffraction (EBSD) maps of the cross section of some deposits (e.g., Specimen #21) to verify the formation of equiaxed grains near the surface, as it is difficult to distinguish them from the reoriented columnar dendrites by means of optical micrographs.

To extend the epitaxial dendritic  $\langle 001 \rangle$  growth further to the top of the deposit a comet-shaped melting pool is necessary. This requires of a higher laser beam traveling speed but this increase must be compensated by the used of a higher laser power input. So that an energy density in the range of 179-244 J/mm<sup>2</sup> must be met to achieve the required penetration depth. Moreover, laser power  $P$  and traveling speed  $v_t$  must be selected carefully so that the  $G_L/R_L$  ratio, evaluated at the free surface of the melt pool, is less than or equal to the columnar-to-equiaxed transition critical value for the Ni-base superalloy.

#### 5.4 MECHANICS OF THE LASER RASTER-SCANNING SURFACE INTERACTION

The equivalence equation (Chapter II Eq. 2.6 and 2.11) is a general and useful relationship that allows comparison of surfaces that have been laser processed and thus modified by line or raster scanned sources, keeping constant in both cases the Andrew's number by varying the percent beam overlap  $\phi$  and scan speed  $V_s$ , when  $W$ ,  $L$ ,  $D$  and traveling speed  $V_t$  are kept constant.

Increasing the number of scan lines ( $N$ ) while keeping constant the traveling speed ( $V_L=V_t$ ) and laser power ( $P$ ) produces higher peak temperatures after heating intervals that approach the limiting value given by a  $(D/V_L)$  for a line source traveling at the same speed. This is because the percent overlap,  $\phi$ , is increased towards 1.

For a fixed traveling speed, increasing the number of scan lines increases the scan speed provided the length-to-width ( $L/W$ ) aspect ratio is kept constant. If the number of scan lines were now reduced, not only the peak temperature is reduced but also the heating interval is shorter than the limiting value as the percentage overlap is decreased.

Understanding the influence of scan geometry ( $L$ - $W$  aspect ratio), percent overlapping ( $\phi$ ) and number of scan lines ( $N$ ), on the raster-scan surface processing provides a method to tailor the surface peak temperature and heating interval as well as the heating and cooling rates. This in turns affects the

solidification or sintering conditions of the process and therefore the mechanical properties of the parts obtained.

## 5.5 REFERENCES

1. T.R. Anthony and H.E. Cline, *J. Applied Phys.*, 48, 9, 3888-3894 (1977).
2. V.S. Avanesov and M.A. Zuev, "Investigation of surface topography after melting by laser beam", SPIE, v.2713, 340-343.
3. H.S. Hu, A. Joshi, J.S. Lee, "Microstructural evaluations of Si-Hf-Cr fused slurry coating on graphite for oxidation protection", *J. Vac. Sci. Technol. A9*, 3, 1535-1938 (1991).
4. M. Gäumann *et al.*, "Epitaxial laser metal forming: analysis of microstructure formation", *Mat. Sci. Eng. A*, 271, 232-241 (1999).

## APPENDIX A: I. Modeling code for laser raster-scan temperature history (written in MathCad Profesional 2001)

### Physical properties

Properties for Cu-Sn (95-5 wt.%) rule of mixtures (ASM Metals Handbook v 2 9th Ed.)

Thermal conductivity:

$$K_{br} := (0.95 \cdot 386 + 0.05 \cdot 64) \frac{W}{m \cdot K}$$

$$K_{br} = 369.9 \frac{W}{m \cdot K}$$

Density:

$$\rho_{br} := (0.95 \cdot 8954 + 0.05 \cdot 7304) \frac{kg}{m^3}$$

$$\rho_{br} = 8.871 \times 10^3 \frac{kg}{m^3}$$

Specific heat capacity:

$$C_{pbr} := (383 \cdot 0.95 + 0.05 \cdot 226) \frac{joule}{kg \cdot K}$$

$$C_{pbr} = 375.15 \frac{joule}{kg \cdot K}$$

Thermal diffusivity:

$$\alpha_{br} := \frac{K_{br}}{\rho_{br} \cdot C_{pbr}}$$

$$\alpha_{br} = 1.111 \times 10^{-4} \frac{m^2}{s}$$

Melting temperature:

$$T_{mbr} := 1085 \cdot 0.95 + 232 \cdot 0.05$$

$$T_{mbr} = 1.042 \times 10^3$$

Processing parameters:

width of track:      beam diameter:      scan lines:      track length:      percent overlap:

$$W := 1.9\text{-mm} \quad D := 0.4\text{-mm} \quad N := 2000 \quad L := 25\text{-mm} \quad \phi := 1 - \frac{L}{N \cdot D}$$

scan speed:      number of cycles:      width of beam:      position:

$$vs := 700 \frac{\text{mm}}{\text{sec}} \quad n := \frac{1}{1 - \phi} \quad w := 0.39\text{-mm} \quad x := 1\text{-mm}$$

Uniaxial temperature distribution in z direction:

$$I(P, w, d, \epsilon) := \frac{P \cdot 4 \cdot (1 - \epsilon)}{\pi \cdot (w \cdot d)}$$

$$T(z, t) := \frac{I}{Kbr} \left[ \sqrt{\frac{4 \cdot \alpha br \cdot t}{\pi}} \cdot \exp\left(-\frac{z^2}{4 \cdot \alpha br \cdot t}\right) - x \cdot \left(1 - \operatorname{erf}\left(\frac{z}{\sqrt{4 \cdot \alpha br \cdot t}}\right)\right) \right]$$

Surface temperature (at z =0)

$$T0(t, P, w, d, \epsilon) := \frac{I(P, w, d, \epsilon)}{Kbr} \left( \sqrt{\frac{4 \cdot \alpha br \cdot t}{\pi}} \right)$$

Expression for the surface temperature of a heating-cooling cycle for a energy-line source:

$$Tline(P, vs, D, w, t, \epsilon) := \left[ T0\left(t, P, w, D, \epsilon\right) \cdot \Phi\left(\frac{t}{\text{sec}}\right) - T0\left(t - \frac{D}{vs}, P, w, D, \epsilon\right) \cdot \Phi\left[\frac{\left(t - \frac{D}{vs}\right)}{\text{sec}}\right] \right]$$

Expression for surface temperature after multiple heating-cooling cycles due to a raster-scan energy source:

First interaction at a starting position  $x$ ,  $0 < x < W$

$$f_0(W, \phi, P, vs, D, w, t, \epsilon) := \sum_{i=0}^{\frac{1}{1-\phi}} [1 - (1 - \phi) \cdot i] \cdot \left[ \begin{array}{l} T_0 \left[ t - \frac{(W \cdot 2 \cdot i)}{vs}, P, w, D, \epsilon \right] \cdot \Phi \left[ \frac{t - \frac{(W \cdot 2 \cdot i)}{vs}}{\text{sec}} \right] \dots \\ + -T_0 \left[ t - \frac{\frac{D}{2} + (W \cdot 2 \cdot i)}{vs}, P, w, D, \epsilon \right] \cdot \Phi \left[ \frac{t - \frac{\frac{D}{2} + (W \cdot 2 \cdot i)}{vs}}{\text{sec}} \right] \end{array} \right]$$

Consecutive interactions after moving to the left of  $x$ ,

$$A(t, x, W, D, vs, i) := \Phi \left[ \frac{t - \frac{(W - x) \cdot 2 + W \cdot 2 \cdot i + D \left[ 1 - 0.5 \left( \text{if} \left( 0 < \frac{x}{W} < 1, 0, 1 \right) + \delta \left( \text{floor} \left( \frac{x}{W} \right), 1 \right) \right] \right]}{vs}}{\text{sec}} \right]$$

$$f_1(W, \phi, P, vs, D, w, t, x, \epsilon) := \sum_{i=0}^{\frac{1}{1-\phi}} [1 - (1 - \phi) \cdot i] \cdot \left[ \begin{array}{l} T_0 \left[ t - \frac{(W - x) \cdot 2 + W \cdot 2 \cdot i}{vs}, P, w, D, \epsilon \right] \cdot \Phi \left[ \frac{t - \frac{(W - x) \cdot 2 + W \cdot 2 \cdot i}{vs}}{\text{sec}} \right] \dots \\ + -T_0 \left[ t - \frac{(W - x) \cdot 2 + W \cdot 2 \cdot i + D \left[ 1 - 0.5 \left( \text{if} \left( 0 < \frac{x}{W} < 1, 0, 1 \right) + \delta \left( \text{floor} \left( \frac{x}{W} \right), 1 \right) \right] \right]}{vs}, P, w, D, \epsilon \right] \cdot A(t, x, W, D, vs, i) \end{array} \right]$$

Consecutive interactions after moving to the right of x,

$$f_2(W, \phi, P, vs, D, w, t, x, \epsilon) := \sum_{i=0}^{\frac{1}{1-\phi}} [1 - (1 - \phi)^i] \cdot \left[ \begin{array}{l} T_0 \left[ t - \frac{W \cdot 2 \cdot (i + 1)}{vs}, P, w, D, \epsilon \right] \cdot \Phi \left[ \frac{t - \frac{W \cdot 2 \cdot (i + 1)}{vs}}{sec} \right] \dots \\ + -T_0 \left[ t - \frac{W \cdot 2 \cdot (i + 1) + \frac{D \cdot \delta \left( \text{ceil} \left( \frac{x}{W} \right), 1 \right)}{2}}{vs}, P, w, D, \epsilon \right] \cdot \Phi \left[ \frac{t - \frac{W \cdot 2 \cdot (i + 1) + \frac{D \cdot \delta \left( \text{ceil} \left( \frac{x}{W} \right), 1 \right)}{2}}{vs}}{sec} \right] \right] \end{array} \right]$$

overall surface temperature expression for multiple cycles:

$$T(W, P, vs, D, w, \phi, x, t, \epsilon) := f_0(W, \phi, P, vs, D, w, t, \epsilon) + f_1(W, \phi, P, vs, D, w, t, x, \epsilon) + f_2(W, \phi, P, vs, D, w, t, x, \epsilon)$$

## APPENDIX A: II. Modeling code for surface shallow melting (written in MathCad Professional 2001)

### Physical properties

Data for Cu-Sn (95-5 wt.%) rule of mixtures (ASM Metals Handbook v. 2 9th Ed.):

Thermal conductivity of the solid :

$$k := (0.95 \cdot 386 + 0.05 \cdot 64) \cdot \frac{\text{watt}}{\text{m} \cdot \text{K}}$$

Specific heat capacity of the solid and liquid:

$$C_{ps} := (383 \cdot 0.95 + 0.05 \cdot 226) \cdot \frac{\text{joule}}{\text{kg} \cdot \text{K}} \quad C_{pl} := 647 \cdot \frac{\text{joule}}{\text{kg} \cdot \text{K}}$$

Density:

$$\rho := (0.95 \cdot 8954 + 0.05 \cdot 7304) \cdot \frac{\text{kg}}{\text{m}^3}$$

Melting temperature, vaporization temperature and room temperature in Celcius:

$$T_f := 1080 \quad T_v := 2500 \quad T_o := 25$$

Data for Cu fom (Eustathopoulos):

Surface energies: liquid-vapor, solid-vapor and solid-liquid:

$$\sigma_{lv} := 1.385 \cdot \frac{\text{joule}}{\text{m}^2} \quad \sigma_{sv} := 1.64 \cdot \frac{\text{joule}}{\text{m}^2} \quad \sigma_{sl} := 0.255 \cdot \frac{\text{joule}}{\text{m}^2}$$

Viscosity of the liquid:

$$\eta := 4.3 \cdot 10^{-3} \cdot \text{Pa} \cdot \text{sec}$$

Latent heat of melting:

$$L := \left( \frac{13.05}{63.54} \cdot 0.95 + 0.05 \cdot \frac{7.029}{118.69} \right) \cdot 10^6 \cdot \frac{\text{joule}}{\text{kg}}$$

Thermal diffusivity of the solid:

$$\alpha := \frac{k}{\rho \cdot C_{ps}} \quad \alpha = 1.111 \times 10^{-4} \frac{\text{m}^2}{\text{sec}}$$



Processing parameters:

Laser power:

$$P := 565 \cdot \text{watt}$$

Beam diameter:

$$D := 0.39 \cdot \text{mm}$$

Track width:

$$w := 1.9 \cdot \text{mm}$$

Particle radius:

$$R := 10 \cdot \mu\text{m}$$

Heat losses by surface reflectivity, convection and radiation:

$$\varepsilon := 0.55$$

slab thickness:

$$\delta := 7 \cdot \text{mm}$$

Processing time, and scan velocity:

$$t := \begin{pmatrix} 3.25 \\ 3.5 \\ 3.75 \\ 4 \\ 4.25 \\ 4.5 \end{pmatrix} \text{sec}$$

$$vs_i := \frac{w}{\left( \frac{t_i}{1800} \right)}$$

$$vs = \begin{pmatrix} 1.052 \times 10^3 \\ 977.143 \\ 912 \\ 855 \\ 804.706 \\ 760 \end{pmatrix} \frac{\text{mm}}{\text{sec}}$$

Energy density:

$$E_i := \frac{P \cdot t_i}{D \cdot \pi \cdot vs_i}$$

$$E = \begin{pmatrix} 175.288 \\ 188.771 \\ 202.255 \\ 215.739 \\ 229.222 \\ 242.706 \end{pmatrix} \frac{\text{joule}}{\text{cm}^2}$$

Interaction time:

$$\Delta t(D, vs) := \frac{D}{vs}$$

$$\Delta t(D, vs_i) =$$

$3.706 \cdot 10^{-4}$	sec
$3.991 \cdot 10^{-4}$	
$4.276 \cdot 10^{-4}$	
$4.561 \cdot 10^{-4}$	
$4.846 \cdot 10^{-4}$	
$5.132 \cdot 10^{-4}$	

Travelling speed:

$$vt_i := \frac{25.4}{t_i} \cdot \text{mm}$$

$$vt = \begin{pmatrix} 7.815 \\ 7.257 \\ 6.773 \\ 6.35 \\ 5.976 \\ 5.644 \end{pmatrix} \frac{\text{mm}}{\text{sec}}$$

Uniaxial temperature profile for semi-infinite body not including change of phase:

$$T_{\text{surf}}(t, P, D) := \frac{1}{k} \cdot \frac{4 \cdot P}{\pi \cdot D^2} \cdot \left( \frac{4 \cdot \alpha \cdot t}{\pi} \right)^{0.5}$$

$$T(r, t, P, D) := T_{\text{surf}}(t, P, D) \cdot \left[ \exp\left(\frac{-r^2}{4 \cdot \alpha \cdot t}\right) - \left[ 1 - \operatorname{erf}\left[\frac{r}{(4 \cdot \alpha \cdot t)^{0.5}}\right] \right] \cdot r \cdot \left(\frac{4 \cdot \alpha \cdot t}{\pi}\right)^{-0.5} \right]$$

Number of spheres that are covered by the laser beam:

$$Cl(D) := \frac{D^2}{4 \cdot R^2} \qquad Cl(D) = 380.25$$

Volume of a half sphere:

$$V(r) := \frac{2}{3} \cdot \pi \cdot r^3$$

Lumped energy balance to obtain the final radius r up to which the spheres will melt

Energy to melt a certain volume of sphere from a radius R to a radius r:

$$f(r, \varepsilon, i) := Cl(D) \cdot (V(R) - V(r)) \cdot \rho \cdot \left[ C_{ps} \cdot (T_f - T_o) + L + C_{pl} \cdot \left[ \left[ \left[ T(0 \text{ mm}, \Delta t(D, v_{s_i}), P, D) \cdot (1 - \varepsilon) + T_o \right] \cdot 0.4 + T_f \cdot 0.6 \right] - T_f \right] \right]$$

Energy to heat solid sphere of radius r:

$$g(r, \varepsilon, i) := Cl(D) \cdot V(r) \cdot \rho \cdot C_{ps} \cdot (T_f - T_o)$$

Energy to heat substrate:

$$h(r, \varepsilon, i) := \rho \cdot C_{ps} \cdot \pi \cdot \frac{D^2}{4} \cdot (1 - \varepsilon) \cdot \int_R^\delta T(a, \Delta t(D, v_{s_i}), P, D) \, da$$

Overall balance made equal to energy input from laser beam:

$$F(r, \epsilon, b, i) := f(r, \epsilon, i) + g(r, \epsilon, i) + h(r, \epsilon, i) \cdot b - (1 - \epsilon) \cdot P \cdot \Delta t(D, v_{s,i})$$

Fitting coefficients

$$b := 1.0185$$

Solving for the radius up to which melting takes place:

Given

$$F(r_0, \epsilon, b, 0) = 0$$

$$F(r_1, \epsilon, b, 1) = 0$$

$$F(r_2, \epsilon, b, 2) = 0$$

$$F(r_3, \epsilon, b, 3) = 0$$

$$F(r_4, \epsilon, b, 4) = 0$$

$$F(r_5, \epsilon, b, 5) = 0$$

$$r := \text{Find}(r_0, r_1, r_2, r_3, r_4, r_5)$$

$$r = \begin{pmatrix} 8.608 \\ 8.529 \\ 8.468 \\ 8.424 \\ 8.392 \\ 8.371 \end{pmatrix} \mu\text{m}$$

Surface temperature:

$$T_{\text{surf}}(\Delta t(D, v_{s,i}), P, D) \cdot (1 - \epsilon) + T_o =$$

$1.343 \cdot 10^3$
$1.392 \cdot 10^3$
$1.44 \cdot 10^3$
$1.487 \cdot 10^3$
$1.532 \cdot 10^3$
$1.576 \cdot 10^3$

Average temperature at the melt:

$$[T_{\text{surf}}(\Delta t(D, v_{s,i}), P, D) \cdot (1 - \epsilon) + T_o] \cdot 0.4 + T_f \cdot 0.6 =$$

$1.185 \cdot 10^3$
$1.205 \cdot 10^3$
$1.224 \cdot 10^3$
$1.243 \cdot 10^3$
$1.261 \cdot 10^3$
$1.278 \cdot 10^3$

Determination of filled height:

Volume in between spheres that is to be filled with spreading liquid:

$$\Delta V_{\text{fill}}(z, r) := z \cdot \sqrt{3} \cdot R^2 - \frac{\pi}{3} \cdot \left[ r^3 - \frac{1}{2} \cdot (r - z)^2 \cdot (2 \cdot r + z) \right]$$

To find the height z of molten liquid transferred to the through:

$$f(z, i) := \Delta V_{\text{fill}}(z, r_i) - \frac{V(R) - V(r_i)}{2}$$

Given

$$f(z_0, 0) = 0$$

$$f(z_1, 1) = 0$$

$$f(z_2, 2) = 0$$

$$f(z_3, 3) = 0$$

$$f(z_4, 4) = 0$$

$$f(z_5, 5) = 0$$

$$z := \text{Find}(z_0, z_1, z_2, z_3, z_4, z_5)$$

Estimated as-received roughness:

$$r_m := R$$

$$z_f := 0 \cdot m$$

$$R_2 := \sqrt{r_m^2 - z_f^2} \quad z_{\text{bar}} := \frac{\pi \cdot (r_m)^2}{4 \cdot R} - \left[ \frac{(r_m)^2}{2 \cdot R} \cdot \text{asin}\left(\frac{z_f}{r_m}\right) + \frac{z_f \cdot R_2}{2 \cdot R} \right] + z_f$$

$$R_1 := \sqrt{r_m^2 - z_{\text{bar}}^2} \quad z_{\text{bar}} = 7.854 \mu\text{m}$$

$$\begin{aligned} Ra_0 := & \frac{R_1}{R_2} \cdot \left[ (r_m)^2 - (R_1)^2 \right]^{\frac{1}{2}} - \frac{(r_m)^2 \cdot i}{R_2} \cdot \ln \left[ \frac{R_1 \cdot i + \left[ (r_m)^2 - (R_1)^2 \right]^{\frac{1}{2}}}{m} \right] + \frac{(r_m)^2 \cdot i}{2 \cdot R_2} \cdot \ln \left( \frac{r_m}{m} \right) \dots \\ & + \left[ \frac{1}{2} \cdot \left[ (r_m)^2 - (R_2)^2 \right]^{\frac{1}{2}} - \frac{1}{2} \cdot \frac{(r_m)^2 \cdot i}{R_2} \cdot \ln \left[ \frac{R_2 \cdot i + \left[ (r_m)^2 - (R_2)^2 \right]^{\frac{1}{2}}}{m} \right] \right] + \left[ \left( 1 - \frac{R_1}{R_2} \right) \cdot 2 \cdot z_{\text{bar}} - z_f \right] \end{aligned}$$

$$Ra_0 = 9.667 \times 10^{-6} \text{ m}$$

Average surface roughness after laser melting:

$$rm := r$$

$$zf := z$$

$$R2_i := \sqrt{(rm_i)^2 - (zf_i)^2}$$

$$z\_bar_i := \frac{\pi \cdot (rm_i)^2}{4 \cdot R} - \left[ \frac{(rm_i)^2}{2 \cdot R} \operatorname{asin} \left( \frac{zf_i}{rm_i} \right) + \frac{zf_i \cdot R2_i}{2 \cdot R} \right] + zf_i$$

$$R1 := \sqrt{rm^2 - z\_bar^2}$$

$$R2 = \begin{pmatrix} 6.781 \times 10^{-6} \\ 6.627 \times 10^{-6} \\ 6.51 \times 10^{-6} \\ 6.423 \times 10^{-6} \\ 6.362 \times 10^{-6} \\ 6.322 \times 10^{-6} \end{pmatrix} m$$

$$z\_bar = \begin{pmatrix} 6.865 \times 10^{-6} \\ 6.827 \times 10^{-6} \\ 6.798 \times 10^{-6} \\ 6.776 \times 10^{-6} \\ 6.762 \times 10^{-6} \\ 6.752 \times 10^{-6} \end{pmatrix} m$$

$$R1 = \begin{pmatrix} 5.193 \times 10^{-6} \\ 5.113 \times 10^{-6} \\ 5.051 \times 10^{-6} \\ 5.004 \times 10^{-6} \\ 4.971 \times 10^{-6} \\ 4.949 \times 10^{-6} \end{pmatrix} m$$

Expression for the surface roughness :

$$Ra_j := \frac{R1_j}{R2_j} \cdot \left[ (rm_j)^2 - (R1_j)^2 \right]^{\frac{1}{2}} - \frac{(rm_j)^2 \cdot i}{R2_j} \cdot \ln \left[ \frac{R1_j \cdot i + \left[ (rm_j)^2 - (R1_j)^2 \right]^{\frac{1}{2}}}{m} \right] + \frac{(rm_j)^2 \cdot i}{2 \cdot R2_j} \cdot \ln \left( \frac{rm_j}{m} \right) \dots$$

$$+ \left[ \frac{1}{2} \cdot \left[ (rm_j)^2 - (R2_j)^2 \right]^{\frac{1}{2}} - \frac{1}{2} \cdot \frac{(rm_j)^2 \cdot i}{R2_j} \cdot \ln \left[ \frac{R2_j \cdot i + \left[ (rm_j)^2 - (R2_j)^2 \right]^{\frac{1}{2}}}{m} \right] \right] + \left[ \left( 1 - \frac{R1_j}{R2_j} \right) \cdot 2 \cdot z\_bar_j - zf_j \right]$$

Expression for the % roughness reduction:

$$\%RaV := \frac{Ra}{Ra0} - 1$$

% roughness variation for different laser power:

$$\%RaV225W := \begin{pmatrix} -8.467 \\ -25.64 \\ -34.7 \\ -40.409 \\ -44.345 \\ -47.192 \end{pmatrix} \quad \%RaV334W := \begin{pmatrix} -40.355 \\ -46.487 \\ -50.646 \\ -53.626 \\ -55.828 \\ -57.479 \end{pmatrix} \quad \%RaV420W := \begin{pmatrix} -57.474 \\ -60.546 \\ -62.797 \\ -64.474 \\ -65.731 \\ -66.669 \end{pmatrix} \quad \%RaV565W := \begin{pmatrix} -72.005 \\ -73.536 \\ -74.667 \\ -75.497 \\ -76.09 \\ -76.496 \end{pmatrix}$$

Expression for the average solidification time of molten surface

$$\Delta t_{sol_i} := \frac{L \cdot \rho}{2 \cdot k} \cdot \frac{\left[ R^2 - (r_i)^2 \right]}{\left[ \left[ T_{surf} \left( \Delta t(D, v_{s_i}), P, D \right) \cdot (1 - \epsilon) + 25 \right] \cdot 0.4 + T_f \cdot 0.6 \right] - T_f}$$

$$\Delta t_{sol} = \begin{pmatrix} 5.856 \times 10^{-7} \\ 5.181 \times 10^{-7} \\ 4.66 \times 10^{-7} \\ 4.239 \times 10^{-7} \\ 3.887 \times 10^{-7} \\ 3.586 \times 10^{-7} \end{pmatrix} \text{ sec}$$

Expression for the average surface homogenization time obtained from a pressure balance :

capillary pressure:

$$P_c(x, i) := 2 \cdot \sigma_{lv} \cdot \frac{1 - \frac{x}{z f_i}}{R - r_i}$$

hydrostatic:

$$P_h(x) := \rho \cdot g \cdot x$$

dynamic pressure:

$$P_d(x, i) := \eta \cdot \frac{x}{4(R - r_i)^2} \cdot \frac{d}{dt} x$$

$$\Delta t_{fill_i} := \int_{0 \cdot \mu m}^{z f_i} \left[ \frac{2 \cdot \sigma_{lv}}{\left[ R - r_i \cdot \left( 1 - \frac{x}{z f_i} \right) \right] \cdot 2} - \rho \cdot g \cdot x \right]^{-1} \cdot \left[ \eta \cdot \frac{x}{\left[ \left[ R - r_i \cdot \left( 1 - \frac{x}{z f_i} \right) \right] \cdot 2 \right]^2} \right] dx$$

$$\Delta t_{fill} = \begin{pmatrix} 1.727 \times 10^{-9} \\ 1.756 \times 10^{-9} \\ 1.777 \times 10^{-9} \\ 1.791 \times 10^{-9} \\ 1.8 \times 10^{-9} \\ 1.806 \times 10^{-9} \end{pmatrix} \text{sec}$$

## APPENDIX A: III. Modeling code for surface over melting

(written in MathCad Professional 2001)

### Physical properties

Properties for Fe-Cu-Sn (60-38-2 wt.%) from a rule of mixtures:

(ASM Metals Handbook v.1-3 9th Ed. and Eustathopoulos)

Latent heat of fusion:

$$\Delta h_f := \left[ 0.6 \cdot \left( 0.13 \cdot \frac{16.9}{51.99} + 0.87 \cdot \frac{13.8}{55.85} \right) + 0.4 \cdot \left( \frac{13.05}{63.54} \cdot 0.95 + 0.05 \cdot \frac{7.029}{118.69} \right) \right] \cdot 10^6 \cdot \frac{\text{joule}}{\text{kg}}$$

$$\Delta h_f = 2.336 \times 10^5 \frac{\text{joule}}{\text{kg}}$$

Specific heat:

$$C_p := [ 0.6 \cdot 460 + 0.4 \cdot (383 \cdot 0.95 + 0.05 \cdot 226) ] \cdot \frac{\text{joule}}{\text{kg} \cdot \text{K}}$$

$$C_p = 426.06 \frac{\text{joule}}{\text{kg} \cdot \text{K}}$$

Thermal conductivity:

$$k := [ 0.6 \cdot 24.9 + 0.4 \cdot (0.95 \cdot 386 + 0.05 \cdot 64) ] \cdot \frac{\text{watt}}{\text{m} \cdot \text{K}}$$

$$k = 162.9 \frac{\text{watt}}{\text{m} \cdot \text{K}}$$

Density:

$$\rho := [ 0.6 \cdot 7750 + 0.4 \cdot (0.95 \cdot 8954 + 0.05 \cdot 7304) ] \cdot \frac{\text{kg}}{\text{m}^3}$$

$$\rho = 8.199 \times 10^3 \text{ kg m}^{-3}$$

Thermal diffusivity:

$$\alpha := \frac{k}{\rho \cdot C_p}$$

$$\alpha = 4.663 \times 10^{-5} \text{ m}^2 \text{ sec}^{-1}$$

Coefficient of surface energy variation with temperature

$$g\sigma := \frac{(-0.29 \cdot 0.87 - 0.33 \cdot 0.13) \cdot 0.6 + (-0.19 \cdot 0.95 - 0.11 \cdot 0.05) \cdot 0.4}{1000} \cdot \frac{\text{joule}}{\text{m}^2}$$

$$g\sigma = -2.515 \times 10^{-4} \frac{\text{joule}}{\text{m}^2 \cdot \text{K}}$$



surface energy at the melting point:

$$\sigma := \frac{(1855 \cdot 0.87 + 1628 \cdot 0.13) \cdot 0.6 + (1355 \cdot 0.95 + 505 \cdot 0.05) \cdot 0.4}{1000} \cdot \frac{\text{joule}}{\text{m}^2}$$

$$\sigma = 1.62 \frac{\text{joule}}{\text{m}^2}$$

viscosity at the melting point

$$\mu := \frac{(6.5 \cdot 0.87 + 6 \cdot 0.13) \cdot 0.6 + (4.3 \cdot 0.95 + 1.8 \cdot 0.05) \cdot 0.4}{1000} \cdot \text{Pa} \cdot \text{sec}$$

$$\mu = 5.531 \times 10^{-3} \text{ Pa} \cdot \text{sec}$$

Melting point in Celcius:

$$T_m := 1440$$

$$T_m = 1.44 \times 10^3$$

Vaporization temperature in Celcius:

$$T_v := [0.6 \cdot (0.87 \cdot 3135 + 0.13 \cdot 2945) + 0.4 \cdot (0.05 \cdot 2876 + 0.95 \cdot 2836)] - 273$$

$$T_v = 2.728 \times 10^3$$

Expression for the surface energy as a fuction of temperature:

$$\sigma(T) := \sigma + (T - T_m) \cdot g\sigma$$

Modifidied thermal conductivity to incorporate melting effect:

$$k_{\text{mod}} := \alpha \cdot \rho \cdot \left[ \frac{C_p \cdot (T_m - T_o) + \Delta h_f}{T_m - T_o} \right]$$

$$k_{\text{mod}} = 226.011 \frac{\text{watt}}{\text{m} \cdot \text{K}}$$

As-received surface roughness:

$$Ra_0 := 2.42 \cdot \mu\text{m}$$

Estimated losses by surface refelctivity, convection and radiation:

$$\varepsilon := 0.35$$

Processing parameters:

Laser power, scan speed, traveling speed, track width:

$$\begin{aligned}
 P &:= 334 \text{ watt} \\
 v &:= \begin{pmatrix} 177.2 \\ 162.1 \\ 149.4 \\ 128.9 \\ 113.4 \\ 101.3 \end{pmatrix} \frac{\text{mm}}{\text{sec}} \\
 vt &:= \begin{pmatrix} 1.18 \\ 1.08 \\ 1.00 \\ 0.86 \\ 0.76 \\ 0.68 \end{pmatrix} \frac{\text{mm}}{\text{sec}} \\
 w &:= \begin{pmatrix} 1860.325 \\ 1914.875 \\ 1925.8 \\ 1928.9 \\ 1979.766667 \\ 2013.033333 \end{pmatrix} \mu\text{m}
 \end{aligned}$$

Measured results: rippling wave length, surface roughness and orientation angle

$$\begin{aligned}
 \lambda_m &:= \begin{pmatrix} 349 \\ 375.96 \\ 398.8 \\ 432.13 \\ 458.5 \\ 483 \end{pmatrix} \mu\text{m} \\
 Ra &:= \begin{pmatrix} 1.57 \\ 1.94 \\ 1.98 \\ 1.89 \\ 2.26 \\ 3.24 \end{pmatrix} \mu\text{m} \\
 \theta &:= \begin{pmatrix} 26 \cdot \frac{\pi}{180} \\ 38 \cdot \frac{\pi}{180} \\ 35 \cdot \frac{\pi}{180} \\ 32 \cdot \frac{\pi}{180} \\ 30 \cdot \frac{\pi}{180} \\ 28 \cdot \frac{\pi}{180} \end{pmatrix} \\
 \theta_m &:= 31.5 \cdot \frac{\pi}{180}
 \end{aligned}$$

Temperature distribution according to Rosenthal for a steady state moving heat source:

$$T(x, y, z, i) := T_o + \frac{P \cdot (1 - \epsilon)}{2 \cdot \pi \cdot k_{\text{mod}}} \cdot \left[ \frac{1}{(x^2 + y^2 + z^2)^{0.5}} \right] \cdot \exp \left[ -\frac{v_i}{2 \cdot \alpha} \cdot \left[ (x^2 + y^2 + z^2)^{0.5} + x \right] \right]$$

Finding penetration depth at different speeds:

Need to find coordinate of the center of molten pool along the x direction,

$$x1_i := \text{root}(T_m - T(x, 0 \cdot \text{mm}, 0 \cdot \text{mm}, i), x)$$

$$x2_i := \text{root}(T_m - T(x, 0 \cdot \text{mm}, 0 \cdot \text{mm}, i), x)$$

$$x_m := \frac{x1 + x2}{2}$$

$$x_m = \begin{pmatrix} -14.128 \\ -13.315 \\ -12.594 \\ -11.351 \\ -10.339 \\ -9.5 \end{pmatrix} \mu\text{m}$$

To find the depth of the isotherm corresponding to melting we evaluate the  $T=T_m$  at  $x_m$  and solve for  $z_m$

$$z_{m_1} := \text{root}\left(T(x_{m_1}, z, 0\text{-mm}, i) - T_m, z\right)$$

Double checking with the melting temperature:

$$T(x_{m_2}, z_{m_2}, 0\text{-mm}, 5) = 1.501 \times 10^3$$

$$z_m = \begin{pmatrix} 91.927 \\ 92.971 \\ 93.883 \\ 95.428 \\ 96.661 \\ 97.666 \end{pmatrix} \mu\text{m}$$

First derivative of T with respect to x and z:

$$T_z(z, i) := \frac{-1}{2} \cdot P \cdot \frac{(1 - \epsilon)}{\pi \cdot k_{\text{mod}} \cdot z^2} \cdot \exp\left(\frac{-1}{2} \cdot \frac{v_i}{\alpha} \cdot z\right) - \frac{1}{4} \cdot P \cdot \frac{(1 - \epsilon)}{\pi \cdot k_{\text{mod}} \cdot z} \cdot \frac{v_i}{\alpha} \cdot \exp\left(\frac{-1}{2} \cdot \frac{v_i}{\alpha} \cdot z\right)$$

$$T_x(x, i) := \frac{-1}{2} \cdot P \cdot \frac{(1 - \epsilon)}{\pi \cdot k_{\text{mod}} \cdot x^2} \cdot \exp\left(\frac{-v_i}{\alpha} \cdot x\right) - \frac{1}{2} \cdot P \cdot \frac{(1 - \epsilon)}{\pi \cdot k_{\text{mod}} \cdot x} \cdot \frac{v_i}{\alpha} \cdot \exp\left(\frac{-v_i}{\alpha} \cdot x\right)$$

Temperature of liquid surface below the vicinity of the laser beam :

$$Tl_1 := T(0.045\text{-mm}, 0.045\text{-mm}, 0\text{-mm}, i)$$

$$Tl_5 = 2.16 \times 10^3$$

Expression for the melt front speed from a heat flux balance at the melting front:

$$v_{s,i} := k \cdot \frac{-T_z(z_{m,i}, i)}{\rho \cdot \Delta h_f}$$

$$v_s = \begin{pmatrix} 1.518 \times 10^3 \\ 1.487 \times 10^3 \\ 1.46 \times 10^3 \\ 1.417 \times 10^3 \\ 1.383 \times 10^3 \\ 1.356 \times 10^3 \end{pmatrix} \frac{\text{mm}}{\text{sec}}$$

Expression for the average solidification time:

$$t_{s,i} := \frac{-x_i^2}{v_i}$$

$$t_s = \begin{pmatrix} 0.61 \\ 0.667 \\ 0.723 \\ 0.838 \\ 0.953 \\ 1.067 \end{pmatrix} \text{sec}^2 \text{m}^{-1} \frac{\text{mm}}{\text{sec}}$$

Amplitude of wave due to melt depth h (From Anthony and Klein and modified by Ramos):

$$\Delta h_i := \frac{(T_m - T_{l,i})}{\left[ g \cdot \rho + \sigma \left( \frac{T_m + T_{l,i}}{2} \right) \left( \frac{2 \cdot \pi}{\lambda_{m,i} \cdot \cos(\theta_m)} \right)^2 \right] \cdot z_{m,i}} \cdot g \cdot \sigma \cdot \exp \left[ \frac{-\mu}{\rho} \cdot \left( \frac{2 \cdot \pi}{\lambda_{m,i} \cdot \cos(\theta_m)} \right)^2 \cdot t_{s,i} \right] \cdot \frac{3}{2}$$

$$\Delta h = \begin{pmatrix} 2.662 \times 10^{-6} \\ 3.294 \times 10^{-6} \\ 3.893 \times 10^{-6} \\ 4.891 \times 10^{-6} \\ 5.758 \times 10^{-6} \\ 6.604 \times 10^{-6} \end{pmatrix} \text{m}$$

Expression for estimated percent roughness variation:

$$\%RaVest_1 := \left( \frac{\Delta h_i}{Ra_{0.2}} - 1 \right)$$

Percent roughness variation: measured and estimated

$$\%RaV2 := \begin{pmatrix} -0.28 \\ -0.15 \\ -0.16 \\ -0.22 \\ -0.12 \\ 0.29 \end{pmatrix}$$

$$\%RaVest = \begin{pmatrix} -0.45 \\ -0.319 \\ -0.196 \\ 0.01 \\ 0.19 \\ 0.364 \end{pmatrix}$$

## APPENDIX A: IV. Modeling code of fracture criteria

(written in MathCad Professional 2001)

### Physical properties:

(Ashby, Hertzberg, Lawn, ASM Metals Handbook v1-3 9th Ed., CRC Materials Science and Engineering Handbook)

Heat conductivity:

$$KHf := 20.7 \cdot \frac{W}{m \cdot K}$$

$$KCr := 93.7 \cdot \frac{W}{m \cdot K}$$

$$KSi := 133 \cdot \frac{W}{m \cdot K}$$

$$KCC := 200 \cdot \frac{W}{m \cdot K}$$

Density of solid:

$$\rho Hf := 13.1 \cdot \frac{gm}{cm^3}$$

$$\rho Cr := 7.19 \cdot \frac{gm}{cm^3}$$

$$\rho Si := 2.329 \cdot \frac{gm}{cm^3}$$

$$\rho CC := 1.83 \cdot \frac{gm}{cm^3}$$

Heat capacity of solid:

$$CpHf := 0.144 \cdot \frac{J}{gm \cdot K}$$

$$CpCr := 0.45 \cdot \frac{J}{gm \cdot K}$$

$$CpSi := 0.928 \cdot \frac{joule}{gm \cdot K}$$

$$CpCC := 0.84 \cdot \frac{joule}{gm \cdot K}$$

Thermal diffusivity of solid:

$$\alpha_{diffHf} := \frac{KHf}{\rho Hf \cdot CpHf}$$

$$\alpha_{diffCr} := \frac{KCr}{\rho Cr \cdot CpCr}$$

$$\alpha_{diffSi} := \frac{KSi}{\rho Si \cdot CpSi}$$

$$\alpha_{diffCC} := 10^{-4} \cdot \frac{m^2}{s}$$

Coefficient of linear thermal expansion:

$$\alpha Hf := 5.9 \cdot 10^{-6} \cdot \frac{1}{K}$$

$$\alpha Cr := 6.5 \cdot 10^{-6} \cdot \frac{1}{K}$$

$$\alpha Si := 3.1 \cdot 10^{-6} \cdot \frac{1}{K}$$

$$\alpha CC := 6.94 \cdot 10^{-7} \cdot \frac{1}{K}$$

Youngs modulus at room temperature:

$$EHf := 141 \cdot 10^9 \cdot \frac{newton}{m^2}$$

$$ECr := 279.1 \cdot 10^9 \cdot \frac{newton}{m^2}$$

$$ESi := 110 \cdot 10^9 \cdot \frac{newton}{m^2}$$

$$ECC := 690 \cdot 10^9 \cdot Pa$$

Opening mode I critical fracture toughness:

$$K_{IcHf} := 20 \cdot (10^6 \cdot \text{Pa} \cdot \text{m}^{0.5}) \quad K_{IcCr} := 65 \cdot (10^6 \cdot \text{Pa} \cdot \text{m}^{0.5}) \quad K_{IcSi} := 8 \cdot 10^5 \cdot \text{Pa} \cdot \text{m}^{0.5}$$

Fracture stress at room temperature:

$$\sigma_{fHf} := 700 \cdot 10^6 \cdot \text{Pa} \quad \sigma_{fCr} := 700 \cdot 10^6 \cdot \text{Pa} \quad \sigma_{fSi} := 3500 \cdot 10^6 \cdot \text{Pa} \quad \sigma_{fCC} := 1.85 \cdot 10^9 \cdot \text{Pa}$$

Poisson ration at room temperature:

$$\nu_{Hf} := 0.33 \quad \nu_{Cr} := 0.21 \quad \nu_{Si} := 0.27 \quad \nu_{CC} := 0.07 \cdot 2$$

Physical properties obtained by rule of mixtures:

$$\nu_{avg} := 0.5 \cdot (0.7 \cdot \nu_{Si} + .25 \cdot \nu_{Cr} + 0.05 \cdot \nu_{CC}) + 0.5 \cdot (0.75 \cdot \nu_{Si} + 0.16 \cdot \nu_{Cr} + 0.09 \cdot \nu_{Hf}) \quad \nu_{avg} = 0.257$$

$$K_{avg} := 0.5 \cdot (0.7 \cdot K_{Si} + .25 \cdot K_{Cr} + 0.05 \cdot K_{CC}) + 0.5 \cdot (0.75 \cdot K_{Si} + 0.16 \cdot K_{Cr} + 0.09 \cdot K_{Hf}) \quad K_{avg} = 121.565 \frac{\text{W}}{\text{m} \cdot \text{K}}$$

$$\alpha_{diff} := 0.5 \cdot (0.7 \cdot \alpha_{diffSi} + .25 \cdot \alpha_{diffCr} + 0.05 \cdot \alpha_{diffCC}) + 0.5 \cdot (0.75 \cdot \alpha_{diffSi} + 0.16 \cdot \alpha_{diffCr} + 0.09 \cdot \alpha_{diffHf}) \quad \alpha_{diff} = 5.354 \times 10^{-5} \frac{\text{m}^2}{\text{s}}$$

$$\alpha_{avg} := 0.5 \cdot [0.7 \cdot \alpha_{Si} + .25 \cdot \alpha_{Cr} + 0.05 \cdot (.25 \cdot \alpha_{CC})] + 0.5 \cdot (0.75 \cdot \alpha_{Si} + 0.16 \cdot \alpha_{Cr} + 0.09 \cdot \alpha_{Hf}) \quad \alpha_{avg} = 3.85 \times 10^{-6} \frac{1}{\text{K}}$$

$$E_{avg} := 0.5 \cdot (0.7 \cdot E_{Si} + .25 \cdot E_{Cr} + 0.05 \cdot E_{CC}) + 0.5 \cdot (0.75 \cdot E_{Si} + 0.16 \cdot E_{Cr} + 0.09 \cdot E_{Hf}) \quad E_{avg} = 1.606 \times 10^{11} \text{ Pa}$$

$$K_{Icavg} := 0.5 \cdot (0.7 \cdot K_{IcSi} + .3 \cdot K_{IcCr}) + 0.5 \cdot (0.75 \cdot K_{IcSi} + 0.16 \cdot K_{IcCr} + 0.09 \cdot K_{IcHf}) \quad K_{Icavg} = 1.643 \times 10^7 \text{ Pa} \cdot \text{m}^{0.5}$$

$$\sigma_{favg} := 0.5 \cdot (0.7 \cdot \sigma_{fSi} + .25 \cdot \sigma_{fCr} + 0.05 \cdot \sigma_{fCC}) + 0.5 \cdot (0.75 \cdot \sigma_{fSi} + 0.16 \cdot \sigma_{fCr} + 0.09 \cdot \sigma_{fHf}) \quad \sigma_{favg} = 2.759 \times 10^9 \text{ Pa}$$



Fracture toughness of Si-Cr-Hf-C laser fused coating as obtained by indentation method:

$$K_{Ic} := 3.936 \cdot 10^6 \cdot \text{Pa} \cdot \text{m}^{0.5}$$

Critical energy release rate:

$$G_c := \frac{K_{Ic}^2}{\frac{E_{avg}}{1-\nu_{avg}}} \quad G_c = 71.676 \frac{\text{joule}}{\text{m}^2}$$

Substrate radius:  $\Delta h_{CC} := 5000 \cdot \mu\text{m}$

Coating thickness:  $\Delta h := 300 \cdot \mu\text{m}$

Solution for the heat transfer of two layer cylinder during cooling (from Ozisik)

Inner radius:

$$a := \Delta h_{CC}$$

Outer radius:

$$b := \Delta h + \Delta h_{CC}$$

Heat convection coefficient:

$$h_{con} := 120 \cdot \frac{W}{m^2 \cdot K}$$

Heat conduction coefficient:

$$k_{con} := 0.01772 \cdot 350 \cdot \frac{W}{m \cdot K}$$

Expression for the radiation heat transfer coefficient:

$$h_r := \varepsilon \cdot \sigma \cdot \left[ \left( \frac{T_1}{1} \right)^2 + T_2^2 \right] \cdot \left( \frac{T_1}{1} + T_2 \right)$$

$$h_r = 253.792 \cdot \frac{W}{m^2 \cdot K}$$

Room temperature:

$$T_2 := 25 + 273$$

Initial temperature

$$T_1 := 1290 + 273$$

Emissivity:

$$\varepsilon := 0.95$$

Stefan Boltzman coefficient:

$$\sigma := 5.67 \cdot 10^{-8} \cdot \frac{W}{m^2}$$

Nodimensional numbers:

$$H := b \cdot \frac{h_{con} + h_r}{k_{con}}$$

$$K := \frac{K_{CC}}{K_{avg}} \cdot \left( \frac{\alpha_{diff}}{\alpha_{diffCC}} \right)^{0.5}$$

Initial temperature distribution:

$$T_0(r) := T_1$$

Finding the Eigen values of the equation:

$$M(x) := \begin{bmatrix} J_0 \left[ \frac{x \cdot a}{(\alpha_{diffCC} \cdot s)^{0.5}} \right] & -J_0 \left[ \frac{a}{b} \cdot \frac{b \cdot x}{(\alpha_{diff} \cdot s)^{0.5}} \right] & -Y_0 \left[ \frac{a}{b} \cdot \frac{b \cdot x}{(\alpha_{diff} \cdot s)^{0.5}} \right] \\ K \cdot J_1 \left[ \frac{x \cdot a}{(\alpha_{diffCC} \cdot s)^{0.5}} \right] & -J_1 \left[ \frac{a}{b} \cdot \frac{b \cdot x}{(\alpha_{diff} \cdot s)^{0.5}} \right] & -Y_1 \left[ \frac{a}{b} \cdot \frac{b \cdot x}{(\alpha_{diff} \cdot s)^{0.5}} \right] \\ 0 & \frac{H \cdot (\alpha_{diff} \cdot s)^{0.5}}{b \cdot x} \cdot J_0 \left[ \frac{b \cdot x}{(\alpha_{diff} \cdot s)^{0.5}} \right] - J_1 \left[ \frac{b \cdot x}{(\alpha_{diff} \cdot s)^{0.5}} \right] & \frac{H \cdot (\alpha_{diff} \cdot s)^{0.5}}{b \cdot x} \cdot Y_0 \left[ \frac{b \cdot x}{(\alpha_{diff} \cdot s)^{0.5}} \right] - Y_1 \left[ \frac{b \cdot x}{(\alpha_{diff} \cdot s)^{0.5}} \right] \end{bmatrix}$$

Given

$$|M(x_0)| = 0 \quad |M(x_3)| = 0 \quad |M(x_6)| = 0 \quad |M(x_9)| = 0$$

$$|M(x_1)| = 0 \quad |M(x_4)| = 0 \quad |M(x_7)| = 0 \quad |M(x_{10})| = 0$$

$$|M(x_2)| = 0 \quad |M(x_5)| = 0 \quad |M(x_8)| = 0 \quad |M(x_{11})| = 0$$

$$x := \text{Find}(x_0, x_1, x_2, x_3, x_4, x_5, x_6, x_7, x_8, x_9, x_{10}, x_{11})$$

$$x := x \cdot s^{-0.5}$$

Expression for the different algebraic components of the temperature solution:

$$\Delta(n) := J0 \left[ \frac{a}{b} \cdot \frac{b \cdot x_n}{(\alpha \text{diff})^{0.5}} \right] \cdot Y1 \left[ \frac{a}{b} \cdot \frac{b \cdot x_n}{(\alpha \text{diff})^{0.5}} \right] - J1 \left[ \frac{a}{b} \cdot \frac{b \cdot x_n}{(\alpha \text{diff})^{0.5}} \right] \cdot Y0 \left[ \frac{a}{b} \cdot \frac{b \cdot x_n}{(\alpha \text{diff})^{0.5}} \right]$$

$$A(n) := \frac{1}{\Delta(n)} \cdot \left[ J0 \left[ \frac{x_n \cdot a}{(\alpha \text{diffCC})^{0.5}} \right] \cdot Y1 \left[ \frac{a}{b} \cdot \frac{b \cdot x_n}{(\alpha \text{diff})^{0.5}} \right] - K \cdot J1 \left[ \frac{x_n \cdot a}{(\alpha \text{diffCC})^{0.5}} \right] \cdot Y0 \left[ \frac{a}{b} \cdot \frac{b \cdot x_n}{(\alpha \text{diff})^{0.5}} \right] \right]$$

$$B(n) := \frac{1}{\Delta(n)} \cdot \left[ K \cdot J1 \left[ \frac{x_n \cdot a}{(\alpha \text{diffCC})^{0.5}} \right] \cdot J0 \left[ \frac{a}{b} \cdot \frac{b \cdot x_n}{(\alpha \text{diff})^{0.5}} \right] - J0 \left[ \frac{x_n \cdot a}{(\alpha \text{diffCC})^{0.5}} \right] \cdot J1 \left[ \frac{a}{b} \cdot \frac{b \cdot x_n}{(\alpha \text{diff})^{0.5}} \right] \right]$$

$$N(n) := \frac{KCC}{\alpha \text{diffCC}} \cdot \int_{0. \text{mm}}^a \rho \cdot J0 \left( \frac{x_n \cdot \rho}{\alpha \text{diffCC}^{0.5}} \right)^2 d\rho \dots$$

$$+ \frac{Kavg}{\alpha \text{diff}} \cdot \int_a^b \rho \cdot \left( A(n) \cdot J0 \left( \frac{x_n \cdot \rho}{\alpha \text{diff}^{0.5}} \right) + B(n) \cdot Y0 \left( \frac{x_n \cdot \rho}{\alpha \text{diff}^{0.5}} \right) \right)^2 d\rho$$

Inner layer radial temperature distribution:

$$\theta_1(r,t) := \sum_{n=0}^{11} \frac{1}{N(n)} \cdot \exp\left[-\left(\frac{x_n}{r}\right)^2 \cdot t\right] \cdot J_0\left(\frac{x_n \cdot r}{\alpha_{\text{diffCC}}^{0.5}}\right) \cdot \left[ \frac{KCC}{\alpha_{\text{diffCC}}} \cdot \int_0^a \rho \cdot J_0\left(\frac{x_n \cdot \rho}{\alpha_{\text{diffCC}}^{0.5}}\right) \cdot T_0(\rho) \, d\rho \dots \right. \\ \left. + \frac{K_{\text{avg}}}{\alpha_{\text{diff}}} \cdot \int_a^b \rho \cdot \left( A(n) \cdot J_0\left(\frac{x_n \cdot \rho}{\alpha_{\text{diff}}^{0.5}}\right) \dots \right) \cdot T_0(\rho) \, d\rho \right. \\ \left. + B(n) \cdot Y_0\left(\frac{x_n \cdot \rho}{\alpha_{\text{diff}}^{0.5}}\right) \right]$$

Outer layer radial temperature distribution:

$$\theta_2(r,t) := \sum_{n=0}^{11} \frac{1}{N(n)} \cdot \exp\left[-\left(\frac{x_n}{r}\right)^2 \cdot t\right] \cdot \left( A(n) \cdot J_0\left(\frac{x_n \cdot r}{\alpha_{\text{diff}}^{0.5}}\right) \dots \right) \cdot \left[ \frac{KCC}{\alpha_{\text{diffCC}}} \cdot \int_{0 \cdot \text{mm}}^a \rho \cdot J_0\left(\frac{x_n \cdot \rho}{\alpha_{\text{diffCC}}^{0.5}}\right) \cdot T_0(\rho) \, d\rho \dots \right. \\ \left. + \frac{K_{\text{avg}}}{\alpha_{\text{diff}}} \cdot \int_a^b \rho \cdot \left( A(n) \cdot J_0\left(\frac{x_n \cdot \rho}{\alpha_{\text{diff}}^{0.5}}\right) \dots \right) \cdot T_0(\rho) \, d\rho \right. \\ \left. + B(n) \cdot Y_0\left(\frac{x_n \cdot \rho}{\alpha_{\text{diff}}^{0.5}}\right) \right]$$

Results after 10 milli second of cooling time:

$$t := 0.01 \cdot s$$

Expression for the radial temperature along all the domain :

$$T_{\text{plot}}(r, t) := \text{if}(r < \Delta h_{\text{CC}}, \theta 1(r, t), \theta 2(r, t))$$

Expression for the radial temperature gradient along all the domain:

$$T_{\text{gradient\_plot}}(r, t) := \text{if}\left(r < \Delta h_{\text{CC}}, \frac{d}{dr} \theta 1(r, t), \frac{d}{dr} \theta 2(r, t)\right)$$

Solution to the stress state in two-layer cylinder in plane-stress condition  
(From Boley and Hetnarski)

Approximated temperature below which C/C composite and coating can not accomodate stresses:

$$\theta_{mCC} := 800 \qquad \theta_{mCoat} := 725$$

Pressure exerted by inner cylinder to outer coating ring

$$p := \frac{\alpha_{CC} \cdot ECC}{\Delta h_{CC}^2} \cdot \int_0^{\Delta h_{CC}} (\theta_{mCC} - \theta_1(r, t)) \cdot r \, dr - \alpha_{CC} \cdot ECC \cdot \frac{(\theta_{mCC} - \theta_1(0\text{-mm}, t))}{2}$$

$$p = 3.545 \times 10^6 \text{ Pa}$$

Radial stress state on C/C substrate:

$$\sigma_{r1}(r) := -\alpha_{CC} \cdot \frac{ECC}{r^2} \cdot \int_0^r (\theta_{mCC} - \theta_1(\rho, t)) \cdot \rho \, d\rho + \alpha_{CC} \cdot ECC \cdot \frac{(\theta_{mCC} - \theta_1(0\text{-mm}, t))}{2}$$

$$\sigma_{r1}(\Delta h_{CC}) = -3.545 \times 10^6 \text{ Pa}$$

Hoop stress on C/C substrate:

$$\sigma_{\theta\theta 1}(r) := \frac{\alpha_{CC} \cdot ECC}{r^2} \cdot \int_0^r (\theta_{mCC} - \theta_1(\rho, t)) \cdot \rho \, d\rho - \alpha_{CC} \cdot ECC \cdot \left[ (\theta_{mCC} - \theta_1(r, t)) - \frac{(\theta_{mCC} - \theta_1(0\text{-mm}, t))}{2} \right]$$

$$\sigma_{\theta\theta 1}(\Delta h_{CC}) = -2.027 \times 10^7 \text{ Pa}$$

From the thermal function technique the constant C1 and C2 are determined

$$C2 := \frac{(1 + \nu_{avg})}{E_{avg}} \left[ \frac{1}{(\Delta h_{CC})^2} - \frac{1}{(\Delta h_{CC} + \Delta h)^2} \right]^{-1} \left[ \frac{\alpha_{avg} \cdot E_{avg}}{(\Delta h_{CC} + \Delta h)^2} \int_{\Delta h_{CC}}^{\Delta h + \Delta h_{CC}} (\theta_{mCoat} - \theta_2(r, t)) \cdot r \, dr + p \right]$$

$$C2 = -4.065 \times 10^{-8} \, m^2$$

$$C1 := -p \cdot \frac{(1 - \nu_{avg})}{E_{avg}} + \frac{C2 \cdot (1 - \nu_{avg})}{\Delta h_{CC}^2 \cdot (1 + \nu_{avg})}$$

$$C1 = -9.772 \times 10^{-4}$$

Radial stress state on coating layer:

$$\sigma_{r2}(r) := -\alpha_{avg} \cdot \frac{E_{avg}}{r^2} \int_{\Delta h_{CC}}^r (\theta_{mCoat} - \theta_2(r, t)) \cdot r \, dr + \frac{E_{avg}}{1 - \nu_{avg}} \cdot C1 - E_{avg} \cdot \frac{C2}{(1 + \nu_{avg}) \cdot r^2}$$

$$\sigma_{r2}(\Delta h_{CC}) = -3.545 \times 10^6 \, Pa$$

Hoop stress state on coating layer:

$$\sigma_{\theta\theta 2}(r) := \alpha_{avg} \cdot \frac{E_{avg}}{r^2} \int_{\Delta h_{CC}}^r (\theta_{mCoat} - \theta_2(\rho, t)) \cdot \rho \, d\rho - \alpha_{avg} \cdot E_{avg} \cdot (\theta_{mCoat} - \theta_2(r, t)) + \frac{E_{avg}}{1 - \nu_{avg}} \cdot C1 + E_{avg} \cdot \frac{C2}{(1 + \nu_{avg}) \cdot r^2}$$

$$\sigma_{\theta\theta 2}(\Delta h_{CC}) = 6.834 \times 10^7 \, Pa$$



Solution to the stress state in plane-strain condition (From Hetnarski):

Physical properties for C/C composite and coating expressed in plane-strain condition:

$$v_{CCps} := \frac{v_{CC}}{1 - v_{CC}}$$

$$v_{avgps} := \frac{v_{avg}}{1 - v_{avg}}$$

$$E_{CCps} := \frac{E_{CC}}{1 - v_{CC}^2}$$

$$E_{avgps} := \frac{E_{avg}}{1 - v_{avg}^2}$$

$$\alpha_{CCps} := \alpha_{CC} \cdot (1 + v_{CC})$$

$$\alpha_{avgps} := \alpha_{avg} \cdot (1 + v_{avg})$$

Constant axial strains on C/C composite and coating:

$$\epsilon_{0CC} := 2 \cdot \frac{\alpha_{CCps}}{\Delta h_{CC}^2} \cdot \int_0^{\Delta h_{CC}} (\theta_{mCC} - \theta_1(\rho, t)) \cdot \rho \, d\rho$$

$$\epsilon_{0CC} = -5.919 \times 10^{-4}$$

$$\epsilon_{0avg} := 2 \cdot \frac{\alpha_{avgps}}{\Delta h_{CC}^2 + \Delta h^2} \cdot \int_{\Delta h_{CC}}^{\Delta h_{CC} + \Delta h} (\theta_{mCoat} - \theta_2(\rho, t)) \cdot \rho \, d\rho$$

$$\epsilon_{0avg} = -4.627 \times 10^{-4}$$

Pressure exerted by inner cylinder to outer coating ring

$$p := \frac{\alpha_{CCps} \cdot E_{CCps}}{\Delta h_{CC}^2} \cdot \int_0^{\Delta h_{CC}} (\theta_{mCC} - \theta_1(r, t)) \cdot r \, dr - \alpha_{CCps} \cdot E_{CCps} \cdot \frac{(\theta_{mCC} - \theta_1(0. \text{mm}, t))}{2}$$

$$p = 4.122 \times 10^4 \text{ Pa}$$

From the thermal function technique the constant C1 and C2 are determined

$$C2 := \frac{(1 + \nu_{avgps})}{E_{avgps}} \left[ \frac{1}{\Delta h_{CC}^2} - \frac{1}{(\Delta h_{CC} + \Delta h)^2} \right]^{-1} \left[ \frac{\alpha_{avgps} \cdot E_{avgps}}{(\Delta h_{CC} + \Delta h)^2} \int_{\Delta h_{CC}}^{\Delta h + \Delta h_{CC}} (\theta_{mCoat} - \theta_2(r, t)) \cdot r \, dr + p \right]$$

$$C2 = -5.588 \times 10^{-8} \, m^2$$

$$C1 := -p \cdot \frac{(1 - \nu_{avgps})}{E_{avgps}} + \frac{C2 \cdot (1 - \nu_{avgps})}{\Delta h_{CC}^2 \cdot (1 + \nu_{avgps})} - \nu_{avg} \cdot \epsilon_{0avg}$$

$$C1 = -9.823 \times 10^{-4}$$

Radial stress state on coating layer:

$$\sigma_{rr2ps}(r) := \frac{-\alpha_{avgps} \cdot E_{avgps}}{r^2} \int_{\Delta h_{CC}}^r (\theta_{mCoat} - \theta_2(r, t)) \cdot r \, dr + \frac{E_{avgps}}{1 - \nu_{avgps}} \cdot C1 - E_{avgps} \cdot \frac{C2}{(1 + \nu_{avgps}) \cdot r^2} + \frac{E_{avgps}}{1 - \nu_{avgps}} \cdot (\nu_{avg} \cdot \epsilon_{0avg})$$

Hoop stress state on coating layer:

$$\sigma_{\theta\theta 2ps}(r) := \frac{\alpha_{avgps} \cdot E_{avgps}}{r^2} \int_{\Delta h_{CC}}^r (\theta_{mCoat} - \theta_2(\rho, t)) \cdot \rho \, d\rho - \alpha_{avgps} \cdot E_{avgps} \cdot (\theta_{mCoat} - \theta_2(r, t)) + \frac{E_{avgps}}{1 - \nu_{avgps}} \cdot C1 \dots$$

$$+ E_{avgps} \cdot \frac{C2}{(1 + \nu_{avgps}) \cdot r^2} + \frac{E_{avgps}}{1 - \nu_{avgps}} \cdot (\nu_{avg} \cdot \epsilon_{0avg})$$

Axial stress state on coating layer:

$$\sigma_{zz2}(r) := \sigma_{rr2ps}(r) + \sigma_{\theta\theta 2ps}(r)$$

Criteria for crack stability (From Hutchinson) :

Surface Cracks

Dimensionless driving force:

$$Z := 3.951$$

Critical coating thickness:

evaluated at the substrate-coating interface:

$$\Delta h_{cmax} := G_c \cdot \frac{\frac{E_{avg}}{1-\nu_{avg}}}{Z \cdot \sigma_{\theta\theta 2ps} (\Delta h_{CC})^2}$$

evaluated at the coating surface:

$$\Delta h_{cmin} := G_c \cdot \frac{\frac{E_{avg}}{1-\nu_{avg}}}{Z \cdot \sigma_{\theta\theta 2ps} (\Delta h_{CC} + \Delta h)^2}$$

Results:

$$\Delta h_{cmax} = 600.194 \mu\text{m}$$

$$\Delta h_{cmin} = 1.24 \times 10^3 \mu\text{m}$$

### Channeling

$$Z := 1.976$$

$$\Delta h_{cmax} := Gc \cdot \frac{\frac{E_{avg}}{1 - v_{avg}}}{Z \cdot \sigma_{\theta\theta 2ps}(\Delta h_{CC})^2}$$

$$\Delta h_{cmin} := Gc \cdot \frac{\frac{E_{avg}}{1 - v_{avg}}}{Z \cdot \sigma_{\theta\theta 2ps}(\Delta h_{CC} + \Delta h)^2}$$

$$\Delta h_{cmax} = 1.2 \times 10^3 \mu m$$

$$\Delta h_{cmin} = 2.479 \times 10^3 \mu m$$

### Debond

$$Z := 1.028$$

$$\Delta h_{cmax} := Gc \cdot \frac{\frac{E_{avg}}{1 - v_{avg}}}{Z \cdot \sigma_{\theta\theta 2ps}(\Delta h_{CC})^2}$$

$$\Delta h_{cmin} := Gc \cdot \frac{\frac{E_{avg}}{1 - v_{avg}}}{Z \cdot \sigma_{\theta\theta 2ps}(\Delta h_{CC} + \Delta h)^2}$$

$$\Delta h_{cmax} = 2.307 \times 10^3 \mu m$$

$$\Delta h_{cmin} = 4.765 \times 10^3 \mu m$$

Determination of Mode I critical fracture toughness by the indentation crack method (from Lawn):

Measured data for Si-Cr-Hf-C laser fused coating and pure Si for different indenter loads:

average diagona length

average semi-crack length

indenters load

$$d := \begin{pmatrix} 39.4 \\ 48.5 \\ 59.4 \\ 68.2 \\ 44.2 \\ 54.32 \\ 42.6 \cdot 2 \end{pmatrix} \mu\text{m}$$

$$c := \begin{pmatrix} 26.7 \\ 38.6 \\ 48.5 \\ 53.5 \\ 84.94 \\ 111.84 \\ 59.11 \cdot 2 \end{pmatrix} \mu\text{m}$$

$$P := \begin{pmatrix} 10 \\ 15 \\ 20 \\ 25 \\ 10 \\ 15 \\ 20 \end{pmatrix} \text{newton}$$

indentors tip angle :

Last data points corresponds to pure Si

$$a := 136 \cdot \frac{\pi}{180}$$

Expression for the Vickers hardness:

$$H = 0.319$$

$$H_1 := 2 \cdot P_i \cdot \frac{\sin\left(\frac{a}{2}\right)}{(d_i)^2}$$

Last data points corresponds to pure Si

Expression for mode I critical fracture toughness:

$$K_{c_i} := 0.016 \cdot \left( \frac{E_{avg}}{H_i} \right)^{0.5} \cdot \frac{P_i}{(c_i)^{1.5}}$$

$$K_c = \begin{pmatrix} 4.252 \\ 3.688 \\ 3.703 \\ 4.103 \\ 0.841 \\ 0.837 \\ 1.396 \end{pmatrix} \text{MPa} \cdot \text{m}^{0.5}$$

Last data points corresponds to pure Si

average value of the mode I critical fracture toughness:

$$K_{cavg} := \sum_{i=0}^3 \frac{K_{c_i}}{4}$$

$$K_{cavg} = 3.936 \text{MPa} \cdot \text{m}^{0.5}$$

**APPENDIX B: I. Processing parameters used in laser surface polishing of flat surfaces  
and surface roughness results**

**Specimen #1**

<b>Track #</b>	<b>SS parameter</b>	<b>SP parameter</b>	<b>Voltage V</b>	<b>Power W</b>	<b>Process Time s</b>	<b>Trav. Speed mm/s</b>	<b>Scan Speed mm/s</b>	<b>Energy Den J/cm2</b>
1	760	75	0.25	225	7.10	3.58	537.00	104.75
2	760	100	0.25	225	9.60	2.65	396.88	141.73
3	760	150	0.25	225	13.22	1.92	288.20	195.18
4	760	175	0.25	225	15.13	1.68	251.82	223.38
5	760	200	0.25	225	17.56	1.45	216.97	259.25
6	760	250	0.25	225	21.55	1.18	176.80	318.16
7	760	300	0.25	225	24.91	1.02	152.95	367.77
8	760	350	0.25	225	28.58	0.89	133.33	421.88
9	760	400	0.25	225	33.03	0.77	115.35	487.65
10	760	450	0.25	225	36.41	0.70	104.64	537.55
11	760	500	0.25	225	40.61	0.63	93.82	599.56

<b>Track #</b>	<b>As-received Roughness before process microns</b>	<b>Std Dev</b>	<b>Average Roughness after process microns</b>	<b>Std Dev</b>	<b>%RV</b>	<b>Std Dev %RV</b>
1	2.36	0.13	2.95	0.59	15.34	23.19
2	2.36	0.13	2.28	0.32	-8.60	12.95
3	2.36	0.13	2.26	0.19	-1.93	8.07
4	2.36	0.13	2.04	0.27	-15.81	11.03
5	2.36	0.13	2.27	0.14	-8.79	5.50
6	2.36	0.13	2.65	0.30	20.44	13.65
7	2.36	0.13	2.01	0.26	-14.60	11.01
8	2.36	0.13	2.09	0.21	-17.65	8.30
9	2.36	0.13	2.57	0.42	9.08	17.71
10	2.36	0.13	3.24	0.21	32.61	8.56
11	2.36	0.13	4.57	0.42	77.21	16.17

**Specimen #2**

**Track #**

	<b>SS parameter</b>	<b>SP parameter</b>	<b>Voltage V</b>	<b>Power W</b>	<b>Process Time s</b>	<b>Trav. Speed mm/s</b>	<b>Scan Speed mm/s</b>	<b>Energy Den J/cm2</b>
1								
2	760	50	0.4	334	5.5	4.6	692.7	120.5
3	760	75	0.4	334	7.5	3.4	511.4	163.3
4	760	100	0.4	334	9.5	2.7	403.2	207.1
5	760	125	0.4	334	11.5	2.2	332.8	250.9
6	760	150	0.4	334	13.5	1.9	282.2	295.9
7	760	175	0.4	334	15.5	1.6	245.8	339.7
8	760	200	0.4	334	17.3	1.5	220.9	378.1
9	760	225	0.4	334	19.5	1.3	195.9	426.3
10	760	250	0.4	334	21.5	1.2	177.2	471.2
11	760	275	0.4	334	23.5	1.1	162.1	515.0
12	760	300	0.4	334	25.5	1.0	149.4	558.9
13	760	350	0.4	334	29.6	0.9	128.9	647.6
14	760	400	0.4	334	33.6	0.8	113.4	736.4
	760	450	0.4	334	37.6	0.7	101.3	824.0

<b>Track #</b>	<b>As-received Roughness before process microns</b>	<b>Std Dev</b>	<b>Average Roughness after process microns</b>	<b>Std Dev</b>	<b>%RV</b>	<b>Std Dev %RV</b>
1	2.42	0.29	2.31	0.24	-20.47	8.1
2	2.42	0.29	2.51	0.25	-6.52	9.2
3	2.42	0.29	2.39	0.17	-12.08	6.3
4	2.42	0.29	2.69	0.33	9.13	13.2
5	2.42	0.29	1.87	0.14	-19.39	6.2
6	2.42	0.29	1.93	0.39	-18.05	16.6
7	2.42	0.29	1.51	0.46	-36.71	19.4
8	2.42	0.29	1.92	0.27	-16.12	11.6
9	2.42	0.29	1.57	0.31	-28.37	14.1
10	2.42	0.29	1.94	0.39	-14.74	17.3
11	2.42	0.29	1.98	0.48	-15.62	20.4
12	2.42	0.29	1.89	0.52	-22.28	21.3
13	2.42	0.29	2.26	0.64	-12.20	24.8
14	2.42	0.29	3.24	0.56	28.82	22.5



**Specimen #3**

Track #	SS parameter	SP parameter	Voltage V	Power W	Process Time s	Trav. Speed mm/s	Scan Speed mm/s	Energy Den J/cm2
1	760	30	0.45	420	4.6	5.52	828.26	126.77
2	760	50	0.45	420	5.5	4.62	692.73	151.57
3	760	100	0.45	420	9.6	2.65	396.88	264.57
4	760	125	0.45	420	11.6	2.19	328.45	319.69
5	760	150	0.45	420	13.22	1.92	288.20	364.33
6	760	175	0.45	420	15.13	1.68	251.82	416.97
7	760	200	0.45	420	17.56	1.45	216.97	483.94
8	760	225	0.45	420	19.25	1.32	197.92	530.51
9	760	250	0.45	420	21.55	1.18	176.80	593.90
10	760	300	0.45	420	24.91	1.02	152.95	686.50
11	760	400	0.45	420	33.03	0.77	115.35	910.28

1	760	30	0.45	420	4.6	5.52	828.26	126.77
2	760	50	0.45	420	5.5	4.62	692.73	151.57
3	760	100	0.45	420	9.6	2.65	396.88	264.57
5	760	150	0.45	420	13.22	1.92	288.20	364.33

Track #	As-received Roughness before process microns	Std Dev	Average Roughness after process microns	Std Dev	%RV	Std Dev %RV
1	2.06	0.25	2.49	0.38	19.26	18.01
2	2.06	0.25	2.58	0.80	34.20	41.50
3	2.06	0.25	3.13	0.48	56.40	24.15
4	2.06	0.25	2.53	0.59	20.43	28.04
5	2.06	0.25	2.64	0.22	22.36	10.15
6	2.06	0.25	2.30	0.62	1.84	27.27
7	2.06	0.25	1.65	0.30	-23.74	13.84
8	2.06	0.25	1.70	0.21	-15.42	10.67
9	2.06	0.25	2.19	0.31	9.94	15.67
10	2.06	0.25	2.47	0.30	19.68	14.33
11	2.06	0.25	3.81	0.89	66.25	38.61
1	2.06	0.25	1.60	0.33	-24.91	15.40
2	2.06	0.25	1.68	0.11	-10.57	6.08
3	2.06	0.25	3.63	0.26	83.81	13.02
5	2.06	0.25	5.03	0.56	128.21	25.49

**Specimen #4**

Track #	SS parameter	SP parameter	Voltage V	Power W	Process Time s	Trav. Speed mm/s	Scan Speed mm/s	Energy Den J/cm2
1	760	30	0.65	565	4.5	5.66	849.50	166.27
2	760	65	0.65	565	6.8	3.71	557.02	253.58
3	760	100	0.65	565	9.4	2.71	406.40	347.56
4	760	150	0.65	565	13.6	1.87	279.94	504.57
5	760	200	0.65	565	17.3	1.47	220.10	641.74
6	760	300	0.65	565	25.1	1.01	151.82	930.36
7	760	400	0.65	565	32.6	0.78	116.73	1210.08
1	760	30	0.65	565	4.5	5.66	849.50	166.27
3	760	100	0.65	565	9.4	2.71	406.40	347.56
4	760	150	0.65	565	13.6	1.87	279.94	504.57
6	760	300	0.65	565	25.1	1.01	151.82	930.36
	<b>As-received Roughness before process microns</b>	<b>Std Dev</b>	<b>Average Roughness after process microns</b>	<b>Std Dev</b>	<b>%RV</b>	<b>Std Dev %RV</b>		
1	2.35	0.22	2.53	0.24	2.58	9.75		
2	2.35	0.22	1.78	0.11	-27.74	4.57		
3	2.35	0.22	1.77	0.15	-28.92	6.19		
4	2.35	0.22	1.76	0.13	-30.73	4.94		
5	2.35	0.22	2.21	0.23	-15.92	8.63		
6	2.35	0.22	2.39	0.38	-6.50	14.70		
7	2.35	0.22	2.99	0.71	14.50	27.09		
1	2.35	0.22	3.20	0.33	25.52	12.97		
3	2.35	0.22	3.09	0.48	30.39	20.17		
4	2.35	0.22	3.36	0.41	23.56	15.12		
6	2.35	0.22	3.96	0.22	54.68	8.62		

Appendix B: II. Processing parameters used in laser fusion coatings of C/C flat specimens and laser induced cementation of C/C composite cylindrical specimens.

Flat specimens

Specimen #	Coating type	Scan condition	Atmosphere	Power signal Volts	Speed mm/sec	Results
6f	Si	1	85 mTorr	240	5	Nd:YAG, partial coating
16g	#7	1	200/500 mTorr, Ar	1020	5	Partial coating
16g	#7	2	200/500 mTorr, Ar	1020	16.5	No improvement during spreading
67	#11	Wedge shape, all length coated	150 mTorr / 2 Torr Arg	1020	55	Good spreading , no balling, opaque surface, no defocusing effect observed
71a	#15	Rounded edges sample, all coated front face	150 mTorr / 2 Torr Arg	1020	60	Good spreading, some balling, shiny surface
71b	#11	Same sample, same face, recoated	150 mTorr / 2 Torr Arg	800	80	Good spreading, less balling, less shiny surface
71c	#15	All coated back face	150 mTorr / 2 Torr Arg	1020	65	Good spreading, some balling, shiny surface
71d	#11	Same sample, same face, recoated	150 mTorr / 2 Torr Arg	850	80	Good spreading, less balling, less shiny surface
71e	Silbond	All coated front face	150 mTorr / 2 Torr Arg	280	90	Good spreading, less balling, opaque surface

Slurry PP	Weight (gr)	Wt. %
Ti	0.5085	79%
HfC	0.1285	20%
PVB	0.0045	1%
<b>Total</b>	<b>0.6415</b>	
Slurry QQ	Weight (gr)	Wt. %
Si	0.14063	18%
HfC	0.5198	67%
Ti	0.1073	14%
PVB	0.0035	0%
<b>Total</b>	<b>0.77123</b>	

Slurry RR	Weight (gr)	Wt. %
CrCl3	1.0016	99%
PVB	0.0133	1%
<b>Total</b>	<b>1.0149</b>	
Slurry SS	Weight (gr)	Wt. %
Si	0.9998	47.9%
SiC	0.248	11.9%
CrCl3	0.2147	10.3%
HfC	0.6121	29.3%
PVB	0.0121	0.6%
<b>Total</b>	<b>2.0867</b>	

Specimen #	Coating type	Scan condition	Atmosphere	Power signal Volts	Speed mm/sec	Remarks
259	PP-0.07 gr.	Position#3, side A	1 mTorr+Argon	1.1-0.4	28/190	Good spreading
259	PP-0.15 gr.	Position#2 side B	1 mTorr+Argon	1.1-0.45	28/190	Good spreading
259	PP-0.04 gr.	Position#3 side A	1 mTorr+Argon	1.3-0.55	28/190	Some coating burned off
259	QQ-0.29 gr.	Position#3 side B	1 mTorr+Argon	1.1-0.45	28/190	Spreading with uneven thickness
259	QQ-0.13 gr.	Position#3 side A	1 mTorr+Argon	1.1-0.35	28/190	Good spreading
259	QQ-0.13 gr.	Position #3 side B	1 mTorr+Argon	1.1-0.45	28/190	Good spreading
259	QQ-0.13 gr.	Position #3 side B	1 mTorr+Argon	1.1-0.45	28/190	Good overall coating
259	QQ-0.09 gr.	Position #3 side A	1 mTorr+Argon	1.1-0.45	28/110	Good overall coating
259	Silbond-0.03 gr.	30 min	Dried in air			To Karta for WLT.
261	RR-0.12 gr.	Position #3 side A	1 mTorr+Argon	0.5-0.2	28/190	Some spreading
261	RR-0.34 gr.	Position #3 side B	1 mTorr+Argon	0.4-0.2	28/190	Some spreading
261	SS-0.07 gr.	Position #3 side A	1mmTorr+Argon	1.0-0.4	28/190	Moderate spreading
261	SS-0.07 gr.	Position #3 side A	1mTorr+Argon	1.0-0.4	28/190	Moderate spreading
261	SS-0.1 gr	Position #3 side B	1mTorr+Argon	0.6-0.2	28/190	Good spread, thin
261	SS-0.1 gr	Position#3 side B	1mTorr+Argon	0.6-0.3	28/190	Good spread, thin
261	Silbond??	Sides A and B	Atmospheric			Good, overall coating Sent to KARTA for WLT
270	Cr-0.1 gr	Position # 1 Side A	200mTorr+Argon	0.5-0.3	28/190	Good spreading
270	RR-0.25 gr	Position # 1 Side A	200mTorr+Argon	0.9-0.4	28/190	Good spreading
270	Cr-0.1 gr	Position # 1 Side B	200mTorr+Argon	0.5-0.3	28/190	Good spreading
270	RR-0.25 gr	Position # 1 Side B	200mTorr+Argon	0.9-0.4	28/190	Good spreading, thin
270	Silbond	Sides A and B	Atmospheric			Good, overall coating Sent to KARTA for WLT.

### Cylindrical specimens

Specimen #	Coating type & sequence	Mass mg	Power signal volts	Speed mm/s	Vacuum mTorr	Gas	Remarks
2	CrCl3		0.5	28/140	200	Ar	
	CrCl3		0.4	28/140	200	Ar	
	Si	30	1.5	28/140	200	Ar	
	Si		1.5	28/140	200	Ar	
	Si02-30Si-10SiC	75	0.8	28/140	300	Ar	Mounted for SEM
3	CrCl-30Cr		0.5	28/140	200	Ar	Mounted for SEM

Specimen #	Coating type & sequence	Mass mg	Power signal volts	Speed mm/s	Vacuum mTorr	Gas	Remarks
5	CrCl-30Cr	27	0.5	28/140	200	Ar	
	Si-50HfC		1.2	28/140	200	Ar	
	Si-50HfC	360	1.5	28/140	200	Ar	
	SiO2-30Si-10SiC	56	0.8	28/140	300	Ar	Mounted for SEM
8	CrCl-30Cr	20	0.6	28/140	200	Ar	Mounted for SEM
	Si-35HfCHT750	111	1.0	28/140	250	Ar	
	Si-35HfCHT750		1.0	28/140	200	Ar	Good results
	SiO2-10Si-5SiC	14	1.0	28/140	300	Ar	Good coating, shinny, however not full covered
	SiO2-10Si-5SiC	-23	1.0	28/140	300	Ar	Worse, green deposit
	SiO2-10Si-5SiC	25	0.6	28/140	300	Ar+N 2	Not good, less shiny
15	CrCl-30Cr	26	0.2-0.5	28/140	500	Ar	Good results
15	CrCl-30Cr	26	0.2-0.5	210	500	Ar	Good coating
	Si-25Cr-5C	26	0.2,0.2-0.5, 0.5-0.9	70,30,110	180	Ar	Good coating
	Si-25Cr-5C	86	0.2,0.2-0.9-0.7	70,140	400	Ar	Good coating
	Si-30HfCl-15Cr	87	0.2-0.3,0.2-1.3-0.7	70,140	200	Ar	Good coating
	Si-30HfCl-15Cr	44	0.2-0.4,0.4-1.3-0.7	70,140	2000	Ar	Not good coating
	Si-30HfCl-15Cr	209	0.2-0.4,0.4-1.3-0.8	70,140	300	Ar	Not good coating
	Si-15HfCl-5Cr-5SiC	266	0.2-0.45,0.45-1.3-0.9	70,140	180	Ar	Good coating WLT in air
16	Si-25Cr-5C	110	0.2,0.2-1.0	90,155	200	Ar	Good coating
	Si-25Cr-5C	94	0.2,0.2-1.0-0.7	70,155	180	Ar	Good coating
	Si-30HfCl-15Cr	156	0.2,0.2-0.9-0.7	70,155	500	Ar	Not good coating
	Si-30HfCl-15Cr	95	0.2-0.4,0.4-1.3-0.9	70,155	350	Ar	Good coating
	Si-15HfCl-5Cr-5SiC	308	0.2-0.5,0.5-1.3-0.9	70,155	300	Ar	Good coating WLT in argon
17	Si-25Cr-5C		0.2,0.2-1.0-0.7	70,155	400	Ar	Good coating
	Si-25Cr-5C	135	0.2,0.2-1.0-0.7	70,155	400	Ar	Good coating
	Si-30HfCl-15Cr	77	0.25-0.3,0.3-1.2-0.8	70,155	400	Ar	Good coating
	Si-30HfCl-15Cr	61	0.2-0.4,0.4-1.5-0.9	70,155	350	Ar	Good coating
	Si-15HfCl-5Cr-5SiC	375	0.2-0.7,0.7-1.2-0.9	70,155	180	Ar	Good coating Given to Air Force
18	Si-25Cr-5C		0.2,0.2-0.1.0-0.7	70,155	300	Ar	Good coating
	Si-25Cr-5C	45	0.2,0.2-1.0-0.7	70,155	350	Ar	Good coating
	Si-30HfCl-15Cr	111	0.25-0.3,0.3-1.3-0.9	70,155	400	Ar	Good coating
	Si-30HfCl-15Cr	126	0.2-0.4,0.4-1.4-0.9	70,155		Ar	Not good coating
	Si-30HfCl-15Cr	51	0.2-0.4,0.4-1.1-0.7	70,155	300	Ar	Good coating
	Si-15HfCl-5Cr-5SiC	157	0.2-0.5,0.5-1.4-0.9	70,155	180	Ar	Good coating HT in argon & SEM

Specimen #	Coating type & sequence	Mass mg	Power signal volts	Speed mm/s	Vacuum mTorr	Gas	Remarks
------------	-------------------------	---------	--------------------	------------	--------------	-----	---------

24	35Cr-65CrCl	92	0.2,0.2,0.2	60,135,135	100	Ar	Good coating
	35Cr-65CrCl	121	0.2	155	200	Ar	Good coating
	Si-25Cr-5C	180	0.2-0.3,0.3-0.5,0.5-1.2-0.5	60,155,155	300	Ar	Good coating
	Si-25Cr+5CrCl+5C	135	0.1-0.3,0.4-0.7,0.2-0.7,0.7-1.0	60,165,60,165	200	Ar	Good coating
	Si-35HfCl-15Cr	221	0.1-0.4,0.4-0.8,0.2-0.8,0.8-1.3	60,165,60,165	200	Ar	Good coating
	Si-35HfCl-15Cr	228	0.1-0.4,0.4-0.8,0.2-0.8,0.8-1.3	60,165,60,165	120	Ar	Good coating
	Si-15HfCl-7Cr-7SiC	92	0.2-0.5,0.5-1.0,0.5-1.0,1.0-1.5	60,165,60,165	200	Ar	Lumps presents
	SILBOND						WLT, then SEM

28	35Cr-65CrCl	19	0.2+w, 0.2+w	60,165	150	Ar	Good coating
	Si-30Cr-5CrCl-5C		0.1-0.3,0.3-0.5,0.5-1	60,165,330	2000	Ar	Some oxidation
	Si-25Cr+5CrCl+5C	115	0.1-0.4,0.4-0.7,0.2-0.7,0.7-1.0	60,165,60,165	200	Ar	Good coating
	Si-35HfCl-15Cr	131	0.1-0.4,0.4-0.8,0.2-0.8,0.8-1.3	60,165,60,165	200	Ar	Good coating, kept at UT
29	35Cr-65CrCl	42	0.2+w, 0.2+w	60,165	300	Ar	Some oxidation
	Si-30Cr-5CrCl-5C	146	0.1-0.3,0.4-0.6,0.3-0.7	60,165,330	200	Ar	Black spots
	Si-25Cr+5CrCl+5C	170	0.1-0.4,0.4-0.7,0.2-0.7,0.7-1.0	60,165,60,165	200	Ar	Good coating
	Si-35HfCl-15Cr	75	0.1-0.4,0.4-0.8,0.2-0.8,0.8-1.3	60,165,60,165	200	Ar	Good coating
	Si-15HfCl-7Cr-7SiC	173	0.2-0.5,0.5-1.0,0.5-1.0,1-1.5	60,165,60,165	200	Ar	Good coating, WLT.

Specimen #	Coating type & sequence	ACM mg	CMR mg	Power signal volts	RPS rev/sec	Time sec	Vac mTorr	Gas	Remarks
------------	-------------------------	--------	--------	--------------------	-------------	----------	-----------	-----	---------

32	Cr-70CrCl	120	15	0.2+2,0.2+w	1.6 V 1/165	90s,165t	200	Ar	Some coverage but not shiny
	Si-30Cr-5C	70	35	0.2-0.3,0.3-0.6,0.6-1	1.6 V 1/165	60s,165t,165t	140	Ar	Smooth and overall coated
	Si-30Cr-5C	109	105	0.2-0.3,0.3-0.6,0.6-1	1.6 V 1/165	60s,165t,165t+90	160	N2	Overall coating, dull color
	Si-30HfCl-15Cr	117	50	0.2-0.4,0.4-0.5, 0.5-1.3	1.6 V 1/165	60s,165t,165t	120	Ar	Good overall coating, but not as smooth as previous
	Si-30HfCl-15Cr	160	96	0.2-0.5,0.5-0.9,0.9-1.3	1.6 V 1/165	60s,165t,165t	120	Ar	
	Si-15HfCl-5Cr-5SiC	95	80	0.2-0.5,0.5-1,1-1.4	1.6 V 1/165	60s,165t,165t	120	Ar	Very good results better than previous
	Si-15HfCl-5Cr-5SiC	92	67	0.2-0.5,0.5-1,1-1.5	1.6 V 1/165	60s,165t,165t	120	Ar	Good overall coating
	Total mass deposited		448						

Specimen #	Coating type & sequence	ACM mg	CMR mg	Power signal volts	RPS rev/sec	Time sec	Vac mTr	Gas	Remarks
40	Cr-50CrCl	178	53	0.2,0.5,0.5-0.2	3.2 V, 1/80	80t,80t,80t	100	Ar	Good processing, good overall coating, silver
	Si-25Cr-5CrCl-5C	125	85	0.2-0.5,0.5-0.75,0.75-1,1-0.2	3.2 V, 1/80	60s,80t,80t,40t	150	Ar	Good processing, good coating
	Si-30HfCl-10Cr	80	74	0.2-0.5,0.5,0.5-1.0,1-0.2	3.2 V, 1/80	75s,80t,80t,25t	100	Ar	Best coating so far
	Glazing	0		0.2-0.75,0.75-1.5,1.5-0.2	3.2 V, 1/80	80t,80t,80t	200	Ar	More smooth and shinier
	Total mass		212						

43	Cr-60CrCl	203	32	0.15+w	1.6 V	160t	120	Ar	Less bright processing, not very good but coating is present.
	Si-25Cr-5CrCl-5C	69	NA	0.15,0.2	1.6 V	30,160t	180	Ar	Bright processing, not good, carbon soot and oxidation present.
	Si-25Cr-5CrCl-5C	NA	NA	0.15,0.2-0.3,0.3-0.2	1.6 V	30,160t,80t	120	Ar	Orange processing, good results, overall coating some oxidation is present.
	Si-30Cr-5C	211	147	0.2-0.3,0.3-0.4,0.3-0.6,0.6-0.2	1.6 V	30,160t,160t,80t	150	Ar	Good processing, good results.
	Si-15Cr-15HfCl	419	139	0.2-0.3,0.3,0.3-0.8,0.8-0.2	1.6 V	45,160t,160t,80t	100	Ar	Good processing.
	Laser cleaning		-6	0.2-10,-0.2	1.6 V	160t	150	Ar	Good processing.
	Total mass added		>312						
	Na <sub>2</sub> CO <sub>3</sub> -70SiO <sub>2</sub> +waterglass			0.2-1.5	1.6 V	240	64	Ar	No rotation of sample, line gash was then filled with water-glass.
	WLT at 1000oC in air								WLT then SEM.
44	Cr-40CrCl	105	37	0.15-0.2	1.6 V	160t	100	Ar	Bright processing, good results only were laser was at 0.15 V.
	Si-25Cr-5C	127	113	0.15-0.2,0.2-0.6,0.6-0.2	2.0 V 1/135	30,135t,67t	200	Ar	Good average process, excellent results. Full coverage and shiny.
	Si-150Cr-15HfCl	214	112	0.15-0.2,0.25-0.6,0.6-1,1-0.3	2 V, 3.2 V	45,135t,80t,10t	170	Ar	Good processing, excellent good result overall shiny.
	Total mass added		262						
	Na <sub>2</sub> O+2SiO <sub>2</sub> +waterglass	406	160					Ar/Air	Fired at 300 °C for 15 min and then at 850 °C for 15 min. Sent to Air Force for WLT.
45	Cr-40CrCl	145	46	0.15	1.6 V	160t	200	Ar	Bright processing full coverage but not shiny.
	Si-25Cr-5C	98	75	0.15-0.2,0.2-0.6,0.6-0.2	2.0 V	30, 135t, 67t	200	Ar	Good average processing, excellent results.
	Si-15Cr-15HfCl	211	145	0.15-0.2,0.25-0.6,0.6-1.0,1-0.2	2.0, 3.2 V	30,135t,80t,15t	180	Ar	Good processing, overall good results.
	Total mass added		266						
	Na <sub>2</sub> O+2SiO <sub>2</sub> +waterglass	544	240					Ar	Fired at 300 °C for 15 min and then at 850 °C for 15 min.

Specimen #	Coating type & sequence	ACM mg	CMR mg	Power signal volts	RPS rev/sec	Time sec	Vac mTorr	Gas	Remarks
46	Cr-40CrCl	105	35	0.15	1.6 V	160t	80	Ar	Bright processing full coverage but not gold in color.
	Si-25Cr-5C	92	61	0.15-0.2,0.25-0.7,0.7-0.2	2.0 V	30,135t,67t	200	Ar	Good processing, excellent result.
	Si-15Cr-15HfCl	224	157	0.15-0.2,0.2-0.6,0.6-1,1-0.2	2.0V,3.2 V	30,135t,80t,20t	180	Ar	Good processing, excellent results shiny all covered.
	Total mass added		253						
	SiO <sub>2</sub> +waterglass (two powders grain size used)	307							
47	Cr-40CrCl	160	NA	0.2	1.6 V	160t	80	Ar	Bright processing full coverage but not shiny some soot spots.
	Si-25Cr-5C	NA	NA	0.15-0.2,0.25-0.7,0.7-0.2	2.0 V	30,135t,67t	200	Ar	Good processing.
	Si-15Cr-15HfCl	204	148	0.15-0.2,0.2-0.6,0.6-1,1-0.2	2.0V,3.2 V	30,135t,80t,20t	200	Ar	Good processing, orange color excellent results shiny all covered.
	Total mass added		>148						
	SiO <sub>2</sub> +waterglass (two powders grain size used)	353	167					Ar	Fired at 300 °C for 15 min and then at 850 °C for 15 min. Sent to Air Force for WLT.

ACM: applied coating mass before process  
CMR: coating mass remaining after process



APPENDIX B: III. Process parameters of single layer laser powder masked deposits.

Specimen #	P W	L mm	W mm	$\Delta t$ s	$1-\phi$	$V_t$ mm/s	$V_s$ mm/s	E $J/mm^2$	CR $^{\circ}C/s$	$G_L$ $^{\circ}C/mm$	$T_o$ $^{\circ}C$	$R_L=V_t$ in/s	$G_L$ $^{\circ}F/in$
21	235	27.6	1.40	19	0.01089	1.5	533.1	115.7	2012	1384	25	0.057	59135
22	235	27.6	1.40	19	0.01089	1.5	533.1	115.7	2012	1384	25	0.057	59135
31	230	27.6	1.40	19	0.01089	1.5	533.1	113.2	487	335	700	0.057	14312
51	125	28.5	0.76	26.4	0.01125	1.1	209.3	151.7	519	480	775	0.043	20523
52	140	28.5	0.76	26.4	0.01125	1.1	209.3	169.9	464	429	775	0.043	18324
53	250	27.6	0.95	15	0.01089	1.8	460.4	142.5	360	196	830	0.073	8361
54	205	27.6	0.95	26.5	0.01089	1.0	260.6	206.5	249	239	830	0.041	10196
55	250	27.6	0.95	15	0.01089	1.8	460.4	142.5	353	192	835	0.073	8198

## REFERENCES

- J.C. Ambrose, M.G. Nicholas and A.M. Stoneham, *Acta. Metall. Mater.* 40, 2483 (1992).
- G.R. Anstis, P. Chantikul, B.R. Lawn, D.B. Marshall, *Journal of the American Ceramic Society*, v. 64, No. 9, 533-538 (1981).
- S. Ahn, Ph.D. Dissertation Thesis, in progress, University of Texas at Austin, 2003.
- T.R. Anthony and H.E. Cline, *J. Applied Physics*, Vol. 48, No 9, 3888-3894 (1977).
- M.F. Ashby, Materials Selection in Mechanical Design, (Butterworth Heinemann, 1992).
- ASM Metals Handbook, 9<sup>th</sup> edition, v.1,2,3, (Metals Park, Ohio, 1987).
- V.S. Avanesov and M.A. Zuev, "Investigation of surface topography after melting by laser beam", SPIE, Vol. 2713, 340-343.
- J.C. Bailar, H.J. Emeleus, R. Nyholm and A.F. Trotman-Dickenson, Eds., Comprehensive Inorganic Chemistry, v.3, (Elmsford, N. Y., 1973).
- M.W. Barsoum, Fundamental of Ceramics, (McGraw Hill, 1997).
- H. D. Batha, C.R. Rowe, "Structurally reinforced carbon-carbon composites", Engineered Materials Handbook, v. 1, Composites, ASM International, Metals Park, OH, 922-924 (1987).
- J.J. Beaman, J.W. Barlow, D.L. Bourell, and R.H. Crawford, Solid Freeform Fabrication: A New Direction in Manufacturing, (Kluwer Academic, 1997).
- Bestenlehrer, "Polierwerkstatt fuer Stahlformen," US Patent 6043452, (March 2000).
- B. Boley, J. Weiner, Theory of Thermal Stresses, (Dover, 1988).
- Leo Brewer, "Chemical Bonding Theory Applied to Metals", Alloying, J.L. Walter, M.R. Jackson, and C.T. Sims Eds., (ASM International, 1988).
- D. Burgreen, Elements of Thermal Stress Analysis, (C.P. Press, 1971).
- J.D. Buckley, "Carbon-Carbon: an overview", *Ceram. Bull.*, v. 67, 2, 364-368 (1988).

M. Burns, Automated Fabrication: Improving Productivity in Manufacturing (Prentice-Hall, 1993).

C.A.A. Cairo, M.L.A. Graca, C.R.M. Silva, J.C. Bressiani, *Journal of the European Ceramic Society*, 21, 325-329 (2001).

H.S. Carls and J.C. Jaegger, Conduction of Heat in Solids, (Oxford, 1996).

J. Connolly, Direct Rapid Manufacturing – Is it Possible?, *Time Compression Technologies*, May (2001), pp. 46-47.

A. Conde, R. Colaco, R. Vilar, J. de Damborenea, “Corrosion behavior of steels after laser surface melting”, *Materials & Design*, 21, 441-445 (2000).

G. Danyo, M.Sc. Thesis, University of Texas at Austin, (1998).

N.B. Dahotre, Lasers in Surface Engineering: Surface Engineering Series, v. 1, (ASM International, 1999).

S. Das, Ph.D. Dissertation, University of Texas at Austin, December 1998.

S. Das *et al.*, “Direct laser fabrication of a gas turbine engine component – microstructure and properties – part I”, *SFF Symposium Proc*, 10, 1-9 (1998).

C.R. Deckard, “Method and apparatus for producing part by selective sintering”, US Patent 4863538 (September 1989).

J. Th. M. De Hosson, “Laser synthesis and properties of ceramics”, in Intermetallic and Ceramic Coatings, Eds. N.B. Dahotre and T.S. Sudarshan, (Marcel Dekker, 1999).

DTM-Corporation, “Housings for hearing aid transmitter created within two month window”, *Horizons Q3*, 5-7 (2001).

J. Dundurs, *Journal of Applied Mechanics*, 36, 650 (1968).

N. Eustathopoulos, M.G. Nicholas, and B. Drevet Wettability at High Temperatures. Pergamon Materials Series Volume 3, Editor R.W. Cahn, (Pergamon, 1999).

G. Evans, M.D. Drory, M.S. Hu, “The cracking and decohesion of thin films, *J. Matter. Res.* 3, 1043-1049 (1988).

A. Favre, H. Fuzellier and J. Suptil, *Ceramics International*, 29, 235-243 (2003).

- A. Favre, H. Fuzellier and J. Suptil, *Ceramics International*, 29, 235-243 (2003).
- J.Feng, M.G.S. Ferreira, R. Vilar, "Laser cladding of Ni-Cr/Al<sub>2</sub>O<sub>3</sub> composite coatings on AISI 304 stainless steel", *Surface and Coatings Technology*, 88 212-218 (1996).
- F.CJ. Fellowes, W.M. Steen, K.S. Coley, *Eng. Matter.*, 46-47 (1990).
- David R. Gaskell, Introduction to the Thermodynamics of Materials, 3<sup>rd</sup> ed., (Taylor Francis, 1995).
- M. Gäumann *et al.*, "Epitaxial laser metal forming: analysis of microstructure formation", *Mat. Sci. Eng. A*, 271, 232-241 (1999).
- R.M. German, Liquid Phase Sintering, (Plenum Press, New York 1985).
- P. Gordon , Principles of Phase Diagrams in Materials Systems, (Krieger, 1983).
- R. Govindarajuand and J.A. Ramos, "Development of laser fusion coatings for improving oxidation resistance of carbon-carbon composites", 46<sup>th</sup> International SAMPE Symposium, April 2001.
- D.J. Green, An introduction to Mechanical Properties of Ceramics, (Cambridge 1998).
- Ø. Grong, N. Christensen, *J. Mater. Sci. and Tech.*, v. 2, 967-973 (1986).
- Ø. Grong, Metallurgical Modelling of Welding, Materials Modelling Series, (The Institute of Materials, 1994).
- M. Hansen and K Anderko, Constitution of Binary Alloys, (McGraw Hill, 1958).
- R.W. Hertzberg, Deformation and Fracture Mechanics of Engineering Materials, 4<sup>th</sup> ed., (Wiley, 1996).
- J.W. Hutchinson and Z. Suo, "Mixed mode cracking in layered materials"; in v. 29, Advances in Applied Mechanics. Edited by . J.W. Hutchinson and T.Y. Wu. (Academic Press, Inc., 1992).
- J. Hecht, Laser Pioneers 2<sup>nd</sup> edition (Press Academic, 1992).
- R.W.K. Honeycombe and H.K.D.H Bahadेशia, *Steels: Microstructure and Properties*, 2<sup>nd</sup> ed., (Edward Arnold, 1995).

- H.S. Hu, A. Joshi, J.S. Lee, "Microstructural evaluations of Si-Hf-Cr fused slurry coating on graphite for oxidation protection", *J.Vac. Sci. Technol.* A9, 3, 1535-1938 (1991).
- J.D. Hunt, "Steady state columnar and equiaxed growth of dendrites and eutectic", *Mat. Sci. Eng.*, 65, 75-83 (1984).
- F. P. Incropera, Fundamentals of Heat and Mass Transfer, 4th ed. (New York, 1996).
- C. Isola, P. Appendino, F. Bosco, M. Ferraris, and M. Salvo, "Protective glass coating for carbon-carbon composites." *Carbon*, v. 36, No 7-8, 1213-1218 (1998).
- U.K. Jarosch *et al*, "From welding to polishing", *Industrial Laser Solutions*, April (2003), pp.10-12.
- H.V. Johnson, US Pat. 1,948,382 (February 20, 1934).
- A.S. Khanan, High Temperature Oxidation and Corrosion, (ASM International, 2002).
- W. Kurz, D.J. Fisher, Fundamentals of Solidification, 4<sup>th</sup> ed. (Trans Tech Publication, 1998).
- K. Landry and N. Eustathopoulos, *Acta. Mater.* v.44, No 10, 3923-3932.
- F.F. Lange, "Healing of surface cracks in ceramics", Proc. Symposium Science of Ceramics Machining and Surface Finishing, 233-236 (1970).
- A. Joshi L.S. Lee, US Pat. 5,554,390 (September 10, 1996).
- K. Lappo, J.A. Ramos, J. Murphy, K. Wood, D.L. Bourell, J.J. Beaman in *Rapid Prototyping of Materials*, edited by F.D.S. Marquis and D.L. Bourell, (TMS, Warrendale PA, 2002), 185-190.
- B. Lawn, Fracture of Brittle Solids, 2<sup>o</sup> ed., (Cambridge, 1998).
- A. Joshi, J.S. Lee, "Microstructure and properties of protective coatings and carbon processed by fused slurry method", 39<sup>th</sup> International SAMPE Symposium, April (1994).
- A. Joshi, L.S. Lee, "Coatings with particulate dispersions for high temperature oxidation protection of carbon and C/C composites", *Composites - Part A: Applied Science and Manufacturing*, v. 28, No 2, 181-189 (1997).

- M.F. Kanninen, Advanced Fracture Mechanics, (Oxford University Press, 1985).
- L. Lü, J. Fuh and Y.S. Wong, Laser Induced Materials and Processes for Rapid Prototyping, (Kluwer Academic, 2001).
- J.A. McDonald, C.J. Ryall and D.I. Wimpenny, Rapid Prototyping Casebook, (Professional Engineering Publishing, 2001).
- M. McLean, Directionally Solidified Materials for High Temperature Service, (The Metals Society, London 1983).
- D.W. McKee, C.L. Spiro, E.J. Lamby, “The inhibition of graphite oxidation by phosphorous additives”, *Carbon*, v. 22, 3, 285-290 (1984).
- T. Morimoto, Y. Ogura, M. Kondo, and T. Ueda, “Multilayer coating for carbon-carbon composites”; *Carbon*, v.33, No 4, 351-357 (1995).
- J.Murphy, M.Sc. Thesis, in progress, University of Texas at Austin, 2003.
- S. Musikant, What Every Engineer Should Know About Ceramics , (Marcel Dekker, 1991).
- J.V. Naidich, "The wettability of solids by liquid metals" *Prog. Surf. Memb. Sci.*, 14, 353-484 (1981).
- N. Noda, R.B. Hetnarski and Y. Tanigawa, Thermal Stresses, (Lastran, 2000).
- M. A. Otooni, Elements of Rapid Solidification, Springer Series in Materials Science 29, (SpringerVerlag, 1998).
- N. Özisik, Heat Conduction, 2<sup>nd</sup> ed., (John Willey, 1993).
- T.S. Piwonka, “The influence of the mold/metal interface on casting quality in sand castings”, Solidification Science and Processing, Eds. I. Ohnaka, and D.M.Stefanescu, (TMS publishing, 1995).
- D.A. Porter and K.E. Easterling, Phase Transformations in Metals and Alloys, 2<sup>nd</sup> ed., (Chapman & Hall, 1992).
- J. Powell, P.S. Henry and W.M. Steen, “Laser cladding with preplaced powder: analysis of thermal cycling and dilution effects”, *Surface Engineering*, 4, 141-149, (1988).

A.M. Prokhorov, V.I.Konov, I. Ursu and I.N.Mihăilescu, Laser Heating of Metals, (Adam Hilger, 1990) pp.115-124.

V. Raghavan, Phase Diagram of Ternary Iron Alloys, Part 6B, (Indian Institute of Metals, Calcutta, 1992).

J.A. Ramos *et al.*, “Surface modification of 347 stainless steel by rapid mirror scanning of a high power CO<sub>2</sub> laser”, Proceedings of International Conference of Applied Lasers and Electro Optics, October 2002.

J.A. Ramos, D.L. Bourell and J.J. Beaman, Proceedings of the 2002 MRS Spring Meeting, Symposium LL, A. Piqué; A.S. Holmes; D. Dimos Eds., 53-61 (2003).

J.A. Ramos, D.L. Bourell in Rapid Prototyping of Materials, F.D.S. Marquis; D.L. Bourell Eds., TMS, Warrendale PA, 191-201 (2002).

J.F. Ready, ed., Lasers in Modern Industry (Society of Manufacturing Engineers, 1979).

J.F. Ready, D.F. Farson, and T. Feeley, eds., LIA Handbook of Laser Materials Processing (Laser Institute of America, Magnolia Publishing Inc., 2001).

J. R. Rice, *Journal of Applied Mechanics*, 55, 98 (1988).

D. Rosenthal, *Trans. ASME*, v. 68, 849-865 (1946).

R.C. Rossi, *Ceram. Bull.* 48(7), 736, (1969).

P. Shewmon, Diffusion in Solids, 2<sup>nd</sup> edition, (TMS, 1989).

D.Shi and I.Gibson, “Surface finishing of selective laser sintering parts with robot”, *SFF Symposium Proc.*, 9, 27-35 (1998).

L. Snell, A. Nelson and P. Molian, “A novel laser technique for oxidation-resistance coating of carbon-carbon composite”, *Carbon*, 39, 991-999 (2001).

J.L. Smialek, “Processing of fused silicide coatings for carbon-based materials”, Proc. of 7<sup>th</sup> annual Conf. on Composites & Advanced Ceramics Materials, 757-783 (1983).

J.D. Spencer, R.C. Cobb, and P.M. Dickens, “Vibratory finishing of stereolithography Parts”, *SFF Symposium Proc.*, 4, 27-39 (1993).

- J. F. Shackelford, W. Alexander, Eds. CRC –Materials Science and Engineering Handbook, 3<sup>rd</sup> ed. (CRC Press, 2001).
- M.C. Shaw, Metal Cutting Principles, (Oxford Science Publications, 1997).
- P. G. Shewmon, Diffusion in Solids, (TMS, 1990).
- J.E. Sheehan, “Oxidation protection for carbon fiber composites”, *Carbon*, v. 27, 5, 709-715 (1989).
- W.M. Steen, Laser Material Processing, 2<sup>nd</sup> edition, (Springer Verlag, 1993).
- D. Schuocker, High Power Lasers in Production Engineering, (Imperial College Press, World Scientific, 1999).
- J. R. Strife and J.E. Sheenan, “Ceramic coatings for carbon-carbon composites”, *Ceram. Bull.*, v. 67, 2, 369-374 (1988).
- J.N. Stuecker, D.A. Hirshfeld, D.S. Martin, “Oxidation protection of carbon-carbon composites by sol-gel ceramic coatings”, *Journal of Materials Science*, 34, 5443-5447 (1999).
- P.A. Temple, D. Milam, and W.H. Lowdermilk, *Applied Optics*, 21, 3249 (1982).
- I.Y.Tumer *et al.*, “Characterization of surface fault patterns with application to a layered manufacturing process”, *Journal of Manufacturing Systems*, 17 (1) (1998).
- P. Villars, A. Prince, H. Okamoto, Hand book of Ternary Alloy Phase Diagrams, v.7, (ASM, 1995).
- R. Voitovitch, A. Mortesen, F. Hodaj and N. Eutathoupoulos, *Acta Mater.* v.47 1117-1128 (1999).
- H.-Y.Wang, D.L.Bourell, and J.J.Beaman, “Laser polishing of silica slotted rods”, *Materials Science and Technology*, v. 19, (2003).
- M. E. Westwood *et al.*, “Review: oxidation protection for carbon fibre composites”, *Journal of Material Science*, 31, 1389-1397 (1996).
- J.H. Westbrook, Ed., Moffatt’s Handbook of Binary Phase Diagrams, (Genium Publishing Corp., 1997).



T. Young, *Philosophical Transactions of The Royal Society of London*, 95, 65 (1805).

X.B. Zhou and J. Th.M. De Hosson, "Influence of surface roughness on the wetting angle", *J. Mater. Res.*, v.10, N° 8, 1984-1992 (1995).

X.B. Zhou and J.Th.M.De Hosson, *Acta Metall.*, 39, 226, (1991).

X.B. Zhou, "Reaction coatings on metals by laser processing – a study on interface structures and wetting phenomena", Ph.D. Dissertation Thesis, University of Groningen, The Netherlands, October 1995.

## VITA

Jorge Andrés Ramos Grez was born in Santiago Chile on January 9, 1969, the son of Rolando Ramos Muñoz and Olga Grez Sahr. He finished his high school at the International School of Berne, Switzerland. He obtained his Bachelors degree in Engineering Sciences with a Major in Mechanical Engineering from Pontificia Universidad Católica de Chile (PUCCh) in spring 1993. He joined the Department of Mechanical and Metallurgical Engineering of the same university as an instructor in 1994. In 1996 he was granted a British Council Scholarship for graduate studies in the UK and obtained a Masters of Science and Engineering degree in laser materials processing from The University of Liverpool in fall 1997. He then returned to Chile to his former instructor position at PUCCh. In fall 1999 he joined the Materials Science and Engineering Program at The University of Texas at Austin where he started pursuing a Ph.D. degree in laser materials processing. In spring 2003 he obtained a Masters of Science degree in materials science and engineering. He also holds the Professional Industrial Engineer title granted by PUCCh (1994) as well as the Euro-Laser Engineer title from Technische Universität Wien (1997). He is married to Soledad Cahis and their two children, Catalina and Benjamín, were born in Austin Texas during this Ph.D. research period. He has been an active member of the Laser Institute of America since 1998 and has been involved for over 10 years in laser technology transfer to developing countries in South America. Currently he has been appointed Assistant Professor at the Department of Mechanical and Metallurgical Engineering of PUCCh.

Permanent address:

Gertrudis Echeñique 234 Depto. 602 / Las Condes / Santiago / CHILE

This dissertation was typed by the author.